Multirate modeling and simulation of pulse-width modulated power converters

TECHNISCHE
UNIVERSITÄT
DARMSTADT

et:t

ce   T E M F

Multirate modeling and simulation of pulse-width modulated power converters
Multiratenmodellierung und -simulation von pulsweitenmodulierten Stromrichtern

genehmigte Dissertation von Andreas Pels, geboren in Gießen, Deutschland
Fachbereich Elektrotechnik und Informationstechnik, Technische Universität Darmstadt

1. Gutachten: Prof. Dr. rer. nat. Sebastian Schöps
2. Gutachten: Prof. Dr. ir. Ruth V. Sabariego

Tag der Einreichung: 06. August 2019
Tag der Prüfung: 18. Oktober 2019

Darmstadt – D 17

Multirate modeling and simulation of pulse-width modulated power converters

Andreas Pels

Examination committee:
Prof. Dr.-Ing. H. De Gersem, chair
Prof. Dr. rer. nat. S. Schöps, supervisor
Prof. Dr. ir. R. V. Sabariego, supervisor
Prof. Dr. ir. S. Vandewalle
Prof. Dr.-Ing. G. Griepentrog
Prof. Dr. ir. J. Gyselinck

Dissertation presented in partial
fulfillment of the requirements for the
degree of Doctor of Engineering Science
(PhD): Electrical Engineering

January 2020

Zusammenfassung

Pulsweitenmodulierte Stromrichter transformieren elektrische Leistung zwischen verschiedenen Spannungs- und Stromebenen, um verschiedene Anwendungen zu versorgen. Im Vergleich zu herkömmlichen Transformatoren verwenden sie Transistoren und andere Halbleiterbauelemente, die die Eingangsspannung abrupt ein- und ausschalten, um am Ausgang des Stromrichters die gewünschte zeitgemittelte Spannung oder den gewünschten zeitgemittelten Strom zu erzeugen. Die so generierte gepulste Spannung wird üblicherweise durch aktive oder passive Filter gefiltert, um hochfrequente Signalanteile zu unterdrücken und die Ausgangsspannung zu glätten. Die numerische Simulation dieser Stromrichter ist aufwändig, da konventionelle Zeitschrittverfahren sehr kleine Zeitschritte benötigen, um die durch die Schaltvorgänge ausgelösten scharfen Transienten vernünftig darzustellen. Wenn das Schaltverhalten der Transistoren als ideal angenommen wird, ist es häufig sogar nötig, algorithmisch die zeitliche Position eines solchen Schaltvorgangs zu erkennen, da sonst ein Absturz des Zeitschrittalgorithmus die Folge sein könnte.

In dieser Dissertation wird ein effizienter Multiraten-Ansatz entwickelt. Die Idee besteht darin, die Lösung der gewöhnlichen Differentialgleichungen oder differential-algebraischen Gleichungen, die den Stromrichter beschreiben, in sich langsam verändernde Anteile (Einhüllende) und schnell verändernde periodische Anteile (Welligkeit) zu zerlegen. Dafür werden die Differentialgleichungen in einem ersten Schritt umgeformt in sogenannte Multiraten Partielle Differentialgleichungen (MPDEs). Diese erlauben es, verschiedene Lösungskomponenten explizit verschiedenen Zeitskalen zuzuordnen. Um die MPDEs zu lösen, werden zwei Methoden angewandt. Zunächst wird ein Galerkin Ansatz verwendet, um entlang der schnellen Zeitskala zu lösen. Drei verschiedene Typen von Basisfunktionen werden angesetzt: PWM Basisfunktionen, PWM Eigenfunktionen und B-spline Basisfunktionen. Als Nächstes wird auf das noch übrig gebliebene Differentialgleichungssystem ein konventionelles Zeitschrittverfahren angewandt, um es entlang der langsamen Zeitskala zu lösen. Dabei wird das Schaltverhalten der Transistoren als ideal angenommen, sodass diese sich durch ideale gepulste Spannungsquellen ersetzen lassen. Die Lösungskomponenten entlang der schnellen Zeitskala, also die Welligkeit der Lösung, wird mithilfe von Basisfunktionen dargestellt. Durch die Schaltvorgänge entstehen in manchen Lösungskomponenten C^0 stetige Stellen, die schon in der Konstruktion der Basisfunktionen berücksichtigt werden.

Der MPDE Ansatz wird auf verschiedene Testbeispiele angewandt, um die Genauigkeit und Effizienz numerisch zu überprüfen. Bisher lässt sich der Ansatz für einphasige DC-DC und DC-AC Stromrichter verwenden. Falls nichtlineare Bauelemente in den Stromrichtern oder den angeschlossenen Geräten vorkommen, erhöht sich der Rechenaufwand des Verfahrens. Für nichtlineare Bauelemente, z.B. nichtlineare Spulen, wird eine Vereinfachung vorgeschlagen, die weiterhin eine effiziente Simulation zulässt. Zur Generation der gepulsten Eingangsspannung erlaubt der MPDE Ansatz eine Pulsweitenmodulation (PWM) mit konstanter Schaltfrequenz und variablem Tastverhältnis. Als Trägersignal lassen sich Sägezahn- und Dreieckssignal einsetzen. Natürliche und digitale Abtastung werden unterstützt. Neben Schaltungen wird das Verfahren auch auf ein Feld-Netzwerk Modell angewandt.

Abstract

Pulse-width modulated power converters are devices which transform voltages and currents between different levels to meet the requirements of the appliances. In contrast to conventional transformers, they use transistors and other semiconductor components to abruptly switch on and off the input voltage source to generate an output voltage or current which, averaged in time, equals the desired values. The so-generated pulsed signal is usually filtered by an active or passive filter to suppress the high-frequency components and thus smoothen the output. The numerical simulation of these devices is computationally expensive since with conventional time discretization very small time steps are necessary to properly represent the steep transients induced by the abrupt switching of the semiconductor devices. If the semiconductor behavior is idealized, a switch event detection is often necessary to prevent a failure of the time integration algorithm.

In this dissertation a multirate approach is developed to efficiently tackle these problems. The idea is to split the solution of the ordinary differential or differential-algebraic equations describing the power converters into slowly varying parts and fast varying parts. The output of the converter is represented as a sum of fast periodically varying ripples and a slowly varying envelope. The differential equations are, in a first step, reformulated into so-called multirate partial differential equations (MPDEs), which allow to explicitly split the solution by associating the different components to different artificial time scales. The MPDEs are solved using a combination of two methods. First, a Galerkin approach is applied to solve along the fast time scale. Three different types of basis functions, namely PWM basis functions, PWM eigenfunctions and B-spline basis functions, are employed. Second, a conventional time integration algorithm is used on the remaining differential equation system. It is assumed that the semiconductor switching behavior can be idealized as such that it can be represented by an ideal pulsed voltage source. The solution components along the fast varying time scale, i.e. the ripples, are represented by basis functions, which are specifically designed for this purpose. Since in some of the solution components the ripples are only continuous and not smooth, the basis functions take these points of C^0 continuity at the proper position into account by construction.

The MPDE approach is applied to different examples to demonstrate its accuracy and efficiency. It is applicable to single-phase DC-DC and DC-AC power converters. If the power converter or the application consists of nonlinear elements the computational effort increases. For nonlinear elements, e.g. nonlinear inductors, a simplification is proposed which keeps the simulation efficient. To generate the pulsed excitation, a pulse-width modulation (PWM) with constant switching frequency and varying duty cycle is applicable. It is generated by either sawtooth or triangle carriers. Both natural or regular sampling are supported. Besides circuit simulation the method is also applied to a field-circuit coupled model.

Contents

List of figures

List of tables

List of acronyms

BDFs	backward differentiation formulas
BVP	boundary value problem
DAE	differential-algebraic equation
DOF	degree of freedom
FD	finite difference
FE	finite element
FEM	finite element method
IBVP	initial boundary value problem
IGBT	insulated-gate bipolar transistor
IRK	implicit Runge-Kutta
IVP	initial value problem
MPDE	multirate partial differential equation
MNA	modified nodal analysis
MQS	magnetoquasistatic
MVP	magnetic vector potential
ODE	ordinary differential equation
PEC	perfect electric conductor
PDE	partial differential equation
PDAE	partial differential-algebraic equation
PWM	pulse-width modulation
STA	sparse tableau approach
WaMPDE	warped MPDE

List of symbols

Continuous field quantities

Symbol	Unit	Description
$\mathbf{b}$	T	Magnetic flux density
$\mathbf{h}$	A/m	Magnetic field strength
$\mathbf{d}$	C/m^2	Electric flux density
$\mathbf{e}$	V/m	Electric field strength
$\mathbf{j}$	A/m^2	Total electric current density
$\mathbf{j_s}$	A/m^2	Impressed electric current density
$\mathbf{a}$	Wb/m	Magnetic vector potential
$\mathbf{a}^\star$	Wb/m	Modified magnetic vector potential
a_z	Wb/m	z-component of $\mathbf{a}^\star$
$\widetilde{a}_z$	Wb/m	Modified magnetic vector potential a_z with zero Dirichlet boundary conditions
u_g	Wb/m	Arbitrary function fulfilling non-homogeneous Dirichlet boundary condition
$j_{s,z}$	A/m^2	z-component of $\mathbf{j_s}$
ϕ	V	Electric potential
ρ	C/m^3	Electric charge density
q	C	Electric charge
ϵ	F/m	Electric permittivity
μ	H/m	Magnetic permeability
ν	m/H	Magnetic reluctivity
σ	S/m	Electrical conductivity
$\mathbf{r}$		Position vector
Ω		2D computation domain
Γ_N		Neumann boundary
Γ_D		Neumann boundary
γ_D	Wb/m	Dirichlet boundary condition
γ_N	A/m	Neumann boundary condition
Φ	Wb	Magnetic flux
$\boldsymbol{\chi}_\mathrm{str}$	1/m^2	Continuous winding function

Discrete field quantities

$\mathbf{a}_z$	Wb/m	Discretized modified magnetic vector potential a_z

$\widetilde{\mathbf{a}}_\mathrm{z}$	Wb/m	Discretized modified magnetic vector potential $\widetilde{a}_\mathrm{z}$
$\mathbf{u}_g$	Wb/m	Discretized u_g
$\mathbf{j}_\mathrm{s,z}$	A	Discretized current density vector $j_\mathrm{s,z}$
$\boldsymbol{\gamma}_\mathrm{N}$	A	Discretized Neumann boundary condition
$\mathbf{X}_\mathrm{str}$		Discretized winding function
$\mathbf{K}$	m/H	Magnetoquasistatic stiffness matrix
$\mathbf{M}$	Sm	Magnetoquasistatic mass matrix

Electric circuit quantities

Symbol	Unit	Description
v	V	Electric voltage
i	A	Electric current
L	H	Inductance
C	F	Capacitance
R	Ω	Resistance

Pulse-width modulation quantities

Symbol	Unit	Description
f_s	Hz	Switching frequency
f_ac	Hz	Frequency of sinusoidal reference signal
T_s	s	Switching cycle
D		Duty cycle
d		Reference signal
s		Carrier signal

MPDE approach quantities

Symbol	Description
$\mathbf{A}$	Mass matrix ODEs/DAEs
$\mathbf{B}$	System matrix ODEs/DAEs
$\mathbf{c}$	Right-hand side ODEs/DAEs
$\widehat{\mathbf{c}}$	Multirate right-hand side
$\mathbf{x}$	Solution of system of ODEs/DAEs
$\widehat{\mathbf{x}}$	Multirate solution of system of ODEs/DAEs
$\widehat{x}_j$	j-th element of the vector function $\widehat{\mathbf{x}}$
$\widehat{x}_j^h$	Approximation of $\widehat{x}_j$ in time
θ	Warping function

ω	Local frequency function
Υ	Single-rate time interval
$\widehat{\Upsilon}$	Multirate time interval
$t_1, \ldots, t_m$	Multirate time scales
t	Single-rate time
τ	Relative time
$\mathcal{A}$	Mass matrix of ODEs/DAEs after semi-discretization
$\mathcal{B}$	System matrix of ODEs/DAEs after semi-discretization
$\mathcal{C}$	Right-hand side of ODEs/DAEs after semi-discretization
$\mathbf{y}$	Vector of all coefficients
$\mathbf{y}_j$	Vector of $k = 0, \ldots, N_{\mathrm{p}}$ coefficients associated to the j-th solution component
$y_{j,k}$	Single coefficient
$\widetilde{\mathcal{J}}, \widetilde{\mathcal{Q}}, \widetilde{\mathcal{U}}$	Matrices consisting of products of basis functions and their derivatives
$\mathcal{J}, \mathcal{Q}, \mathcal{U}$	Integral of the matrices $\widetilde{\mathcal{J}}, \widetilde{\mathcal{Q}}, \widetilde{\mathcal{U}}$ with respect to the fast time scale t_2
d_1	Reference signal 1
d_2	Reference signal 2
$d_{\mathrm{del},1}$	Delayed reference signal 1
$d_{\mathrm{del},2}$	Delayed reference signal 2

Basis functions

Symbol	Description
$\mathbf{w}$	vector of basis functions
$\mathbf{w}_{\mathrm{pwm}}$	vector of PWM basis functions
$w_{\mathrm{pwm},i}$	i-th PWM basis function
$\mathbf{w}_{\mathrm{eig}}$	vector of PWM eigenfunctions
$w_{\mathrm{eig},i}$	i-th PWM eigenfunction
$P_{i,p}$	i-th B-spline basis function of degree p

Other quantities

Symbol	Description
L^2	Space of square integrable functions
C^0	Space of continuous functions
C^1	Space of continuous functions with one continuous derivative
$\mathbf{I}$	Identity matrix
λ	Eigenvalue
$\mathbf{v}$	Eigenvector
ϵ	Error
$N_{\mathrm{p}} + 1$	Total number of basis functions
N_{s}	Size of original equation systems

1 Introduction and motivation

Switch-mode power converters are found in a variety of applications [68] from everyday life to industrial appliances. Examples are mobile phone chargers, computer power supplies, electric cars, industrial welding, utility systems and more. These power converters transform electric power, i.e. voltage, current and/or frequency, between different levels to ensure compatibility between devices. They use power electronic switches, e.g. modern transistors, to periodically cut off and switch on the input voltage. Thereby the average output voltage is controlled which, after filtering the high-frequency components, supplies the application.

To control the transistor switching and provide the desired output voltage, a technique called pulse-width modulation (PWM) is often utilized. In such cases the power converters are also called PWM power converters. A typical PWM signal is depicted in Fig. 1.1. Important quantities are the switching frequency f_s, its corresponding switching period $T_s = \frac{1}{f_s}$ and the duty cycle D as further elaborated in Section 2.6. An exemplary power converter, namely a DC-DC buck converter (step-down converter) is depicted in Fig. 1.2. The insulated-gate bipolar transistor (IGBT), DC voltage source V_0 and the PWM signal generate the pulsed voltage $v_i(t)$. The diode acts as a valve to allow current flow while the transistor is in opened state. The rest of the circuit consists of the inductor L, the inductor resistance R_L and the capacitor C which together with the resistive load R form a low-pass filter circuit. It suppresses high-frequency components. Fig. 1.3 depicts the voltage at the capacitor/load and the current through the inductor for a sample excitation $v_i(t)$ with constant duty cycle and switching frequencies of $f_s = 500\,\text{Hz}$ and $f_s = 5000\,\text{Hz}$. Usually the power converters are equipped with a control scheme to ensure the stability of the output voltage or power for instance when a load change occurs. A comprehensive introduction into power converters can be found in [68, 118].

To design, test and layout power converters, filters and control systems, numerical simulations are employed. Following [41], power converters and connected appliances are commonly considered in simulations
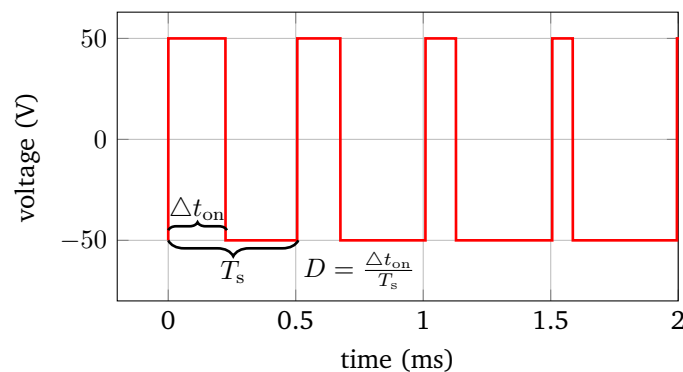
Figure 1.1: Typical PWM signal.
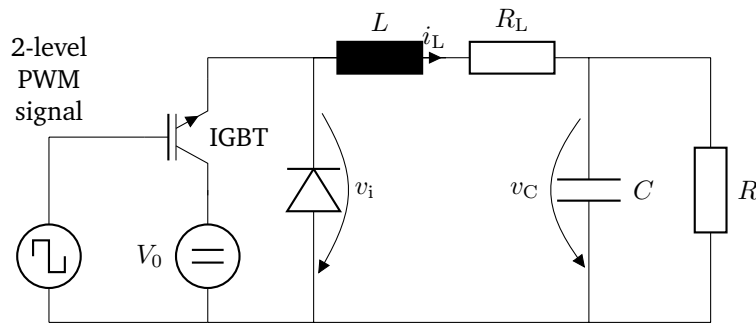
Figure 1.2: Circuit of a DC-DC buck converter. Figure adapted from [80] ©2019 IEEE.

on one of the following fidelity levels:

- Simulation of the entire system including the transistor switching behavior. This is necessary, e.g. for the design of snubber circuits (circuit to protect the semiconductors from electrical stresses) [68, Chapter 27]. It is the most computationally expensive approach since the switching behavior of the semiconductors is simulated in detail.

- Neglecting the switching behavior of the transistors, i.e. replacing the transistor output by an ideal pulsed signal. This reduces the computational effort for solving and thus enables to focus on a more complex simulation of the application. This allows for instance to utilize coupled simulations in which the power converter circuit is coupled to a field model of the application, e.g. a finite element (FE) model of a motor, see [39].

- The power converter circuitry is completely neglected and the application is directly excited by a PWM signal, e.g. as in [37, 55, 94].

Commonly, time integration algorithms are applied for the simulation. Numerical challenges arise due to widely separated characteristic time constants leading to different dynamics in the solution components. This is denoted as "multirate" behavior. These time constants can range from microseconds (e.g. PWM switching time intervals) over milliseconds (e.g. time constants in power electronic circuitry) up to seconds (e.g. for the start-up of an electrical machine). For illustration consider again the already introduced example of the buck converter. Its solution depicted in Fig. 1.3 consists of fast varying ripples which are modulated onto a slowly varying transient. The transient originates from the initially uncharged filter circuit. With a conventional time discretization, e.g. using implicit Runge-Kutta (IRK) methods or backward differentiation formulas (BDFs), very small time steps are necessary to resolve the solution. The switching frequency in modern converters starts in the low kilohertz range and reaches up into the megahertz range [68]. The higher the switching frequency is, the smaller the ripples become and the more there are in the same time interval. Higher switching frequency therefore leads to higher number of necessary time steps. Even when the power converter is in steady state, i.e. there is no slow transient behavior any more, the time integration algorithm still takes as many steps as before to properly resolve the fast periodic ripples. This leads to prohibitively long simulation times, especially if a field-circuit coupling is applied. In power electronics literature often equivalent circuit models are applied, e.g. to represent an inverter-cable-motor system [92]. This technique offers an approximation to the behavior of the electrical elements, which may be sufficient in certain applications. However it is insufficient if one is interested in the detailed physical phenomena taking place inside these components, e.g. eddy-current losses in electrical machines [55, 94], influence of geometric uncertainties in electric machines [6] or electromagnetic interference with other electric devices [67]. An accurate physical representation is only provided by field models. Consider as another illustrative
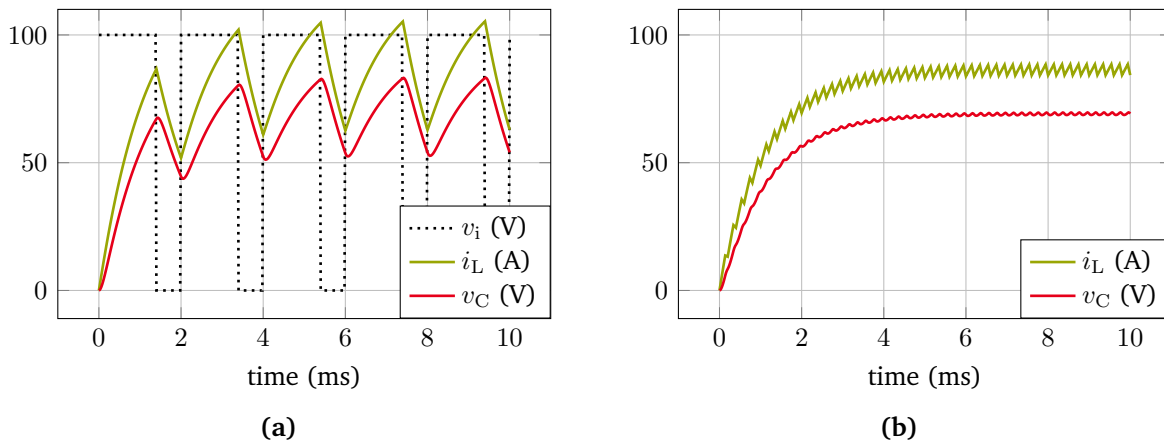
Figure 1.3: Exemplary solution of the buck converter depicted in Fig. 1.2. (a) Switching frequency $f_s = 500\,\text{Hz}$. (b) Switching frequency $f_s = 5000\,\text{Hz}$. Figures adapted from [80] ©2019 IEEE.

example an inductive power transfer system as utilized in modern electric cars to charge the battery [117]. The equivalent model presented in [117] represents the coils for power transfer when they are perfectly aligned. However the effect of metallic objects lying between the car and the coil embedded in the ground or a misalignment of the system cannot be taken into account. A field-circuit coupling may be applied to take into account the power converter circuitry and possible field models of inductors, electric machines or other devices. In cases where a monolithic (strong) coupling between circuit and field models is sought, the resulting system of differential equations describing the problem may become very large. As a result, a time-domain solution using conventional time integration schemes takes even longer than when using only circuit models.

To this end, the aim of this thesis is to develop a time-domain multirate method based on the concept of multirate partial differential equations (MPDEs) specifically for power converter simulation and evaluate its efficiency and accuracy. Before defining the research goals in detail, the following section gives an overview of related works in the area of multirate modeling.

1.1 Related works

With no claim to completeness, this section provides an overview over the most commonly used multirate methods.

Envelope-following methods One of the first methods to calculate the envelope of a highly oscillating solution has been proposed by Petzold et al. [83]. The method can be applied to ordinary differential equations (ODEs). Its idea is to calculate one cycle of the oscillating solution in detail by very fine time stepping and then calculate the secant between the beginning and the end point of the cycle. This secant is used to estimate the solution a few cycles further without the need to calculate the cycles in detail. At the new solution point, another detailed simulation is necessary to reestimate the secant and proceed further. A disadvantage of this method is that the high-frequent oscillation is neglected and only the envelope is calculated. In [59, 120] the method is applied to simulate a power converter with constant switching frequency and duty cycle. An extension of the method to varying switching times which allows to simulate power converters with

closed-loop control schemes (using state variables as input) has been proposed in [52]. Wang et al. [119] extended the concept further to be applicable when using PWM and/or pulse-frequency modulation (PFM) with varying switching frequencies.

Multirate time integration methods   Another possibility to efficiently deal with multirate behavior is to split the differential equations into several subsystems according to their activity. For example in highly integrated electrical circuits with many elements some parts of the circuit might be latent while others are active at the same time [40]. The resulting subsystems of equations are coupled with each other using coupling variables. Each subsystem is solved by an appropriate method and time step. First works on this approach which split the circuits according to the activity of the solution and which use different time steps for the subsystems have been proposed by Andrus [1] who bases it upon Runge-Kutta formulas. The theory on multirate Runge-Kutta methods has been analyzed by Kvaerno [61]. Gear et al. [38] and Skelboe [108] use linear multistep methods and Günther et al. [40] developed a multirate Rosenbrock-Wanner method. Savcenco et al. [103] propose a multirate second-order Rosenbrock method with adaptivity in each solution component. Multirate time integration has eventually been extended to simple examples of differential-algebraic equations (DAEs) in [3, 111, 112]. For a more comprehensive review, see for example [57]. A slightly different approach proposed by Biesiadecki et al. [4] splits the differential equations according to the activity of the right-hand side. Instead of differently large time steps, Engstler and Lubich [25, 26] propose a Richardson extrapolation of different orders. The slow and fast varying components are automatically detected during the process of building the extrapolation tableau and the increasing of the extrapolation order is stopped as soon as the desired accuracy is reached for a solution component.

In the field of power electronics, similar methods have been developed. Most of the time, the coupling between the resulting differential equations differs. For instance Kato et al. [54] propose a method in which the slow subsystem uses a macro time step which is an integer multiple of the micro time step employed in the slow subsystem. The coupling variables are synchronized between the subsystems in certain time intervals at which both systems of equations are solved together. In between the time instants of synchronization, the fast subsystem predicts the solution of the slow subsystem through extrapolation. Fung et al. [35] propose to split the circuit into subcircuits by using transmission line models for the coupling. Deml et al. [21] split the circuit at reactive electrical components, i.e. capacitors and inductors. The coupling is established through averaging fast variables and extrapolation of slow variables. Pekarek et al. [77] propose a method, which also splits the differential equations into active and latent parts. The coupling is established by a synchronization of the coupling variables in certain time intervals. The slow and fast subsystem can be solved by different time integration methods. Between the time instants of synchronization, the fast subsystem calculates the solution of the slow subsystem by using a backward Euler step and interpolation. The solution of the fast subsystem within the slow subsystem is calculated using averaging. Kato et al. [53] propose an automatic approach which splits the circuits at series inductors and parallel capacitors and replaces them with current and voltage sources by using a forward Euler difference formula.

Multirate partial differential equations   Another general concept to deal with multirate problems are the MPDEs [10, 97], which are the basis of this work. The idea is to split the solution into several solution components which vary with different rates in time. These solution components are associated to different artificial time scales. As a result the ODEs or DAEs describing the problem to be solved can be reformulated into partial differential equations (PDEs) (or partial differential-algebraic equations (PDAEs)) which

are called multirate PDEs (or PDAEs), abbreviated by MPDEs[1]. These MPDEs can then be solved with well known methods for PDEs. This concept has been studied mainly for problems in radio-frequency engineering, in which the solution is oscillatory and consists of widely separated frequencies. Brachtendorf et al. [10] solve the MPDEs in a high-frequency setting with multiple fundamental frequencies using a harmonic balance approach for all time scales. The resulting method is called multitone harmonic balance and is capable of simulating the steady state of a problem, i.e., a quasi-periodicity of the solution is assumed. Also for quasi-periodic solutions, Pulch et al. [90] proposed a method of characteristics to solve the MPDEs with two time scales. In [8] a combination of two methods, namely a finite difference and a harmonic balance method is presented. A combination of finite difference methods to solve along both time scales seems to offer the possibility of parallelization [85, 86]. To calculate the initial transient response of an oscillator, in [9, 72] a harmonic balance method is applied to the fast time scale which leads to a system of DAEs, i.e., an initial value problem (IVP). These may be solved by conventional time discretization methods with relatively large time steps since the fast variations are already taken into account by the harmonic balance method. Roychowdhury et al. [97, 98, 100] proposed different combinations of solution methods to solve MPDEs and presented different application examples. They categorize the methods into frequency-domain (e.g. harmonic balance on both time scales), mixed frequency-time domain (e.g. combination of harmonic balance and finite difference method) and time-domain methods (e.g. finite different method and backward Euler time integration). If the solution consists of a periodic component modulated onto an envelope the solution is termed envelope-modulated. The problem can be solved by mixed frequency-time domain or time domain methods. The difficulty in choosing the initial values for the IVPs resulting from envelope-modulated MPDE methods has been recognized and analyzed in [99] where an approximative solution of the problem has been proposed. The stability of different combinations of time-domain methods has been analyzed in [66]. Finally in [96] the simulation of problems with closely spaced frequencies is addressed, while former literature only focused on widely separate frequencies and time scales. The use of a Galerkin approach and different basis functions than in harmonic balance has been proposed in [5, 7, 56]. While Knorr and Bittner et al.[5, 56] focus on adaptive wavelet basis functions, Brachtendorf et al. [7] propose the use of cubic and exponential splines. These basis functions have superior approximation properties compared to harmonic balance basis functions when steep transients shall be approximated. The simulation of varying frequency problems, e.g. voltage-controlled oscillators is not possible with the MPDEs [70]. For this purpose the concept of MPDEs has been extended in such a way, that the fast time scale may be warped. This is realized by using a so-called warping function. The resulting equations are called warped MPDEs (WaMPDEs). To find the warping function (and its derivative, the local frequency function), additional conditions have to be added to the WaMPDEs. Different of these conditions have been proposed in [49, 70, 71, 87–89]. A survey presenting different solution methods and additional conditions may be found in [91].

Combinations of multirate methods and field-circuit coupled problems   Combinations of the aforementioned multirate methods have also been proposed. For instance Oliveira et al. [74–76] suggest to use a combination of MPDEs and multirate methods which split the systems of equations into subsystems according to their activity. In [75] the MPDEs with two time scales are semi-discretized by a fixed-step backward Euler method along the slow time scale. The remaining boundary value problems are solved using shooting and a multirate time integration scheme. In [74], even three time scale MPDEs are used to describe heterogeneous radio-frequency circuits. The solution is found by a combination of finite differences and a multirate Runge-Kutta scheme [61]. In [76] the two time scale MPDEs are solved using harmonic balance and a backward Euler finite difference scheme. The number of basis functions in harmonic balance is chosen differently

---

[1]In literature also the term multirate partial differential-algebraic equations (MPDAEs) is used. We only use the term MPDEs in the remainder of this work and mean with it both partial differential or differential-algebraic equations arising from ODEs or DAEs.

for each solution component to take into account different activities.

In field-circuit coupled problems often a splitting in subsystems with different activity is possible. If both the field and circuit part describe the same physical phenomenon, the corresponding characteristic time constants are similar. The aforementioned methods may be applied in such a case. If the simulation takes into account different physical phenomena, these phenomena may exhibit different characteristic time constants (e.g. electro-thermal coupling). This leads to different rates of variations in the unknowns. A weak coupling to cope with the phenomenon in machine simulation is proposed in [2, 19, 39, 105]. The circuit and the machine model, whose time constants can be highly different, are simulated separately and coupled (iteratively) by a temporary lumped-parameter model. This increases the numerical efficiency of the circuit simulation but comes with the drawback that high-frequency effects within the machine model are not resolved.

The first mention of a power converter, namely a DC-DC buck converter, solved using MPDEs can be found in [95, 101], where a reduced-order model based on MPDEs is proposed for radio-frequency circuits and the buck converter is used as a demonstration example. A similar example has been presented in [97], where a combination of so-called hierarchical shooting and either FDTD or shooting is employed to solve the arising MPDEs. Also in [74–76] a simple buck converter is part of the examples. However a more detailed investigation and application of MPDEs with focus specifically on power electronic problems has to the author's knowledge not been pursued.

1.2 Research goals

As already mentioned, the aim of this work is to develop a multirate method based on the concept of MPDEs. The idea is to split the solution into fast varying and slowly varying components. The fast varying components are the ripples of the power converter solution. The slowly varying components are slow transient processes, e.g. at converter start-up or to control an inverter's (DC-AC converter) sine output frequency. These solution components are associated with two artificial time scales. The resulting MPDEs are solved using a combination of a Ritz-Galerkin approach and a time integration algorithm. The research goals can be summarized as follows:

1. Investigation of suitable basis functions for the solution expansion in the Galerkin approach. The basis functions shall take the known C^0 continuity in the power converter current ripple into account by construction, e.g. as suggested by Gyselinck et al. [41].

2. Simulation of different power converter types, namely DC-DC and DC-AC power converters with different types of PWMs (different carriers and sampling techniques). For DC-AC power converters it is investigated if WaMPDEs offer a possible solution to model the varying duty cycle.

3. Efficient modeling of weak nonlinearities, e.g. as they occur in inductors, in the power converter circuits.

4. Simulation of field-circuit coupled problems. The arising large equation systems which are even further enlarged by the Galerkin approach need to be dealt with.

5. Investigation of the accuracy and the efficiency of the approach for different numerical examples.

1.3 Structure of this treatise

The structure of the thesis is as follows. Chapter 2 briefly introduces the mathematical tools and concepts from electrical engineering which are necessary to understand the remainder of this work. The main Chapter 3 discusses the methodological aspects. It introduces the concept of MPDEs and describes their discretization. Suitable basis functions are presented. Furthermore, a reasonable choice of initial values is discussed as well as the extension to different PWMs. In the end, the suitability of WaMPDEs for the simulation of DC-AC power converters is analyzed. Chapter 4 presents different numerical examples and their simulation using the MPDE approach. Accuracy and efficiency of the approach is analyzed by comparing it with conventional time discretization. Finally, Chapter 5 summarizes the main achievements of the thesis and proposes steps for future research.

2 Fundamentals

This chapter reviews the tools and methods from mathematics and electrical engineering which are important throughout this thesis. It provides the basic knowledge to better understand the following chapters. For a more detailed introduction to the particular topics, the interested reader is referred to the literature specified in each section.

2.1 The MAXWELL equations

In this section, the MAXWELL equations and their simplifications are discussed. The information is mainly a summary from standard literature, for instance [51, 62, 69], to which the interested reader is referred for more details.

Electromagnetic phenomena on a macroscopic level are described by the MAXWELL Equations [65]. These date back to the 19th century. James Clerk MAXWELL was the physicist who combined the state of the art knowledge at that time into a feasible set of partial differential equations today known as the MAXWELL equations. As such, he laid the foundation of what is known as classical electrodynamics. The following vectorial quantities describe electromagnetic fields depending on the position $\mathbf{r} \in \mathbb{R}^3$ and the time $t \in \mathbb{R}$: The electric field or electric field strength $\mathbf{e}(\mathbf{r}, t) \in \mathbb{R}^3$, the electric displacement or electric flux density $\mathbf{d}(\mathbf{r}, t) \in \mathbb{R}^3$, the magnetic field or magnetic field strength $\mathbf{h}(\mathbf{r}, t) \in \mathbb{R}^3$, and the magnetic induction or magnetic flux density $\mathbf{b}(\mathbf{r}, t) \in \mathbb{R}^3$. Furthermore, there are the electric charge density $\rho(\mathbf{r}, t) \in \mathbb{R}$ and the electric current density $\mathbf{j}(\mathbf{r}, t) \in \mathbb{R}^3$. The MAXWELL equations relating these field quantities are, in their integral form, given by

$$\int_{\partial S} \mathbf{e}(\mathbf{r}, t) \cdot \mathbf{dl} = -\frac{\mathrm{d}}{\mathrm{d}t} \int_S \mathbf{b}(\mathbf{r}, t) \cdot \mathbf{dS} \tag{2.1}$$

$$\int_{\partial S} \mathbf{h}(\mathbf{r}, t) \cdot \mathbf{dl} = \int_S \frac{\partial \mathbf{d}(\mathbf{r}, t)}{\partial t} \cdot \mathbf{dS} + \int_S \mathbf{j}(\mathbf{r}, t) \cdot \mathbf{dS} \tag{2.2}$$

$$\int_{\partial V} \mathbf{d}(\mathbf{r}, t) \cdot \mathbf{dS} = \int_V \rho(\mathbf{r}, t) \, \mathrm{d}V \tag{2.3}$$

$$\int_{\partial V} \mathbf{b}(\mathbf{r}, t) \cdot \mathbf{dS} = 0, \tag{2.4}$$

where V is an arbitrary simply connected volume with ∂V being its boundary surface and S denotes an arbitrary simply connected surface with ∂S being its boundary contour. The vector $\mathbf{dS}$ denotes an infinitesimally small surface element with orientation, which in case of a volume is by convention always directed

outwards of the volume and is perpendicular to the surface. The vector $\mathbf{dl}$ denotes an infinitesimally small curve with orientation parallel to the surface contour. We assume that the volumes and surfaces are constant, i.e. independent of time.

Equation (2.1) is the FARADAY law. It states that the electric field strength $\mathbf{e}$ integrated along the closed curve ∂S equals the time derivative of the magnetic flux defined by

$$\Phi = \int_S \mathbf{b}(\mathbf{r}, t) \cdot \mathbf{dS}. \tag{2.5}$$

The integral of the electric field strength along a path l (in this case $l = \partial S$) is called electric voltage

$$v(t) = \int_l \mathbf{e}(\mathbf{r}, t) \cdot \mathbf{dl}. \tag{2.6}$$

The FARADAY law is also called induction law because it describes the induction of an electric voltage when the magnetic flux density changes in time.

Equation (2.2) is the AMPÈRE-MAXWELL law. It states that the magnetic field strength along the contour of a surface results from either electric currents, i.e.

$$i(t) = \int_S \mathbf{j}(\mathbf{r}, t) \cdot \mathbf{dS}, \tag{2.7}$$

flowing through the surface, or a temporal change of the electric flux density through the surface (displacement currents). The displacement currents were contributed by MAXWELL. They are not part of the original AMPÈRE law.

Finally, equations (2.3) and (2.4) are the electric and magnetic GAUSS laws, respectively. The electric GAUSS law states that the electric flux density $\mathbf{d}$ flowing through the surface of a volume equals the electric charge

$$q(t) = \int_V \rho(\mathbf{r}, t) \, dV. \tag{2.8}$$

Consequently the electric flux density is divergence free if there is no charge inside the considered volume. The electric charge is conserved as long as the divergence of the electric flux density is constant. The magnetic GAUSS law states that there are no magnetic charges and thus the magnetic flux density is divergence free.

The field quantities $\mathbf{b}$ and $\mathbf{h}$, and $\mathbf{d}$ and $\mathbf{e}$ are related by material parameters, which can, in the linear case, be written as

$$\mathbf{b} = \mu_0 \mathbf{h} + \mathbf{m}, \tag{2.9}$$
$$\mathbf{d} = \varepsilon_0 \mathbf{e} + \mathbf{p}, \tag{2.10}$$

where μ_0 and ε_0 are the vacuum permeability and vacuum permittivity, respectively, and $\mathbf{m}$ and $\mathbf{p}$ are called magnetization and polarization. Magnetization and polarization are associated to the reaction of the material's magnetic and electric dipoles, respectively, onto externally applied fields.

In diamagnetic and paramagnetic materials the magnetization is linearly related to the applied field and can be written as $\mathbf{m} = \mu_0 \chi_\mathrm{m}(\mathbf{r})\mathbf{h}$ with $\chi_\mathrm{m}(\mathbf{r})$ the magnetic susceptibility. Similarly in dielectric materials the

polarization can be written as $\mathbf{p} = \varepsilon_0 \chi_{\mathrm{e}}(\mathbf{r})\mathbf{e}$ with $\chi_{\mathrm{e}}(\mathbf{r})$ the electric susceptibility. Inserting this into (2.9) and (2.10) leads to

$$\mathbf{b} = \underbrace{(1 + \chi_{\mathrm{m}}(\mathbf{r}))}_{\mu_{\mathrm{r}}(\mathbf{r})} \mu_0 \mathbf{h} = \mu_{\mathrm{r}}(\mathbf{r})\mu_0 \mathbf{h}, \tag{2.11}$$

$$\mathbf{d} = \underbrace{(1 + \chi_{\mathrm{e}}(\mathbf{r}))}_{\varepsilon_{\mathrm{r}}(\mathbf{r})} \varepsilon_0 \mathbf{h} = \varepsilon_{\mathrm{r}}(\mathbf{r})\varepsilon_0 \mathbf{e}, \tag{2.12}$$

where $\mu_{\mathrm{r}}(\mathbf{r})$ and $\varepsilon_{\mathrm{r}}(\mathbf{r})$ are called relative permeability and relative permittivity, respectively. They are either positive real-valued scalar functions of position (isotropic material) or positive definite real-valued 3×3 matrix functions of position (anisotropic material). For some types of materials (e.g. ferromagnetic materials, electrets), the magnetization $\mathbf{m}$ and polarization $\mathbf{p}$ depend nonlinearly on the field quantities $\mathbf{h}$, $\mathbf{b}$, $\mathbf{e}$, $\mathbf{d}$ and can also be non-zero without externally applied fields. Furthermore, their magnetization or polarization might depend not only on the currently applied fields but also on the fields applied to it in the past (hysteresis). Note that there are also materials in which the polarization and magnetization depend on frequency. Those are called dispersive materials. In all these cases the relations (2.11) and (2.12) become more complicated.

There is an additional relation between the electric field and the current density

$$\mathbf{j} = \mathbf{j_s} + \mathbf{j_e} + \mathbf{j_c} = \mathbf{j_s} + \sigma(\mathbf{r})\mathbf{e} + \mathbf{j_c}, \tag{2.13}$$

which states that the overall current density consists of imprinted electric currents $\mathbf{j_s}$, currents $\mathbf{j_e} = \sigma(\mathbf{r})\mathbf{e}$ induced in a conductive material by the electric field, and convection currents $\mathbf{j_c}$ as a result of free moving charges. The conductivity $\sigma(\mathbf{r})$ depends on the material and is either a positive scalar function of position (isotropic material) or a symmetric positive semi-definite 3×3 matrix function of position.

Besides the integral form, the MAXWELL equations can also be written in differential form, using the nabla operator $\nabla = \begin{bmatrix} \frac{\partial}{\partial x} & \frac{\partial}{\partial y} & \frac{\partial}{\partial z} \end{bmatrix}^{\top}$, as

$$\nabla \times \mathbf{e}(\mathbf{r}, t) = -\frac{\partial \mathbf{b}(\mathbf{r}, t)}{\partial t} \tag{2.14}$$

$$\nabla \times \mathbf{h}(\mathbf{r}, t) = \frac{\partial \mathbf{d}(\mathbf{r}, t)}{\partial t} + \mathbf{j}(\mathbf{r}, t) \tag{2.15}$$

$$\nabla \cdot \mathbf{d}(\mathbf{r}, t) = \rho(\mathbf{r}, t) \tag{2.16}$$

$$\nabla \cdot \mathbf{b}(\mathbf{r}, t) = 0 \tag{2.17}$$

which is equivalent to (2.1)-(2.4). To switch between both forms, the theorems of STOKES and GAUSS are applied. These are given by

$$\int_S (\nabla \times \mathbf{F}) \cdot \mathrm{d}\mathbf{S} = \int_{\partial S} \mathbf{F} \cdot \mathrm{d}\mathbf{l}, \quad \text{and} \tag{2.18}$$

$$\int_V \nabla \cdot \mathbf{F} \, \mathrm{d}V = \int_{\partial V} \mathbf{F} \cdot \mathrm{d}\mathbf{S}, \tag{2.19}$$

respectively, where $\mathbf{F}$ is any vector field.

In many applications it is reasonable to use simplified formulations of the MAXWELL equations to obtain more easily solvable equations. In the following the magnetoquasistatic approximation is focused on. For other simplifications the interested reader is referred to [22, 45].

2.1.1 Magnetoquasistatic approximation

The magnetoquasistatic (MQS) formulation of the MAXWELL equations is useful in applications in which the derivative of the electric displacement $\left\|\frac{\partial \mathbf{d}}{\partial t}\right\|$ is much smaller than the current density $\|\mathbf{j}\|$, i.e. $\left\|\frac{\partial \mathbf{d}}{\partial t}\right\| \ll \|\mathbf{j}\|$, and thus can be neglected [104]. To obtain equations which can be solved reasonably simple one writes the magnetic flux density $\mathbf{b}$ and electric field strength $\mathbf{e}$ in terms of potentials $\mathbf{a}(\mathbf{r}, t)$ and $\phi(\mathbf{r}, t)$ (so called A-ϕ formulation) [18] such that

$$\mathbf{b} = \nabla \times \mathbf{a} \tag{2.20}$$

$$\mathbf{e} = -\frac{\partial \mathbf{a}}{\partial t} - \nabla \phi. \tag{2.21}$$

These fulfill equations (2.14) and (2.17). The gauge freedom allows to define the modified magnetic vector potential (MVP) [24]

$$\mathbf{a}^{\star} = \mathbf{a} + \int \nabla \phi \, \mathrm{d}t, \tag{2.22}$$

which leads to $\mathbf{e} = -\frac{\partial \mathbf{a}^{\star}}{\partial t}$. Inserting this and (2.20) into (2.15) yields (assuming zero convection currents)

$$\nabla \times \left(\mu^{-1} \nabla \times \mathbf{a}^{\star}\right) = -\sigma \frac{\partial \mathbf{a}^{\star}}{\partial t} + \mathbf{j_s}, \tag{2.23}$$

which possesses a unique solution in conducting domains ($\sigma > 0$). In non-conducting domains ($\sigma = 0$) an additional gauge condition, e.g. the Coulomb gauge ($\nabla \cdot \mathbf{a}^{\star} = 0$), has to be applied.

Since in this work only 2D magnetoquasistatic simulations with in-plane magnetic flux and current density perpendicular to that plane are employed, we assume $\mathbf{a}^{\star} = \begin{bmatrix} 0 & 0 & a_z \end{bmatrix}^{\top}$. Furthermore, we utilize only linear isotropic material, which means that μ is a scalar function of position. From (2.23) we obtain

$$-\nabla \cdot (\nu \nabla a_z) = -\sigma \frac{\partial a_z}{\partial t} + j_{s,z}, \tag{2.24}$$

where $\nu = \mu^{-1}$ and $j_{s,z}$ denotes the z-component of the current density $\mathbf{j_s}$. For the solution of this parabolic-elliptic PDE on a given domain Ω, boundary and initial conditions have to be specified. Dirichlet and Neumann boundary conditions are the most basic types. Consider the domain Ω as given in Fig. 2.1. Part of its boundary denoted by $\Gamma_N \subset \partial\Omega$ is a Neumann boundary, the other $\Gamma_D \subset \partial\Omega$ is a Dirichlet boundary. The following listing explains both conditions and their effect on the magnetic flux density $\mathbf{b}$.

1. *Dirichlet boundary conditions:* The unknown solution, in 2D magnetoquasistatics the MVP a_z, is given as a function on the boundary, i.e.

$$a_z(\mathbf{r}, t) = \gamma_D(\mathbf{r}), \quad \mathbf{r} \in \Gamma_D. \tag{2.25}$$

It controls the normal component of the magnetic flux density, i.e.

$$\mathbf{b}(\mathbf{r}, t) \cdot \mathbf{n}(\mathbf{r}) = \nabla \cdot \left(\begin{bmatrix} 0 \\ 0 \\ \gamma_D(\mathbf{r}) \end{bmatrix} \times \mathbf{n}(\mathbf{r}) \right), \quad \mathbf{r} \in \Gamma_D, \tag{2.26}$$

where $\mathbf{n}(\mathbf{r})$ is the normal vector on the surface of Ω. A special case is $\gamma_D(\mathbf{r}) = 0$ in which the Dirichlet boundary condition is called homogeneous. It forces the normal component of the magnetic flux density to zero such that there is only a tangential component.
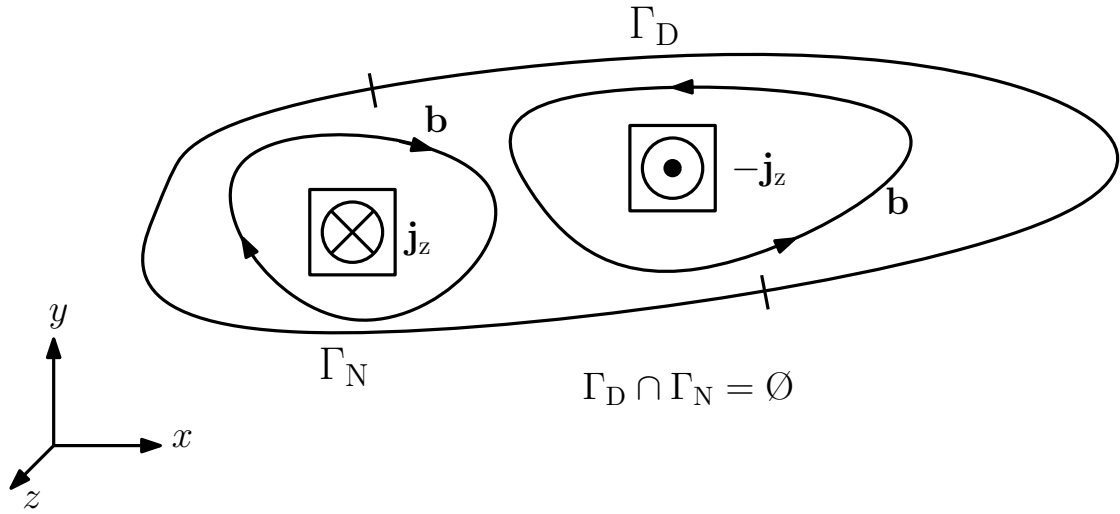
Figure 2.1: Exemplary 2D computation domain with Dirichlet and Neumann boundary.

2. *Neumann boundary condition:* The derivative of the unknown solution a_z is given as a function, i.e.

$$\nu \nabla a_z(\mathbf{r}, t) \cdot \mathbf{n}(\mathbf{r}) = \gamma_N(\mathbf{r}), \quad \mathbf{r} \in \Gamma_N. \tag{2.27}$$

It controls the tangential component of the magnetic field strength, i.e.

$$\mathbf{h}(\mathbf{r}, t) \times \mathbf{n}(\mathbf{r}) = \begin{bmatrix} 0 \\ 0 \\ \gamma_N(\mathbf{r}) \end{bmatrix}, \quad \mathbf{r} \in \Gamma_N. \tag{2.28}$$

Again, a special case is $\gamma_N(\mathbf{r}) = 0$, which is called homogeneous Neumann boundary condition. It forces the tangential component of the magnetic flux density to zero such that there is only a normal component.

2.2 Electric circuits

Electric circuits are a connection of different electrical devices with each other. In contrast to field models, the focus is on the interaction between multiple lumped electric elements. The electrical phenomena governing these devices are described in a single or multiple equations, which take the physics of the MAXWELL equations into account, often in a simplified form. As a result the detailed processes inside the individual elements are not considered. The most basic elements in a circuit are resistors, inductors, capacitors and voltage and current sources. In layouts of electrical circuits they may be represented by symbols as given in Fig. 2.2. The depicted elements have two ports. Each element forms a branch and is connected through numbered nodes to the other elements. There are also elements with more than two ports, e.g. transistors, operational amplifiers and others. The quantities of interest in electric circuits are the voltage $v(t)$, which can be measured between two nodes, and the current $i(t)$ flowing through the elements (branches). Fig. 2.3 shows a simple example of a low-pass filter, i.e. a circuit, which allows low-frequent signals to pass from the voltage source v_i to the load R and which blocks high-frequent signals.
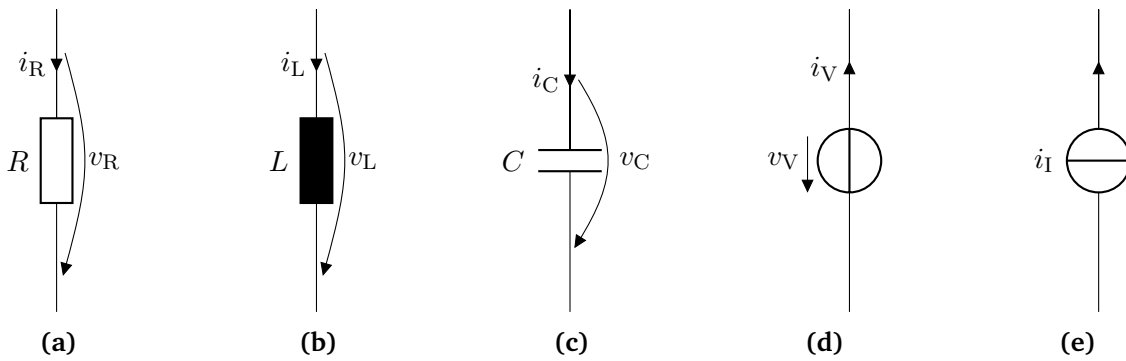
Figure 2.2: Representation of the basic electrical elements: (a) resistor, (b) inductor, (c) capacitor, and (d) voltage and (e) current source.

Before we take a closer look at the behavior of the single elements, let us focus on the properties of the entire electric circuit on a macroscopic level, i.e. the distribution of voltages and currents in the network. Those are provided by the two KIRCHHOFF laws. To obtain the first law of KIRCHHOFF, we apply the divergence to the AMPÈRE law (2.15) and obtain

$$0 = \nabla \cdot \frac{\partial \mathbf{d}}{\partial t} + \nabla \cdot \mathbf{j}, \tag{2.29}$$

where the vector identity $\nabla \cdot (\nabla \times \mathbf{h}) = 0$ was used. Inserting (2.16) into this equation yields the continuity equation

$$\nabla \cdot \mathbf{j} = -\frac{\partial \rho}{\partial t}, \tag{2.30}$$

or in integral form

$$\int_{\partial V} \mathbf{j} \cdot \mathrm{d}\mathbf{S} = - \int_{V} \frac{\partial \rho}{\partial t} \, \mathrm{d}V. \tag{2.31}$$

It states that if the charge inside a volume does not change, then the amount of current flowing in and out must be the same. In other words, for instance, if a current only flows into a volume, the charge inside the volume increases. In Fig. 2.4a, one node of a circuit is shown to which different branches are connected. We define a volume V around this node which surface consists of different subsurfaces S_k. These subsurfaces are intersected by the currents i_k. Inside the volume V one assumes that no charges can be stored. Consequently
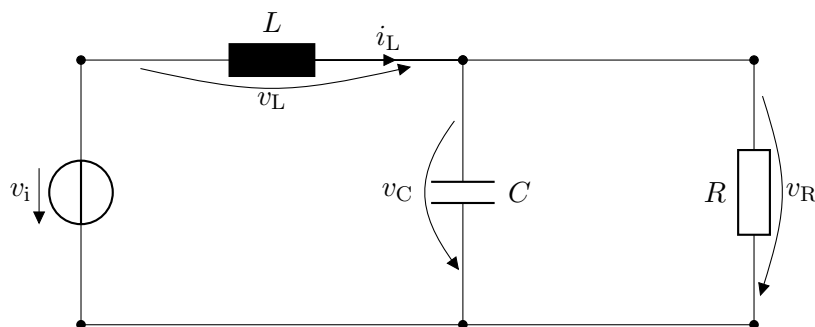
Figure 2.3: Simple circuit example.
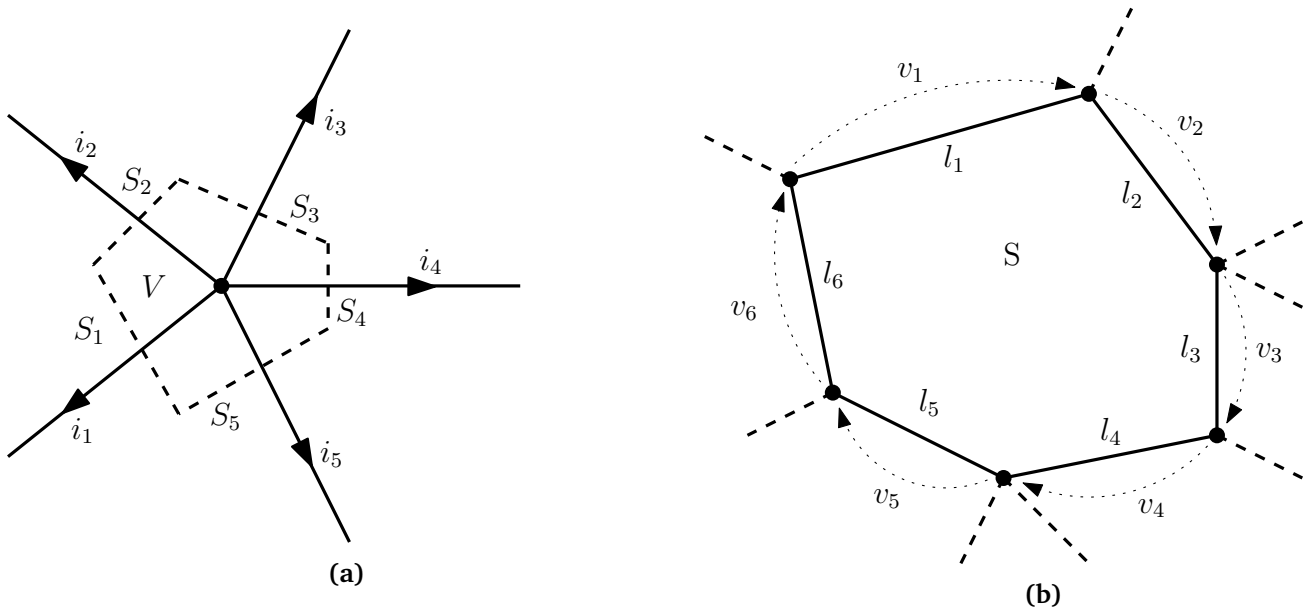
Figure 2.4: (a) Circuit branches connected to a node. (b) Circuit branches connected to each other forming a loop. The branches can consist of any electrical element which is a two-port.

the right-hand side of (2.31) vanishes and the left-hand side integral becomes

$$\int_{\partial V} \mathbf{j} \cdot \mathrm{d}\mathbf{S} = \int_{S_1} \mathbf{j} \cdot \mathrm{d}\mathbf{S} + \int_{S_2} \mathbf{j} \cdot \mathrm{d}\mathbf{S} + \ldots + \int_{S_{N_\mathrm{b}}} \mathbf{j} \cdot \mathrm{d}\mathbf{S} = \sum_{k=1}^{N_\mathrm{b}} \underbrace{\int_{S_k} \mathbf{j} \cdot \mathrm{d}\mathbf{S}}_{=i_k} = \sum_{k=1}^{N_\mathrm{b}} i_k = 0, \tag{2.32}$$

where N_b is the number of branches connected to the node. This is the first KIRCHHOFF law and states that the sum of all currents flowing to a node must be zero. For the second KIRCHHOFF law consider the loop depicted in Fig. 2.4b. A loop is a set of N_l branches with length l_k, $k \in 1, \ldots, N_\mathrm{l}$ connected to nodes as such that they form a closed curve. The branches define the contour of the surface S. Assuming no magnetic flux is flowing through this surface S, the FARADAY law (2.1) becomes

$$\int_{\partial S} \mathbf{e} \cdot \mathrm{d}\mathbf{l} = \sum_{k=1}^{N_\mathrm{l}} \underbrace{\int_{l_k} \mathbf{e} \cdot \mathrm{d}\mathbf{l}}_{=v_k} = \sum_{k=1}^{N_\mathrm{l}} v_k = 0. \tag{2.33}$$

This is the second KIRCHHOFF law and states that the sum of voltages across branches in a loop is always zero.

The behavior of the individual electrical elements, i.e. the relation between voltage across the element and current through the element, are determined from the MAXWELL equations. For resistors, capacitors and inductors they are given in the following enumeration:

1. Resistors are devices consisting of conductive material with a high conductivity. Consequently they dissipate electrical energy as heat (Joule heating). The relation between voltage and current in a resistor is given by

$$v(t) = R\, i(t). \tag{2.34}$$

Fig. 2.5a shows the simplest case of a resistor. It consists of two perfect electric conductor (PEC) ports between which a conductive material with conductivity σ is present. Its resistance R is calculated by

$$R = \frac{v(t)}{i(t)} = \frac{\int\limits_l \mathbf{e}(\mathbf{r},t) \cdot \mathbf{dl}}{\int\limits_S \mathbf{j_e}(\mathbf{r},t) \cdot \mathbf{dS}} = \frac{\int\limits_l \mathbf{e}(\mathbf{r},t) \cdot \mathbf{dl}}{\int\limits_S \sigma\,\mathbf{e}(\mathbf{r},t) \cdot \mathbf{dS}} = \frac{l}{\sigma S}, \tag{2.35}$$

where l is the distance between the resistor ports and S is the cross-section area of the ports as depicted in Fig. 2.5a.

2. Capacitors are devices which store energy in form of electric charges. A capacitor is characterized by its capacitance C, which defines the amount of electrical charges $q(t)$ the capacitor stores when a voltage $v(t)$ is applied to it. The relation is given by

$$q(t) = C\,v(t). \tag{2.36}$$

The simplest capacitor model is depicted in Fig. 2.5b. It consists of two PEC ports. The volume between the ports is filled with dielectric material with permittivity ϵ. The capacitance of this capacitor is sought by

$$C = \frac{q(t)}{v(t)} = \frac{\int\limits_V \rho(\mathbf{r},t)\,\mathrm{d}V}{\int\limits_l \mathbf{e}(\mathbf{r},t) \cdot \mathbf{dl}} = \frac{\int\limits_{\partial V} \mathbf{d}(\mathbf{r},t) \cdot \mathbf{dS}}{\int\limits_l \mathbf{e}(\mathbf{r},t) \cdot \mathbf{dl}} = \frac{\int\limits_{\partial V} \epsilon\,\mathbf{e}(\mathbf{r},t) \cdot \mathbf{dS}}{\int\limits_l \mathbf{e}(\mathbf{r},t) \cdot \mathbf{dl}} = \frac{\epsilon S}{l}, \tag{2.37}$$

where the electric GAUSS law (2.3) is applied. l is the distance between the capacitor ports and S is the cross-section area of the ports as depicted in Fig. 2.5b. The change of electrical charges inside the capacitor is associated to the current flowing through the capacitor

$$i(t) = \frac{\mathrm{d}}{\mathrm{d}t}\,q(t). \tag{2.38}$$

This can be obtained from the continuity equation (2.30). Differentiating (2.36) with respect to t and inserting (2.38) leads to

$$\frac{\mathrm{d}}{\mathrm{d}t}\,v(t) = \frac{1}{C}i(t), \tag{2.39}$$

which describes the relation between current and voltage of a capacitor.

3. Inductors are devices which store energy in form of magnetic fields. An inductor is characterized by its inductance L which relates the magnetic flux through the inductor to the current, i.e.

$$\Phi(t) = L\,i(t). \tag{2.40}$$

In Fig. 2.6 a solenoidal inductor is depicted. To calculate its inductance, the expression

$$L = \frac{\Phi(t)}{i(t)} = \frac{\int\limits_S \mathbf{b}(\mathbf{r},t) \cdot \mathbf{dS}}{i(t)} = \frac{\int\limits_S \mu\,\mathbf{h}(\mathbf{r},t) \cdot \mathbf{dS}}{i(t)} \tag{2.41}$$

needs to be solved. This is accomplished by calculating the magnetic field strength $\mathbf{h}$ generated by the current $i(t)$ and inserting into the above expression. The magnetic field strength is implicitly given by the AMPÈRE law. If the iron core of the inductor in Fig. 2.6 is removed, its inductance can be estimated by

$$L \approx \frac{\mu_0 N_\mathrm{t}^2 S}{l}, \tag{2.42}$$
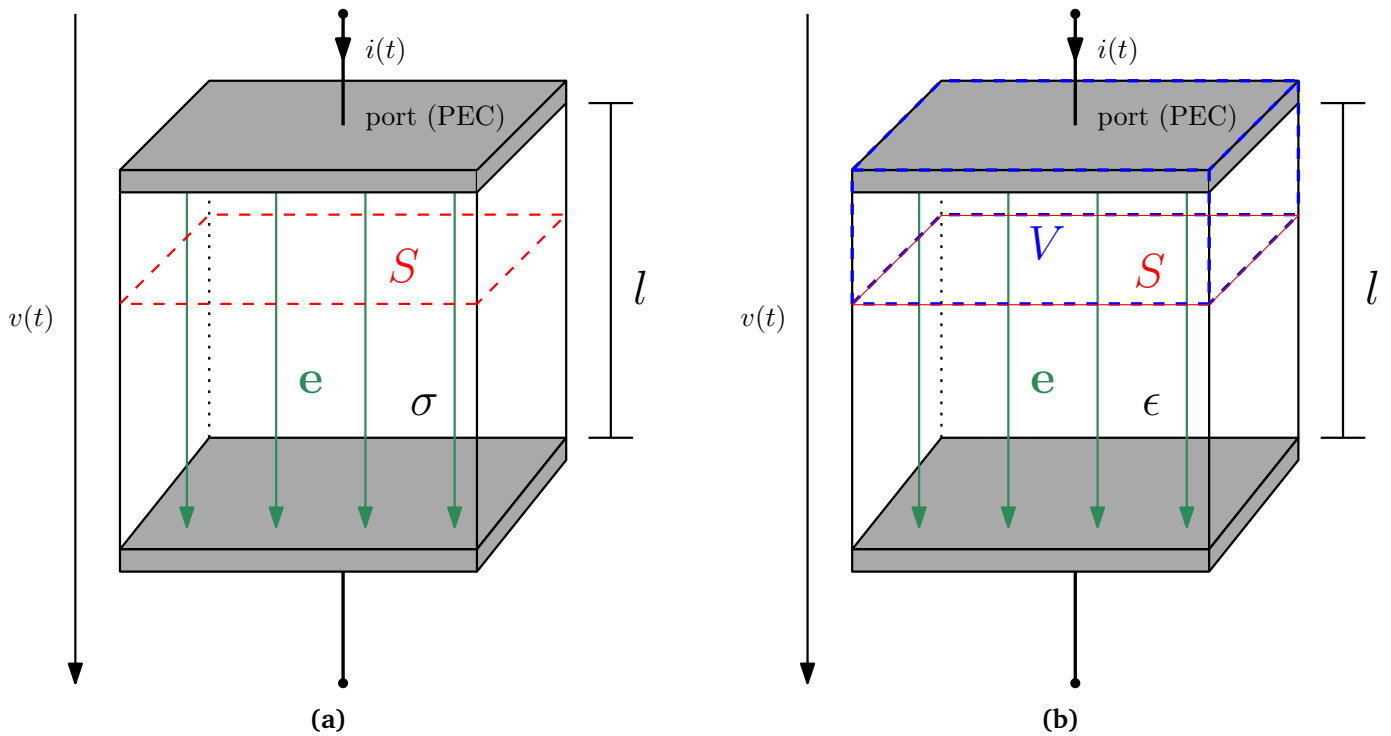
Figure 2.5: (a) Simple resistor model consisting of two perfectly conducting ports. The volume in between is filled with conductive material. (b) Simple capacitor model consisting of two perfectly conducting ports (PEC). The volume in between is filled with dielectric material.

where N_t is the number of turns of copper wire, l is the longitudinal length of the wounded coil and S is the cross-section area as depicted in Fig. 2.6. Using the relation

$$v(t) = \frac{\mathrm{d}}{\mathrm{d}t}\,\Phi(t), \tag{2.43}$$

which can be derived from FARADAY's law (2.1), the final constitutive equation is

$$v(t) = L\frac{\mathrm{d}}{\mathrm{d}t}\,i(t). \tag{2.44}$$

For ideal resistors, capacitors and inductors, the characteristic quantities R, C and L are constant. In reality these elements are often nonlinear or suffer from parasitic effects which might need to be taken into account. In those cases R, C and L may be functions of time, frequency, voltage and/or current. Note that in those cases the chain rule of differentiation has to be applied in equations (2.38) and (2.43).

To complete the enumeration of electrical elements displayed in Fig. 2.2, ideal voltage and current sources are power sources which provide as much power as the circuit needs and are not limited in their power output. As a consequence, a voltage source provides a given voltage and as much current as a circuit needs and a current source provides a given current and as much voltage as a circuit needs.

The elements depicted in Fig. 2.2 are only the most common ones. As already mentioned, there are other devices like transistors, diodes, operational amplifiers and many more, whose relation between voltages and currents is often nonlinear.
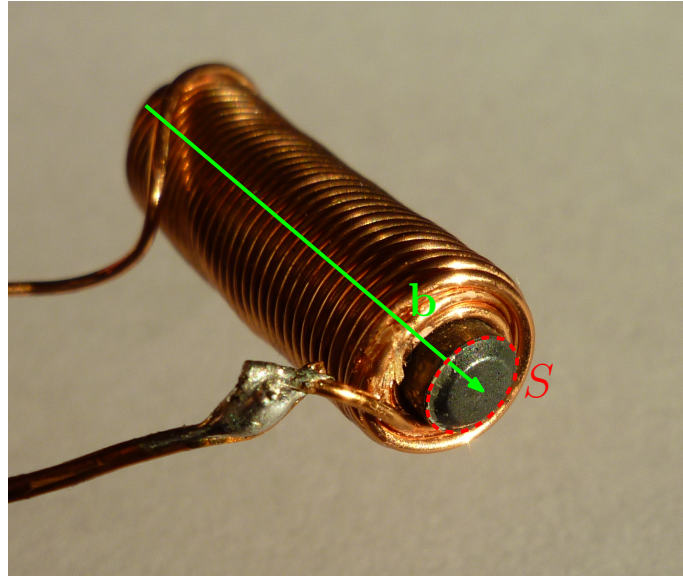
Figure 2.6: Inductor consisting of an iron core and two layers of copper wire. The magnetic flux density $\mathbf{b}$ inside the iron core is decisive for the inductance.

To calculate the voltages and currents throughout the electric circuit, the KIRCHHOFF laws and constitutive equations of the elements are used to obtain a system of equations in which the unknowns are the voltages and/or currents. To automate this process on a computer, different methods have been developed. Among those are the modified nodal analysis (MNA) [46] and the sparse tableau approach (STA) [42]. Where necessary the MNA is employed in this work. It uses graph theory to obtain so called incidence matrices, which are necessary to construct the final systems of equations. For more information on the arising DAEs the interested reader is referred to, for instance, [27, 29, 30].

2.3 Discretization using finite element methods

The finite element method (FEM) is a common approach to discretize the MAXWELL equations and thus enable a numerical solution on the computer. Its idea is to use a set of basis functions to approximate the solution. In classical FEM one usually utilizes so-called Whitney elements of lowest order. A weak formulation of the PDEs in question is derived to accommodate the smoothness of the basis functions employed for the approximation. This process is briefly described in the following. In a first step the necessary function spaces are defined and the concept of weak derivatives is explained. In the second part the weak formulation is derived. As example equation the magnetostatic form of (2.24) is used, i.e, the time dependency is neglected, leading to the elliptic problem

$$-\nabla \cdot (\nu \nabla a_{\mathrm{z}}(\mathbf{r})) = j_{\mathrm{s,z}}(\mathbf{r}). \tag{2.45}$$

The presented information follows [11, 31, 93].

2.3.1 Introduction to Hilbert spaces

Let Ω be an open, bounded, convex subset of $\mathbb{R}^2$ with Lipschitz continuous boundary $\partial\Omega$. The space of square-integrable functions $L^2(\Omega)$ is defined by

$$L^2(\Omega) = \left\{ u(\mathbf{r}) \,\middle|\, \int_\Omega |u(\mathbf{r})|^2 \, \mathrm{d}\Omega < \infty \right\}. \tag{2.46}$$

Equipped with the scalar product

$$(u, w)_{L^2(\Omega)} = \int_\Omega u(\mathbf{r}) \, w(\mathbf{r}) \, \mathrm{d}\Omega, \tag{2.47}$$

and the norm

$$\|u\|_{L^2(\Omega)} = \sqrt{(u, u)_{L^2(\Omega)}}, \tag{2.48}$$

it forms a Hilbert space [11, Chapter 2.§1].

To understand weak derivatives, let $C_0^\infty(\Omega)$ be the space of infinitely continuously differentiable functions which vanish on the boundary. Furthermore, define a differential operator $\mathcal{D}^\alpha$ for any $w(\mathbf{r}) \in C_0^\infty(\Omega)$ such that

$$\mathcal{D}^\alpha w = \frac{\partial^{|\alpha|} w}{\partial r_1^{\alpha_1} \, \partial r_2^{\alpha_2}}, \tag{2.49}$$

where $\alpha = (\alpha_1, \alpha_2)$, $\alpha_k \in \mathbb{N} \; \forall k = 1, 2$ is a multi-index, $|\alpha| = \alpha_1 + \alpha_2$, and r_1, r_2 are the components of the vector $\mathbf{r}$. A function $u \in L^2(\Omega)$ possesses the weak derivative φ in $L^2(\Omega)$, if the equation [11, Chapter 2.§1]

$$(w, \varphi)_{L^2(\Omega)} = (-1)^{|\alpha|} (\partial^\alpha w, u)_{L^2(\Omega)} \quad \forall \, w \in C_0^\infty(\Omega) \tag{2.50}$$

holds. Often the weak derivative is also denoted by $\varphi = \mathcal{D}^\alpha u$.

The $L^2(\Omega)$ space contains functions which are discontinuous. For some quantities more regularity is required. Therefore one defines another Hilbert space, denoted by $H^1(\Omega)$, which contains all functions u in $L^2(\Omega)$ whose weak derivatives are also in $L^2(\Omega)$. The space is thus given by

$$H^1(\Omega) := \left\{ u \in L^2(\Omega) \,\middle|\, \mathcal{D}^\alpha u \in L^2(\Omega), |\alpha| \leq 1 \right\} \tag{2.51}$$

and equipped with the scalar product [11, Chapter 2.§1]

$$(u, w)_{H^1(\Omega)} = \sum_{|\alpha| \leq 1} (\partial^\alpha u, \partial^\alpha w)_{L^2(\Omega)} \tag{2.52}$$

and the corresponding norm

$$\|u\|_{H^1(\Omega)} = \sqrt{(u, u)_{H^1(\Omega)}}. \tag{2.53}$$

For more information on Hilbert spaces for the parabolic problem (2.24) (without neglecting the time dependency), the reader is referred to [31, Chapter 7.1].

2.3.2 Weak formulation

The weak formulation of equation (2.45) is derived by multiplying it with test functions $w \in W$, where W is a function space, and integrating over the computation domain Ω, i.e.

$$\int_\Omega -\nabla \cdot (\nu \nabla a_z)\, w \, \mathrm{d}\Omega = \int_\Omega j_{s,z}\, w \, \mathrm{d}\Omega. \tag{2.54}$$

Using the vector identity $w\, \nabla \cdot (\nu \nabla a_z) = \nabla \cdot (w\, \nu\, \nabla a_z) - \nu\, \nabla a_z \cdot \nabla w$ on the left-hand side leads to

$$-\int_\Omega \nabla \cdot (w\, \nu\, \nabla a_z)\, \mathrm{d}\Omega + \int_\Omega \nu\, \nabla a_z \cdot \nabla w \, \mathrm{d}\Omega = \int_\Omega j_{s,z}\, w \, \mathrm{d}\Omega. \tag{2.55}$$

This can be rewritten, using the theorem of GAUSS (2.19) on the first term, such that

$$-\int_{\partial\Omega} w\, \nu\, \nabla a_z \cdot \mathbf{n} \, \mathrm{d}\Gamma + \int_\Omega \nu\, \nabla a_z \cdot \nabla w \, \mathrm{d}\Omega = \int_\Omega j_{s,z}\, w \, \mathrm{d}\Omega, \tag{2.56}$$

where $\mathbf{n}$ is the normal unit vector perpendicular to the surface $\partial\Omega$. To obtain (2.56) from (2.54) it is also possible to apply the GREEN formula [93, Chapter 1.3]. Defining the bilinear form

$$a(u, w) = \int_\Omega \nu\, \nabla u \cdot \nabla w \, \mathrm{d}\Omega = (\nu\, \nabla u, \nabla w)_{L^2(\Omega)}, \tag{2.57}$$

equation (2.56) can be written as

$$a(a_z, w) = (j_{s,z}, w)_{L^2(\Omega)} + (\nu\, \nabla a_z \cdot \mathbf{n}, w)_{L^2(\partial\Omega)}, \tag{2.58}$$

where the second term on the right-hand side is the boundary term.

To solve this problem on the domain depicted in Fig. 2.1, the Dirichlet and Neumann boundary conditions (2.25) and (2.27), respectively, have to be incorporated. This is achieved by taking the Neumann boundary into account through the boundary term in (2.58) and the Dirichlet boundary through a proper modification of the spaces. Consequently, the Neumann boundary condition is called natural boundary condition, while the Dirichlet boundary condition is called essential boundary condition. To implement non-homogeneous Dirichlet boundary conditions the solution a_z is written as $a_z = \widetilde{a}_z + u_g$, where $u_g \in H^1(\Omega)$ is an arbitrary but fixed function which fulfills the Dirichlet boundary condition, i.e. $u_g|_{\Gamma_D} = \gamma_D$. The resulting problem can now be written as follows:

Find $\widetilde{a}_z \in W = \left\{ w \in H^1(\Omega) \,\middle|\, w|_{\Gamma_D} = 0 \right\}$ such that

$$a(\widetilde{a}_z, w) = (j_{s,z}, w)_{L^2(\Omega)} + (\gamma_N, w)_{L^2(\Gamma_N)} - a(u_g, w), \quad \forall\, w \in W. \tag{2.59}$$

Note that since w vanishes on the Dirichlet boundary, the boundary term is only evaluated on the Neumann part of the boundary. The final solution is given by $a_z = \widetilde{a}_z + u_g$. As one can see, the test functions w are from the same space in which $\widetilde{a}_z$ is sought. The resulting method, after discretization, is called a Ritz-Galerkin method. If the spaces of solution and test functions are different, one speaks of a Petrov-Galerkin method. Existence and uniqueness of the solution of (2.59) is provided by the Lax-Milgram theorem, see e.g. [93, Chapter 5.1.1] for more details.

2.3.3 Ritz-Galerkin approach

To solve (2.59) numerically on a computer, it needs to be discretized. Let W_h be a finite dimensional subspace of W. The subscript denotes a mesh parameter $h > 0$ but small. It can be the element size in case finite elements are used, or the inverse of the polynomial degree, in case a spectral method is used [93, Chapter 5.2]. From this subspace we expect that

$$\lim_{h \to 0} \inf_{w_h \in W_h} \|w - w_h\| = 0 \quad \forall w \in W, \tag{2.60}$$

holds, meaning that for smaller h, the quality of approximation of functions in W by functions in W_h improves. In a next step a basis w_k, $k = 0, \ldots, N_{\mathrm{p}}$ of the space W_h is chosen and the unknown $\widetilde{a}_{\mathrm{z}}$ from (2.59) is represented by a sum of these basis functions weighted with coefficients such that

$$\widetilde{a}_{\mathrm{z}}(\mathbf{r}) \approx \sum_{k=0}^{N_{\mathrm{p}}} \widetilde{a}_{\mathrm{z,k}}\, w_k(\mathbf{r}), \tag{2.61}$$

where $\widetilde{a}_{\mathrm{z,k}}$ are the coefficients. The same holds for the already known Dirichlet boundary conditions, i.e.

$$u_g(\mathbf{r}) \approx \sum_{k=0}^{N_{\mathrm{p}}} u_{g,k}\, w_k(\mathbf{r}). \tag{2.62}$$

Inserting the solution expansion into (2.59) and writing the equations for each of the test functions w_k, a system of linear equations arises

$$\sum_{k=0}^{N_{\mathrm{p}}} \widetilde{a}_{\mathrm{z,k}} \underbrace{\int_\Omega \nu\, \nabla w_k \cdot \nabla w_l\, \mathrm{d}\Omega}_{K_{lk}} = \underbrace{\int_\Omega j_{\mathrm{s,z}}\, w_l\, \mathrm{d}\Omega}_{j_{\mathrm{s,z},l}} + \underbrace{\int_{\partial\Omega} \gamma_{\mathrm{N}}\, w_l\, \mathrm{d}\Gamma}_{\gamma_{\mathrm{N},l}} - \sum_{k=0}^{N_{\mathrm{p}}} u_{g,k} \underbrace{\int_\Omega \nu\, \nabla w_k \cdot \nabla w_l\, \mathrm{d}\Omega}_{K_{lk}}, \tag{2.63}$$

where K_{lk} is the entry in row l and column k of the matrix $\mathbf{K}$, $j_{\mathrm{s,z},l}$ and $\gamma_{\mathrm{N},l}$ are the l-th entry of the column vectors $\mathbf{j}_{\mathrm{s,z}}$ and $\boldsymbol{\gamma}_{\mathrm{N}}$, respectively, and $\widetilde{a}_{\mathrm{z,k}}$ and $u_{g,k}$ are the k-th entry of the column vector $\widetilde{\mathbf{a}}_{\mathrm{z}}$ and $\mathbf{u}_g$, respectively. With these abbreviations the equation system is

$$\mathbf{K}\,\widetilde{\mathbf{a}}_{\mathrm{z}} = \mathbf{j}_{\mathrm{s,z}} + \boldsymbol{\gamma}_{\mathrm{N}} - \mathbf{K}\,\mathbf{u}_g. \tag{2.64}$$

The matrix $\mathbf{K}$ is in analogy with mechanics often called stiffness matrix.

If the magnetoquasistatic problem (2.24) is considered, there exists an additional term in the final system of equations leading to the IVP

$$\mathbf{M}\frac{\mathrm{d}\widetilde{\mathbf{a}}_{\mathrm{z}}(t)}{\mathrm{d}t} + \mathbf{K}\,\widetilde{\mathbf{a}}_{\mathrm{z}}(t) = \mathbf{j}_{\mathrm{s,z}} + \boldsymbol{\gamma}_{\mathrm{N}} - \mathbf{K}\,\mathbf{u}_g$$
$$\widetilde{\mathbf{a}}_{\mathrm{z}}(0) = \widetilde{\mathbf{a}}_{\mathrm{z}}^{(0)}, \tag{2.65}$$

where

$$M_{lk} = \int_\Omega \sigma\, w_k\, w_l\, \mathrm{d}\Omega, \tag{2.66}$$

are the entries of the conductivity matrix and $\widetilde{\mathbf{a}}_{\mathrm{z}}^{(0)}$ is the initial value. The coefficients $\widetilde{\mathbf{a}}_{\mathrm{z}}$ are functions of time such that the solution a_{z} is now a function of time as well and given by

$$a_{\mathrm{z}}(\mathbf{r}, t) = \sum_{k=0}^{N_{\mathrm{p}}} (\widetilde{a}_{\mathrm{z,k}}(t) + u_{g,k})\, w_k(\mathbf{r}) \tag{2.67}$$
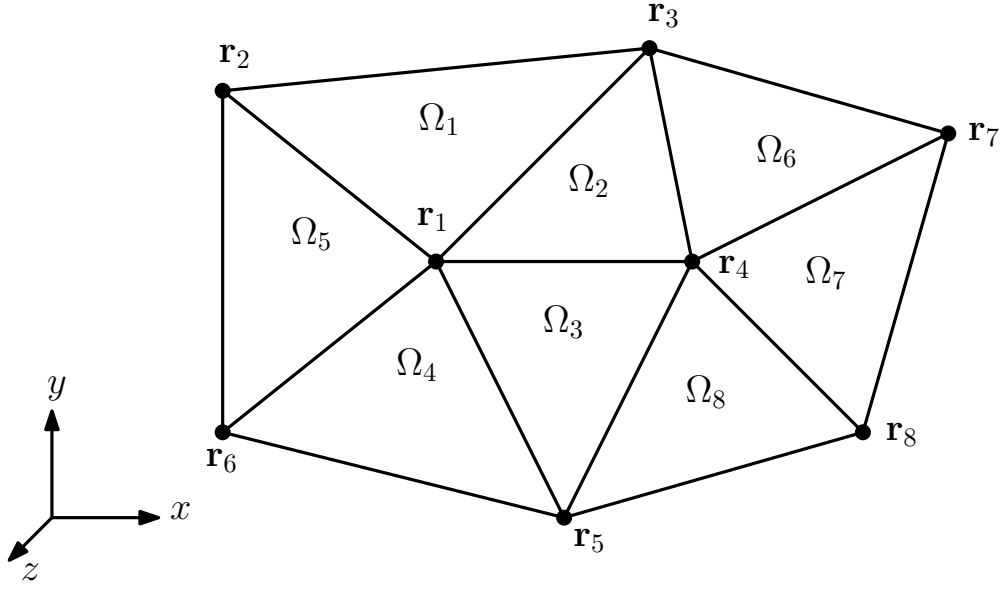
Figure 2.7: Exemplary mesh with elements and nodes.

2.3.4 Classical finite element basis functions

The computation domain in classical 2D FEM is usually discretized by a triangular mesh [102]. Each triangle is called an element and is defined by three nodes. The k-th node of the mesh is associated with a so-called nodal basis function w_k, which is maximum at this particular node and decays linearly (in case of lowest order basis functions) towards the neighboring nodes in each element. An exemplary mesh with a few elements and nodes is depicted in Fig. 2.7. The nodal basis functions w_k are given by

$$w_k(\mathbf{r}) = \begin{cases} \varsigma_{1,k,l}\, r_1 + \varsigma_{2,k,l}\, r_2 + \varsigma_{3,k,l} & \text{for all } \mathbf{r} \in \Omega_l \wedge \text{ node } k \text{ is a vertex of } \Omega_l \\ 0 & \text{otherwise,} \end{cases} \tag{2.68}$$

where $\varsigma_{1,k,l}$, $\varsigma_{2,k,l}$, $\varsigma_{3,k,l}$ are coefficients and r_1, r_2 correspond to the x, y coordinate, respectively. On each triangle Ω_l the $\varsigma_{1,k,l}$, $\varsigma_{2,k,l}$, $\varsigma_{3,k,l}$ are found by stipulating that

$$w_k(\mathbf{r}) = \begin{cases} 1 & \text{for } \mathbf{r} = \mathbf{r}_k \text{ where } \mathbf{r}_k \text{ is a vertex of } \Omega_l \\ 0 & \text{for } \mathbf{r} = \mathbf{r}_m \text{ where } \mathbf{r}_m \text{ is a vertex of } \Omega_l \wedge m \neq k, \end{cases} \tag{2.69}$$

where $\mathbf{r}_k$ denotes the position of node k in the computational domain according to Fig. 2.7. This means that the basis functions are 1 at their respective nodes and decay linearly towards the neighboring nodes, where they finally become zero. Due to the resulting shape of the basis functions, they are also called hat functions.

For easing the construction of the matrices in (2.65), usually a mapping of each of the triangles towards a reference triangle is established. For more information on this, the interested reader is referred to [69].

2.4 Coupling of field and circuit models

In many applications the simulation using only a field or a circuit model may not be sufficient to obtain the required results. The reason for this is twofold. First, circuit models simplify the electrical elements to enable a very simple description by only a few or one parameter. This can be disadvantageous if a higher model accuracy is required, but advantageous because the computational effort is relatively small. Secondly, field models are accurate in terms of modeling the physical phenomena, but also very expensive in terms of computational effort. Therefore a mixture of both is often desirable. To establish a field-circuit coupling it is necessary to connect the degrees of freedom of the field model, e.g. the MVP $\mathbf{a}$ in case of magnetostatic or -quasistatic problems, with the voltages and currents which are associated with an electrical element in the circuit model. The electrical element is characterized by the voltage v_{str} and the current i_{str}. For the coupling, the concept of winding functions [106] is utilized. Depending on the type of conductor which is used in the field model, i.e. stranded conductor or solid conductor, the winding function model differs. A stranded conductor consists of many thin conducting wires (diameter below skin depth) which are isolated from each other while a solid conductor is made of a massive block of conducting material. Therefore a solid conductor is prone to eddy current losses, while in a stranded conductor they are small or often even neglected. In the following the focus lies on the stranded-conductor model which is commonly employed for coils.

The essential assumption of (current-oriented) stranded-conductor models is that on the cross-section of each wire the current density is constant [106]. This way in a 2D field model, assuming there is only one coil, it can be expressed as

$$j_{\mathrm{s,z}}(\mathbf{r}, t) = \chi_{\mathrm{str},z}(\mathbf{r})\, i_{\mathrm{str}}(t), \tag{2.70}$$

where $\chi_{\mathrm{str},z}$ is the winding function distributing the current i_{str} across the conductors in the computation domain, i.e. $\mathbf{r} \in \Omega$. It has to fulfill the condition

$$\int_{\Omega} \chi_{\mathrm{str},z}(\mathbf{r})\, \mathrm{d}\Omega = N_{\mathrm{t}}, \tag{2.71}$$

where Ω is the 2D computation domain and N_{t} is the number of turns of the coil.

To obtain the voltage drop along the conductors, the magnetic flux linkage is needed. It is given by

$$\Phi(t) = \int_{\Omega} \chi_{\mathrm{str},z}(\mathbf{r})\, a_{\mathrm{z}}(\mathbf{r}, t)\, l_z\, \mathrm{d}\Omega, \tag{2.72}$$

where l_z is the length of the field model in z-direction. According to the FARADAY law (2.1) the voltage drop along the stranded conductor consists of an induced voltage, i.e. $\frac{\mathrm{d}\Phi(t)}{\mathrm{d}t}$. Additionally there is also a resistive voltage drop due to the non-zero conductivity of the stranded conductors leading to

$$v_{\mathrm{str}}(t) = R_{\mathrm{str}} i_{\mathrm{str}}(t) + \frac{\mathrm{d}\Phi(t)}{\mathrm{d}t}, \tag{2.73}$$

where R_{str} is the resistance of the stranded conductor. It can be calculated by

$$R_{\mathrm{str}} = \int_{\Omega} \frac{(\chi_{\mathrm{str},z}(\mathbf{r}))^2\, l_z}{\sigma_{\mathrm{str}} \gamma_{\mathrm{str}}}\, \mathrm{d}\Omega. \tag{2.74}$$

where σ_{str} is the conductivity of the conductor material and $\gamma_{\mathrm{str}} \in (0, 1]$ is called fill factor. It defines how much conducting material compared to isolating material is used, considering the cross-section of the stranded conductor. If the factor is 1 it only contains conducting material, if near 0, the material is mostly made of isolating material.

The discretization of the continuous formulation towards a discrete field model is straight-forward and similar as in (2.63). The discretized winding function is a vector $\mathbf{X}_{\mathrm{str}} \in \mathbb{R}^{(N_{\mathrm{P}}+1) \times 1}$, where the l-th element is given by

$$X_{\mathrm{str},l} = \int_{\Omega} \chi_{\mathrm{str},z}(\mathbf{r})\, w_l(\mathbf{r})\, \mathrm{d}\Omega. \tag{2.75}$$

The discrete counterpart to (2.70) is consequently

$$\mathbf{j}_{\mathrm{s,z}}(t) = \mathbf{X}_{\mathrm{str}} i_{\mathrm{str}}(t). \tag{2.76}$$

Similarly, the magnetic flux linkage (2.72) becomes

$$\Phi(t) \approx \mathbf{X}_{\mathrm{str}}^{\top}\, \mathbf{a}_{\mathrm{z}}(t)\, l_z, \tag{2.77}$$

where $\mathbf{a}_{\mathrm{z}}(t)$ is the discrete vector of the MVP. Those in combination with (2.73) give voltage and current necessary for the coupling with a circuit. For more information on field-circuit coupling the reader is referred to [18, 20, 106] and the references therein. They also treat the coupling for solid conductors which has not been discussed here.

2.5 Ordinary differential and differential-algebraic equations

Natural phenomena, which are deterministic, can often be described by ordinary differential equations (ODEs) or differential-algebraic equations (DAEs). For instance the movement of a pendulum in angular coordinates is modeled using a simple ODE. However, in cartesian coordinates the equations of the pendulum become a rather complicated DAE, see [43, page 463]. Another example are electrical circuits, or field models which are semi-discretized in space. The resulting equations describe the phenomena depending only on time and not on space.

In this section ODEs and DAEs are introduced. The explanations start with ODEs and the existence and uniqueness of solutions thereof. Subsequently the difference to DAEs is highlighted and the index concept to characterize DAEs is mentioned. The section is concluded by explaining two discretization techniques to numerically solve ODEs and DAEs. The summarized information follows commonly known literature [12, 17, 43, 64].

The equation system given by

$$\frac{\mathrm{d}}{\mathrm{d}t}\, \mathbf{x}_{\mathrm{d}} = \mathbf{f}(\mathbf{x}_{\mathrm{d}}, t) \tag{2.78}$$

is called a first-order system of ODEs, where $\mathbf{x}_{\mathrm{d}}(t) \in \mathbb{R}^{N_{\mathrm{d}}}$ is the unknown solution vector, $\mathbf{f}(\mathbf{x}_{\mathrm{d}}, t) \in \mathbb{R}^{N_{\mathrm{d}}}$ is a vector function and $t \in \mathbb{R}$ is the time. The Jacobian matrix of $\mathbf{f}(\mathbf{x}_{\mathrm{d}}, t)$ is denoted by $\frac{\partial \mathbf{f}}{\partial \mathbf{x}_{\mathrm{d}}}$ and shall be non-singular. The term "first-order" denotes that only the first derivative of the solution is present. To solve these ODEs, initial values have to be specified, often denoted by $t^{(0)}$ and $\mathbf{x}_{\mathrm{d}}^{(0)} = \mathbf{x}_{\mathrm{d}}(t^{(0)})$. The set of equations (2.78) with initial values, called initial value problem (IVP), has a unique solution if $\mathbf{f}$ is Lipschitz-continuous [64, Chapter V.2]. Weakened conditions are provided by Carathéodory, under which a solution even exists if

$\mathbf{f}$ is only continuous for almost all t [33, Chapter 1]. In the case of ideal pulsed excitations as in the following Section 2.6, the problem can also be regarded as a sequence of IVPs, where for each IVP the function $\mathbf{f}$ is Lipschitz-continuous again. Besides existence and uniqueness of the solution another important property of the IVP is stability. The notion of stability deals with the error in the solution of (2.78) resulting from small perturbations in the initial values and/or the right-hand side $\mathbf{f}$. If the error remains bounded for any $t > t^{(0)}$, the IVP is called Lyapunov stable [64, Chapter V.2]. If the function $\mathbf{f}$ is linearly dependent on the solution, i.e. for instance if $\mathbf{f}(\mathbf{x}_d, t) = \mathbf{B}\,\mathbf{x}_d + \mathbf{c}(t)$, and $\mathbf{c}(t)$ is sufficiently simple, then an analytic solution is possible [17].

Adding additional algebraic constraints to (2.78) leads to a modified system of equations

$$\frac{\mathrm{d}}{\mathrm{d}t}\,\mathbf{x}_d = \mathbf{f}(\mathbf{x}_d, \mathbf{x}_a, t), \tag{2.79}$$

$$0 = \mathbf{g}(\mathbf{x}_d, \mathbf{x}_a), \tag{2.80}$$

where $\mathbf{x}_a(t) \in \mathbb{R}^{N_a}$ are additional variables and $\mathbf{g} \in \mathbb{R}^{N_a}$ is the constraint function. The system (2.79), (2.80) is called differential-algebraic, since not only a differential but also an algebraic part is present. The DAEs in this form are also called semi-explicit [12, Chapter 1.2].

The difficulty solving DAEs is generally higher than when solving ODEs. The theory on existence and uniqueness of solutions is more involved [12, Chapter 2]. The same holds for the stability properties [60]. Additionally the choice of initial values is not trivial any more, since they need to satisfy the constraints (2.80). To characterize the DAEs the concept of DAE index is used. There are a number of these index concepts, e.g. differentiability index, tractability index, perturbation index, see [28] for more details. In the following the differentiability index is shortly explained on the DAEs (2.79), (2.80). Differentiating the constraint term (2.80) leads to [12, Chapter 2.2]

$$\frac{\partial \mathbf{g}}{\partial \mathbf{x}_d}\frac{\mathrm{d}\mathbf{x}_d}{\mathrm{d}t} + \frac{\partial \mathbf{g}}{\partial \mathbf{x}_a}\frac{\mathrm{d}\mathbf{x}_a}{\mathrm{d}t} = \frac{\mathrm{d}\mathbf{g}}{\mathrm{d}t}. \tag{2.81}$$

If the Jacobian matrix $\frac{\partial \mathbf{g}}{\partial \mathbf{x}_a}$ is non-singular, then this is a differential equation determining the additional variables $\mathbf{x}_a(t)$ and in connection with (2.79) leads to a system of ODEs. This way, the system of DAEs was reduced to a system of ODEs (index reduction). The differentiability index denotes the number of differentiations which are necessary to reduce the DAEs (2.79), (2.80) to ODEs. If the Jacobian matrix $\frac{\partial \mathbf{g}}{\partial \mathbf{x}_a}$ is non-singular, the index is 1, otherwise the index is 2 or higher. In the remainder of this work only DAEs of index 1 are considered.

To find consistent initial values of the index-1 system (2.79), (2.80) the following procedure is applied

1. The differential variables are fixed to the desired initial values $\mathbf{x}_d^{(0)}$ at $t^{(0)}$.

2. The algebraic variables are calculated solving (2.80) by a Newton-Raphson scheme, yielding $\mathbf{x}_a^{(0)}$.

3. The initial slope is calculated by inserting $t^{(0)}$, $\mathbf{x}_d^{(0)}$, $\mathbf{x}_a^{(0)}$ into (2.79) and evaluating which leads to $\left.\frac{\mathrm{d}\mathbf{x}_d(t)}{\mathrm{d}t}\right|_{t=t^{(0)}}$

2.5.1 Discretization using backward differentiation formulas and Runge-Kutta methods

The DAEs (2.79), (2.80) can often be written as

$$\mathbf{A}\frac{\mathrm{d}\mathbf{x}}{\mathrm{d}t} = \mathbf{c}(t) - \mathbf{B}(\mathbf{x}, t)\,\mathbf{x}(t), \tag{2.82}$$

which means that differential and algebraic variables are summarized in the same vector $\mathbf{x}$ and the information about which variables are differential and which are algebraic is incorporated in the mass matrix $\mathbf{A}$. If $\mathbf{A}$ is singular, (2.82) are DAEs, otherwise ODEs.

To solve these ODEs or DAEs there are a number of numerical methods. One distinguishes generally between explicit and implicit methods. Although the explicit methods are computationally less expensive than implicit ones, the focus here lies on implicit methods only, since they provide the necessary numerical stability for the differential equations at hand. What is more, explicit methods cannot be applied in case of DAEs due to the algebraic equations. In the following the class of backward differentiation formulas (BDFs) and implicit Runge-Kutta (IRK) methods are discussed briefly. Furthermore, the notion of stiffness of ODEs and DAEs and the stability of the discussed time integration schemes are summarized.

The idea of the BDFs is to replace the derivative from (2.82) at time instant $t^{(n)}$ by finite difference (FD) formulas

$$\left.\frac{\mathrm{d}\mathbf{x}}{\mathrm{d}t}\right|_{t=t^{(n)}} \approx \frac{1}{h}\sum_{i=0}^{m_{\mathrm{fd}}} \alpha_i^{\mathrm{fd}}\,\mathbf{x}^{(n-i)}, \tag{2.83}$$

where α_i^{fd} are coefficients and $\mathbf{x}^{(n-i)} = \mathbf{x}(t^{(n-i)})$. Inserting this into the differential equations (2.82) yields

$$\mathbf{A}\frac{1}{h}\sum_{i=0}^{m_{\mathrm{fd}}} \alpha_i^{\mathrm{fd}}\,\mathbf{x}^{(n-i)} = \mathbf{c}\left(t^{(n)}\right) - \mathbf{B}\left(\mathbf{x}^{(n)}, t^{(n)}\right)\mathbf{x}^{(n)}, \tag{2.84}$$

which uses the solution at m_{fd} past time instants to offer the solution at the current time instant $t^{(n)}$. For the simple backward difference formula with $m_{\mathrm{fd}} = 1$, $\alpha_0^{\mathrm{fd}} = 1$, $\alpha_1^{\mathrm{fd}} = -1$, the resulting method is called backward Euler or BDF1. For $m_{\mathrm{fd}} > 1$ the coefficients α_i^{fd} are found by requiring optimal consistency order [64, Chapter VIII.6]. To solve the nonlinear equations (2.84) in each step, usually a Newton-Raphson scheme is applied. Due to the fact that BDFs use the solution at several distinct time instants, they belong to the class of linear multi-step methods. For more information the interested reader is referred to [64, Chapter VII.1] or [12, Chapter 3.1].

Opposed to the BDFs, the IRK methods are one-step methods. To obtain the same accuracy as BDFs, they typically need more evaluations of the right-hand side of (2.82). Applying an IRK method to (2.82) yields

$$\mathbf{x}^{(n)} = \mathbf{x}^{(n-1)} + h\sum_{l=1}^{m_{\mathrm{irk}}} \alpha_l^{\mathrm{irk}}\mathbf{k}_l, \tag{2.85}$$

$$0 = \mathbf{c}\left(t^{(n-1)} + \beta_i^{\mathrm{irk}}h\right) - \mathbf{B}\left(\mathbf{x}^{(n-1)} + h\sum_{j=1}^{m_{\mathrm{irk}}} \gamma_{ij}^{\mathrm{irk}}\mathbf{k}_j, t^{(n-1)} + \beta_i^{\mathrm{irk}}h\right)\left(\mathbf{x}^{(n-1)} + h\sum_{j=1}^{m_{\mathrm{irk}}} \gamma_{ij}^{\mathrm{irk}}\mathbf{k}_j\right) - \mathbf{A}\,\mathbf{k}_i, \tag{2.86}$$

for all $1 \leq i \leq m_{\mathrm{irk}}$, where h is the step size, α_i^{irk}, β_i^{irk}, $\gamma_{ij}^{\mathrm{irk}}$ are coefficients and m_{irk} is called the number of stages of the IRK method. Similarly as for the BDFs, to solve the nonlinear equations (2.86) in each step,

a Newton-Raphson scheme is applied. For a compact notation of the scheme, the Butcher tableau can be utilized. For more information see [64, Chapter III.1] and [12, Chapter 4].

To determine stability of the time integration schemes, they are (theoretically) applied to the scalar Dahlquist test equation [43]

$$\frac{\mathrm{d}x}{\mathrm{d}t} = \lambda x(t), \tag{2.87}$$

where $\lambda \in \mathbb{C}$ is a parameter to control the stiffness. The solution of this equation is given by

$$x(t) = \mathrm{e}^{\lambda t}. \tag{2.88}$$

This means that if λ contains an imaginary part, there will be a harmonic (sinusoidal) solution component and the real part of λ determines whether the solution is undamped ($\mathfrak{Re}(\lambda) = 0$), damped ($\mathfrak{Re}(\lambda) < 0$) or amplified ($\mathfrak{Re}(\lambda) > 0$). The amplified case is typically not interesting since without an excitation no physically existing system will amplify itself. Discretizing (2.87), the solution at time steps $t^{(n)}, t^{(n+1)}, \ldots$ can be written as

$$x^{(n+1)} = \Psi(\lambda h)\, x^{(n)} \tag{2.89}$$

where $\Psi(\lambda h)$ is called increment function [64, Chapter VIII.4], λ is the parameter from (2.87) and h is the step size. Each time integration scheme has its individual increment function. The stability region S of a time integration scheme is defined by [64, Chapter VIII.5]

$$S := \left\{ z \in \mathbb{C} \,\middle|\, |\Psi(z)| \leq 1 \right\}, \tag{2.90}$$

where $z = \lambda h$. This is the region, where the time integration scheme does not artificially amplify the magnitude of the solution. A method is called A-stable if the stability region contains the negative complex half-plane, i.e.

$$\left\{ z \in \mathbb{C} \,\middle|\, \mathfrak{Re}(z) \leq 0 \right\} \subset S. \tag{2.91}$$

It is called A(α)-stable if

$$\left\{ z \in \mathbb{C} \,\middle|\, -\alpha < \pi - \arg(z) < \alpha,\, 0 < \alpha < \frac{\pi}{2} \right\} \subset S. \tag{2.92}$$

The BDFs (2.84) for $m_{\mathrm{fd}} \leq 2$ are A-stable. For $2 < m_{\mathrm{fd}} \leq 6$ they are only A(α)-stable [64, Chapter VIII.5]. The stability regions for $m_{\mathrm{fd}} = 3$ and $m_{\mathrm{fd}} = 5$ are exemplary depicted in Fig. 2.8. Concerning the IRK methods, it is possible to construct methods which are A-stable, see [43, Chapter IV.5]. The advantage of A-stable methods is that the step size h is not restricted by stability concerns. There are differential equations, in which this is of particular importance. Those differential equations are called stiff. With explicit schemes which only exhibit a very limited stability region, it is hardly possible to solve these equations efficiently since the step size must often be chosen excessively small to guarantee a convergence of the solution even if the accuracy of the solution does not require such a small step size.

2.6 Pulse-width modulation and pulsed excitation

The term pulse-width modulation (PWM) is often used when speaking about power converters. Essentially a PWM signal is a pulsed signal as depicted in Fig. 2.9, whose pulse lengths are modulated in a specific way. In power converters this technique is applied to control the output voltage or current of the converter. The aim
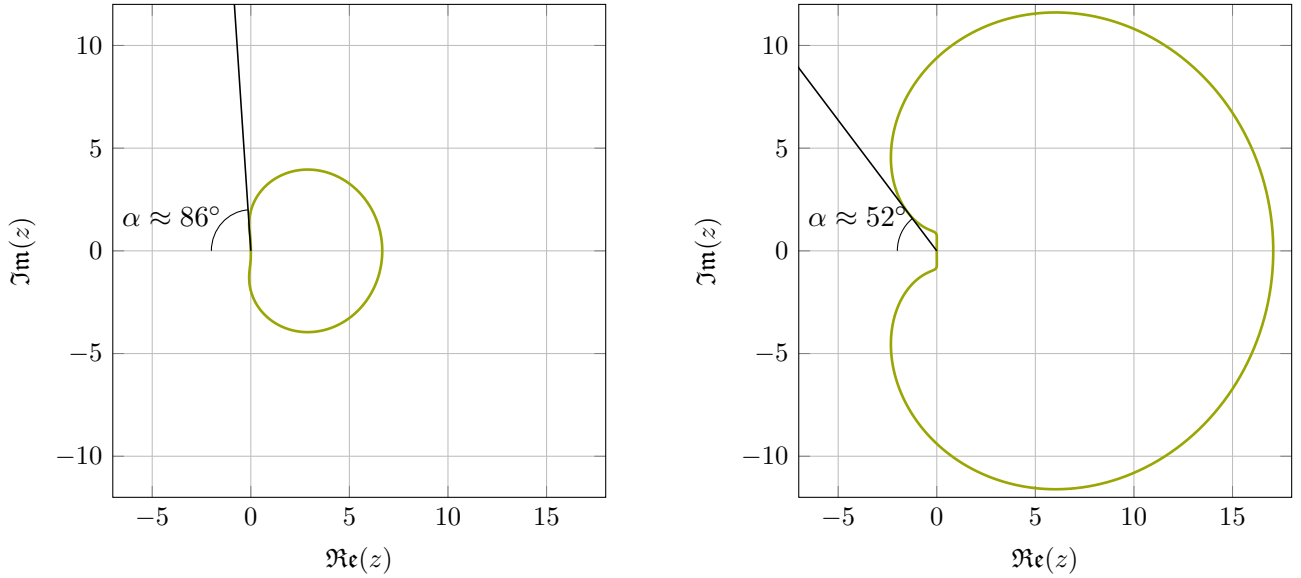
Figure 2.8: Stability region of BDF methods for (a) $m_{\text{fd}} = 3$ and (b) $m_{\text{fd}} = 5$. If z lies in the area outside the green line, there is no numerical instability.

of the PWM signal is that its time-averaged value is the same or at least closely related to a reference signal. This section introduces a few of the different concepts to generate PWM signals. It follows the information given in [47, 68, 118].

The exemplary PWM signal depicted in Fig. 2.9 is ideal meaning that the rise and fall times of the signal are zero and thus the steepness of the rising flank and falling flank are infinite. This is unlike in reality, when generating the PWM signal with a circuit using transistors. However, also in reality the steepness of the flanks is usually very high and thus the rise and fall times can often be neglected [118, Chapter 2.1]

There are four important quantities of PWM signals. First, the switching frequency f_{s}, which is the inverse of the switching period T_{s} of one pulse (on and off time). The switching period is often also referred to as switching cycle or switching interval. One distinguishes between constant and varying switching-frequency PWM. In the following only constant switching-frequency PWM is considered. Second, the duty cycle D which is the relation between the on-time $\triangle t_{\text{on}}$ and the switching period, i.e. $D = \frac{\triangle t_{\text{on}}}{T_{\text{s}}}$. The third and fourth quantity are given by the amplitude modulation ratio (or index) and the frequency modulation ratio (or index) [68, Chapter 8.2.1]. Given a reference signal $d(t)$, the corresponding PWM signal is generated by comparing the reference to a carrier $s(t)$. The result is mathematically given by

$$c(t) = \text{sgn}(d(t) - s(t)), \tag{2.93}$$

where sgn is the sign function. The amplitude modulation index is the ratio between the maximum values of the usually sinusoidal reference signal and the carrier signal, i.e.

$$m_{\text{a}} = \frac{\max\limits_{t} |d(t)|}{\max\limits_{t} |s(t)|}. \tag{2.94}$$

If $0 \leq m_{\text{a}} \leq 1$ the amplitude of the fundamental frequency component of the output signal $c(t)$ is proportional to m_{a}. If $m_{\text{a}} > 1$ one speaks of overmodulation. The frequency modulation index is given by the ratio of the
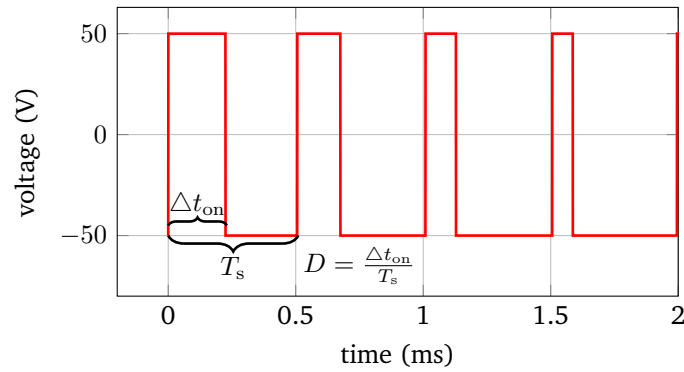
Figure 2.9: Generic PWM signal.

(a) Sawtooth

(b) Inverted sawtooth

(c) Triangle
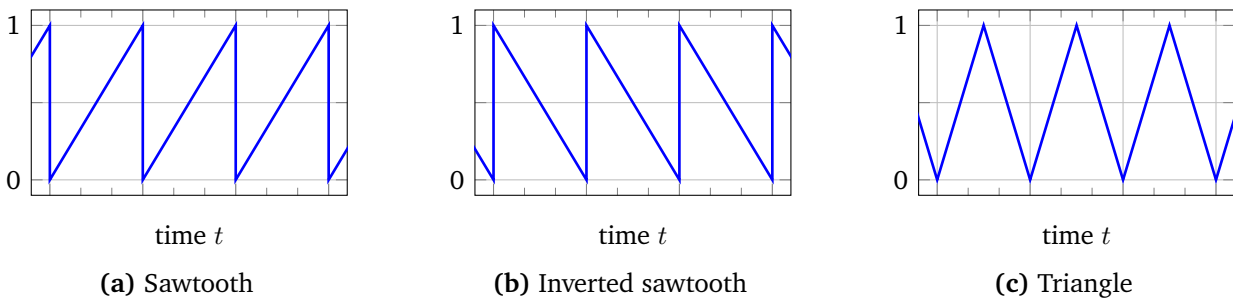
Figure 2.10: The three different carriers mainly used in PWM generation.

reference signal frequency f_{ac} and the carrier frequency

$$m_f = \frac{f_{ac}}{f_s}. \tag{2.95}$$

The frequency modulation index has an influence on the harmonics of the output signal, while the amplitude modulation index only has an influence in the case $m_a > 1$.

The most commonly applied carriers are listed in the following [118, Chapter 2.1]:

- The **sawtooth carrier** is depicted in Fig. 2.10a. It leads to a PWM signal in which the rising flank is always at fixed time instants. In this case, always at the beginning of a switching interval. The falling flank, in contrast, is modulated with respect to the reference signal.

- The **inverted sawtooth carrier** is depicted in Fig. 2.10b. Since the sawtooth is inverted, the rising flank of the PWM signal is now modulated while the falling flank is at fixed time instants, namely the end of the switching interval.

- The **triangle carrier** is depicted in Fig. 2.10c. In this case both, the rising and falling flank of the PWM signal are modulated.

All three carriers are different with regard to their harmonic properties and are therefore used in different applications. For more information the interested reader is referred to [118, Chapter 2.2].

The generation of a PWM signal as given by (2.93) requires that the reference signal $d(t)$ is continuously given for any time instant. Although this is true for an analog application with analog circuitry, it is unpractical
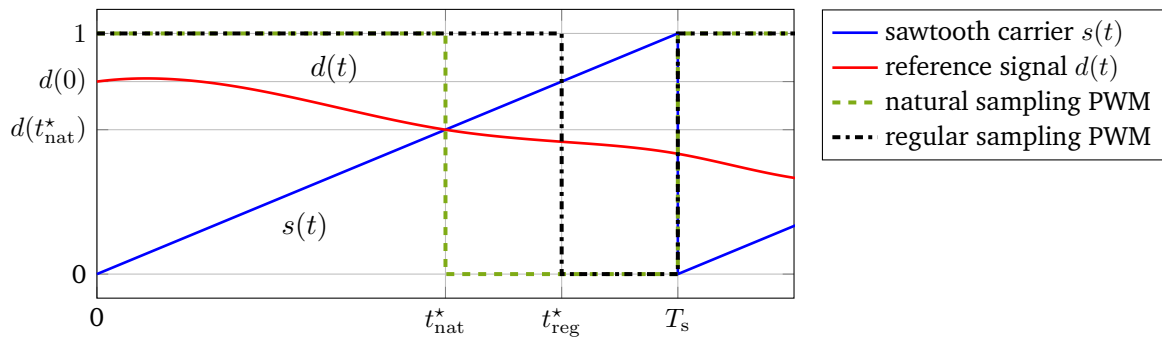
Figure 2.11: Regular versus natural sampling and its effect on the generated PWM signal. For natural sampling the switching occurs at the intersection of $d(t)$ and $s(t)$. For regular sampling, the value $d(0)$ is held constant throughout the interval and thus the switching occurs at a different time.

when considering digital applications. The reason for this is that in digital applications the signals are sampled in certain time intervals and thus are only given as a set of discrete values and not as continuous functions. Besides the technical problems in reality, using (2.93) in combination with a control system in a computer simulation can cause extremely small time steps and thus excessively long simulation durations. To overcome this problem, the reference signal is sampled before using (2.93) and held constant until the next sample is taken. Usually the samples are taken at the beginning or end of a switching period or at the position of the peak or valley of the carrier signal. The resulting PWM signal is called **regularly sampled** opposed to the analog variant without sampling, which is referred to as **natural sampling**. Another sampling technique called "Direct PWM" is mentioned in [47, Chapter 3.1].

In Fig. 2.11 the resulting PWM signal when using regular sampling and natural sampling is depicted. The reference signal in this example is sampled at the beginning of the switching interval. The carrier is a sawtooth.

3 Efficient power converter simulation using multirate partial differential equations

The conventional time discretization of power converters with idealized pulse-width modulation (PWM) excitation is computationally expensive since small time steps are necessary to resolve the ripples in the power converter output (solution) or the discontinuities in the excitation with the desired accuracy. If the solver features adaptive time stepping a switch event detection is often necessary [114]. The switch event detection recognizes when the excitation abruptly changes its state and restarts the solver at this position with the updated excitation. As initial value the result of the last step is used. The switch event detection limits the applicability of high-order multi-step solvers since they require a certain number of known solutions at past time instances. These are not necessarily available if the switching periods are small. Moreover if switch events do not occur at the beginning or end of time steps, according to [114], many tools for electromagnetic transient simulation either perform the switch event at the end of a time step or use linear interpolation to calculate the approximate position of the switch event. This reduces the order of the overall time stepping to linear or quadratic even if higher order methods are used between the switch events. If no switch event detection is available, the adaptive time stepping may take smaller and smaller time steps until the solver aborts the calculation because the time steps become too small to be numerically resolved on a computer.

This chapter proposes a multirate approach for a more efficient simulation of switch-mode power converters. It is based on the concept of multirate partial differential equations (MPDEs) [10, 97]. These allow to associate different solution components with different time scales. Consider the example of the buck converter circuit as depicted in Fig. 3.1. This converter belongs to the class of DC-DC converters generating an output voltage smaller than the input voltage. The excitation, capacitor voltage and inductor current are shown in Fig. 3.2. The capacitor voltage and inductor current can be split into fast varying periodic ripples which are modulated onto a slowly varying transient. Using the MPDEs these two components can be associated to a
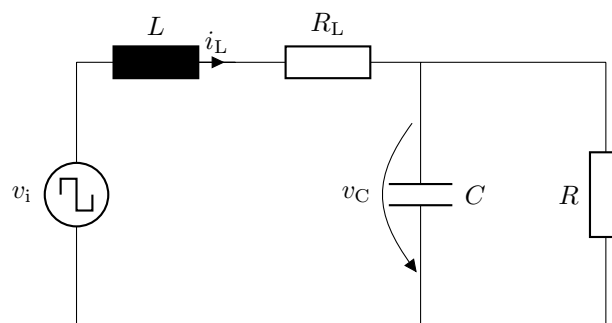
Figure 3.1: Example of a simplified buck converter circuit. Figure based on [80] ©2019 IEEE.
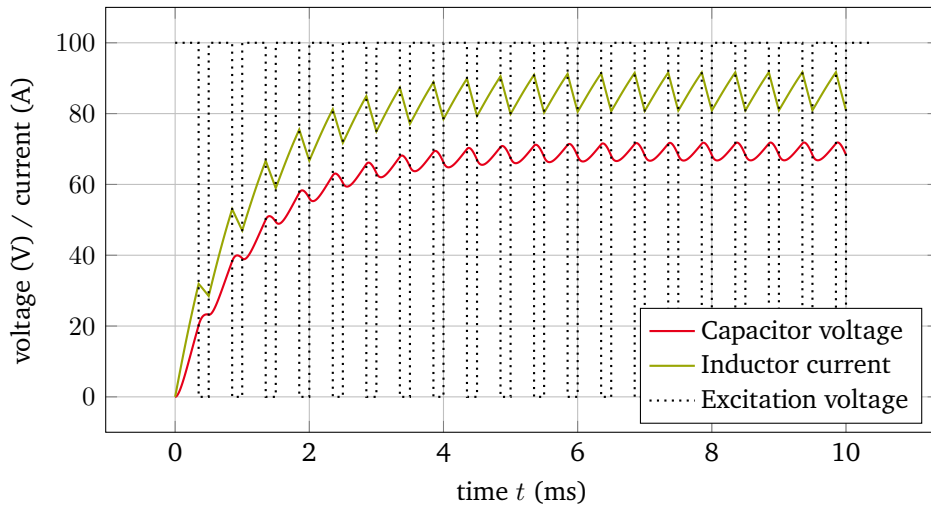
Figure 3.2: Solution and excitation of the simplified buck converter at a switching frequency of $f_s = 2000\,\text{Hz}$.

slowly varying and a fast varying time scale. The MPDEs are solved using two methods to solve along both time scales. By taking advantage of periodicities, an efficient simulation is accomplished.

The structure of this chapter is as follows: In the first Section 3.1 the MPDEs are introduced. The relation between those equations and the original problem described by ordinary differential equations (ODEs) or differential-algebraic equations (DAEs) is established. To provide a well-posed problem, different possibilities of boundary conditions are discussed. In the second Section 3.2 the MPDEs are semi-discretized by a Galerkin approach to resolve the fast varying periodic ripples. It describes how to handle different carriers used to generate the PWM excitation as well as the treatment of nonlinearities in the differential equations describing the power converters. The subsequent Section 3.3 introduces three different types of basis functions which are used for the solution expansion in the Galerkin approach. After the semi-discretization of the MPDEs the remaining differential equations are solved using a conventional time integration method as described in Section 3.4. The proper choice of the multivariate right-hand side, the choice of initial values for the differential equations and the complexity of the MPDE approach are discussed in this section. The chapter is concluded by a proposal on how to deal with regular sampling PWM, since the method inherently only supports natural sampling PWM (Section 3.5). Furthermore an advanced concept of MPDEs, the so-called warped MPDEs (WaMPDEs), is presented in Section 3.6. Its applicability to problems with varying duty cycle is discussed. Finally the chapter is briefly summarized.

3.1 Multirate partial differential equations

The concept of MPDEs is a recent development. It was first introduced by Brachtendorf et al. [10] in 1996, who employed it in the simulation of high-frequency circuits in which more than one fundamental frequency is present. For a comprehensive review of the existing literature see Chapter 1.

We start with a system of ODEs or DAEs. This system can, e.g. represent a circuit, a field-model or a

field-circuit coupled model and is given by

$$\mathbf{A}(\mathbf{x})\frac{\mathrm{d}}{\mathrm{d}t}\mathbf{x}(t) + \mathbf{B}(\mathbf{x})\mathbf{x}(t) = \mathbf{c}(t), \tag{3.1}$$

$$t \in \Upsilon = (0, \mathcal{T}), \tag{3.2}$$

$$\mathbf{x}(0) = \mathbf{x}^{(0)}, \tag{3.3}$$

where $\mathbf{A}(\mathbf{x}) \in \mathbb{R}^{N_s \times N_s}$ is a possibly singular matrix, $\mathbf{B}(\mathbf{x}) \in \mathbb{R}^{N_s \times N_s}$ is a regular matrix, $\mathbf{x}(t)$ and $\mathbf{c}(t)$ are the unknown solution vector and the excitation, respectively, and the second and third line specifies simulation interval and the initial conditions, which completes (3.1) - (3.3) to an initial value problem (IVP). We assume in the remainder of this work that in case of DAEs the specified initial conditions (3.3) are consistent.

To obtain the MPDEs, which correspond to (3.1), new artificial time scales $t_1, \dots, t_m$ are introduced. As a result, the excitation and solution vector are not depending on t any more but on the new artificial time scales $t_1, \dots, t_m$. These multivariate excitation and solution are denoted by $\widehat{\mathbf{c}}(t_1, \dots, t_m)$ and $\widehat{\mathbf{x}}(t_1, \dots, t_m)$, respectively. The MPDEs can now be written as [10]

$$\mathbf{A}(\widehat{\mathbf{x}})\left(\frac{\partial \widehat{\mathbf{x}}(t_1, \dots, t_m)}{\partial t_1} + \dots + \frac{\partial \widehat{\mathbf{x}}(t_1, \dots, t_m)}{\partial t_m}\right) + \mathbf{B}(\widehat{\mathbf{x}})\,\widehat{\mathbf{x}}(t_1, \dots, t_m) = \widehat{\mathbf{c}}(t_1, \dots, t_m), \tag{3.4}$$

$$(t_1, t_2, \dots, t_m) \in \widehat{\Upsilon} = (0, \mathcal{T}_1) \times (0, \mathcal{T}_2) \times \dots \times (0, \mathcal{T}_m). \tag{3.5}$$

As one can see, opposed to (3.1) - (3.3), no initial or boundary conditions are specified yet. Since (3.4) is a partial differential equation, a combination of both initial and boundary conditions can be applied, leading to different types of problems. This will be discussed in the section after the next.

3.1.1 Relation between MPDEs and ODEs/DAEs

Up to now, the relation between the solution and excitation of the original ODEs/DAEs (3.1) and the MPDEs (3.4) is unclear. It is established in the following theorem and proof.

Theorem 1 (adapted from [10, 97]). *Let $\mathbf{x}(t) \in C^1(\Upsilon)$ and $\mathbf{c}(t) \in C^0(\Upsilon)$ be a solution and excitation of the ODEs/DAEs* (3.1)*, respectively. Then the multivariate solution and excitation given by*

$$\widehat{\mathbf{x}}(t + \widehat{\alpha}_1, t + \widehat{\alpha}_2, \dots, t + \widehat{\alpha}_m) = \mathbf{x}(t), \tag{3.6}$$

$$\widehat{\mathbf{c}}(t + \widehat{\alpha}_1, t + \widehat{\alpha}_2, \dots, t + \widehat{\alpha}_m) = \mathbf{c}(t), \tag{3.7}$$

satisfy the MPDEs (3.4) *for any fixed constants $\widehat{\alpha}_1, \widehat{\alpha}_2, \dots, \widehat{\alpha}_m \in \mathbb{R}$.*

Proof. see Appendix 6.1

This theorem is the foundation of this work. It allows to choose any right-hand side $\widehat{\mathbf{c}}$ of the MPDEs as long as it fulfills relation (3.7) and guarantees that a solution of the original ODEs/DAEs $\mathbf{x}$ can be extracted from the MPDE solution $\widehat{\mathbf{x}}$ by using (3.6). At first glance the solution process for the MPDEs is computationally more expensive than that of the ODEs/DAEs, since the computational domain is multi-dimensional whereas that of the ODEs/DAEs is one-dimensional in time. However there are choices of the right-hand side $\widehat{\mathbf{c}}$, which, together with carefully chosen solution methods, lead to a highly efficient solution process. This
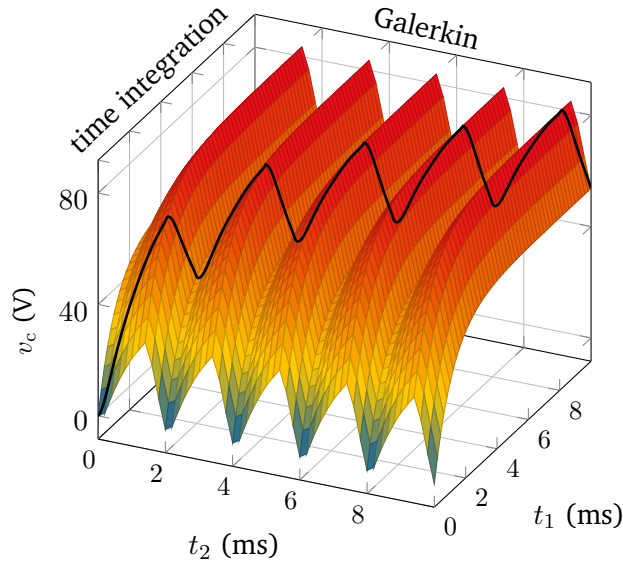
Figure 3.3: Example of a multivariate solution of a buck converter (specifically the voltage at the capacitor). It depends on the two time scales t_1 and t_2. The solution of the original problem is marked as a black curve. Figure adapted from [80] ©2019 IEEE.

is detailed for the case of PWM power converters in the following sections. Fig. 3.3 shows an example of a multivariate solution of the buck converter. The solution depends on two time scales. The solution of the ODEs describing the problem is marked as a black curve. In this case it is extracted along a diagonal through the two-dimensional time domain. This corresponds to $\widehat{\alpha}_1$ and $\widehat{\alpha}_2$ set to zero in Theorem 1.

If the solution and excitation provide less smoothness than stated in Theorem 1, a piecewise analysis is possible. In case of switching excitation, the simulation interval Υ is divided into subintervals. In each subinterval the solution is calculated using the solution at the end of the last subinterval as initial value. The right-hand side on each subinterval is constant. Within the subintervals the solution and excitation thus satisfy the conditions of Theorem 1.

3.1.2 Boundary conditions

Boundary conditions need to be imposed in order to solve the MPDEs (3.4). In the literature the resulting problem is classified into the following two classes depending on the boundary condition [97]:

1. The boundary conditions are chosen as such that a periodicity occurs in each time scale. The solution satisfies

$$\widehat{\mathbf{x}}(t_1 + T_1, \ldots, t_m + T_m) = \widehat{\mathbf{x}}(t_1, \ldots, t_m), \tag{3.8}$$

where $T_1, \ldots, T_m > 0$ are the time intervals of periodicity for each of the time scales $t_1, \ldots, t_m$. The resulting problem, i.e, the MPDEs (3.4) with the boundary conditions (3.8), is called boundary value problem (BVP). The solution of the MPDEs is called periodic while the extracted solution of the original ODEs/DAEs is called quasi-periodic.

2. A mixture of boundary and initial conditions are specified, i.e. the solution satisfies the conditions

$$\widehat{\mathbf{x}}(t_1, t_2 + T_2, \ldots, t_m + T_m) = \widehat{\mathbf{x}}(t_1, t_2, \ldots, t_m)$$
$$\widehat{\mathbf{x}}(0, t_2, \ldots, t_m) = \widehat{\mathbf{x}}^{(0)}(t_2, \ldots, t_m), \tag{3.9}$$

where $T_2, \ldots, T_m > 0$ are, again, the time intervals of periodicity for each of the time scales $t_2, \ldots, t_m$ and $\widehat{\mathbf{x}}^{(0)}(t_2, \ldots, t_m)$ is the function defining the initial condition. The resulting problem, i.e, the MPDEs (3.4) with the boundary conditions (3.9), is called mixed initial boundary value problem (IBVP). The solution along the slow time scale t_1 is called the envelope. For this reason the solutions are also called envelope-modulated.

Now that the key relation between MPDEs and ODEs/DAEs is established and boundary conditions are specified, the system of MPDEs (3.4) is properly defined.

3.2 Semi-discretization using a Galerkin approach

The main idea of the MPDE approach [78, 80–82] is to represent the fast periodically varying ripples by basis functions, which are periodic on the switching interval. This is accomplished by a Ritz-Galerkin approach, i.e. the test functions are the same as the trial functions, see Section 2.3. Due to the ideal switching excitation, some solution components contain a finite number of points of C^0 continuity which the basis functions take into account by construction. The resulting system of ODEs/DAEs after the Galerkin approach are solved using a conventional time integration algorithm. Since we split our solution into slowly and fast varying parts, two artificial time scales are associated with the corresponding components. The slowly varying solution components are associated to the slow time scale t_1 and the fast varying solution components are associated to the fast time scale t_2. We start from a system of N_s ODEs/DAEs given by

$$\mathbf{A}(\mathbf{x}) \frac{\mathrm{d}\mathbf{x}(t)}{\mathrm{d}t} + \mathbf{B}(\mathbf{x})\,\mathbf{x}(t) = \mathbf{c}(t),$$
$$\mathbf{x}(0) = \mathbf{x}^{(0)} \tag{3.10}$$

Before continuing let us make an assumption on the solution of these differential equations:

Assumption 1. *The solution of the ODEs/DAEs (3.10) is at least continuous, i.e.* $\mathbf{x} \in C^0(\Upsilon)$.

If this assumption is not fulfilled, the employed basis functions in the Galerkin approach are too smooth to properly represent the solution components. For two time scales the MPDEs according to Section 3.1 read

$$\mathbf{A}(\widehat{\mathbf{x}}) \left(\frac{\partial \widehat{\mathbf{x}}(t_1, t_2)}{\partial t_1} + \frac{\partial \widehat{\mathbf{x}}(t_1, t_2)}{\partial t_2} \right) + \mathbf{B}(\widehat{\mathbf{x}})\,\widehat{\mathbf{x}}(t_1, t_2) = \widehat{\mathbf{c}}(t_1, t_2). \tag{3.11}$$

As boundary conditions we use

$$\widehat{\mathbf{x}}(t_1, t_2) = \widehat{\mathbf{x}}(t_1, t_2 + T_\mathrm{s}), \tag{3.12}$$
$$\widehat{\mathbf{x}}(0, t_2) = \widehat{\mathbf{x}}^{(0)}(t_2), \tag{3.13}$$

leading to an IBVP.

The representation of the ripples in the solution is accomplished by using $N_\mathrm{p} + 1$ basis functions. These are denoted by $w_k(\tau, D), \forall k = 0, \ldots, N_\mathrm{p}$ where τ is called relative time and D is a parameter associated to
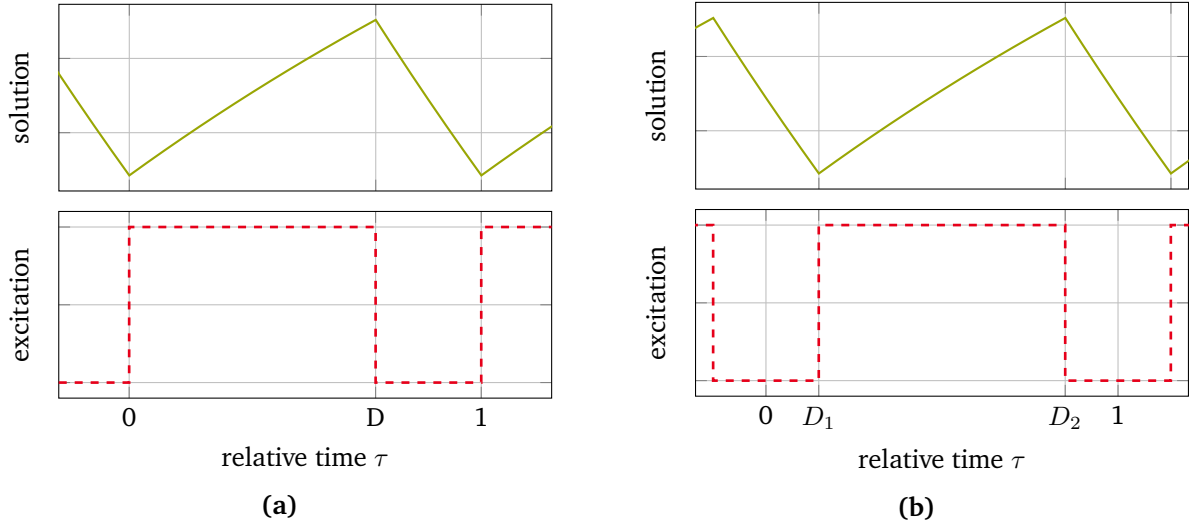
Figure 3.4: (a) Exemplary current ripple when using sawtooth carrier. There are points of C^0 continuity in the solution at $t^{(i)}$ where $\tau(t^{(i)}) = 0$ and $\tau(t^{(i)}) = D$. (b) Exemplary current ripple when using triangle carrier. In contrast to (a), the points of C^0 continuity in the solution are at $t^{(i)}$ where $\tau(t^{(i)}) = D_1$ and $\tau(t^{(i)}) = D_2$ and thus both are inside the switching interval.

the position of the point of C^0 continuity. The basis functions are periodic on the switching interval and only defined in the interval $[0, 1)$. The mapping to the entire computation domain is accomplished by defining the relative time τ as [41]

$$\tau(t) := \frac{t}{T_\mathrm{s}} \bmod 1, \tag{3.14}$$

where mod is the modulo operator and T_s is the switching period. This mapping enforces the periodicity and has the desired side effect of producing points of C^0 continuity in the solution at $t^{(i)}$ where $\tau(t^{(i)}) = 0$. The first mention of time-domain basis functions specifically developed for the representation of the ripples in the power converter output can be found in [41]. Therein the basis functions are constructed for use with a sawtooth carrier, i.e. one point of C^0 continuity is always at the beginning of the switching interval, and the other one is varying its position inside the switching interval and is at $t^{(i)}$ where $\tau(t^{(i)}) \in (0, 1)$. This position is supplied to the basis functions by means of the parameter D, which is chosen to be equivalent to the duty cycle of the exciting PWM signal. Fig. 3.4a shows an exemplary current ripple and corresponding PWM excitation to illustrate this.

If a triangle carrier is used to generate a PWM signal, the situation is different. There are still two points of C^0 continuity in the ripples, but both now vary their position inside the switching interval depending on the duty cycle. This is illustrated in Fig. 3.4b. To cope with this difference we use the same basis functions as before, but shift them in time and supply them with a modified duty cycle such that both points of C^0 continuity are at the proper position. According to the Galerkin approach, the MPDE solution is expanded into basis functions and coefficients, which yields

$$\widehat{x}_j^h(t_1, t_2) = \sum_{k=0}^{N_\mathrm{p}} y_{j,k}(t_1)\, w_k\Big(\tau\big(t_2 - d_1(t_1)T_\mathrm{s}\big), d_2(t_1) - d_1(t_1)\Big), \tag{3.15}$$

where $y_{j,k}(t_1)$ are the coefficients, w_k are the basis functions depending on the relative time and the duty cycle and the superscript h denotes an approximation in time. Since the basis functions represent the fast

varying ripples, they depend on the fast time scale t_2. Additionally they depend through the functions $d_1(t_1)$ and $d_2(t_1)$ on the reference signal $d(t_1)$ introduced in Section 2.6. The variations in the reference signal are much slower than those of the ripples, therefore it depends on the slow time scale t_1. How the functions $d_1(t_1)$ and $d_2(t_1)$ are associated to the reference signal $d(t_1)$ to obtain the desired representation of the ripples for sawtooth and triangle carrier is discussed in the following subsection. The slowly varying envelope which cannot be represented by the basis functions is stored in the coefficients. As a result they depend on the slow time scale t_1. Summarizing the basis functions and coefficients into the vectors

$$
\mathbf{w} = \begin{bmatrix} w_0 \\ w_1 \\ \vdots \\ w_{N_{\mathrm{p}}} \end{bmatrix}, \quad \mathbf{y}_j = \begin{bmatrix} y_{j,0} \\ y_{j,1} \\ \vdots \\ y_{j,N_{\mathrm{p}}} \end{bmatrix}, \tag{3.16}
$$

the solution expansion can be written as vector product

$$
\widehat{x}_j^h(t_1, t_2) = \mathbf{w}^\top \Big(\tau\big(t_2 - d_1(t_1)T_{\mathrm{s}}\big), d_2(t_1) - d_1(t_1) \Big) \mathbf{y}_j(t_1). \tag{3.17}
$$

A Ritz-Galerkin approach is applied to the MPDEs (3.11) along the fast time scale t_2, i.e. the equations are multiplied with test functions w_l and integrated on the interval $[0, T_{\mathrm{s}}]$ which corresponds to one switching interval. This weakening approach yields

$$
\int_0^{T_{\mathrm{s}}} \mathbf{A}(\widehat{\mathbf{x}}^h) \frac{\partial \widehat{\mathbf{x}}^h}{\partial t_1} w_l \, \mathrm{d}t_2 + \int_0^{T_{\mathrm{s}}} \mathbf{A}(\widehat{\mathbf{x}}^h) \frac{\partial \widehat{\mathbf{x}}^h}{\partial t_2} w_l \, \mathrm{d}t_2 + \int_0^{T_{\mathrm{s}}} \mathbf{B}(\widehat{\mathbf{x}}^h) \widehat{\mathbf{x}}^h w_l \, \mathrm{d}t_2 = \int_0^{T_{\mathrm{s}}} \widehat{\mathbf{c}} \, w_l \, \mathrm{d}t_2, \quad \forall l = 0, \ldots, N_{\mathrm{p}}, \tag{3.18}
$$

where the time scale dependency of the solution, right-hand side and basis functions have been omitted for the sake of readability. Integrating the second term by parts leads to

$$
\int_0^{T_{\mathrm{s}}} \mathbf{A}(\widehat{\mathbf{x}}^h) \frac{\partial \widehat{\mathbf{x}}^h}{\partial t_2} w_l \, \mathrm{d}t_2 = - \int_0^{T_{\mathrm{s}}} \mathbf{A}(\widehat{\mathbf{x}}^h) \widehat{\mathbf{x}}^h \frac{\partial w_l}{\partial t_2} \, \mathrm{d}t_2 + \underbrace{\left(\mathbf{A}(\widehat{\mathbf{x}}^h) \widehat{\mathbf{x}}^h w_l \right) \Big|_{t_2=0}^{t_2=T_{\mathrm{s}}}}_{=0}. \tag{3.19}
$$

The boundary term vanishes since the basis functions are periodic on $[0, T_{\mathrm{s}}]$ with respect to t_2. Inserting back into the equations (3.18) gives

$$
\int_0^{T_{\mathrm{s}}} \mathbf{A}(\widehat{\mathbf{x}}^h) \frac{\partial \widehat{\mathbf{x}}^h}{\partial t_1} w_l \, \mathrm{d}t_2 - \int_0^{T_{\mathrm{s}}} \mathbf{A}(\widehat{\mathbf{x}}^h) \widehat{\mathbf{x}}^h \frac{\partial w_l}{\partial t_2} \, \mathrm{d}t_2 + \int_0^{T_{\mathrm{s}}} \mathbf{B}(\widehat{\mathbf{x}}^h) \widehat{\mathbf{x}}^h w_l \, \mathrm{d}t_2 = \int_0^{T_{\mathrm{s}}} \widehat{\mathbf{c}} \, w_l \, \mathrm{d}t_2, \quad \forall l = 0, \ldots, N_{\mathrm{p}}. \tag{3.20}
$$

Let us rewrite the integrals step by step by starting with inserting the solution expansion (3.15) into the remaining partial derivatives of $\widehat{\mathbf{x}}(t_1, t_2)$. This leads to

$$
\begin{aligned}
\frac{\partial \widehat{x}_j^h(t_1, t_2)}{\partial t_1} = &- \frac{\partial \mathbf{w}^\top \Big(\tau(t_2 - d_1 T_{\mathrm{s}}), d_2 - d_1 \Big)}{\partial \tau} \frac{\mathrm{d}\, d_1(t_1)}{\mathrm{d}t_1} \mathbf{y}_j \\
&+ \frac{\partial \mathbf{w}^\top \Big(\tau(t_2 - d_1 T_{\mathrm{s}}), d_2 - d_1 \Big)}{\partial (d_2 - d_1)} \left(\frac{\mathrm{d}\, d_2(t_1)}{\mathrm{d}t_1} - \frac{\mathrm{d}\, d_1(t_1)}{\mathrm{d}t_1} \right) \mathbf{y}_j + \mathbf{w}^\top \frac{\mathrm{d}\mathbf{y}_j(t_1)}{\mathrm{d}t_1}.
\end{aligned} \tag{3.21}
$$

In a next step we substitute t_2 by τ in the left-hand side of equations (3.20). To obtain the new limits of the integrals we take advantage of the periodicity of the basis functions. Utilizing $\frac{\partial \tau}{\partial t_2} = \frac{1}{T_\mathrm{s}}$, which holds almost everywhere, and inserting (3.21) into (3.20) finally gives

$$
-\frac{\mathrm{d}\,d_1(t_1)}{\mathrm{d}t_1}\int_0^1 \mathbf{A}(\widehat{\mathbf{x}}^h)
\begin{bmatrix}
\frac{\partial \mathbf{w}^\top(\tau, d_2 - d_1)}{\partial \tau}\mathbf{y}_1 \\
\vdots \\
\frac{\partial \mathbf{w}^\top(\tau, d_2 - d_1)}{\partial \tau}\mathbf{y}_{N_\mathrm{s}}
\end{bmatrix} T_\mathrm{s} w_l \,\mathrm{d}\tau
$$

$$
+\left(\frac{\mathrm{d}\,d_2(t_1)}{\mathrm{d}t_1} - \frac{\mathrm{d}\,d_1(t_1)}{\mathrm{d}t_1}\right)\int_0^1 \mathbf{A}(\widehat{\mathbf{x}}^h)
\begin{bmatrix}
\frac{\partial \mathbf{w}^\top(\tau, d_2 - d_1)}{\partial (d_2 - d_1)}\mathbf{y}_1 \\
\vdots \\
\frac{\partial \mathbf{w}^\top(\tau, d_2 - d_1)}{\partial (d_2 - d_1)}\mathbf{y}_{N_\mathrm{s}}
\end{bmatrix} T_\mathrm{s} w_l \,\mathrm{d}\tau
+ \int_0^1 \mathbf{A}(\widehat{\mathbf{x}}^h)
\begin{bmatrix}
\mathbf{w}^\top \frac{\mathrm{d}\mathbf{y}_1(t_1)}{\mathrm{d}t_1} \\
\vdots \\
\mathbf{w}^\top \frac{\mathrm{d}\mathbf{y}_{N_\mathrm{s}}(t_1)}{\mathrm{d}t_1}
\end{bmatrix} T_\mathrm{s} w_l \,\mathrm{d}\tau
$$

$$
-\int_0^1 \mathbf{A}(\widehat{\mathbf{x}}^h)
\begin{bmatrix}
\mathbf{w}^\top(\tau, d_2 - d_1)\,\mathbf{y}_1 \\
\vdots \\
\mathbf{w}^\top(\tau, d_2 - d_1)\,\mathbf{y}_{N_\mathrm{s}}
\end{bmatrix}\frac{\partial w_l}{\partial \tau}\underbrace{\frac{\partial \tau}{\partial t_2}}_{=\frac{1}{T_\mathrm{s}}} T_\mathrm{s}\,\mathrm{d}\tau
+ \int_0^1 \mathbf{B}(\widehat{\mathbf{x}}^h)
\begin{bmatrix}
\mathbf{w}^\top(\tau, d_2 - d_1)\,\mathbf{y}_1(t_1) \\
\vdots \\
\mathbf{w}^\top(\tau, d_2 - d_1)\,\mathbf{y}_{N_\mathrm{s}}(t_1)
\end{bmatrix} T_\mathrm{s} w_l \,\mathrm{d}\tau
$$

$$
= \int_0^{T_\mathrm{s}} \widehat{\mathbf{c}}(t_1, t_2)\, w_l \,\mathrm{d}t_2, \quad \forall l = 0, \dots, N_\mathrm{p}, \tag{3.22}
$$

where $\widehat{\mathbf{x}}^h = \widehat{\mathbf{x}}^h(t_1, T_\mathrm{s}\tau)$. To rewrite this equation system into a more readable form, let us for the sake of illustration only consider the third term of the left-hand side, i.e.

$$
\boldsymbol{\mathcal{Z}}_l = \int_0^1 \mathbf{A}(\widehat{\mathbf{x}}^h)
\begin{bmatrix}
\mathbf{w}^\top \frac{\mathrm{d}\mathbf{y}_1(t_1)}{\mathrm{d}t_1} \\
\vdots \\
\mathbf{w}^\top \frac{\mathrm{d}\mathbf{y}_{N_\mathrm{s}}(t_1)}{\mathrm{d}t_1}
\end{bmatrix} T_\mathrm{s} w_l \,\mathrm{d}\tau. \tag{3.23}
$$

Assembling all the $\boldsymbol{\mathcal{Z}}_l$ and ordering them leads to

$$
\boldsymbol{\mathcal{Z}} = T_\mathrm{s} \underbrace{
\begin{bmatrix}
\int_0^1 A_{1,1} w_0 w_0 \,\mathrm{d}\tau & \dots & \int_0^1 A_{1,1} w_0 w_{N_\mathrm{p}} \,\mathrm{d}\tau & \int_0^1 A_{1,2} w_0 w_0 \,\mathrm{d}\tau & \dots \\
\vdots & \ddots & \vdots & \vdots & \\
\int_0^1 A_{1,1} w_{N_\mathrm{p}} w_0 \,\mathrm{d}\tau & \dots & \int_0^1 A_{1,1} w_{N_\mathrm{p}} w_{N_\mathrm{p}} \,\mathrm{d}\tau & \int_0^1 A_{1,2} w_{N_\mathrm{p}} w_0 \,\mathrm{d}\tau & \dots \\
\int_0^1 A_{2,1} w_0 w_0 \,\mathrm{d}\tau & \dots & \int_0^1 A_{2,1} w_0 w_{N_\mathrm{p}} \,\mathrm{d}\tau & \int_0^1 A_{2,2} w_0 w_0 \,\mathrm{d}\tau & \dots \\
\vdots & & \vdots & \vdots & \ddots
\end{bmatrix}}_{\boldsymbol{\mathcal{A}}(\widehat{\mathbf{x}}^h, t_1)}
\frac{\mathrm{d}}{\mathrm{d}t_1}
\underbrace{
\begin{bmatrix}
y_{1,0}(t_1) \\
\vdots \\
y_{1,N_\mathrm{p}}(t_1) \\
y_{2,0}(t_1) \\
\vdots
\end{bmatrix}}_{\mathbf{y}(t_1)}, \tag{3.24}
$$

where $A_{i,j}$, $i, j \in \{1, \dots, N_\mathrm{s}\}$ is the i-th element in column j of the matrix $\mathbf{A}(\widehat{\mathbf{x}}^h)$. Each element of this matrix is multiplied by the product of the basis functions. By introducing the matrix

$$
\widetilde{\boldsymbol{\mathcal{J}}}(\tau, d_1, d_2) = T_\mathrm{s}\mathbf{w}(\tau, d_2 - d_1)\,\mathbf{w}^\top(\tau, d_2 - d_1), \tag{3.25}
$$

and using the Kronecker product denoted by $\otimes$, the matrix $\boldsymbol{\mathcal{A}}$ can be written as

$$
\boldsymbol{\mathcal{A}}(\widehat{\mathbf{x}}^h, t_1) = \int_0^1 \mathbf{A}(\widehat{\mathbf{x}}^h) \otimes \widetilde{\boldsymbol{\mathcal{J}}}(\tau, d_1(t_1), d_2(t_1)) \,\mathrm{d}\tau \tag{3.26}
$$

For the other terms present in (3.22), we define additionally the matrices $\widetilde{\mathcal{Q}}$ and $\widetilde{\mathcal{U}}$ as

$$\widetilde{\mathcal{Q}}(\tau, d_1, d_2) = -\frac{\partial \mathbf{w}(\tau, d_2 - d_1)}{\partial \tau} \mathbf{w}^\top(\tau, d_2 - d_1) \tag{3.27}$$

and

$$\widetilde{\mathcal{U}}(\tau, d_1, d_2) = T_{\mathrm{s}} \mathbf{w}(\tau, d_2 - d_1) \frac{\partial \mathbf{w}^\top(\tau, d_2 - d_1)}{\partial (d_2 - d_1)}. \tag{3.28}$$

With their help the equations (3.22) can finally be summarized into

$$\boldsymbol{\mathcal{A}}(\widehat{\mathbf{x}}^h, t_1) \frac{\mathrm{d}\mathbf{y}(t_1)}{\mathrm{d}t_1} + \boldsymbol{\mathcal{B}}(\widehat{\mathbf{x}}^h, t_1)\, \mathbf{y}(t_1) = \boldsymbol{\mathcal{C}}(t_1), \tag{3.29}$$

where $\mathbf{y}(t_1) = \left[y_{1,0}(t_1), \ldots, y_{1,N_\mathrm{p}}(t_1), y_{2,0}(t_1), \ldots\right]^\top$, $\boldsymbol{\mathcal{A}}$ as in (3.26) and

$$
\begin{aligned}
\boldsymbol{\mathcal{B}}(\widehat{\mathbf{x}}^h, t_1) = \int_0^1 &\left(T_{\mathrm{s}} \frac{\mathrm{d}\, d_1(t_1)}{\mathrm{d}t_1} \mathbf{A}(\widehat{\mathbf{x}}^h) \otimes \widetilde{\mathcal{Q}}^\top(\tau, d_1(t_1), d_2(t_1)) \right.\\
&+ \left(\frac{\mathrm{d}\, d_2(t_1)}{\mathrm{d}t_1} - \frac{\mathrm{d}\, d_1(t_1)}{\mathrm{d}t_1} \right) \mathbf{A}(\widehat{\mathbf{x}}^h) \otimes \widetilde{\mathcal{U}}(\tau, d_1(t_1), d_2(t_1))\\
&\left. + \mathbf{A}(\widehat{\mathbf{x}}^h) \otimes \widetilde{\mathcal{Q}}(\tau, d_1(t_1), d_2(t_1)) + \mathbf{B}(\widehat{\mathbf{x}}^h) \otimes \widetilde{\mathcal{J}}(\tau, d_1(t_1), d_2(t_1)) \right) \mathrm{d}\tau,
\end{aligned} \tag{3.30}
$$

$$\boldsymbol{\mathcal{C}}(t_1) = \int_0^{T_{\mathrm{s}}} \widehat{\mathbf{c}}(t_1, t_2) \otimes \mathbf{w}(\tau(t_2) - d_1(t_1), d_2(t_1) - d_1(t_1))\, \mathrm{d}t_2. \tag{3.31}$$

In the remainder of this work, the matrices $\mathbf{A}$ and $\mathbf{B}$ are often independent of the solution, i.e. the problem is linear. In this case the problem is written using the matrices

$$\boldsymbol{\mathcal{J}}(d_1, d_2) = \int_0^1 \widetilde{\mathcal{J}}(\tau, d_1, d_2)\, \mathrm{d}\tau, \tag{3.32}$$

$$\boldsymbol{\mathcal{Q}}(d_1, d_2) = \int_0^1 \widetilde{\mathcal{Q}}(\tau, d_1, d_2)\, \mathrm{d}\tau, \tag{3.33}$$

$$\boldsymbol{\mathcal{U}}(d_1, d_2) = \int_0^1 \widetilde{\mathcal{U}}(\tau, d_1, d_2)\, \mathrm{d}\tau, \tag{3.34}$$

such that

$$\boldsymbol{\mathcal{A}}(t_1) = \mathbf{A} \otimes \boldsymbol{\mathcal{J}}(d_1(t_1), d_2(t_1)), \tag{3.35}$$

$$
\begin{aligned}
\boldsymbol{\mathcal{B}}(t_1) = &-T_{\mathrm{s}} \frac{\mathrm{d}\, d_1(t_1)}{\mathrm{d}t_1} \mathbf{A} \otimes \boldsymbol{\mathcal{Q}}(d_1(t_1), d_2(t_1)) + \left(\frac{\mathrm{d}\, d_2(t_1)}{\mathrm{d}t_1} - \frac{\mathrm{d}\, d_1(t_1)}{\mathrm{d}t_1} \right) \mathbf{A} \otimes \boldsymbol{\mathcal{U}}(d_1(t_1), d_2(t_1))\\
&+ \mathbf{A} \otimes \boldsymbol{\mathcal{Q}}(d_1(t_1), d_2(t_1)) + \mathbf{B} \otimes \boldsymbol{\mathcal{J}}(d_1(t_1), d_2(t_1)),
\end{aligned} \tag{3.36}
$$

$$\boldsymbol{\mathcal{C}}(t_1) = \int_0^{T_{\mathrm{s}}} \widehat{\mathbf{c}}(t_1, t_2) \otimes \mathbf{w}(\tau(t_2) - d_1(t_1), d_2(t_1) - d_1(t_1))\, \mathrm{d}t_2. \tag{3.37}$$

Note that the matrix $\mathcal{Q}$ is skew symmetric, i.e. $\mathcal{Q}^\top = -\mathcal{Q}$, which was used in (3.36) to avoid using the transposed. The relation can be derived by applying integration by parts on (3.33) and using the fact that the basis functions are periodic.

3.2.1 Sawtooth and triangle carrier

It was already mentioned that in case of using a **sawtooth carrier** for the generation of the PWM, the points of C^0 continuity in the inductor current ripple, see Section 2.6, are located at the beginning of each switching interval, i.e at $t^{(i)}$ where $\tau(t^{(i)}) = 0$, and the other one inside the switching interval at $t^{(i)}$ where $\tau(t^{(i)}) \in (0, 1)$. The basis functions are constructed for that, a shift is not necessary, i.e. the function $d_1(t_1) = 0$. As a result, the function $d_2(t_1) = d(t_1)$ and thus is identical to the reference signal.

If a **triangle carrier** is used, both switching instants vary their position in the switching interval, i.e. they are at $t^{(i)}$ where $\tau(t^{(i)}) \in (0, 1)$. To calculate d_1 and d_2 as functions of the reference signal $d(t)$, consider the time instants at which the equation

$$s(t) = d(t) \tag{3.38}$$

is satisfied. These are the time instants where the triangle carrier denoted by $s(t)$ intersects the reference signal $d(t)$. For illustration we only consider the first switching cycle. The switching instants are given by $D_1 T_\mathrm{s}$ and $D_2 T_\mathrm{s}$, see Fig. 3.4b. The triangle carrier $s(t)$ in the first switching cycle is given by

$$s(t) = \begin{cases} 2f_\mathrm{s}t & \forall t \in [0, 0.5T_\mathrm{s}) \\ 2(1 - f_\mathrm{s}t) & \forall t \in [0.5T_\mathrm{s}, T_\mathrm{s}] \end{cases}, \tag{3.39}$$

where $f_\mathrm{s} = 1/T_\mathrm{s}$ is the switching frequency. Inserting the switching instants $D_1 T_\mathrm{s}$ and $D_2 T_\mathrm{s}$ into (3.38) and solving the resulting equations for D_1 and D_2 gives

$$D_1 = 0.5d(D_1 T_\mathrm{s}), \tag{3.40}$$
$$D_2 = 1 - 0.5d(D_2 T_\mathrm{s}). \tag{3.41}$$

The functions $d_1(t_1)$ and $d_2(t_1)$ are chosen according to this condition as

$$d_1(t_1) = 0.5d(t_1), \tag{3.42}$$
$$d_2(t_1) = 1 - 0.5d(t_1). \tag{3.43}$$

To verify that this choice actually leads to the desired behavior of the basis functions, the switching instants $D_1 T_\mathrm{s}$ and $D_2 T_\mathrm{s}$ are inserted into the basis functions from (3.15). As we are interested in the behavior of the reconstructed solution, the time scales t_1 and t_2 are equated, i.e. $t = t_1 = t_2$. For $t = D_1 T_\mathrm{s}$ this yields

$$w_k\Big(\tau\big(D_1 T_\mathrm{s} - d_1(D_1 T_\mathrm{s})T_\mathrm{s}\big), d_2(D_1 T_\mathrm{s}) - d_1(D_1 T_\mathrm{s})\Big) \tag{3.44}$$

$$\overset{(3.42)}{=} w_k\Big(\tau\big(D_1 T_\mathrm{s} - 0.5d(D_1 T_\mathrm{s})T_\mathrm{s}\big), d_2(D_1 T_\mathrm{s}) - d_1(D_1 T_\mathrm{s})\Big) \tag{3.45}$$

$$\overset{(3.40)}{=} w_k\Big(\tau\big(\underbrace{D_1 T_\mathrm{s} - D_1 T_\mathrm{s}}_{0}\big), d_2(D_1 T_\mathrm{s}) - d_1(D_1 T_\mathrm{s})\Big), \tag{3.46}$$

and for $t = D_2 T_\mathrm{s}$ it leads to

$$w_k \Big(\tau \big(D_2 T_\mathrm{s} - d_1(D_2 T_\mathrm{s}) T_\mathrm{s} \big), d_2(D_2 T_\mathrm{s}) - d_1(D_2 T_\mathrm{s}) \Big) \tag{3.47}$$

$$\overset{(3.43)}{=} w_k \Big(\tau \big(D_2 T_\mathrm{s} - d_1(D_2 T_\mathrm{s}) T_\mathrm{s} \big), 1 - 0.5 d(D_2 T_\mathrm{s}) - d_1(D_2 T_\mathrm{s}) \Big) \tag{3.48}$$

$$\overset{(3.41)}{=} w_k \Big(\tau \big(D_2 T_\mathrm{s} - d_1(D_2 T_\mathrm{s}) T_\mathrm{s} \big), D_2 - d_1(D_2 T_\mathrm{s}) \Big) \tag{3.49}$$

$$= w_k \Big(D_2 - d_1(D_2 T_\mathrm{s}), D_2 - d_1(D_2 T_\mathrm{s}) \Big), \tag{3.50}$$

which is exactly what we desire: The points of C^0 continuity of the basis functions lie at both desired time instants because the basis functions are properly shifted and the duty cycle is properly set. Note that (3.42) and (3.43) are valid for all switching cycles, i.e. in the entire simulation interval.

3.2.2 Evaluation of nonlinearities

In the general case in which the matrices $\mathbf{A}$ and $\mathbf{B}$ depend on the solution, i.e. the problem is nonlinear, the integrals in (3.26) and (3.30) need to be re-evaluated for each $\mathbf{y}$ and t_1. In a numerical setting, this can be accomplished using a quadrature rule, e.g. Gaussian quadrature [44]. The integrals are approximated as a sum of weights and function values. For instance for the mass matrix (3.26) this yields

$$\boldsymbol{\mathcal{A}}(\widehat{\mathbf{x}}^h, t_1) = \int_0^1 \mathbf{A}(\widehat{\mathbf{x}}^h) \otimes \widetilde{\boldsymbol{\mathcal{J}}}(\tau, d_1(t_1), d_2(t_1)) \, \mathrm{d}\tau \tag{3.51}$$

$$\approx \sum_{i=0}^{N_\mathrm{gk}-1} \alpha_i^\mathrm{gk} \mathbf{A}\left(\widehat{\mathbf{x}}^h \left(t_1, T_\mathrm{s} \tau^{(i)} \right) \right) \otimes \widetilde{\boldsymbol{\mathcal{J}}}(\tau^{(i)}, d_1(t_1), d_2(t_1)), \tag{3.52}$$

where N_gk is the number of quadrature points, α_i^gk are the weights and $\tau^{(i)} \in [0, 1)$ are the actual quadrature points. Since the solution $\widehat{\mathbf{x}}^h$ contains a point of C^0 continuity along τ, the quadrature points and weights have to be chosen accordingly for instance by splitting the integral in (3.51) into two parts at the point of C^0 continuity. Each part is approximated separately by Gaussian quadrature and the sum of both is the resulting approximation to the entire integral. For the system matrix (3.30) the evaluation is analog. Note that this evaluation can be computationally expensive for three reasons:

1. the matrices $\mathbf{A}(\widehat{\mathbf{x}}^h)$, $\mathbf{B}(\widehat{\mathbf{x}}^h)$ have to be evaluated N_gk times for the different $\tau^{(i)}$;

2. the basis functions have to be evaluated for the different $\tau^{(i)}$. This can be cheap depending on the type of basis function but might also require a rebuild of the entire basis;

3. the Kronecker product has to be evaluated.

A simplification of the evaluation of nonlinearities can be achieved by using the fact, that the ripples are often small in amplitude compared to the envelope. This is especially true if the switching frequency is high. Therefore it is reasonable to assume that the nonlinearities will mainly be influenced by the amplitude of the envelope and the influence of the ripples is neglectable. One possible simplification thus is to approximate the nonlinearity by only using the envelope to evaluate. This small signal approach has been proposed in [78, 81] and is described in the following. Let

$$\mathbf{x}_\mathrm{env} = f_\mathrm{env}(\mathbf{y}) \tag{3.53}$$

be the envelope which is extracted from the vector of coefficients by the function $f_{\mathrm{env}} : \mathbb{R}^{N_{\mathrm{s}}(N_{\mathrm{P}}+1)} \to \mathbb{R}^{N_{\mathrm{s}}}$.

The mass matrix (3.26) using the envelope instead of the full solution simplifies to

$$\boldsymbol{\mathcal{A}}(\mathbf{y}, t_1) = \int_0^1 \mathbf{A}(f_{\mathrm{env}}(\mathbf{y})) \otimes \widetilde{\boldsymbol{\mathcal{J}}}(\tau, d_1(t_1), d_2(t_1)) \, \mathrm{d}\tau \tag{3.54}$$

$$\overset{(3.53)}{=} \int_0^1 \mathbf{A}(\mathbf{x}_{\mathrm{env}}) \otimes \widetilde{\boldsymbol{\mathcal{J}}}(\tau, d_1(t_1), d_2(t_1)) \, \mathrm{d}\tau \tag{3.55}$$

$$= \mathbf{A}(\mathbf{x}_{\mathrm{env}}) \otimes \int_0^1 \widetilde{\boldsymbol{\mathcal{J}}}(\tau, d_1(t_1), d_2(t_1)) \, \mathrm{d}\tau \tag{3.56}$$

$$\overset{(3.32)}{=} \mathbf{A}(\mathbf{x}_{\mathrm{env}}) \otimes \boldsymbol{\mathcal{J}}(d_1(t_1), d_2(t_1)) \tag{3.57}$$

Compared with (3.52), this is considerably more efficient from a computational point of view since only one evaluation of $\mathbf{A}$ is necessary instead of N_{gk} evaluations in case of Gauss quadrature.

3.3 Basis functions

For the solution expansion (3.15) there are many possible choices of basis functions. Which choice is optimal depends on the application. Aspects which have to be considered are for instance properties of the solution like symmetries or smoothness, but also computational aspects like the structure of the arising matrices in the equation systems or the computational cost to calculate them. In the following, three types of basis functions are presented, which are all suitable for use with the MPDE approach. The basis functions are:

1. the PWM basis functions originally proposed in [41];

2. the improved PWM eigenfunctions which are obtained from the PWM basis functions through a basis transformation [79];

3. the B-spline basis functions, see e.g. [82, 84].

3.3.1 PWM basis functions

The PWM basis functions were originally proposed in [41]. They are a spectral basis [15], i.e. the basis functions are global polynomials which support the entire interval $[0, 1]$. The zero-th basis function is given by

$$w_{\mathrm{pwm},0}(\tau, D) = 1, \quad \forall \tau \in [0, 1], \tag{3.58}$$

where $D \in (0, 1)$ is the duty cycle. The basis functions of higher order are built by integrating and orthonormalizing starting from the linear function

$$w_{\mathrm{pwm},1}(\tau, D) = \begin{cases} \sqrt{3} \, \frac{2\tau - D}{D} & \text{if } 0 \leq \tau < D \\ \sqrt{3} \, \frac{1 + D - 2\tau}{1 - D} & \text{if } D \leq \tau \leq 1 \end{cases}, \tag{3.59}$$
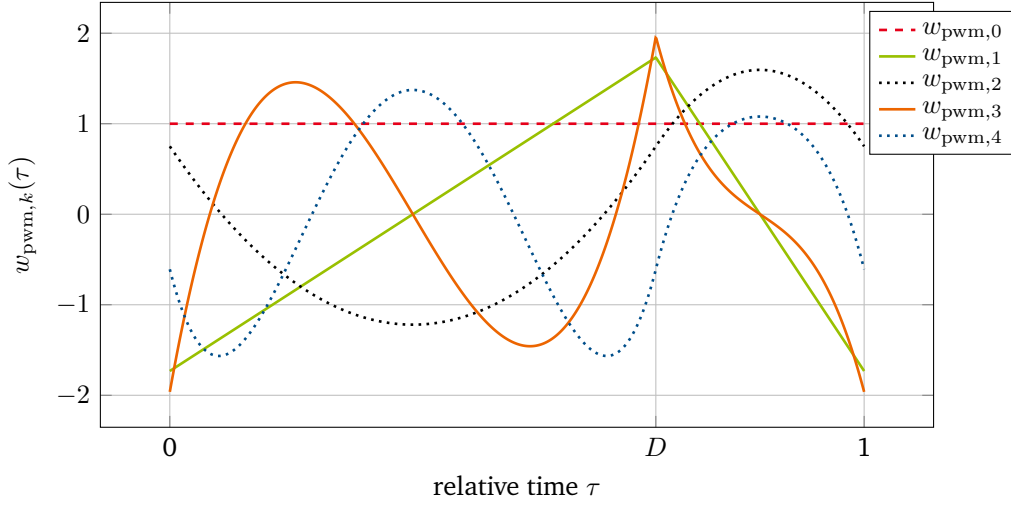
Figure 3.5: PWM basis functions $w_{\mathrm{pwm},k}(\tau, D)$ for $N_{\mathrm{p}} = 4$, i.e. $k \in \{0, 1, 2, 3, 4\}$. Figure adapted from [79].

which is essentially a scaled and translated hat function. The integration of the basis functions yields

$$w_{\mathrm{int},k}(\tau, D) = \int_{D}^{\tau} w_{k-1}(\tau', D) \, \mathrm{d}\tau' \,. \tag{3.60}$$

The basis functions are successively orthonormalized, first by orthogonalizing, i.e.

$$w_{\mathrm{orth},k}(\tau, D) = w_{\mathrm{int},k}(\tau, D) - \sum_{l=0}^{k-1} w_{\mathrm{pwm},l}(\tau, D) \int_{0}^{1} w_{\mathrm{pwm},l}(\tau, D) \, w_{\mathrm{int},k}(\tau, D) \, \mathrm{d}\tau \,, \quad \forall \, k \geq 2, \tag{3.61}$$

and normalizing

$$w_{\mathrm{pwm},k}(\tau, D) = \frac{w_{\mathrm{orth},k}(\tau, D)}{\sqrt{\int_{0}^{1} w_{\mathrm{orth},k}(\tau, D) \, w_{\mathrm{orth},k}(\tau, D) \, \mathrm{d}\tau}} \,. \tag{3.62}$$

This corresponds to a Gram-Schmidt orthonormalization procedure [115]. The resulting PWM basis functions are depicted in Fig. 3.5. Their periodicity is ensured by the orthogonalization process, specifically the orthogonalization against the constant basis function.

The PWM basis functions can also be calculated analytically. This is advantageous because the coefficients of the polynomials can be calculated before using them so that only an evaluation of the polynomial is necessary instead of recalculating the basis functions according to the described orthonormalization process.

Note that with increasing number of PWM basis functions N_{p}, the degree of the polynomial functions rises. Numerically this may lead to instabilities, if the number of basis functions is too high. Practical experiments have shown that N_{p} should be less or equal 12 to avoid these problems. The observed instabilities are machine and implementation dependent and might vary.

For an efficient solution of (3.29) the structure of the matrices $\mathcal{J}$ and $\mathcal{Q}$ is of interest. In case of the PWM basis functions, the matrix $\mathcal{J}$ is T_{s} times the identity matrix. This comes from the orthonormality of
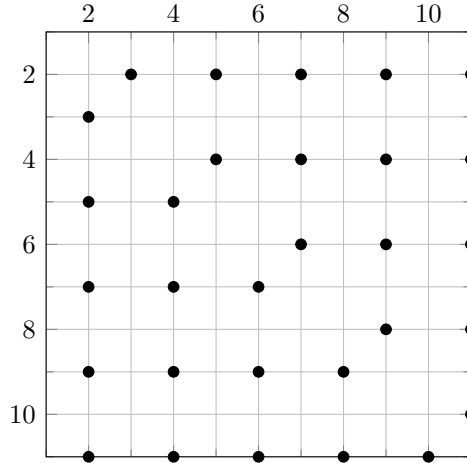
Figure 3.6: Structure of $\mathcal{Q}$. Non-zero entries are marked with a black dot.

the basis functions, i.e.

$$\int\limits_0^1 w_{\mathrm{pwm},k}(\tau,D)w_{\mathrm{pwm},l}(\tau,D)\,\mathrm{d}\tau = \left\{ \begin{array}{ll} 1 & \text{for } k = l \\ 0 & \text{otherwise} \end{array} \right. . \tag{3.63}$$

The matrix $\mathcal{Q}$ in contrast is a full matrix with around 75% of zero entries. The structure is depicted in Fig. 3.6. To avoid confusion in the following sections, the matrices $\mathcal{J}$ and $\mathcal{Q}$ will be marked with a subscript denoting the type of basis functions. For PWM basis functions we call them $\mathcal{J}_{\mathrm{pwm}}$ and $\mathcal{Q}_{\mathrm{pwm}}$. Note that the PWM basis functions are only used for applications with constant duty cycle in this work. Therefore the matrix $\mathcal{U}$ is not considered even though the PWM basis functions could be used with varying duty cycle. Their suitability for varying duty cycle applications with regard to the efficiency needs to be determined in future works.

The numerical properties of the PWM basis functions have first been studied in [41] numerically. Analytically for a duty cycle of $D = 0.5$ they have been analyzed in [80]. The following theorem establishes the symmetry conditions the PWM basis functions adhere to.

Theorem 2 ([80] ©2019 IEEE)**.** *The symmetry of the PWM basis functions defined by* (3.59)-(3.62) *with duty cycle $D = 0.5$ is given by*

$$-w_{\mathrm{pwm},k}(\tau) = w_{\mathrm{pwm},k}(\tau + 0.5), \quad \forall\, k = 1,\ldots,N_{\mathrm{p}}, \text{ and } \forall\, \tau \in (0,0.5).$$

Proof. see Appendix 6.2.1. □

The symmetry of the PWM basis functions gives us an insight into what problems they are suited for, i.e. which solutions they can actually represent. This is summarized in

Remark 1 ([80] ©2019 IEEE)**.** *The PWM basis functions are suited to approximate the solutions of linear ODEs with 2-level pulsed excitation. The solution of these ODEs are given by piecewise exponential functions which fulfill the symmetry condition stated in Theorem 2.*

Proof. see Appendix 6.2.2. □
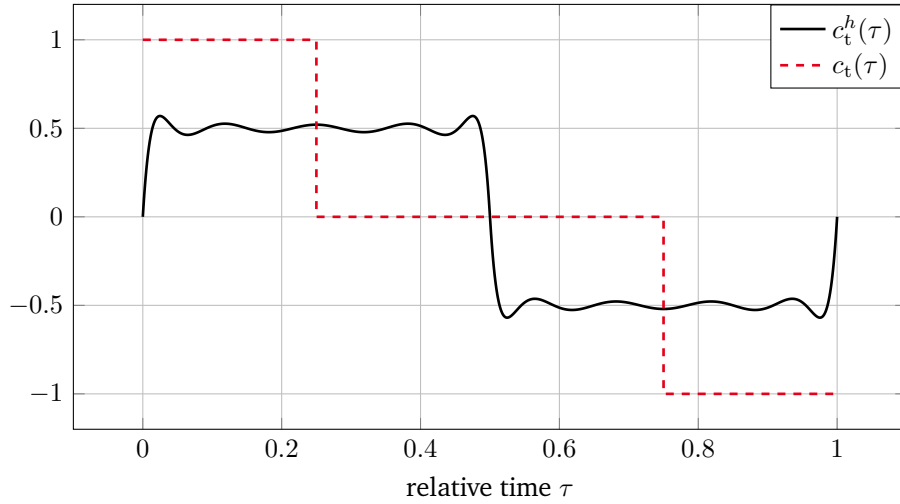
Figure 3.7: Projection $c_t^h(\tau)$ of the 3-level pulsed excitation $c_t(\tau)$ onto the space spanned by $w_{\mathrm{pwm},k}(\tau)$ with $N_\mathrm{p} = 10$. Figure adapted from [80] ©2019 IEEE.

Now that we know what the PWM basis functions are suited for it is also important to establish what their limitations are. This is proposed in the following remark along with an example for a case in which they are provably not suited.

Remark 2 ([80] ©2019 IEEE). *The PWM basis functions may not be suited to represent the solution of linear or nonlinear ODEs with arbitrary excitations. A counter example is an ODE with a 3-level pulsed excitation (see Fig. 3.7), for which it can be shown that the approximation fails.*

Proof. see Appendix 6.2.3.

The projection of the 3-level pulsed excitation $c_t(\tau)$ in Fig. 3.7 is accomplished by applying a Galerkin approach, see Section 2.3, to the equation $c_t^h(\tau) = c_t(\tau)$. The projected solution c_t^h is sought by expanding it into basis functions and coefficients. Solving the resulting equation system for the coefficients and reconstructing the solution leads to the $c_t^h(\tau)$ as displayed in the figure.

3.3.2 PWM eigenfunctions

When using the PWM basis functions, the entire system (3.29) has to be solved at once. A parallel time-domain solution is only feasible per time step, i.e. one may use iterative or (sparse) direct solvers for the linear equation systems that exploit some level of parallelism. However, a parallel solution on the entire simulation interval is not feasible since the degrees of freedom are coupled. To decouple the equations in case of linear differential equations, a basis transformation is applied. This has been proposed in [79] and is presented in this section. The resulting basis functions are called PWM eigenfunctions. They lead to diagonal matrices $\mathcal{J}$ and $\mathcal{Q}$ such that the degrees of freedom in (3.29) are decoupled. The $N_\mathrm{p} + 1$ equation systems with size N_s can thus be solved in parallel.

The transformed PWM basis functions are a linear combination of the PWM basis functions, i.e.

$$w_{\mathrm{eig},k}(\tau) = \sum_{l=0}^{N_{\mathrm{p}}} v_{k,l}\, w_{\mathrm{pwm},l}(\tau), \quad \forall\, k = 0, \ldots, N_{\mathrm{p}}, \tag{3.64}$$

where the coefficients $v_{k,l}$ are yet unknown. The functions $w_{\mathrm{eig},k}(\tau)$ are eigenfunctions of the derivative operator, i.e.

$$\frac{\mathrm{d}}{\mathrm{d}\tau} w_{\mathrm{eig},k}(\tau) = \lambda_k w_{\mathrm{eig},k}(\tau). \tag{3.65}$$

A Galerkin approach is applied to enforce (3.65) in a weak sense which, after integration by parts and using the periodicity of the basis functions, gives

$$-\int_0^1 w_{\mathrm{eig},k}(\tau) \frac{\mathrm{d}w_{\mathrm{pwm},m}(\tau)}{\mathrm{d}\tau}\, \mathrm{d}\tau = \lambda_k \int_0^1 w_{\mathrm{eig},k}(\tau)\, w_{\mathrm{pwm},m}(\tau)\, \mathrm{d}\tau, \quad \forall\, m = 0, \ldots, N_{\mathrm{p}}. \tag{3.66}$$

Inserting (3.64) leads to the (generalized) eigenvalue problem

$$T_{\mathrm{s}} \boldsymbol{\mathcal{Q}}_{\mathrm{pwm}} \mathbf{v}_k = \lambda_k \boldsymbol{\mathcal{J}}_{\mathrm{pwm}} \mathbf{v}_k, \tag{3.67}$$

where $\mathbf{v}_k = [v_{k,0}, v_{k,1}, \ldots, v_{k,N_{\mathrm{p}}}]^\top$. Thanks to the orthonormality of the PWM basis functions, the matrix $\boldsymbol{\mathcal{J}}_{\mathrm{pwm}}$ is T_{s} times the identity matrix. Therefore $\mathbf{v}_k$ and λ_k are the eigenvectors and eigenvalues of the matrix $\boldsymbol{\mathcal{Q}}_{\mathrm{pwm}}$, respectively. The matrix $\boldsymbol{\mathcal{Q}}_{\mathrm{pwm}}$ is real-valued and skew symmetric, see Section 3.2. As a result its eigenvectors $\mathbf{v}_k$ are orthonormal and the eigenvalues are purely imaginary, see Appendix 6.5.1. The PWM eigenfunctions consist of pairs of conjugate complex basis functions. They are depicted in Fig. 3.8.

Since the PWM eigenfunctions are complex-valued, the application of the Galerkin approach in (3.18) has to be modified. Instead of utilizing the L^2 scalar product for real-valued functions as defined in (2.47), the L^2 scalar product for complex-valued functions has to be applied. It reads

$$(u, w)_{L^2(\Omega)} = \int_\Omega u(\mathbf{r})\, \overline{w}(\mathbf{r})\, \mathrm{d}\Omega, \tag{3.68}$$

where the bar denotes the complex conjugate. The matrices $\boldsymbol{\mathcal{J}}_{\mathrm{eig}}$ and $\boldsymbol{\mathcal{Q}}_{\mathrm{eig}}$ when using the PWM eigenfunctions are derived in the following. The matrix $\boldsymbol{\mathcal{Q}}_{\mathrm{eig}}$ is given by

$$(\boldsymbol{\mathcal{Q}}_{\mathrm{eig}})_{m,k} = -\int_0^1 \frac{\mathrm{d}\overline{w}_{\mathrm{eig},m}}{\mathrm{d}\tau} w_{\mathrm{eig},k}\, \mathrm{d}\tau = -\int_0^1 \sum_l \overline{v}_{m,l} \frac{\mathrm{d}w_{\mathrm{pwm},l}}{\mathrm{d}\tau} w_{\mathrm{eig},k}\, \mathrm{d}\tau \tag{3.69}$$

$$= -\sum_l \overline{v}_{m,l} \int_0^1 \frac{\mathrm{d}w_{\mathrm{pwm},l}}{\mathrm{d}\tau} w_{\mathrm{eig},k}\, \mathrm{d}\tau \overset{(3.66)}{=} \sum_l \overline{v}_{m,l}\, \lambda_k \int_0^1 w_{\mathrm{pwm},l}\, w_{\mathrm{eig},k}\, \mathrm{d}\tau \tag{3.70}$$

$$= \sum_l \overline{v}_{m,l}\, \lambda_k \sum_j v_{k,j} \underbrace{\int_0^1 w_{\mathrm{pwm},l}\, w_{\mathrm{pwm},j}\, \mathrm{d}\tau}_{= \begin{cases} 1 & \text{for } l = j \\ 0 & \text{otherwise} \end{cases}} = \sum_l \overline{v}_{m,l}\, \lambda_k\, v_{k,l}. \tag{3.71}$$
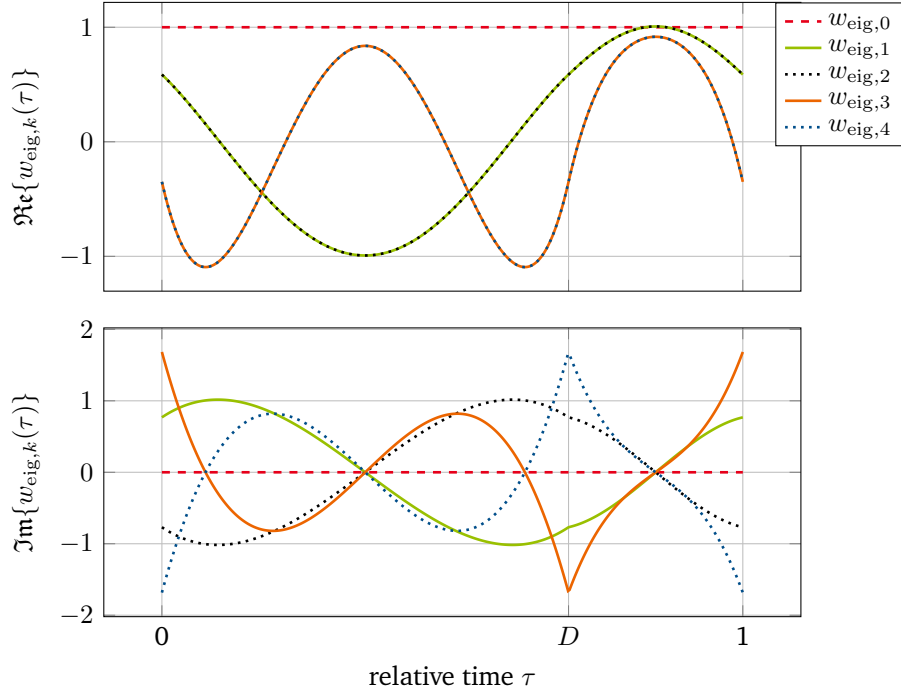
Figure 3.8: PWM eigenfunctions $w_{\mathrm{eig},k}(\tau)$ for $N_{\mathrm{p}} = 4$ and thus $k = \{0, 1, 2, 3, 4\}$. (top) real part. (bottom) imaginary part. Figures adapted from [79].

Introducing a diagonal matrix $\boldsymbol{\lambda}$ with the eigenvalues λ_k on its diagonal, and the matrix $\mathbf{V} = \left[\mathbf{v}_0, \mathbf{v}_1, \ldots, \mathbf{v}_{N_{\mathrm{p}}}\right]$, the expression can be written as

$$(\boldsymbol{\mathcal{Q}}_{\mathrm{eig}})_{m,k} = \sum_l \overline{v}_{m,l}\, \lambda_k\, v_{k,l} = \sum_l (\overline{\mathbf{V}})_{l,m}\,(\mathbf{V})_{l,k}\,(\boldsymbol{\lambda})_{k,k}, \tag{3.72}$$

which finally leads to

$$\boldsymbol{\mathcal{Q}}_{\mathrm{eig}} = \mathbf{V}^{\mathrm{H}}\,\mathbf{V}\,\boldsymbol{\lambda} = \boldsymbol{\lambda}, \tag{3.73}$$

where the superscript H denotes the complex conjugate transposed. Since the eigenvectors are orthonormal, the product of $\mathbf{V}^{\mathrm{H}}$ and $\mathbf{V}$ is the identity matrix such that only $\boldsymbol{\lambda}$ remains in the above expression. The matrix $\boldsymbol{\mathcal{J}}_{\mathrm{eig}}$ is given by

$$\boldsymbol{\mathcal{J}}_{\mathrm{eig}} = T_{\mathrm{s}} \int\limits_0^1 \overline{\mathbf{w}}_{\mathrm{eig}}\, \mathbf{w}_{\mathrm{eig}}^{\top}\, \mathrm{d}\tau = T_{\mathrm{s}} \int\limits_0^1 \overline{\mathbf{V}^{\top}\mathbf{w}_{\mathrm{pwm}}}\,(\mathbf{V}^{\top}\mathbf{w}_{\mathrm{pwm}})^{\top}\, \mathrm{d}\tau \tag{3.74}$$

$$= T_{\mathrm{s}} \int\limits_0^1 \mathbf{V}^{\mathrm{H}}\mathbf{w}_{\mathrm{pwm}}\, \mathbf{w}_{\mathrm{pwm}}^{\top}\mathbf{V}\, \mathrm{d}\tau = T_{\mathrm{s}}\, \mathbf{V}^{\mathrm{H}} \underbrace{\int\limits_0^1 \mathbf{w}_{\mathrm{pwm}}\, \mathbf{w}_{\mathrm{pwm}}^{\top}\, \mathrm{d}\tau}_{\text{identity matrix}}\, \mathbf{V} = T_{\mathrm{s}}\, \mathbf{V}^{\mathrm{H}}\mathbf{V} = T_{\mathrm{s}}\mathbf{I}, \tag{3.75}$$

$$\tag{3.76}$$

where $\mathbf{I}$ is the identity matrix. In analogy to "harmonic balance method", the resulting MPDE approach with PWM eigenfunctions is called "multirate PWM balance method".

3.3.3 B-spline basis functions

The next type of basis which is considered are B-splines. They provide local support, i.e. the time interval $[0, 1]$ is divided into elements and the basis functions are non-zero on one or more of these elements and zero everywhere else. B-splines allow to approximate the solution by piecewise high-order polynomials. The regularity across element boundaries can be controlled, which allows to capture the point of C^0 continuity in the current ripple. As it turns out they also lead to advantageous properties of the arising matrices in the MPDE approach with varying duty cycle. Those have been proposed in [82]. The remainder of this subsection follows the information of this paper. For additional background on B-splines, the interested reader is referred to [84].

3.3.3.1 Introduction to B-splines

B-splines are built recursively starting from zero-th order basis functions. The time interval is divided into elements by defining a knot vector $\Xi = \{\xi_0, \dots, \xi_m\}$ sorted in ascending order $\xi_i \leq \xi_{i+1}$, $i = 0, \dots, m-1$, which delimits the elements. The zero-th order ($p = 0$) basis functions are piecewise constant and are given by

$$P_{i,0}(\xi) = \begin{cases} 1 & \text{for } \xi_i \leq \xi < \xi_{i+1} \\ 0 & \text{otherwise} \end{cases} . \tag{3.77}$$

The basis functions of higher order are calculated using the Cox-DeBoor recurrence formula [84]

$$P_{i,p}(\xi) = \frac{\xi - \xi_i}{\xi_{i+p} - \xi_i} P_{i,p-1}(\xi) + \frac{\xi_{i+p+1} - \xi}{\xi_{i+p+1} - \xi_{i+1}} P_{i+1,p-1}(\xi). \tag{3.78}$$

The B-splines are determined by the knot vector Ξ and the degree p of the polynomials. In the following the knot vector is assumed to be open (also called nonperiodic or clamped). This means that the first and last knots appear $p + 1$ times. Consequently, the knot vector takes the form

$$\Xi = \{\underbrace{\xi_0, \dots, \xi_p}_{p+1}, \xi_{p+1}, \dots, \xi_{m-p-1}, \underbrace{\xi_{m-p}, \dots, \xi_m}_{p+1}\}, \tag{3.79}$$

with $\xi_0 = \dots = \xi_p$ and $\xi_{m-p} = \dots = \xi_m$. This ensures that the B-splines at the boundary are $P_{0,p}(\xi_0) = 1$ and $P_{m-p-1,p}(\xi_m) = 1$, where $m - p$ is the total number of basis functions. The remaining B-splines are zero at $\xi = \xi_0$ and $\xi = \xi_m$.

The regularity of the basis functions across the knots is determined by knot multiplicities. A regularity $\mathfrak{r}_j$ across the knot ξ_j, $j = p+1, \dots, m-p-1$ means that the reconstructed solution, i.e. a linear combination of all the basis functions, across this knot will be $C^{\mathfrak{r}_j}$ continuous. The knot multiplicity is denoted by $\mathfrak{s}_j$. A multiplicity of $\mathfrak{s}_j = 1$ means that the knot appears once in the knot vector and is not repeated. To obtain a $C^{\mathfrak{r}_j}$ continuity, the knot multiplicity of the corresponding knot is given by $\mathfrak{s}_j = p - \mathfrak{r}_j$. Therefore the maximum regularity across a knot without repetition is $\mathfrak{r}_{j,\max} = p - 1$. A C^0 continuity, for instance, is obtained by a multiplicity of $\mathfrak{s}_{j,\mathrm{co}} = p - 0 = p$.
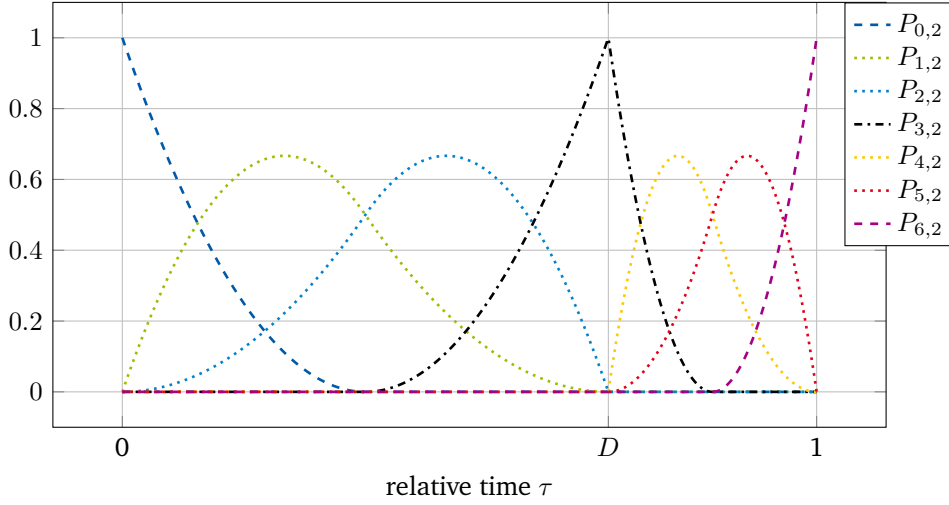
Figure 3.9: B-spline basis functions with degree $p = 2$ and refinement factor $K = 1$ ($\alpha_1 = 0.5$, $\beta_1 = 0.5$). Figure adapted from [82].

3.3.3.2 Choice of knot vector

The basis functions should be able to represent the point of C^0 continuity in the inductor current ripple by construction. As a result, the knot vector needs to take this into account by appropriate knot multiplicities. The simplest knot vector fulfilling this purpose is given by

$$\Xi_p = \{\underbrace{0, \ldots, 0}_{p+1}, \underbrace{D, \ldots, D}_{p}, \underbrace{1, \ldots, 1}_{p+1}\}, \tag{3.80}$$

where $D \in (0, 1)$ is the duty cycle which determines the position of the C^0 continuity. The basis functions shall be defined in terms of the relative time which has been accounted for by defining the knot vector from 0 to 1. If additional knot refinement similar to h-refinement in finite element method (FEM) is desired, the knot vector becomes

$$\Xi_{p,K} = \{\underbrace{0, \ldots, 0}_{p+1}, \alpha_1 D, \ldots, \alpha_K D, \underbrace{D, \ldots, D}_{p}, \beta_1(1 - D) + D, \ldots, \beta_K(1 - D) + D, \underbrace{1, \ldots, 1}_{p+1}\}, \tag{3.81}$$

where $0 < \alpha_1 < \ldots < \alpha_K < 1$, $0 < \beta_1 < \ldots < \beta_K < 1$ and K is the number of knots additionally inserted before and after the point of C^0 continuity. A refinement of $K = 0$ means that no refinement is desired, i.e. the knot vector is given by (3.80). The B-splines form a set of $2(p + K) + 1$ functions depending on the relative time τ and on the duty cycle D as given by

$$\{P_{0,p}(\tau, D), \ldots, P_{2p+2K,p}(\tau, D)\} \tag{3.82}$$

The basis functions are depicted in Fig. 3.9 for $K = 1$ ($\alpha_1 = 0.5$, $\beta_1 = 0.5$) and $p = 2$. The periodicity of the basis functions can be enforced in two ways:

- An additional constant basis function $P_{2p+2K+1,p}(\xi, D) = 1 \, \forall \xi \in [0, 1]$ is added to the set (3.82). The basis functions at the boundaries, i.e. $P_{0,p}(\xi, D)$ and $P_{2p+2K,p}(\xi, D)$ are removed from the set. This leads to

$$\{1, P_{1,p}(\tau, D), \ldots, P_{2p+2K-1,p}(\tau, D)\}. \tag{3.83}$$

- The equation system after the Galerkin approach (3.29) is modified as such that it ensures periodic boundary conditions. The coefficients associated with the basis functions $P_{0,p}(\xi, D)$ and $P_{2p+2K,p}(\xi, D)$ are equal. This process is detailed in Appendix 6.6.

Using the B-spline basis functions (3.82) the resulting matrices (3.32)-(3.34) are denoted by $\mathcal{J}_{\mathrm{bspl}}$, $\mathcal{Q}_{\mathrm{bspl}}$ and $\mathcal{U}_{\mathrm{bspl}}$. They are sparsely populated and banded, though the banded structure is slightly impaired in case of using the additional constant basis function to ensure the periodicity as described above. The matrices have properties which are advantageous in simulations with varying duty cycle. It can be shown that the entries of these matrices depend linearly on the duty cycle or are even independent of it. This enables a cheap calculation on a computer. Even though for a low order basis like hat functions ($p = 1$) this is rather obvious, it is more involved in the case of higher order B-splines due to their non-local support. Hence this property is summarized in the following theorem.

Theorem 3 ([82]). *Using the B-spline basis functions* (3.82), *only the matrix* $\mathcal{J}_{\mathrm{bspl}}$ *from* (3.32) *depends linearly on the duty cycle, i.e.* $\mathcal{J}_{\mathrm{bspl}}(D) = \frac{\mathcal{J}_{\mathrm{bspl}}(D_0) - \mathcal{J}_{\mathrm{bspl}}(D_1)}{D_0 - D_1}(D - D_0) + \mathcal{J}_{\mathrm{bspl}}(D_0)$, *with* $D_0, D_1 \in (0, 1)$ *and* $D_0 \neq D_1$, *and the matrices* $\mathcal{Q}_{\mathrm{bspl}}, \mathcal{U}_{\mathrm{bspl}}$ *from* (3.33), (3.34), *respectively, are independent of the duty cycle.*

Proof. see Appendix 6.3.

In the following, when knot refinement is used ($K \geq 1$), we employ homogeneous refinement, i.e.

$$\alpha_l = \beta_l = \frac{l}{1 + K} \quad \forall l = 1, \ldots, K. \tag{3.84}$$

3.4 Time discretization

After the semi-discretization using the Galerkin approach, the remaining ODEs/DAEs are solved using conventional time integration algorithms as for example implicit Runge-Kutta (IRK) methods and backward differentiation formulas (BDFs) as described in Subsection 2.5.1. To obtain an efficient approach three questions need to be answered:

1. How do we choose the right-hand side of the MPDEs, i.e. $\widehat{\mathbf{c}}(t_1, t_2)$?

2. What are reasonable initial values to the ODEs/DAEs (3.29)?

3. What stability properties does the time integration algorithm need to provide?

These questions are answered in the following subsections, concluded by a discussion on the complexity of the MPDE approach.

3.4.1 Choice of the right-hand side and efficiency of the approach

Theorem 1 states that the solution $\mathbf{x}(t)$ of the original ODEs/DAEs (3.1) can be extracted from the solution $\widehat{\mathbf{x}}(t_1, t_2)$ of the corresponding MPDEs (3.4). This is accomplished by $\mathbf{x}(t) = \widehat{\mathbf{x}}(t, t)$, as long as the right-hand sides satisfy the relation $\mathbf{c}(t) = \widehat{\mathbf{c}}(t, t)$ (without loss of generality, we assumed $\widehat{\alpha}_1 = 0$, $\widehat{\alpha}_2 = 0$). As a result, there are infinitely many possibilities to choose the right-hand side, which all fulfill the relation $\mathbf{c}(t) = \widehat{\mathbf{c}}(t, t)$.

Nevertheless only a few of the choices lead to an efficient approach. Consider for illustration the pulsed excitation

$$\mathbf{c}(t) = \mathbf{f}_{\text{pro}} \operatorname{sgn}\big(d(t) - s(t)\big), \tag{3.85}$$

where $\mathbf{f}_{\text{pro}} \in \mathbb{R}^{N_s}$ is a vector which assigns the scalar excitation to the proper component of the vectorial function $\mathbf{c}(t)$. The functions $d(t)$ and $s(t)$ are the reference signal and a carrier as described in Section 2.6. One of the obvious choices for the multivariate right-hand side would be

$$\widehat{\mathbf{c}}(t_1, t_2) = \mathbf{f}_{\text{pro}} \operatorname{sgn}\big(d(t_1) - s(t_1)\big). \tag{3.86}$$

Inserting this into the right-hand side after the Galerkin approach (3.31) leads to

$$\boldsymbol{\mathcal{C}}(t_1) = \int_0^{T_s} \widehat{\mathbf{c}}(t_1, t_2) \otimes \mathbf{w}\Big(\tau\big(t_2 - d_1(t_1)T_s\big), d_2(t_1) - d_1(t_1)\Big) \, \mathrm{d}t_2 \tag{3.87}$$

$$= \int_0^{T_s} \mathbf{f}_{\text{pro}} \operatorname{sgn}\big(d(t_1) - s(t_1)\big) \otimes \mathbf{w}\Big(\tau\big(t_2 - d_1(t_1)T_s\big), d_2(t_1) - d_1(t_1)\Big) \, \mathrm{d}t_2 \tag{3.88}$$

$$= \mathbf{f}_{\text{pro}} \operatorname{sgn}\big(d(t_1) - s(t_1)\big) \otimes \int_0^{T_s} \mathbf{w}\Big(\tau\big(t_2 - d_1(t_1)T_s\big), d_2(t_1) - d_1(t_1)\Big) \, \mathrm{d}t_2. \tag{3.89}$$

The dynamic of $\mathbf{c}(t)$ is completely transferred to the right-hand side $\boldsymbol{\mathcal{C}}(t_1)$ of the ODEs/DAEs (3.29). As a result the number of time steps to find the solution of (3.29) will be similar to the one for the original ODEs/DAEs (3.1). In addition the size of the equation systems after the Galerkin approach is enlarged such that the time to solution will be even higher than that of the original problem. This is therefore not a practical choice of the right-hand side.

Another possible choice is

$$\widehat{\mathbf{c}}(t_1, t_2) = \mathbf{f}_{\text{pro}} \operatorname{sgn}\big(d(t_2) - s(t_2)\big). \tag{3.90}$$

In this case the entire dynamic is captured by the Galerkin approach, which leads to

$$\boldsymbol{\mathcal{C}}(t_1) = \text{constant}. \tag{3.91}$$

However this choice conflicts with the fact that the reference signal $d(t)$ is usually not periodic on each switching interval. Furthermore it is a slowly varying quantity and thus should be associated with time scale t_1. This leads us to the reasonable choice for the right-hand side given by

$$\widehat{\mathbf{c}}(t_1, t_2) = \mathbf{f}_{\text{pro}} \operatorname{sgn}\big(d(t_1) - s(t_2)\big), \tag{3.92}$$

which ensures, on the one hand, that the fast varying changes induced by the pulses are captured by the Galerkin approach and the basis functions, and on the other hand, that the slow variations due to the duty cycle are still resolved by the time discretization algorithm. This will, consequently take much less time steps for the solution compared to the original problem and thus leads to an efficient method.

3.4.2 Choice of initial values

Just as there are infinitely many choices of right-hand sides for the MPDE approach which all lead to a solution, there are infinitely many possibilities to choose the initial values for the resulting ODEs/MPDEs (3.29). The

Dahlquist test equation

$$\frac{\mathrm{d}x(t)}{\mathrm{d}t} = -\lambda x(t) + c(t), \quad x(0) = 0, \tag{3.93}$$

with pulsed excitation (switching frequency $T_{\mathrm{s}} = 2000\,\mathrm{Hz}$, constant duty cycle $D = 0.7$)

$$c(t) = \begin{cases} 1000 & \text{for } \tau(t) \leq D \\ 0 & \text{otherwise} \end{cases} \tag{3.94}$$

and $\lambda = 800$ shall serve as example to derive an understanding of what "good" and "bad" initial values are. Applying the MPDE approach leads to the system of ODEs

$$\boldsymbol{\mathcal{J}}(0, D)\frac{\mathrm{d}\mathbf{y}(t_1)}{\mathrm{d}t_1} = -\lambda\boldsymbol{\mathcal{J}}(0, D)\,\mathbf{y}(t_1) - \boldsymbol{\mathcal{Q}}(0, D)\,\mathbf{y}(t_1) + \boldsymbol{\mathcal{C}}(t_1), \quad \mathbf{y}(0) = \mathbf{y}^{(0)}, \tag{3.95}$$

with $\boldsymbol{\mathcal{J}}$, $\boldsymbol{\mathcal{Q}}$ and $\boldsymbol{\mathcal{C}}$ as in (3.32), (3.33) and (3.31), respectively. For simplicity we write $\boldsymbol{\mathcal{J}}$, $\boldsymbol{\mathcal{Q}}$ and $\boldsymbol{\mathcal{C}}$ and omit the arguments in the remainder of this subsection.

The (numerical) solution of the Dahlquist equation (3.93) is depicted in Fig. 3.10a. The time integration algorithm, namely `ode5r` (Octave, `odepkg` [116]), is instructed to provide very good accuracy (`abstol` = 10^{-12}, `reltol` = 10^{-10}) such that the reference solution (conventional time discretization) $x_{\mathrm{ref}}(t)$ can be expected to be reasonably accurate. The same settings are used in the following for the MPDE approach. The initial conditions for the MPDE approach equation system (3.95), i.e, $\mathbf{y}(0) = \mathbf{y}^{(0)}$, must satisfy

$$x(0) = \widehat{x}^h(0, 0) = \sum_{k=0}^{N_{\mathrm{p}}} y_k(0)\,w_k\big(0, D\big) = \mathbf{w}^\top(0, D)\,\mathbf{y}^{(0)}. \tag{3.96}$$

The simplest possible choice is

$$\mathbf{y}^{(0)} = \mathbf{0}. \tag{3.97}$$

To setup (3.95), B-spline basis functions ($p = 2$, $K = 0$) are employed. Their periodicity is ensured by enforcing periodic boundary conditions in the system of equations (3.95) (see Appendix 6.6). The solution of (3.95) after reconstruction using (3.15) is shown in Fig. 3.10a. The absolute L^2 error between the MPDE solution and the reference solution is calculated in the middle of each switching interval as

$$\epsilon_{\mathrm{abs}}(t) = \left\|x_{\mathrm{ref}}(t) - \widehat{x}^h(t, t)\right\|_{L^2([t-T_{\mathrm{s}}/2, t+T_{\mathrm{s}}/2])}. \tag{3.98}$$

It is depicted in Fig. 3.10b. As one can see the MPDE solution is not correct in the beginning and converges towards the proper solution when approaching steady state. If a different set of initial values are provided, e.g.

$$\mathbf{y}^{(0)} = \big(\boldsymbol{\mathcal{Q}} + \lambda\boldsymbol{\mathcal{J}}\big)^{-1}\boldsymbol{\mathcal{C}}(0) - \alpha^{\mathrm{s}}, \tag{3.99}$$

where α^{s} is chosen such that the initial conditions $x(0) = \widehat{x}(0, 0)$ are satisfied, the situation is different. The result is depicted in Fig. 3.10a and Fig. 3.10b as well. They show that the solution accuracy is much better from the beginning and that the error is almost constant throughout the simulation interval. Let us have a glance at the coefficients $\mathbf{y}(t_1)$. They are pictured in Fig. 3.12 for $\mathbf{y}^{(0)} = \mathbf{0}$ as initial values. Oscillations are visible which diminish towards reaching steady state. If the other initial values (3.99) are utilized, see Fig. 3.13, there are no oscillations visible. The solution without oscillations can be calculated more efficiently than the one with oscillations since the time integration algorithm does not need to resolve the oscillations. How the expression (3.99) is found becomes clear later in this subsection.

Note that Theorem 1 holds independently of the initial values as long as $x(0) = \widehat{x}(0,0)$ is fulfilled. Therefore when increasing discretization accuracy either by using higher number of basis functions or by using finer time steps, we expect the accuracy of the solution to improve even with "wrong" initial values. This is demonstrated by improving the B-spline discretization accuracy. Using the setting $p = 2$, $K = 10$, the overall error becomes smaller but the initial values $\mathbf{y}^{(0)} = \mathbf{0}$ still lead to worse accuracy than the others. This is shown in Figs. 3.11a and 3.11b, which depict the solution and the error, respectively.

To understand where the observed phenomena come from, let us in a first step rewrite the equation system (3.95) arising from the MPDE approach by solving it for the derivative. This leads to

$$\frac{d\mathbf{y}(t_1)}{dt_1} = \underbrace{\left(-\lambda\mathbf{I} - \boldsymbol{\mathcal{J}}^{-1}\,\boldsymbol{\mathcal{Q}}\right)}_{\mathbf{Z}}\mathbf{y}(t_1) + \boldsymbol{\mathcal{J}}^{-1}\,\boldsymbol{\mathcal{C}}(t_1), \tag{3.100}$$

where $\mathbf{I}$ is the identity matrix. The matrix $\boldsymbol{\mathcal{Q}}$ is skew-symmetric by construction, see Section 3.2. The matrix $\boldsymbol{\mathcal{J}}$ is real symmetric positive definite (cf. "mass matrix" [93, p. 148]). Consequently the matrix $\boldsymbol{\mathcal{J}}^{-1}\,\boldsymbol{\mathcal{Q}}$ has eigenvalues which are purely imaginary or zero and the eigenvectors are linear independent, see Appendix 6.5.2. As a result the matrix $\mathbf{Z}$ has linear independent eigenvalues as well. The analytical solution for (3.100) is given by [32]

$$\mathbf{y}(t_1) = \eta_0\,e^{\lambda_{Z,0}t_1}\,\mathbf{v}_{Z,0} + \eta_1\,e^{\lambda_{Z,1}t_1}\,\mathbf{v}_{Z,1} + \ldots$$
$$+ \eta_{N_\mathrm{p}}\,e^{\lambda_{Z,N_\mathrm{p}}t_1}\,\mathbf{v}_{Z,N_\mathrm{p}} - \mathbf{Z}^{-1}\boldsymbol{\mathcal{J}}^{-1}\boldsymbol{\mathcal{C}}, \tag{3.101}$$

where $\eta_0, \ldots, \eta_{N_\mathrm{p}} \in \mathbb{R}$ are constants depending on the initial values, $\lambda_{Z,0}, \ldots, \lambda_{Z,N_\mathrm{p}} \in \mathbb{C}$ are the eigenvalues and $\mathbf{v}_{Z,0}, \ldots, \mathbf{v}_{Z,N_\mathrm{p}} \in \mathbb{C}^{N_\mathrm{P}\times 1}$ are the eigenvectors of $\mathbf{Z}$. The properties of the solution thus depend on the eigenvalues and eigenvectors of $\mathbf{Z}$. Since the matrices $\mathbf{I}$ and $\boldsymbol{\mathcal{J}}^{-1}\,\boldsymbol{\mathcal{Q}}$ are commutative, i.e.

$$\mathbf{I}\,\boldsymbol{\mathcal{J}}^{-1}\,\boldsymbol{\mathcal{Q}} = \boldsymbol{\mathcal{J}}^{-1}\,\boldsymbol{\mathcal{Q}}\,\mathbf{I}, \tag{3.102}$$

the eigenvalues of $\mathbf{Z}$ can be written as [110, p. 57]

$$\lambda_{Z,k} = -\lambda - \lambda_{\mathrm{IQ},k} \quad \forall k = \{0, \ldots, N_\mathrm{p}\}, \tag{3.103}$$

where λ is the parameter from the Dahlquist equation (3.93) and $\lambda_{\mathrm{IQ},k}$ are the eigenvalues of the matrix $\boldsymbol{\mathcal{J}}^{-1}\,\boldsymbol{\mathcal{Q}}$. The eigenvalues of $\mathbf{Z}$ are thus influenced by a part which stems from the original problem, i.e. the Dahlquist equation, and a part which stems from the semi-discretization with the Galerkin approach.

As already mentioned the matrix $\boldsymbol{\mathcal{J}}^{-1}\,\boldsymbol{\mathcal{Q}}$ has eigenvalues which are purely imaginary or zero. Additionally since it is a real matrix, the imaginary eigenvalues and eigenvectors come in pairs of complex conjugates [109, p. 338]. Note that for the PWM eigenfunctions from Subsection 3.3.2 the matrix $\boldsymbol{\mathcal{Q}}_{\mathrm{eig}}$ is skew-hermitian, and thus the aforementioned properties are not directly valid. However it is a diagonal matrix, whose eigenvalues are equal to its diagonal entries. Those are the eigenvalues of the matrix $\boldsymbol{\mathcal{Q}}_{\mathrm{pwm}}$ of the original PWM basis functions. As a result the following analysis is valid for the PWM eigenfunctions as well. Let $\{0, \ldots, 0, \lambda_{\mathrm{IQ},M}, \ldots, \lambda_{\mathrm{IQ},N_\mathrm{p}}\}$ be the eigenvalues and $\{\mathbf{v}_{\mathrm{IQ},0}, \mathbf{v}_{\mathrm{IQ},1}, \ldots, \mathbf{v}_{\mathrm{IQ},N_\mathrm{p}}\}$ be the corresponding eigenvectors of $\boldsymbol{\mathcal{J}}^{-1}\,\boldsymbol{\mathcal{Q}}$. The purely imaginary eigenvalues lead to oscillating components in the solution (3.101) which are unphysical in the sense that they do not come from the eigenvalues of the original Dahlquist equation (3.93). The $\eta_M, \ldots, \eta_{N_\mathrm{p}}$ in (3.101) may be chosen as such that the oscillating components due to the imaginary eigenvalues and their complex conjugate counterparts cancel each other out. The remaining terms

(a)

(b)
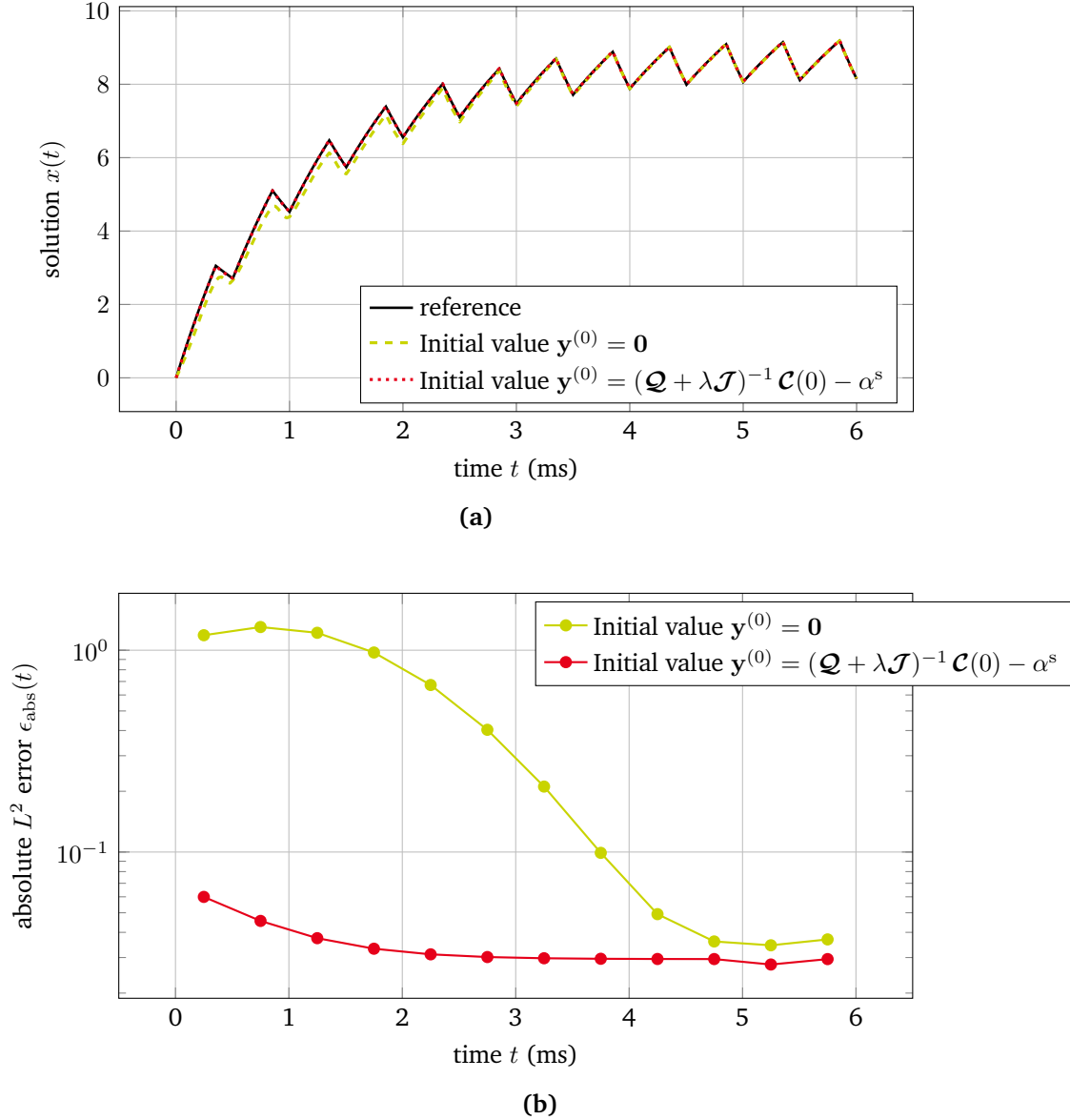
Figure 3.10: (a) Solution of the Dahlquist equation using the MPDE approach with B-splines ($p = 2$, $K = 0$) and two different initial values. Using $\mathbf{y}^{(0)} = \mathbf{0}$, solving the equation systems takes 781 time steps. Using $\mathbf{y}^{(0)} = (\mathbf{\mathcal{Q}} + \lambda \mathbf{\mathcal{J}})^{-1} \mathbf{\mathcal{C}}(0) - \alpha^{\mathrm{s}}$ the solution takes only 82 time steps. The calculation of the reference solution takes 170 time steps. (b) Absolute L^2 error calculated according to (3.98) in the middle of each switching interval. Dots mark the position of actual calculation, the lines are linear interpolations.

(a)

(b)
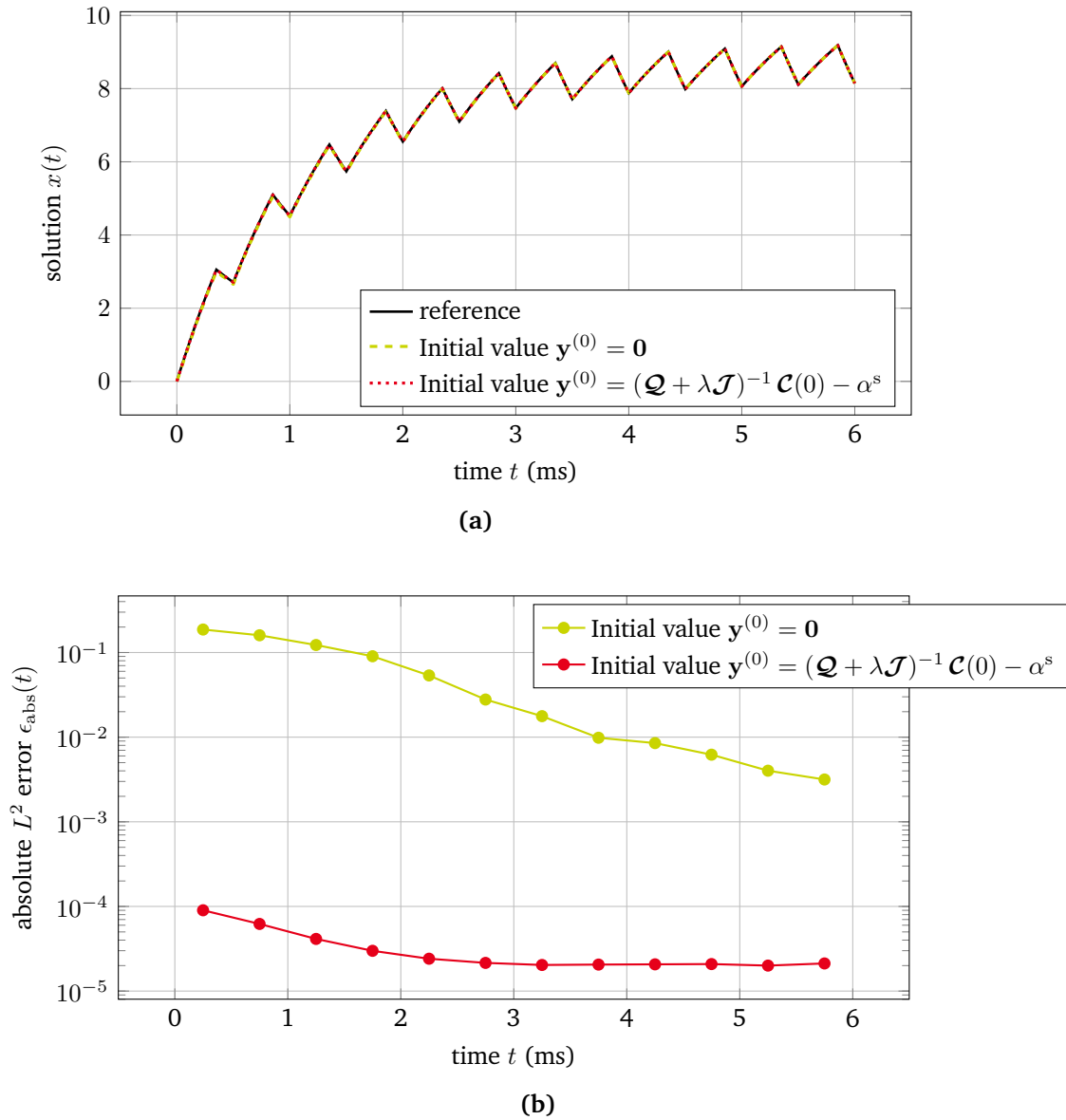
Figure 3.11: (a) Solution of the Dahlquist equation using the MPDE approach with B-splines ($p = 2$, $K = 10$) and two different initial values $\mathbf{y}^{(0)} = \mathbf{0}$ and $\mathbf{y}^{(0)} = (\boldsymbol{\mathcal{Q}} + \lambda\boldsymbol{\mathcal{J}})^{-1}\boldsymbol{\mathcal{C}}(0) - \alpha^{\mathrm{s}}$. (b) Absolute L^2 error calculated according to (3.98) in the middle of each switching interval. Dots mark the position of actual calculation, the lines are linear interpolations.
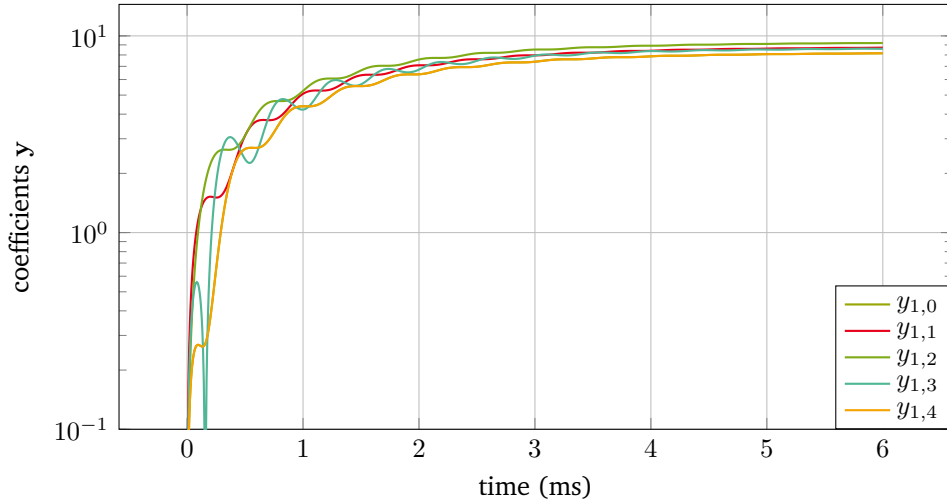
Figure 3.12: Coefficients $\mathbf{y}(t_1)$ for B-splines ($p = 2$, $K = 0$) when using $\mathbf{y}^{(0)} = \mathbf{0}$.

involving $\eta_0, \ldots, \eta_{M-1}$ correspond to the zero eigenvalue components and do not cause unphysical oscillations. They can thus be setup as such that the initial condition (3.96) is fulfilled. In practice, we setup the initial values as follows: Calculate

$$\mathbf{y}^{\star} = -\mathbf{Z}^{-1}\boldsymbol{\mathcal{J}}^{-1}\boldsymbol{\mathcal{C}}(0). \tag{3.104}$$

When the simulation is started with this choice of initial values, the differential equation system (3.100) is directly in steady state. This means that the $\eta_0, \ldots, \eta_{N_{\mathrm{p}}}$ from (3.101) are implicitly given as such that no oscillations occur. However this choice does not yet fulfill the initial conditions (3.96). Thus we modify $\mathbf{y}^{\star}$ as such that the initial conditions are satisfied. This is achieved by changing the components corresponding to the zero eigenvalues by means of $\eta_0, \ldots, \eta_{M-1}$. The initial values $\mathbf{y}$ are now given by

$$\mathbf{y}^{(0)} = \mathbf{y}(0) = \mathbf{y}^{\star} - \eta_0^{\star}\mathbf{v}_{Z,0} - \ldots - \eta_{M-1}^{\star}\mathbf{v}_{Z,M-1}. \tag{3.105}$$

In case of $M > 1$ (M depends on the basis functions and boundary conditions along the fast time scale t_2), there must be additional conditions to uniquely define $\eta_0^{\star}, \ldots, \eta_{M-1}^{\star}$. How these conditions look like in general is not clear and a topic for future research. The initial values (3.99) earlier used in the illustrative example are the special case of (3.105) when using B-splines as basis functions. The obtained knowledge is also applicable to systems of ODEs and might be applicable to DAEs.

In case of linear problems with varying duty cycle the initial values can be found similarly as in the case of constant duty cycle, however the mathematical analysis as discussed so far is not applicable any more for the entire simulation interval. In essence the duty cycle is frozen at its initial point to calculate the initial values. Oscillations might still arise during the simulation.

The choice of initial values in case of nonlinear problems is more complicated. The analysis applied in linear problems is not directly applicable. An algorithm for finding an approximation to reasonable initial values has been presented in [99]. It assumes that the solution of the original equation system can be split into an envelope, which can be represented by a linear function, and a rest. This knowledge is used to calculate the ripple. The coefficients $\mathbf{y}(0)$ can be found by projecting them into the solution space spanned by the basis functions using a Galerkin approach (small signal approach on top of the envelope). However this approach only offers an approximation which may lead to some dynamic in the slowly varying coefficients. It should be noted that for some nonlinear problems it is still possible to find the initial values in a more optimal way. In Chapter 4 reasonable choices are discussed for specific examples.
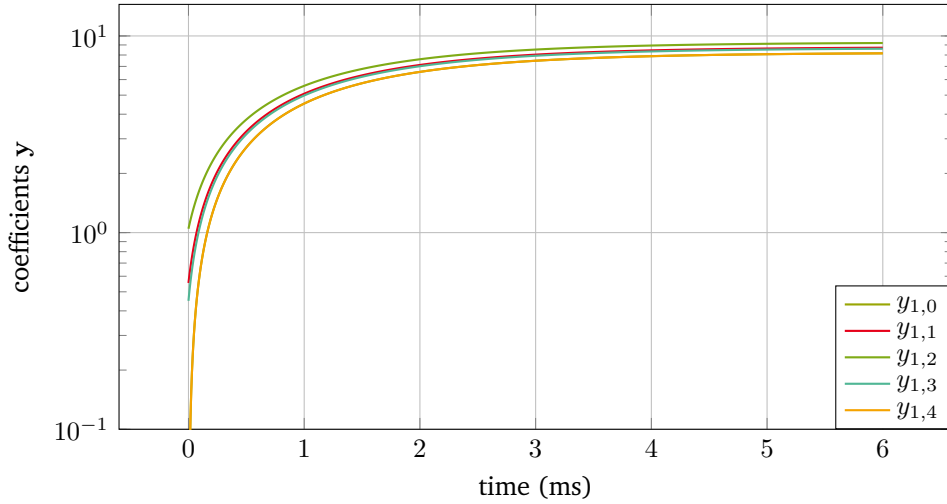
Figure 3.13: Coefficients $\mathbf{y}(t_1)$ for B-splines ($p = 2$, $K = 0$) when using $\mathbf{y}^{(0)} = (\mathbf{\mathcal{Q}} + \lambda \mathbf{\mathcal{J}})^{-1} \mathbf{\mathcal{C}}(0) - \alpha^{\mathrm{s}}$.

3.4.3 Stability of time integration

We found in the previous subsection that the eigenvalues of the original equation system (3.93) are transferred to the equation system after the semi-discretization (3.100) according to (3.103). The imaginary part of the eigenvalues is modified by the purely imaginary eigenvalues of the matrices resulting from the Galerkin approach. As a result, the stability requirement towards the time integration algorithm may be more strict. Consider, e.g. an equation system with only real eigenvalues. This would be solvable by any A(α)-stable solver with $\alpha > 0$, see Section 2.5. However the equation system after the semi-discretization (3.100) has complex eigenvalues with a non-zero imaginary part and as a result the solver needs to be A-stable.

3.4.4 Complexity and efficiency of the MPDE approach

As in many numerical methods, in the MPDE approach there is a trade-off between the efficiency, i.e. the time to solve the problem, and accuracy of the calculated solution. The approach offers two parameters for this purpose. The first parameter is the number of basis functions N_{p}. Increasing this parameter leads to better approximation of the basis functions, however the size of the equation systems is $N_{\mathrm{p}} + 1$ times larger than the original equations. This leads to higher computational effort. The second parameter is the desired accuracy which is provided to the time integration algorithm. Requiring higher accuracy leads to higher number of time steps and thus higher computational effort. Both parameters need to be balanced with each other. Setting a small number of basis functions but requiring high accuracy from the time integration algorithm is not useful since the overall accuracy of the solution is then limited by the small number of basis functions. The same holds the other way around.

It is difficult to theoretically predict the efficiency of the MPDE approach in a practical implementation since many aspects need to be considered, e.g. code efficiency and computational overhead on a computer. However the complexity can be estimated under simplified assumptions. The time integration algorithm usually needs to solve one or more (nonlinear) equation systems per step. This depends on the adaptivity of the algorithm and the nonlinearity of the problem. We assume for simplicity that in each time step the

same number of equation systems has to be solved and that this is the main computational effort. This means that the computational effort for evaluating the matrices in (3.1) and assembling the matrices in (3.29) by integration and Kronecker product is neglected. Let N_{ts} be the number of time steps which are necessary to solve (3.1). The complexity of solving the nonlinear equations shall be estimated by $\mathcal{O}(N_{\mathrm{s}}^{k})$ where N_{s} is the size of the equation system and k depends on the solver. Considering all time steps, the overall complexity to solve the original problem is consequently given by

$$N_{\mathrm{ts}}\,\mathcal{O}(N_{\mathrm{s}}^{k}). \tag{3.106}$$

For the MPDE approach, the number of time steps is denoted by $\widehat{N}_{\mathrm{ts}}$, the size of the equation system (3.29) is given by $N_{\mathrm{s}}(N_{\mathrm{p}}+1)$. As a result, the overall complexity is

$$\widehat{N}_{\mathrm{ts}}\,\mathcal{O}\left((N_{\mathrm{s}}(N_{\mathrm{p}}+1))^{k}\right). \tag{3.107}$$

Comparing both complexities and assuming that the same solver is used for both problems yields that the MPDE approach is more efficient than the conventional time discretization of the original problem if the condition

$$(N_{\mathrm{p}}+1)^{k} < \frac{N_{\mathrm{ts}}}{\widehat{N}_{\mathrm{ts}}} \tag{3.108}$$

is satisfied. Consequently to achieve an efficient simulation, the number of time steps in the MPDE approach must be considerably smaller than that of the conventional time discretization of the original problem. This is often fulfilled. If LU decomposition and forward/backward substitution is used in each step and the matrices are full, the parameter $k = 3$. If the matrices are sparse, the number is usually smaller. There are also methods for solving linear equation systems which can reach linear complexity, meaning that $k = 1$, e.g. Algebraic Multigrid Methods, see [16]. They would be optimal since a relatively high number of basis functions could be used, while still achieving an efficient solution method. Future research must determine if those methods are suitable to solve the equation systems arising in the MPDE approach.

3.5 Natural sampling versus regular sampling

The difference between regular sampling and natural sampling was already discussed in Section 2.6. As can be seen in Fig. 2.11, when natural sampling is used, the switch in the excitation occurs at the point where the reference signal $d(t)$ and the carrier $s(t)$ intersect, i.e. at position $t = t_{\mathrm{nat}}^{\star}$. When using regular sampling, in contrast, the reference signal is sampled at the beginning of the period, i.e. at $t = 0$ and held constant throughout the entire cycle. This leads to a different position of the switching instant, namely $t = t_{\mathrm{reg}}^{\star}$. To accomplish this in the MPDE approach, a naive idea would be to use a sampled version of the reference signal $d(t)$, i.e. a curve $d^{\star}(t)$ which is piecewise constant throughout each switching cycle, for the MPDE approach. Consequently the function $d^{\star}(t)$ would be discontinuous. This would lead to high computational effort along the slow time scale since the duty cycle is assumed to be slowly varying. To avoid this, a "delayed" reference signal $d_{\mathrm{del}}(t)$ is introduced. We require it to fulfill the relation (first switching cycle)

$$d_{\mathrm{del}}(t_{\mathrm{reg}}^{\star}) = d(0), \tag{3.109}$$

such that the switching instant occurs at the correct position. The sawtooth carrier is given by

$$s(t) = \frac{1}{T_{\mathrm{s}}}\,t \ \mathrm{mod}\ 1, \tag{3.110}$$

which means that the switching instant in regular sampling $t = t_{\text{reg}}^\star$ can be calculated by equating (3.109) and (3.110) and solving for t, i.e.

$$t = T_{\text{s}}\, d_{\text{del}}(t). \tag{3.111}$$

A function satisfying the condition (3.109) is naturally given by

$$d_{\text{del}}(t) = d\big(t - T_{\text{s}}\, d_{\text{del}}(t)\big). \tag{3.112}$$

This equation can simply be added as an additional equation into (3.29). The time integration algorithm takes care of solving it. For illustration we only considered the first switching cycle. A generalization is possible by adding multiples of T_{s} to the time variable. Relation (3.112) holds for the entire simulation interval. If the known reference signal also depends on the state variables, i.e. $d(\mathbf{x}, t)$, which is often the case if a control system is used to adjust the output voltage or current of a power converter, then the situation becomes more complicated. Equation (3.112) becomes

$$d_{\text{del}}(\mathbf{x}, t) = d\Big(\mathbf{x}\big(t - T_{\text{s}}\, d_{\text{del}}(\mathbf{x}, t)\big), t - T_{\text{s}}\, d_{\text{del}}(\mathbf{x}, t)\Big), \tag{3.113}$$

which requires the state variables to be available at an earlier time instant. This can either be tackled by solvers for delay differential equations, or, more easily, with an approximation, which allows us to stay in the well-known area of ODEs/DAEs. A first order approximation of the delayed reference signal $d_{\text{del}}(\mathbf{x}, t)$ is given by

$$
\begin{aligned}
d_{\text{del}}(\mathbf{x}, t) &= d\Big(\mathbf{x}\big(t - T_{\text{s}} d_{\text{del}}(\mathbf{x}, t)\big), t - T_{\text{s}} d_{\text{del}}(\mathbf{x}, t)\Big) \\
&= d(\mathbf{x}, t) - d_{\text{del}}(\mathbf{x}, t)\, T_{\text{s}}\, \frac{\mathrm{d}\, d(\mathbf{x}(t), t)}{\mathrm{d}t} + \mathcal{O}\left(\big(d_{\text{del}}(\mathbf{x}, t)\, T_{\text{s}}\big)^2\right) \\
&\approx d(\mathbf{x}, t) - d_{\text{del}}(\mathbf{x}, t)\, T_{\text{s}}\, \frac{\mathrm{d}\, d(\mathbf{x}(t), t)}{\mathrm{d}t}.
\end{aligned}
\tag{3.114}
$$

This equation is an ODE which can be added to the equation system (3.29) to calculate the necessary $d_{\text{del}}(\mathbf{x}, t)$ from the known reference signal $d(\mathbf{x}, t)$. The regular sampling with a triangle carrier is achieved analogously. Corresponding to the functions $d_1(\mathbf{x}, t)$ and $d_2(\mathbf{x}, t)$, there will be delayed functions $d_{\text{del},1}(\mathbf{x}, t)$ and $d_{\text{del},2}(\mathbf{x}, t)$ and an equation (3.114) for each of them, respectively.

3.6 Suitability of warped MPDEs

WaMPDEs are an advanced concept of MPDEs, which can be used when working with frequency modulation. If the frequency of a signal changes, e.g. in a voltage-controlled oscillator, the approach using MPDEs is inefficient [70]. To deal with this problem, in addition to introducing the artificial time scales, some of the time scales are warped, i.e., they are scaled with a function depending on another time scale. This is the origin of the term "warped MPDEs". The concept was introduced in [70] for the first time. The warped MPDEs corresponding to the original ODEs/DAEs (3.1) are given by

$$\mathbf{A}(\widehat{\mathbf{x}}) \left(\frac{\partial \widehat{\mathbf{x}}}{\partial t_1} + \omega_2(t_1) \frac{\partial \widehat{\mathbf{x}}}{\partial t_2} + \ldots + \omega_m(t_1) \frac{\partial \widehat{\mathbf{x}}}{\partial t_m} \right) + \mathbf{B}(\widehat{\mathbf{x}})\, \widehat{\mathbf{x}} = \widehat{\mathbf{c}}, \tag{3.115}$$

where $\widehat{\mathbf{x}} = \widehat{\mathbf{x}}(t_1, \ldots, t_m)$ is the solution and $\widehat{\mathbf{c}} = \widehat{\mathbf{c}}(t_1, \ldots, t_m)$ is the excitation. The functions $\omega_2(t), \ldots, \omega_m(t)$ are called local frequency functions. The relation between the solution and excitation of (3.115) and (3.1) is given by

Theorem 4 (adapted from [71]). *Let a solution and excitation of the ODEs/DAEs (3.1) be given by $\mathbf{x}(t) \in C^1(\Upsilon)$ and $\mathbf{c}(t) \in C^0(\Upsilon)$. Then the multivariate solution $\widehat{\mathbf{x}}(t_1, \dots, t_m)$ and excitation $\widehat{\mathbf{c}}(t_1, \dots, t_m)$ given by*

$$\widehat{\mathbf{x}}\big(t, \theta_2(t), \dots, \theta_m(t)\big) = \mathbf{x}(t), \tag{3.116}$$

$$\widehat{\mathbf{c}}\big(t, \theta_2(t), \dots, \theta_m(t)\big) = \mathbf{c}(t), \tag{3.117}$$

satisfy the WaMPDEs (3.115). The functions $\theta_2(t), \dots, \theta_m(t) \in C^1(\Upsilon)$ are called warping functions.

Proof. see Appendix 6.4. □

The functions $\theta_i(t)$ and $\omega_i(t)$ are related by

$$\omega_i(t) = \frac{\mathrm{d}\theta_i(t)}{\mathrm{d}t}, \quad \forall i = 2, \dots, m. \tag{3.118}$$

Since time cannot run backwards, the derivative of θ must be positive, i.e, $\omega(t) > 0 \; \forall \, t$. A generalization of the relation (3.116), (3.117) similar to (3.6), (3.7), where shifts $\widehat{\alpha}_1, \dots, \widehat{\alpha}_m$ are included is not mentioned in the literature. Note that if the solution, excitation or warping functions provide less smoothness than stated in Theorem 4, a piecewise analysis is possible similar as described in Subsection 3.1.1.

During this research project the question arose if the concept of WaMPDEs is suitable to model a varying duty cycle. This would be a replacement for supplying the basis functions with a duty cycle by using the warping function θ. As discussed in the following this does not yield an efficient simulation method. However the concept may be applied in another context, which is briefly described in the end of this section.

For simplicity we assume that the considered problem is linear. This is sufficient to demonstrate the difficulties with WaMPDEs. We start from the linear system of ODEs

$$\mathbf{A}\frac{\mathrm{d}}{\mathrm{d}t}\mathbf{x}(t) + \mathbf{B}\mathbf{x}(t) = \mathbf{c}(t). \tag{3.119}$$

The corresponding WaMPDEs are given by [70]

$$\mathbf{A}\left(\frac{\partial \widehat{\mathbf{x}}(t_1, t_2)}{\partial t_1} + \omega(t_1)\frac{\partial \widehat{\mathbf{x}}(t_1, t_2)}{\partial t_2}\right) + \mathbf{B}\,\widehat{\mathbf{x}}(t_1, t_2) = \widehat{\mathbf{c}}(t_1, t_2), \tag{3.120}$$

where $\omega(t_1)$ is the local frequency function. The relation between the WaMPDEs and the original ODEs is given by

$$\widehat{\mathbf{x}}(t, \theta(t)) = \mathbf{x}(t), \tag{3.121}$$

$$\widehat{\mathbf{c}}(t, \theta(t)) = \mathbf{c}(t), \tag{3.122}$$

where $\theta(t)$ is the warping function. Similarly as before the solution is now split into basis functions and coefficients

$$\widehat{x}_j^h(t_1, t_2) = \sum_{k=0}^{N_{\mathrm{p}}} y_{j,k}(t_1) w_k\big(\tau(t_2), d_0\big), \tag{3.123}$$

however, the duty cycle is fixed at a constant value $d_0 \in (0, 1)$.
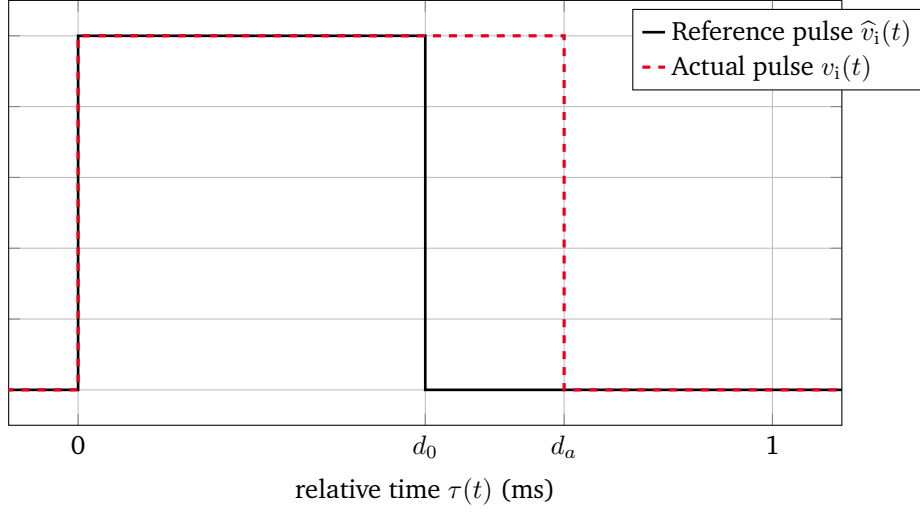
Figure 3.14: Reference and actual pulse. The warping function $\theta(t)$ maps the time between them.

Applying the Galerkin approach analogously to Section 3.2 yields

$$\boldsymbol{\mathcal{A}}_\omega \frac{\mathrm{d}\mathbf{y}}{\mathrm{d}t_1} + \boldsymbol{\mathcal{B}}_\omega(t_1)\,\mathbf{y}(t_1) \;=\; \boldsymbol{\mathcal{C}}_\omega(t_1)\,, \tag{3.124}$$

where

$$\boldsymbol{\mathcal{A}}_\omega = \mathbf{A} \otimes \boldsymbol{\mathcal{J}}(0, d_0), \tag{3.125}$$

$$\boldsymbol{\mathcal{B}}_\omega(t_1) = \mathbf{B} \otimes \boldsymbol{\mathcal{J}}(0, d_0) + \omega(t_1)\mathbf{A} \otimes \boldsymbol{\mathcal{Q}}(0, d_0), \tag{3.126}$$

$$\boldsymbol{\mathcal{C}}_\omega(t_1) = \int\limits_0^{T_\mathrm{s}} \widehat{\mathbf{c}}(t_1, t_2) \otimes \mathbf{w}(\tau(t_2), d_0)\ \mathrm{d}t_2\,. \tag{3.127}$$

Since the duty cycle is assumed to be constant, there is no term involving the derivative of it or the matrix $\boldsymbol{\mathcal{U}}$. The task of varying the duty cycle is realized through the local frequency function $\omega(t_1)$. It has the ability to stretch and compress the fast time scale t_2 and is used to shift the position of the C^0 continuity to fit the actual switching instant. Consequently the next step is to find an appropriate warping function $\theta(t)$ and setup the right-hand side $\widehat{\mathbf{c}}(t_1, t_2)$ of the MPDEs. The original problem is excited by a PWM generated ideal pulsed excitation denoted by v_i, i.e

$$\mathbf{c}(t) = \mathbf{f}_\mathrm{pro} v_\mathrm{i}(t, d(t)), \tag{3.128}$$

with $\mathbf{f}_\mathrm{pro} \in \mathbb{R}^{N_\mathrm{s}}$ a vector, which assigns the excitation to the equations from the system (3.1) that are actually excited and $v_\mathrm{i}(t, d(t))$ is generated as described in Section 2.6 using natural sampling and sawtooth carrier. Since the basis functions w_k from (3.123) are constructed for the duty cycle d_0, the right-hand side of the MPDEs must be chosen with the same duty cycle, i.e.

$$\widehat{\mathbf{c}}(t_1, t_2) = \mathbf{f}_\mathrm{pro} \widehat{v}_\mathrm{i}(t_2), \tag{3.129}$$

where $\widehat{v}_\mathrm{i}(t_2) = v_\mathrm{i}(t_2, d_0)$.

The warping function needs to satisfy (3.122) for all $t \in \Upsilon$, i.e. in the entire simulation interval. This is accomplished when the warping function $\theta(t)$ maps the time as such that the switching instants of the excitations coincide.
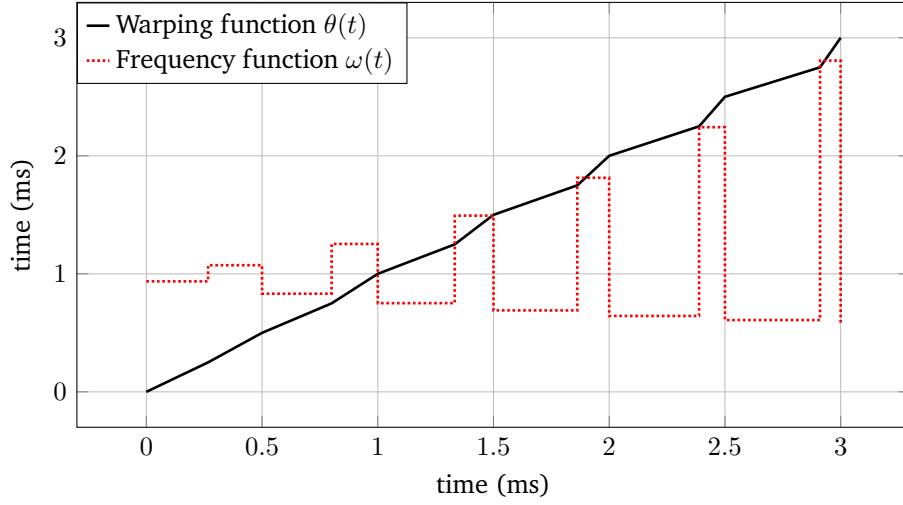
Figure 3.15: Exemplary $\theta(t)$ and $\omega(t)$ for linear interpolation of the warping function ($T_\mathrm{s} = 0.5\,\mathrm{ms}$, $d(t) = 0.40625\sin(100\pi t) + 0.5$, $d_0 = 0.5$). Since the warping function is global in C^0, the frequency function $\omega(t)$ is discontinuous.

For illustration let us assume that in the n-th switching cycle the switching occurs at the time instant t_a, i.e. the duty cycle is $d(t_a) = d_a$. The corresponding ideal right-hand side pulse for the corresponding period $[(n-1)T_\mathrm{s}, nT_\mathrm{s}]$ is depicted in Fig. 3.14. The excitation $\widehat{v}_\mathrm{i}(t)$ leads to a "reference" pulse also depicted in the figure. To map the switching instants onto each other, i.e. to map the points of C^0 continuity of the ripples in the solution onto each other, the warping function must fulfill the conditions

$$\theta\left((n-1)T_\mathrm{s}\right) = (n-1)T_\mathrm{s}$$
$$\theta\left((n-1)T_\mathrm{s} + d_a T_\mathrm{s}\right) = (n-1)T_\mathrm{s} + d_0 T_\mathrm{s}$$
$$\theta(nT_\mathrm{s}) = nT_\mathrm{s}.$$

Then for the interval $[(n-1)T_\mathrm{s}, nT_\mathrm{s}]$, the relation (3.122) is fulfilled. The simplest warping function possible is built by connecting the points by linear interpolation leading to the exemplary warping function as depicted in Fig. 3.15. The corresponding frequency function $\omega(t)$ is depicted as well. Since the smoothness of the frequency function $\omega(t)$ has a direct impact on the regularity of the warped MPDE solution and thus on the convergence of the Galerkin approach, it is advantageous to use higher-order interpolation. An exemplary $\theta(t)$ in this case is shown in Fig. 3.16 for four cycles. Its derivative $\omega(t)$ is depicted in the same figure and still continuous. Looking at the figures it already becomes clear that this kind of modeling will not lead to an efficient simulation. As can be seen the variations in $\omega(t)$ are fast. The time rates are in the same range as T_s and as a result the variations along the slow time scale t_1 will be equally strong as along the fast time scale t_2. This becomes apparent when looking at the system (3.124). The function $\omega(t_1)$ has a direct influence on the slow time scale t_1 and as a result the time integration algorithm will have to cope with fast variations coming from it. Numerical results which support this statement are discussed in Subsection 4.4.3.

Nevertheless there is an application in which the WaMPDEs may be useful. There are applications in which not only the duty cycle of a PWM excitation but also the switching frequency $1/T_\mathrm{s}$ is varying. If the change of the switching frequency is much slower than the switching frequency itself, the warping function may be used. Since it stretches and compresses the entire time scale, the switching frequency would change with it. This is a possible topic for future research.
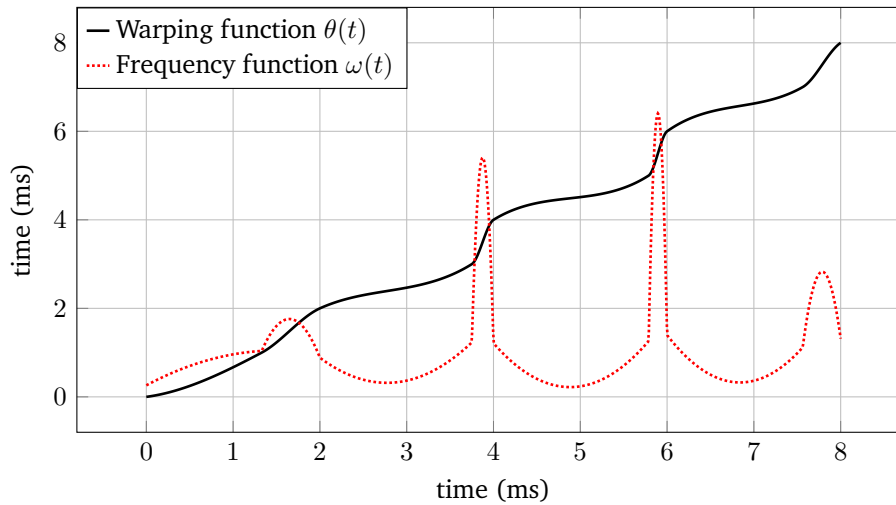
Figure 3.16: Exemplary $\theta(t)$ and $\omega(t)$ for piecewise cubic interpolation of the warping function ($T_\mathrm{s} = 0.5\,\mathrm{ms}$, $d(t) = 0.40625 \sin(100\pi t) + 0.5$, $d_0 = 0.5$). Since the warping function is global in C^1, the frequency function $\omega(t)$ is still continuous.

3.7 Conclusion

In this chapter the methodological aspects of the developed method have been discussed. In a first step, the concept of MPDEs has been introduced and their relation to the differential equations describing the original problem has been derived. Subsequently the MPDEs have been solved by a combination of a Galerkin approach and a conventional time discretization. Since the fast varying periodic ripples are already resolved by the Galerkin approach, the time integration algorithm needs considerably less time steps than for the original differential equation systems. This comes at the price of larger equation systems. Three types of basis functions have been presented which are suited in the application of the MPDE approach to PWM power converters. Furthermore, a technique for dealing with regular sampling has been proposed and the suitability of the concept of WaMPDEs as an alternative to model varying duty cycle has been evaluated. It was found that it is unsuited for that purpose. However it might be used if the switching frequency is slowly varying during the simulation.

4 Numerical applications and results

This chapter presents the numerical applications which are used to demonstrate the efficiency and accuracy of the proposed multirate partial differential equation (MPDE) approach. A simple buck converter (DC-DC converter) and two different inverters (DC-AC converters) are used as test examples. The excitation is idealized, i.e. no transistors or any other highly nonlinear semiconductor components are present in the circuit. The MPDE approach is first applied to the buck converter with linear and nonlinear inductor. Subsequently the inductor is replaced by a field model such that a field-circuit coupled problem arises. As DC-AC applications, an inverter with RLC filter and an inverter with LCL filter and control scheme are employed.

In the course of this chapter, the accuracy of the MPDE approach is determined by comparing quantities of interest in the circuit, i.e. certain voltages and currents, to a reference solution. The relative L^2 error between both is used as a measure of accuracy. It is defined by

$$\epsilon_x = \frac{\left\|x_{\text{ref}}(t) - x^h(t)\right\|_{L^2(\Upsilon)}}{\left\|x_{\text{ref}}(t)\right\|_{L^2(\Upsilon)}}, \tag{4.1}$$

where x represents the actual quantity of interest, the superscript h denotes an approximation, the subscript ref denotes the reference solution and Υ is the simulation time interval. The continuous norms are discretized by using numerical quadrature, namely the mid-point rule, which is of quadratic order [44]. This results in

$$\epsilon_x \approx \frac{\sqrt{\sum\limits_{k=1}^{N_\epsilon} |\Upsilon_k| \left|x_{\text{ref}}(t^{(k)}) - x^h(t^{(k)})\right|^2}}{\sqrt{\sum\limits_{k=1}^{N_\epsilon} |\Upsilon_k| \left|x_{\text{ref}}(t^{(k)})\right|^2}}, \tag{4.2}$$

where the entire simulation interval Υ is split into N_ϵ non-overlapping subintervals Υ_k, and $t^{(k)}$ are the mid-points of these subintervals Υ_k.

The simulations are partly run in Octave [23] and partly in MATLAB. Mainly two different solvers for differential equations are applied, namely ode5r (Octave, odepkg [116]) and ode15s (MATLAB). ode5r implements an implicit Runge-Kutta (IRK) of order 5 with 3 stages. The function is a wrapper to the original FORTRAN code "Radau5" by Hairer et al. [43]. ode15s implements a modified version of the backward differentiation formulas (BDFs) up to order 5 [107]. Both algorithms support dense output, which allows to extract the solution at arbitrary time instants in the simulation interval. The order of accuracy at the additional time points is the same as that of the actual time steps chosen by the time integration algorithm. The solvers use adaptive time stepping to control the accuracy given user-specified relative and absolute tolerances. How the solvers deal with both tolerances is different. The internally estimated solution error needed

(a)

(b)
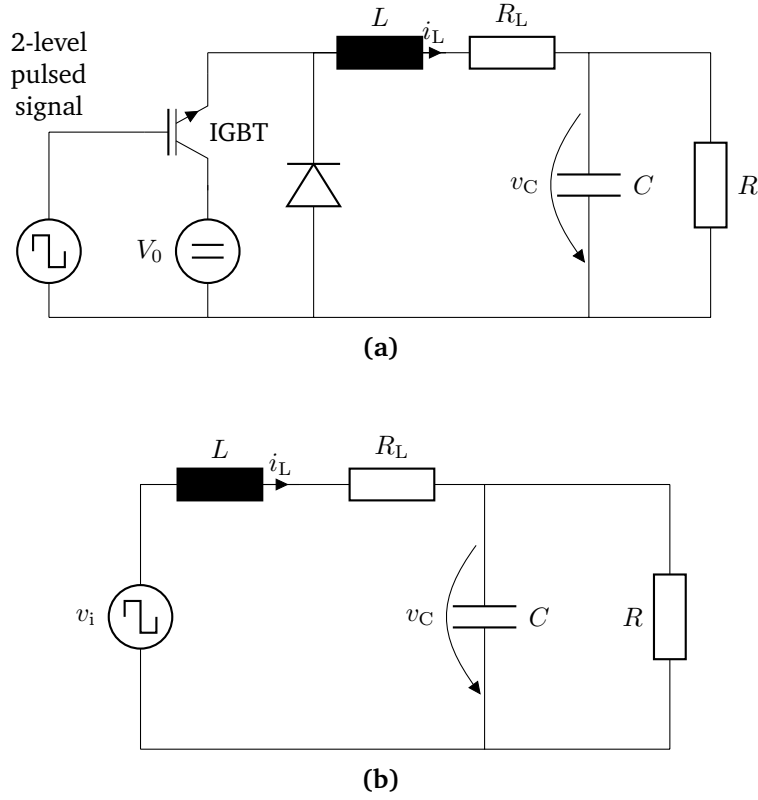
Figure 4.1: (a) Buck converter and (b) simplified buck converter in continuous conduction mode with idealized excitation. Figures based on [80] ©2019 IEEE.

for the adaptivity in `ode5r` is given by [43]

$$\|\mathrm{err}\| = \sqrt{\frac{1}{N} \sum_{i=1}^{N} \left(\frac{\mathrm{err}_i}{\mathrm{sc}_i}\right)^2}, \tag{4.3}$$

where the estimated error of the i-th solution component is denoted by err_i, N is the size of the equation system and sc_i is given by

$$\mathrm{sc}_i = \mathrm{abstol} + \max_{i=1,\dots,N} \left(\left|y_i^{(0)}\right|, \left|y_i^{(1)}\right|\right) \mathrm{reltol}. \tag{4.4}$$

It depends on the absolute and relative tolerance and the i-th solution component of the current and previous step, i.e. $\left|y_i^{(1)}\right|$ and $\left|y_i^{(0)}\right|$, respectively. The step size of the following step is calculated using the estimated error. A detailed discussion can be found in [43, p. 124]. In this work the error estimation (4.3) is modified to use a maximum norm

$$\|\mathrm{err}\| = \max_{i=1,\dots,N} \left|\frac{\mathrm{err}_i}{\mathrm{sc}_i}\right|. \tag{4.5}$$

The reason for changing the estimation is that for linear problems in the MPDE approach, most of the variables stay constant if the initial values are chosen wisely. As such the error of these solution components is very small or even zero. Therefore the original estimate masks the error if new basis functions are added which do not strongly contribute to the error. The result is that the time integration algorithm takes less time steps than is actually necessary to provide the desired accuracy of the reconstructed solution of the MPDE

approach. For `ode15s` the applied norm to calculate if the current step size is acceptable is specified by using the "NormControl" option. In our simulations, this is set to "on" [107].

Both solvers react differently to switching events in the excitation. The MATLAB solver `ode15s` aborts at switching events while `ode5r` simply goes down to finer time steps to guarantee the desired accuracy. To avoid the failure of the MATLAB solver, a switch event detection is implemented. It uses the solver's event function feature to stop the time integration algorithm if a switch event is detected. The solver is subsequently restarted with the updated excitation value. In the end, the solutions on the subintervals are concatenated. To calculate consistent initial values at the beginning of each subinterval the procedure discussed at the end of Section 2.5 is employed. The initial differential variables for the new time interval are set to the end value of the differential variables of the last time interval.

4.1 Buck converter circuit

Let us consider the buck converter as depicted in Fig. 4.1a [41]. It consists of a DC voltage source with voltage V_0, an insulated-gate bipolar transistor (IGBT) and a diode connected to a filter circuit consisting of an inductor L and its resistance R_L, a capacitor C and a load R. In general the load can also consist of capacitive, inductive or other electrical elements. If the buck converter is run in continuous conduction mode, i.e. if the current through the coil is always positive ($i_L > 0$), then the diode can be neglected. By additionally assuming idealized switching behaviour of the transistor, the circuit can be simplified as depicted in Fig. 4.1b. The pulsed voltage is given by

$$v_i(t) = \begin{cases} V_0 & \text{for } \tau(t) \in [0, D] \\ 0 & \text{otherwise} \end{cases}, \tag{4.6}$$

where $\tau(t)$ is the relative time and D is the duty cycle. The circuit is characterized by two state variables, namely i_L and v_C. Using the KIRCHHOFF laws, see Section 2.2, the buck converter can be described by the system of ordinary differential equations (ODEs)

$$\begin{bmatrix} L & 0 \\ 0 & C \end{bmatrix} \frac{\mathrm{d}}{\mathrm{d}t} \begin{bmatrix} i_L \\ v_C \end{bmatrix} + \begin{bmatrix} R_L & 1 \\ -1 & 1/R \end{bmatrix} \begin{bmatrix} i_L \\ v_C \end{bmatrix} = \begin{bmatrix} v_i(t) \\ 0 \end{bmatrix}, \tag{4.7}$$

The following parameter values are employed:

- $V_0 = 100\,\text{V}$;
- $f_s = 500\,\text{Hz}$;
- $D = 0.7$;
- $L = 1\,\text{mH}$, $R_L = 10\,\text{m}\Omega$;
- $C = 100\,\mu\text{F}$;
- $R = 0.8\,\Omega$.

As initial conditions $v_C(0) = 0\,\text{V}$ and $i_L(0) = 0\,\text{A}$ are applied.

For this simple system of ODEs (4.7), it is possible to analytically calculate the reference solution in closed form. For that purpose the simulation interval is split into subintervals $\triangle t^{(k)}$, $k \in \mathbb{N}$ as such that on
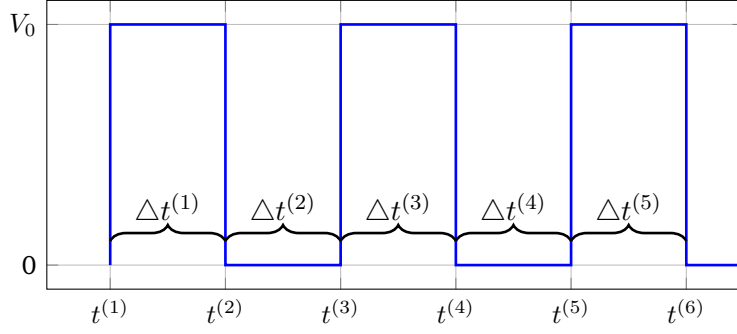
Figure 4.2: Division of simulation interval into subintervals for the calculation of the closed form solution.

each subinterval the excitation is constant, i.e. either V_0 or 0. This is depicted in Fig. 4.2. The solution on subinterval $\triangle t^{(k)}$ is calculated by [78]

$$i_{\mathrm{L}}(t) = \frac{1}{2(R+R_{\mathrm{L}})\zeta_1} \mathrm{e}^{\left(\frac{\zeta_1(t+t^{(k)})+\zeta_2(t^{(k)}-t)}{2CLR}\right)} \left(2V_{\mathrm{in}}\zeta_1 \mathrm{e}^{\left(\frac{-\zeta_1(t+t^{(k)})+\zeta_2(t-t^{(k)})}{2CLR}\right)} + \mathrm{e}^{\left(-\frac{t\zeta_1}{CLR}\right)} \zeta_3 + \mathrm{e}^{\left(-\frac{t^{(k)}\zeta_1}{CLR}\right)} \zeta_4\right),$$

and

$$v_{\mathrm{C}}(t) = \frac{1}{2(R+R_{\mathrm{L}})\zeta_1} \mathrm{e}^{\left(\frac{\zeta_1(t+t^{(k)})+\zeta_2(t^{(k)}-t)}{2CLR}\right)} \left(2RV_{\mathrm{in}}\zeta_1 \mathrm{e}^{\left(\frac{-\zeta_1(t+t^{(k)})+\zeta_2(t-t^{(k)})}{2CLR}\right)} + \mathrm{e}^{\left(-\frac{t\zeta_1}{CLR}\right)} \zeta_5 + \mathrm{e}^{\left(-\frac{t^{(k)}\zeta_1}{CLR}\right)} \zeta_6\right),$$

where

$$\zeta_1 = \sqrt{C^2R^2R_{\mathrm{L}}^2 - 2CLR(2R+R_{\mathrm{L}}) + L^2},$$

$$\zeta_2 = CRR_{\mathrm{L}} + L,$$

$$\zeta_3 = \zeta_1\left(i_{\mathrm{L}}(t^{(k)})(R+R_{\mathrm{L}}) - V_{\mathrm{in}}\right) + CR\left(RR_{\mathrm{L}}i_{\mathrm{L}}(t^{(k)}) + 2v_{\mathrm{C}}(t^{(k)})(R+R_{\mathrm{L}}) - 2RV_{\mathrm{in}} + R_{\mathrm{L}}^2 i_{\mathrm{L}}(t^{(k)}) - R_{\mathrm{L}}V_{\mathrm{in}}\right)$$
$$+ L\left(V_{\mathrm{in}} - i_{\mathrm{L}}(t^{(k)})(R+R_{\mathrm{L}})\right),$$

$$\zeta_4 = \zeta_1\left(i_{\mathrm{L}}(t^{(k)})(R+R_{\mathrm{L}}) - V_{\mathrm{in}}\right) + CR\Big(-RR_{\mathrm{L}}i_{\mathrm{L}}(t^{(k)}) - 2v_{\mathrm{C}}(t^{(k)})(R+R_{\mathrm{L}}) + 2RV_{\mathrm{in}}$$
$$+ R_{\mathrm{L}}^2\left(-i_{\mathrm{L}}(t^{(k)})\right) + R_{\mathrm{L}}V_{\mathrm{in}}\Big) + Li_{\mathrm{L}}(t^{(k)})(R+R_{\mathrm{L}}) - LV_{\mathrm{in}},$$

$$\zeta_5 = L\left(-2R^2 i_{\mathrm{L}}(t^{(k)}) + R\left(-2R_{\mathrm{L}}i_{\mathrm{L}}(t^{(k)}) + V_{\mathrm{in}} + v_{\mathrm{C}}(t^{(k)})\right) + R_{\mathrm{L}}v_{\mathrm{C}}(t^{(k)})\right)$$
$$- (\zeta_1 - CRR_{\mathrm{L}})\left(RV_{\mathrm{in}} - v_{\mathrm{C}}(t^{(k)})(R+R_{\mathrm{L}})\right),$$

$$\zeta_6 = \left(-(\zeta_1 + CRR_{\mathrm{L}})\left(RV_{\mathrm{in}} - v_{\mathrm{C}}(t^{(k)})(R+R_{\mathrm{L}})\right) + LR\left(2i_{\mathrm{L}}(t^{(k)})(R+R_{\mathrm{L}}) - V_{\mathrm{in}}\right) - Lv_{\mathrm{C}}(t^{(k)})(R+R_{\mathrm{L}})\right).$$

As can be seen the solution of the current subinterval depends on the solution at the end of the prior interval. The excitation V_{in} has to be chosen as either V_0 or 0 according to the excitation on the respective subinterval. The solutions of the buck converter for switching frequencies of $f_{\mathrm{s}} = 500\,\mathrm{Hz}$ and $f_{\mathrm{s}} = 5000\,\mathrm{Hz}$ are depicted in Fig. 4.3. They consist of fast varying ripples and a slowly varying envelope. If the switchinig frequency increases, the amplitude of the ripples decreases.

The accuracy and efficiency of the MPDE approach is analyzed on the simplified buck converter example. The calculations were performed on an Intel Core i5-5200U with 2.2 GHz and 16 GB RAM. Most parts of the
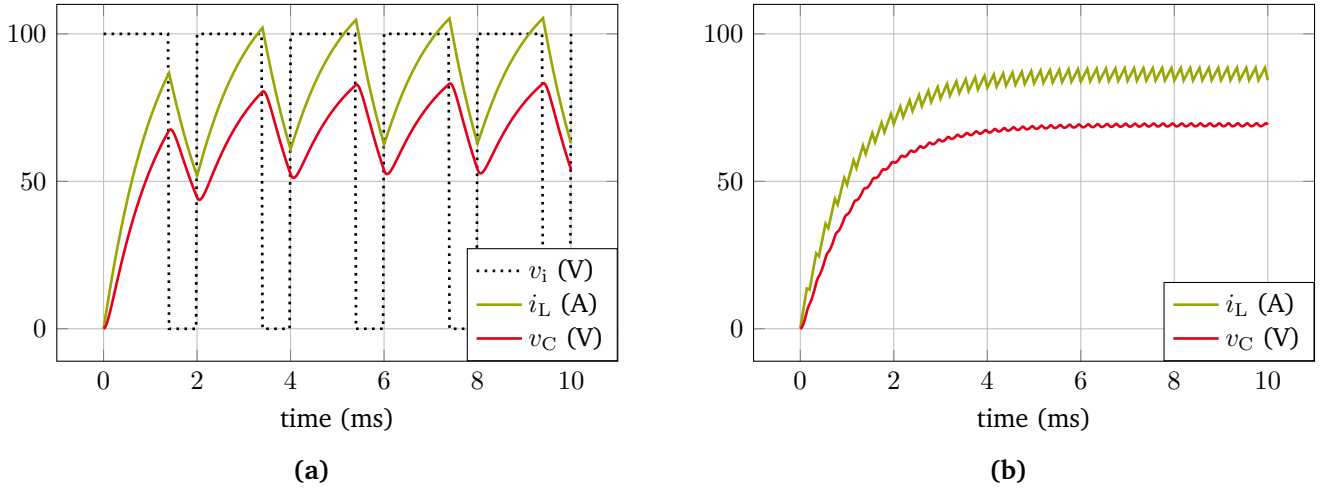
Figure 4.3: Solution of the buck converter for different switching frequencies f_s (switching cycles T_s) and fixed duty cycle $D = 0.7$. (a) $f_\mathrm{s} = 500\,\mathrm{Hz}$, i.e. $T_\mathrm{s} = 2\,\mathrm{ms}$. (b) $f_\mathrm{s} = 5000\,\mathrm{Hz}$, i.e. $T_\mathrm{s} = 0.2\,\mathrm{ms}$. Figures adapted from [80] ©2019 IEEE.

following results are also presented in [78, 80], although the timings differ slightly since another computer was utilized for the calculations. As basis functions the FE nodal functions, the PWM basis functions and the B-splines are used.

The FE nodal functions are B-splines of order 1. The nodes (knots) in the relative time interval $[0, 1]$ are chosen equidistant as such that the jumps in the excitation at $t^{(i)}$ where $\tau(t^{(i)}) = D$ fall exactly onto a node. The corresponding knot vector is given by (differently than in Subsection 3.3.3)

$$\Xi_\mathrm{fe} = [0, 0, 1, 2, \ldots, (N_\mathrm{p,fe} - 2), (N_\mathrm{p,fe} - 1), (N_\mathrm{p,fe} - 1)] / (N_\mathrm{p,fe} - 1), \tag{4.8}$$

with $N_\mathrm{p,fe} \in \{11, 21, 31, 41, \ldots\}$ for $D = 0.7$. The FE nodal functions are given by $w_\mathrm{fe,1}(\tau) = P_{0,1}(\tau), w_\mathrm{fe,2}(\tau) = P_{1,1}(\tau), \ldots, w_{\mathrm{fe},N_\mathrm{p,fe}}(\tau) = P_{N_\mathrm{p,fe}-1,1}(\tau)$. To ensure periodicity, an additional constant basis function $w_\mathrm{fe,0}(\tau) = 1$ is used and the coefficients corresponding to the first and last basis functions $w_\mathrm{fe,1}(\tau)$ and $w_{\mathrm{fe},N_\mathrm{p,fe}}(\tau)$ are set to zero (zero Dirichlet boundary conditions). The resulting basis is exemplary shown for $N_\mathrm{p,fe} = 5$ in Fig. 4.4. If the jump in the excitation does not coincide with a node, it was observed that the convergence order is diminished from quadratic to linear.

For the B-splines, the original knot vector as described in Subsection 3.3.3 is used. To ensure periodicity, the same approach as for the FE nodal functions is employed (see also Subsection 3.3.3). The number of B-spline basis functions $N_\mathrm{p,bspl}$ takes the functions at the boundary into account. Only the degree is used as refinement variable, namely $p \in \{2, \ldots, 10\}$. No additional knots are added, meaning $K = 0$.

In case of the PWM basis functions any number of basis functions $N_\mathrm{p,pwm}$ can be chosen since the duty cycle is already taken into account by construction. However as the PWM basis functions are polynomials, they become numerically unstable for high $N_\mathrm{p,pwm}$ such that the number is restricted to $N_\mathrm{p,pwm} \in \{1, \ldots, 12\}$.

The multivariate right-hand side of the MPDEs (3.11) is chosen according to Subsection 3.4.1, i.e. $\widehat{v}_\mathrm{i}(t_1, t_2) = v_\mathrm{i}(t_2)$. This leads to constant right-hand side of the semi-discretized system of equations (3.29), i.e.

$$\boldsymbol{\mathcal{C}}(t_1) = \text{constant}. \tag{4.9}$$
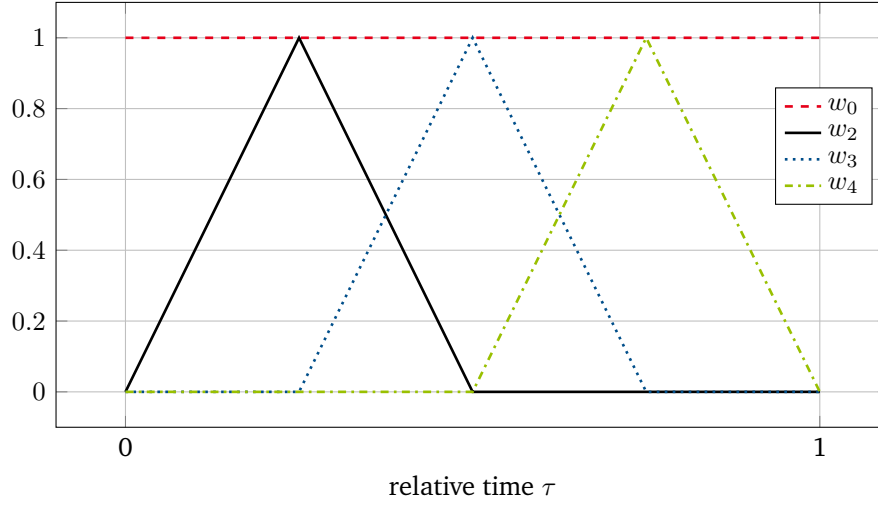
Figure 4.4: FE nodal basis $w_{\text{fe},k}(\tau)$ with $k \in \{0, 2, 3, 4\}$ for $N_{\text{p,fe}} = 5$. Figure adapted from [80] ©2019 IEEE.

The initial values of (3.29) are found as laid out in Subsection 3.4.2. Since the buck converter is a linear problem, the equation system (3.29) is linear as well. The steady-state solution is given by

$$\mathbf{y}^\star = \mathcal{B}^{-1}\mathcal{C}. \tag{4.10}$$

Applying the procedure from Subsection 3.4.2 leads for all three bases to the initial values

$$\mathbf{y}_{j,k}(0) = \begin{cases} y^\star_{j,k} & \text{for } k = 1, \dots, N_{\text{p}} \text{ and } j = 1, \dots, N_{\text{s}} \\ x_j(0) - \sum_{l=1}^{N_{\text{p}}} y^\star_{j,l} w_l(0, D) & \text{for } k = 0 \text{ and } j = 1, \dots, N_{\text{s}}. \end{cases} \tag{4.11}$$

To reconstruct the solution after solving (3.29), the solution expansion (3.15) is used. The time integration algorithm uses less time steps than for the original equations (4.7) therefore the dense output feature is utilized to obtain a reasonably-fine sampled solution. A 3D representation of the multivariate capacitor voltage is shown in Fig. 4.5. The fast periodic ripples evolve along the fast time scale t_2 while the smooth, slowly varying envelope evolves along time scale t_1.

Convergence The accuracy of the method for the different basis functions is analyzed with respect to the number of basis function N_{p}. As a measure of quality the error (4.2) is considered, specifically, the error of the voltage at the capacitor ϵ_v. The results for the current through the inductor are similar. The simulations are conducted in Octave using ode5r as time integrator. The simulation interval is $\Upsilon = [0, 10]\,\text{ms}$. The solution is calculated for 500 samples per switching period T_{s} (using dense output). The absolute tolerance of the time integrator is fixed at $\text{abstol} = 10^{-10}$. According to the error estimation (4.4) and (4.5), the error is then mainly controlled by the relative tolerance reltol. It is set as such that it does not diminish the accuracy of the solution for the highest number of basis functions considered. A value of $\text{reltol} = 10^{-6}$ is employed. To ensure that this value is reasonable, the solutions for $\text{reltol} = 10^{-6}$ and $\text{reltol} = 10^{-8}$ are compared. For the highest number of basis functions, i.e. $N_{\text{p,pwm}} = 12$ (PWM basis functions), $N_{\text{p,fe}} = 131$ (FE nodal functions) and $N_{\text{p,bspl}} = 21$ (B-spline basis functions), the absolute error between the solutions is several orders of magnitude smaller than the obtained error ϵ_v of the capacitor voltage. The relative tolerance $\text{reltol} = 10^{-6}$ is therefore deemed adequate for the calculations in this section. Fig. 4.6 shows
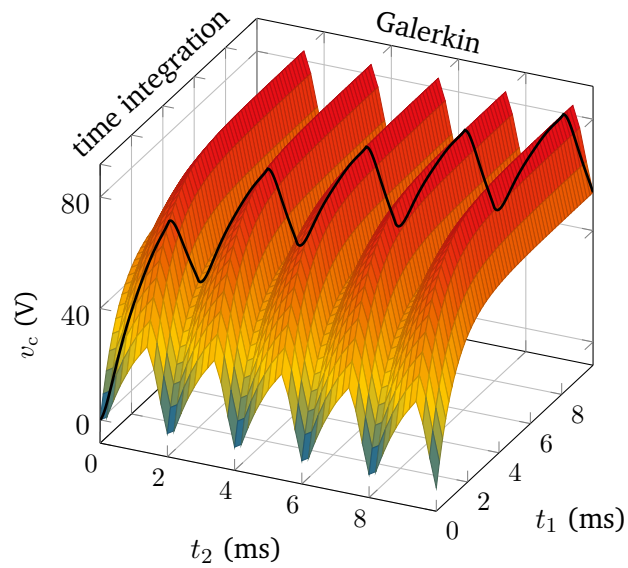
Figure 4.5: Multivariate capacitor voltage using PWM basis functions and a switching frequency of $f_\mathrm{s} = 500\,\mathrm{Hz}$. The solution of the original ODEs (4.7) is marked as a black curve. Figure adapted from [80] ©2019 IEEE.
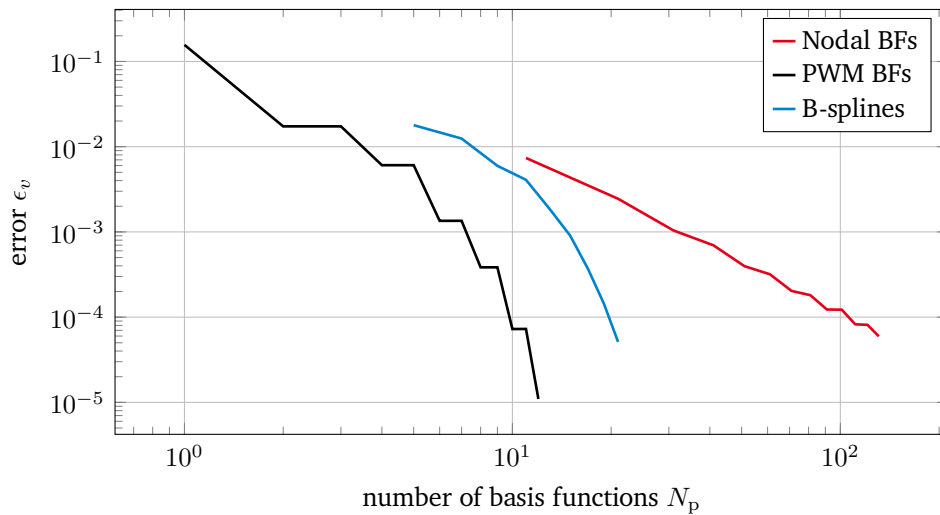
Figure 4.6: Error ϵ_v of the capacitor voltage versus the number of basis functions N_p for the nodal basis functions, the PWM basis functions and the B-spline basis functions. Figure based on [80] ©2019 IEEE.
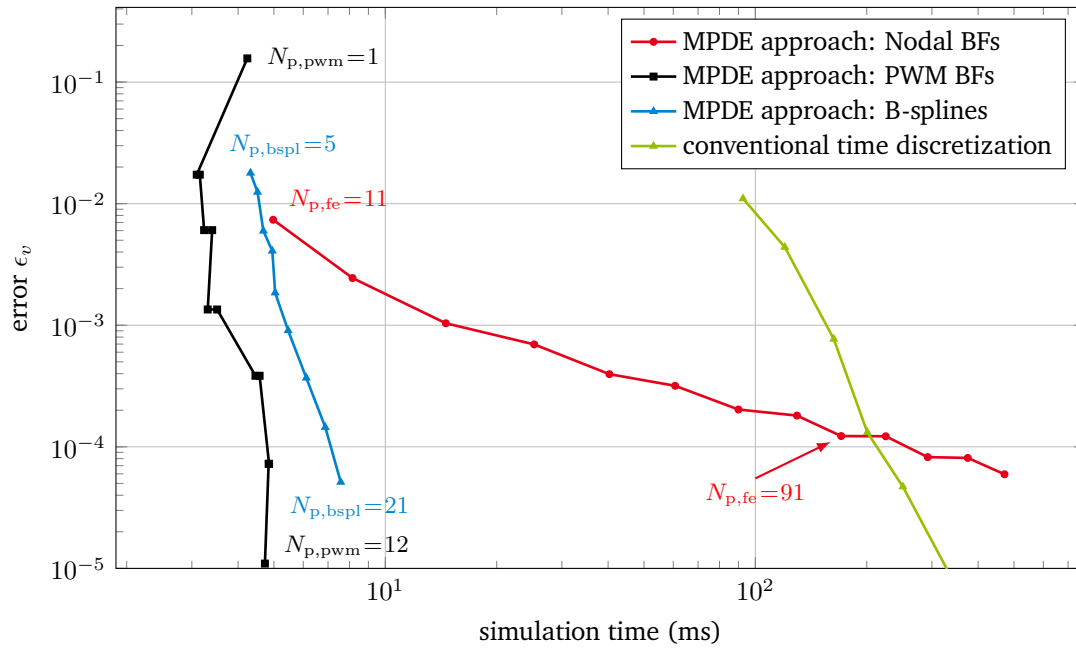
Figure 4.7: Error ϵ_v of the capacitor voltage versus the computation time, i.e. the time for solving the equation system (3.29).

the convergence of the MPDE approach for the different basis functions and with respect to the number of basis functions N_p. As one can see the method converges with all basis functions. The FE nodal functions converge approximately quadratic which is in agreement with mathematical theory [13]. The PWM basis functions exhibit exponential convergence which is also to be expected for a spectral basis [15]. It is not yet fully understood where the areas of stagnation come from. Every second basis function which is added does not contribute to the solution. However if another basis function is added, both contribute again. As a result no basis function may be removed. A possible explanation might be the symmetry conditions that the basis functions fulfill. These prohibit that an additional basis function contributes to the solution until another basis function, which fulfills a different symmetry condition, is added. The symmetry conditions are analyzed in Appendix 6.2.1. The convergence of the B-splines with degree elevation is exponential, which also concurs with the mathematical theory [14].

Efficiency   To assess the efficiency of the MPDE approach, the method is compared to conventional time discretization of the original ODEs (4.7). The time integrator `ode5r` is suited to integrate ODEs with pulsed right-hand side without failure at abrupt switches of the excitation. It takes very small time steps to approximate the transients. The accuracy of the time integrator for the solution of (4.7) is controlled by the relative tolerance setting, while for the MPDE approach the relative tolerance is fixed again (at $\mathrm{reltol} = 10^{-6}$) and the number of basis functions N_p is varied to obtain different accuracies. Fig. 4.7 shows the error ϵ_v versus the computation time. Using the PWM basis functions the MPDE approach yields excellent accuracy at an almost constant computation time, which is much smaller than the one of the conventional simulation. The same holds for the B-splines, although the approach takes slightly more computation time than for the PWM basis functions. With FE nodal functions however, the approach becomes inferior to conventional time discretization for around $N_{p,fe} = 91$ basis functions. To better understand these effects, two additional quantities are considered.
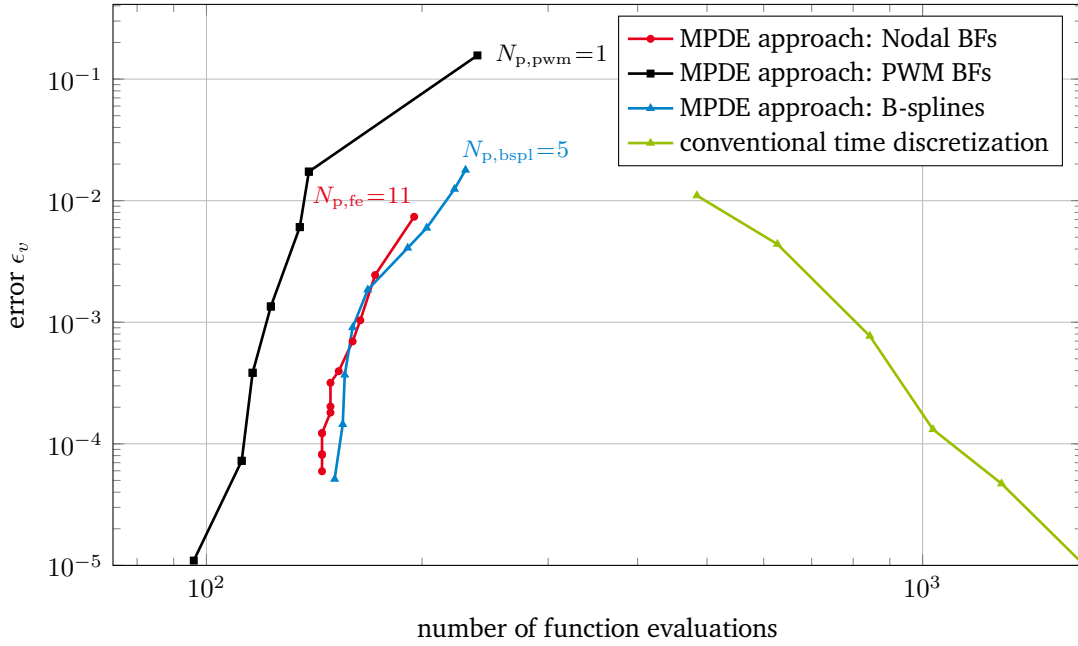
Figure 4.8: Error ϵ_v of the capacitor voltage versus the number of function evaluations.

In Fig. 4.8 the error ϵ_v is plotted versus the number of function evaluations, where function evaluations are the evaluations of the function provided to the time integrator. In this case it is the right-hand side of the reordered system of equations (3.29), i.e.

$$\mathcal{A}\frac{\mathrm{d}}{\mathrm{d}t_1}\mathbf{y}(t_1) = \mathcal{C} - \mathcal{B}\,\mathbf{y}(t_1). \tag{4.12}$$

The number of function evaluations for the conventional time discretization increases to reach a higher accuracy since more time steps are necessary. For the MPDE approach, in contrast, it even decreases with higher accuracy. As more and more basis functions are added to reach higher accuracy, there is more information already taken into account a-priori through the choice of the initial values. Therefore less time steps are necessary and thus less function evaluations. Finally, Fig. 4.9 shows the error versus the average time per function evaluation, which is calculated by dividing the simulation time by the number of function evaluations. For the conventional time discretization it is constant since the size of the equation systems does not change and thus always the same time is required to solve the linear equation systems arising inside the time integration algorithm. For the MPDE approach, in contrast, the time per function evaluation rises with higher number of basis functions (i.e. higher accuracy) since the equation systems become larger with higher N_{p}. For the PWM and B-spline basis functions a relatively small number of basis functions is sufficient to reach the desired accuracy compared to the FE nodal functions. Consequently, for the FE nodal functions the average time per function evaluation becomes comparably large which diminishes the efficiency. Both the effects observed in Figs. 4.8 and 4.9 determince the overall efficiency depicted in Fig. 4.7.

Note that the computational time for reconstructing the solution using (3.15) is not included in the abovementioned results. If the samples per period are known a-priori, the basis functions can be evaluated a-priori, which reduces the computational cost. For the 500 samples per switching period, the computational time is considerably less than $1\,\mathrm{ms}$ and is therefore neglected.

In summary, if too many basis functions are necessary to reach a desired accuracy, the computational effort of solving the arising equation systems diminishes the effect of smaller number of time steps and the
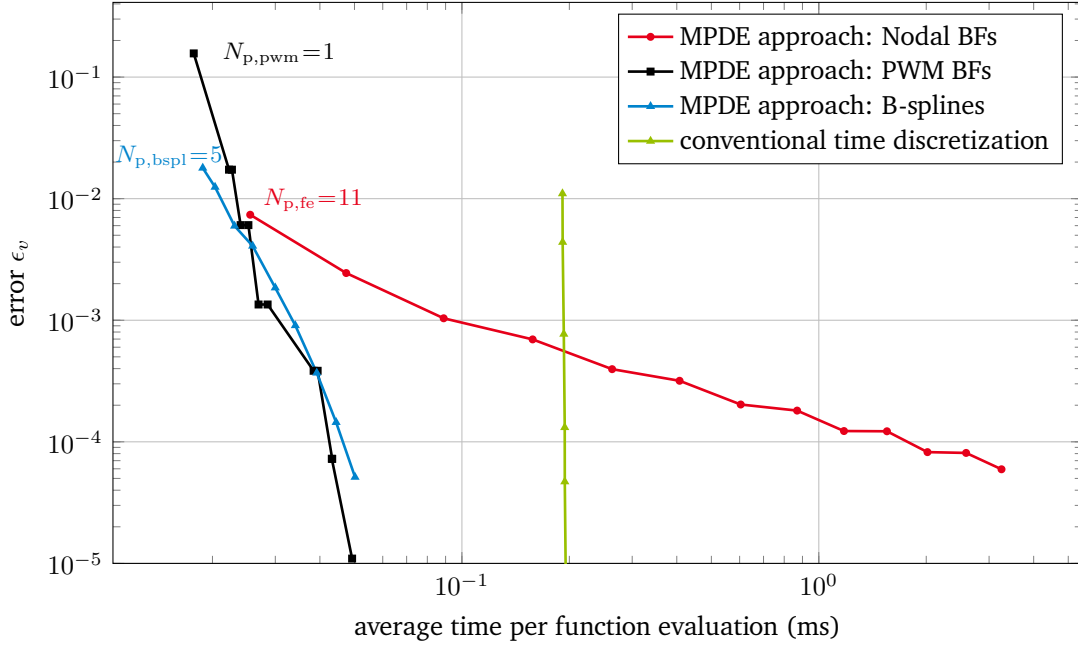
Figure 4.9: Error ϵ_v of the capacitor voltage versus the average time per function evaluation.

MPDE approach is not efficient any more. The time integrator tolerance is as well as the number of basis functions an important parameter of the MPDE approach. If less accuracy is desired, it is sufficient to use a higher relative tolerance without impairing the solution accuracy. An algorithm to automatically choose a good combination is not yet available. However an a-priori estimator can be designed by comparing the solutions for different numbers of basis functions and tolerances and adapt both parameters to reach a desired accuracy while optimizing the efficiency.

Note that the efficiency of the MPDE approach also increases with respect to conventional time discretization if a larger simulation interval is considered. As soon as the buck converter is in steady state, no further time steps are necessary to solve (3.29) since there is no more variation in the envelope **y**. A conventional time discretization always needs a relatively constant amount of computational effort to solve each switching period and takes longer corresponding to the computation interval. The same holds for increasing the switching frequency, which the MPDE approach is invariant to, while the conventional time discretization takes more effort.

4.2 Buck converter with nonlinear inductor

The results presented in the first part of this subsection follow the ones published in [81]. They are also partly presented in [78]. The simplified buck converter depicted in Fig. 4.1b is utilized as test example. Differently than before the inductor is now nonlinear and its characteristic is shown in Fig. 4.10. The index-1 differential-algebraic equations (DAEs) describing this problem are given by

$$\begin{bmatrix} 0 & 0 & 1 \\ 0 & C & 0 \\ 0 & 0 & 0 \end{bmatrix} \frac{\mathrm{d}}{\mathrm{d}t} \begin{bmatrix} i_{\mathrm{L}} \\ v_{\mathrm{C}} \\ \Phi \end{bmatrix} + \begin{bmatrix} R_{\mathrm{L}} & 1 & 0 \\ -1 & \frac{1}{R} & 0 \\ 1 & 0 & -L_{c,\mathrm{coil}}^{-1}(\Phi) \end{bmatrix} \begin{bmatrix} i_{\mathrm{L}} \\ v_{\mathrm{C}} \\ \Phi \end{bmatrix} = \begin{bmatrix} v_{\mathrm{i}}(t) \\ 0 \\ 0 \end{bmatrix}, \tag{4.13}$$
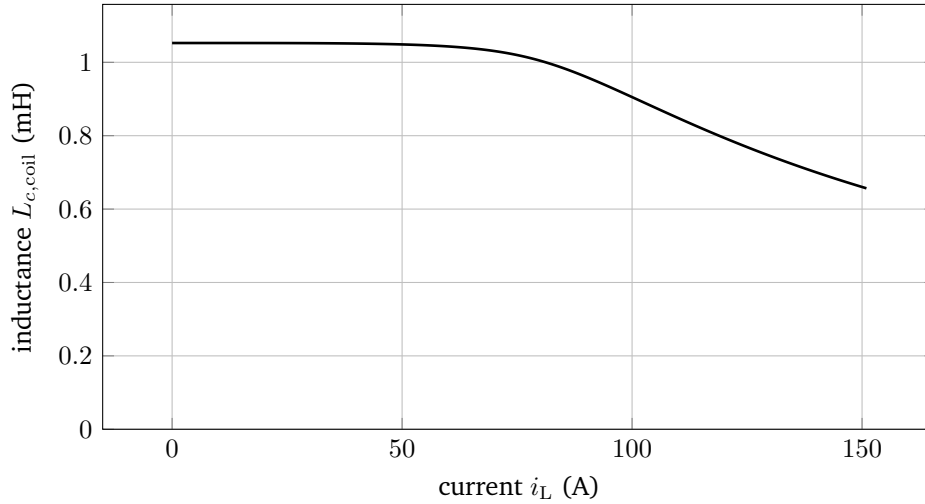
Figure 4.10: Characteristic of the nonlinear inductor. Figure adapted from [81] ©2018 IEEE.

where $L_{c,\text{coil}}$ is the nonlinear inductance [50] according to Fig. 4.10 and the other quantities are as in Section 4.1.

The aim of this section is to assess the efficiency and accuracy of the MPDE approach when the simplified evaluation of the nonlinearity described in Subsection 3.2.2 is employed. The implementation is carried out in Octave. For solving the differential equation systems we employ ode5r. The calculations are carried out on an Intel Core i7-3820 with 3.60 GHz and 16 GB RAM.

All results are compared to a reference solution, which is calculated using a very fine solver tolerance (abstol = reltol = 10^{-12}) to solve the DAEs (4.13). As before, the relative L^2 error (4.2) is used to determine the accuracy of the MPDE approach compared to the reference solution. For all calculations the simulation interval is given by $\Upsilon = [0, 10]$ ms. The switching frequency f_{s} is variable between 500 Hz and 100 kHz. As basis functions the PWM basis functions from Subsection 3.3.1 are employed.

Fig. 4.11 shows an exemplary comparison between the reference solution and the MPDE approach solution. For the MPDE approach, the integrals in (3.29) are evaluated using either Gauss-Kronrod quadrature (denoted as "original approach") or the simplification described in Subsection 3.2.2 (denoted as "simplified approach"). When using $N_{\text{p,pwm}} = 4$ basis functions and abstol = reltol = 10^{-6} there is a clearly distinguishable error between the reference solution and the simplified approach solution at $f_{\text{s}} = 1$ kHz. The original approach solution fits well to the reference solution. The simplification adopted in the simplified approach results in a correct representation of the envelope. However the shape of the ripples is similar as in the linear case. Fig. 4.12b depicts the error ϵ_v of the original and the simplified approach towards the reference solution and depending on the frequency. As expected, the higher the frequency, the smaller the error. This results from the decreasing magnitude of the ripples compared to the envelope when increasing the frequency. The accuracy of the original approach is better than that of the simplified approach since the simplified evaluation of the integrals introduces an error. However the computational time for solving using the original approach is also considerably higher than that when using the simplified approach as shown in Fig. 4.12a. Consequently if the higher accuracy is not required, the simplified approach should be used.

The efficiency of the simplified approach is summarized in Table 4.1. It shows the obtained error and approximate speedup depending on the frequency. For increasing switching frequency the conventional time discretization takes longer and longer to solve since more ripples have to be resolved. In con-
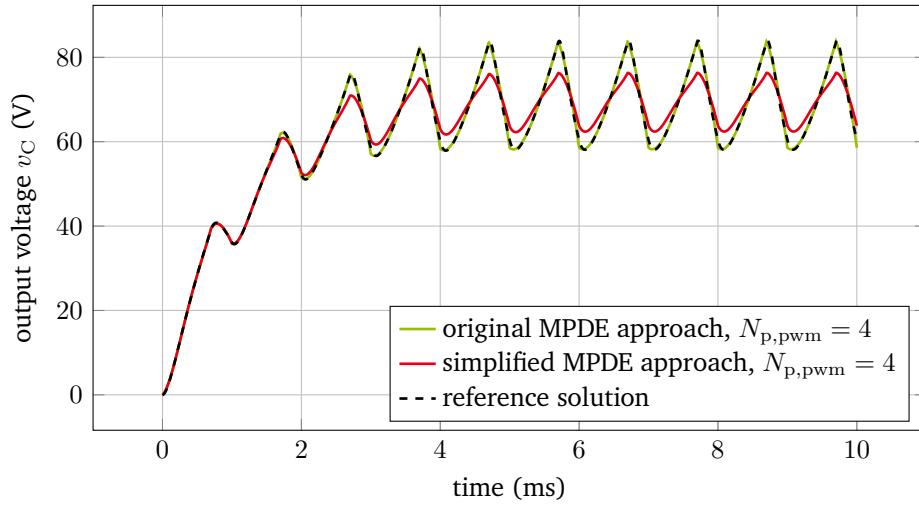
Figure 4.11: Solution of the nonlinear problem using the original and simplified MPDE approach at $f_\mathrm{s} = 1\,\mathrm{kHz}$. Figure adapted from [81] ©2018 IEEE.

(a)

(b)
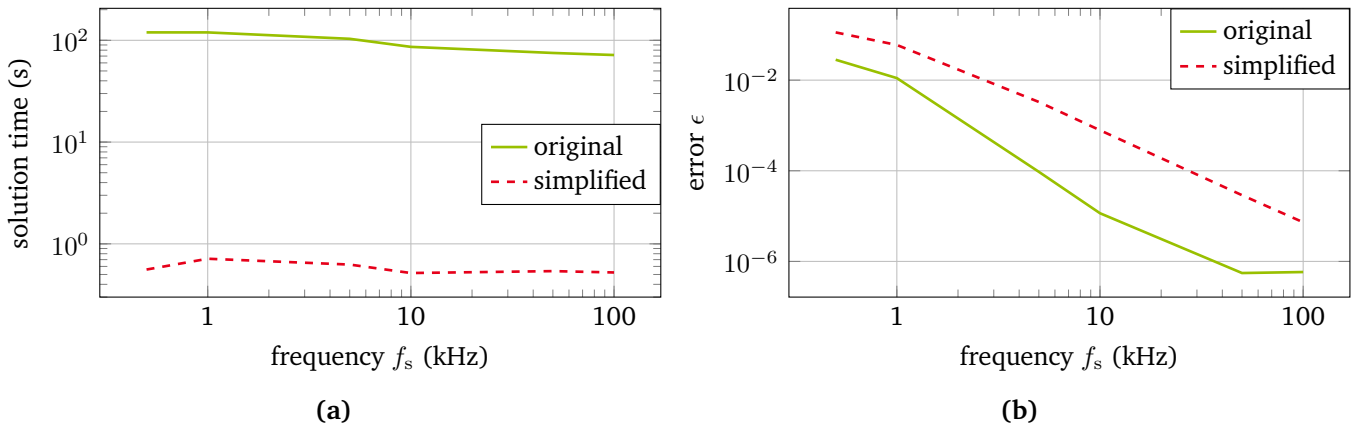
Figure 4.12: (a) Computational time to solution for the original and simplified MPDE approach depending on the switching frequency. (b) Error of the original and simplified MPDE approach using PWM basis functions with respect to the frequency. Figures adapted from [81] ©2018 IEEE.

Table 4.1: MPDE approach speedup for $N_\mathrm{p,pwm} = 4$ and different frequencies in comparison to conventional time discretization [81] ©2018 IEEE.

f_s (kHz)	approx. speedup	approx. error
10	60	8×10^{-4}
50	400	3×10^{-5}
100	1000	7×10^{-6}

Table 4.2: Average number of Newton iterations per time step for the conventional time discretization and the MPDE approach.

	Average number of Newton iterations per time step	
Number of time steps per switching cycle	conventional time disc.	MPDE approach
5	4.24	6
10	3.54	4.18
50	3	2.69
100	2.97	2.43

trast, the time for solving using the simplified approach (or also the original approach) is constant (see Fig. 4.12a) since the envelope does not change. Consequently the speedup increases if a higher frequency is employed.

In the second part of this section we investigate for the original approach, i.e. the MPDE approach with full nonlinear evaluation of the integrals, the number of Newton iterations which are necessary to solve the arising systems of equations. A fixed-time-step integration is applied in this case. The Octave solver `odebwe` from the "odepkg" is utilized. It implements a backward Euler time integration scheme and uses the Newton-Raphson algorithm without damping to solve the nonlinear systems of equations. Note that it also offers a simple adaptive-time-step integration based on Richardson extrapolation. However in this case we examine the influence of different fixed time step sizes onto the number of Newton iterations which are necessary to solve the problems. We employ B-splines ($p = 2$, $K = 2$), see Subsection 3.3.3. The Newton tolerance `NewtonTol` is set to 10^{-4}. The switching frequency of the buck converter is set to $f_\mathrm{s} = 500\,\mathrm{Hz}$. For this frequency the deformation of the ripples due to the nonlinearity is more apparent, see Fig. 4.13. Table 4.2 shows the average number of Newton iterations per time step for the conventional time discretization and the MPDE approach. For increasing number of time steps, the average number of Newton iterations per step decreases since the variations in the solution from step to step become smaller (thanks to the continuity of the solution). Furthermore if more time steps are employed, the solution accuracy increases and the MPDE approach reaches the steady state earlier in this example. Due to this fact, the MPDE approach needs less Newton iterations than the conventional time discretization for large number of time steps. For low number of time steps the conventional time discretization needs less Newton iterations.

4.3 Buck converter with field-circuit coupling

Often the simulation using circuits cannot in detail represent the electromagnetic effects which exist in various electrical elements. An example are eddy current losses which can easily be taken into account in a field model but hardly accurate in a circuit model. The disadvantage of field models is the often very high number of degrees of freedom which greatly increase the size of the equation systems. This leads to unacceptably long simulation times with conventional time discretization methods. In the MPDE approach the size of the equation systems is further increased by applying the Galerkin approach. Even though the number of time steps necessary to calculate the solution is less than in conventional methods, the total computational time is still relatively high. To allow for a cheaper solution of the equation system, a possibility is to decouple the arising equation systems. The PWM eigenfunctions introduced in Subsection 3.3.2 were developed for this purpose. The following numerical tests and results in this section have been published in [79]. As test example the simplified buck converter in Fig. 4.1b is used again. The lumped inductor is replaced by
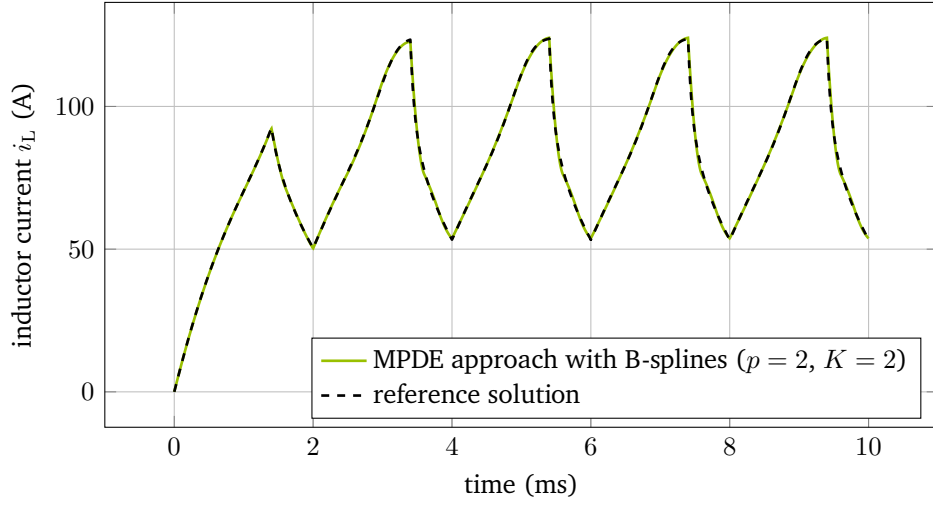
Figure 4.13: Current through the inductor at $f_s = 500\,\text{Hz}$.

a 2D finite element model of a pot inductor. This is shown in Fig. 4.14. The model parameters are given by

- $V_0 = 24\,\text{V}$;
- $f_s = 1000\,\text{Hz}$;
- $D = 0.7$;
- $L \approx 65\,\text{mH}$, $R_L = 800\,\text{m}\Omega$;
- $C = 10\,\mu\text{F}$;
- $R = 30\,\Omega$.

The pot inductor is modeled using 2D finite elements. Its core consists of ferrite material with a conductivity of $\sigma_{\text{fe}} = 250\,\text{S/m}$. According to Section 2.3 and Section 2.4 the discretized magnetoquasistatic problem is described by the equations

$$\mathbf{M}\frac{\mathrm{d}\widetilde{\mathbf{a}}_z(t)}{\mathrm{d}t} + \mathbf{K}\,\widetilde{\mathbf{a}}_z(t) = \mathbf{X}_{\text{str}}i_L(t), \tag{4.14}$$

where it is taken into account that the model uses zero Dirichlet boundary conditions and the coupling to the circuit is established through the winding function. For the field-circuit coupling an additional variable is introduced, namely the magnetic flux linkage $\Phi(t) = l_z\,\mathbf{X}_{\text{str}}^\top\widetilde{\mathbf{a}}_z(t)$, where l_z is the length of the model in z-direction. Coupling the equations describing the field part and the circuit part monolithically into one equation system yields the index-1 DAE [2]

$$\mathbf{M}\frac{\mathrm{d}\widetilde{\mathbf{a}}_z}{\mathrm{d}t} - \mathbf{X}_{\text{str}}i_L + \mathbf{K}\widetilde{\mathbf{a}}_z = 0,$$

$$l_z\,\mathbf{X}_{\text{str}}^\top\widetilde{\mathbf{a}}_z - \Phi = 0,$$

$$\frac{\mathrm{d}\Phi}{\mathrm{d}t} + R_L i_L + v_C = v_i(t).$$

$$C\frac{\mathrm{d}v_C}{\mathrm{d}t} - i_L + \frac{1}{R}v_C = 0, \tag{4.15}$$

This system contains a total of 11053 (11050 field model + 2 circuit model + 1 coupling) degrees of freedom (DOFs) for the example in Fig. 4.14. As initial conditions we consider an uncharged circuit/field model, which
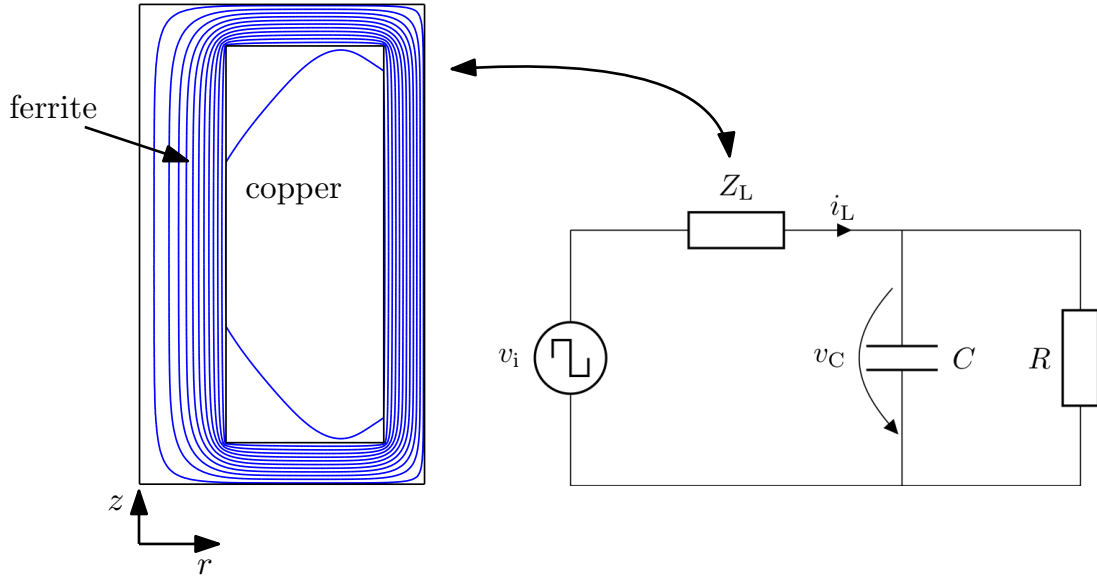
Figure 4.14: Simplified buck converter with coupled field model of the inductor. The pot inductor model is axisymmetric around the z-axis. The equipotential lines of the magnetic vector potential are depicted in the field model part. Image adapted from [79].

means $v_C(0) = 0$, $i_L(0) = 0$ and $\widetilde{\mathbf{a}}_z(0) = \mathbf{0}$. Initial conditions for the corresponding equation system after semi-discretization in the MPDE approach (3.29) are chosen similar to (4.10) and (4.11) in the Section 4.1. The same holds for the multivariate right-hand side of the MPDEs (3.11), i.e. $\widehat{v}_i(t_1, t_2) = v_i(t_2)$. The MATLAB solver `ode15s` is used to calculate the results. The simulation interval is $\Upsilon = [0, 10]$ ms. All calculations are performed on an Intel Xeon E5-2687W with 3.10 GHz and 256 GB RAM. For the MPDE approach the PWM eigenfunctions are utilized (multirate PWM balance method). As parameters a relative and absolute tolerance of 10^{-8} is used for the reference solution while for the MPDE approach a tolerance of 10^{-7} is employed.

The resulting current through the inductor is shown in Fig. 4.15a and the Joule losses in the core material are shown in Fig. 4.15b. As one can see both the reference solution and the one calculated with the multirate PWM balance method fit well. The same holds for the Joule losses calculated by

$$P_{\text{eddy}}(t) = \int_\Omega \mathbf{e}(\mathbf{r}, t) \cdot \sigma(\mathbf{r})\mathbf{e}(\mathbf{r}, t)\, \mathrm{d}\Omega = \left(\mathbf{e}_d(t)^H\right) \mathbf{M}\, \mathbf{e}_d(t), \tag{4.16}$$

where the superscript H denotes the complex conjugate transposed (hermitian) and $\mathbf{e}_d(t) = -\frac{\mathrm{d}}{\mathrm{d}t}\widetilde{\mathbf{a}}_z$ is the discrete line-integrated electric field.

The accuracy and efficiency of the multirate PWM balance method is quantified by comparing it to conventional time discretization and additionally to the MPDE approach with the original PWM basis functions. For this purpose the numerical time to solution for all three methods is measured. The accuracy of the conventional time discretization is controlled by varying the relative and absolute tolerance $\mathrm{abstol} = \mathrm{reltol} \in [10^{-6}, 10^{-1}]$. For the MPDE approach with PWM basis functions and PWM eigenfunctions the absolute and relative tolerance are fixed at $\mathrm{abstol} = \mathrm{reltol} = 10^{-7}$. The number of basis functions is varied in the interval $N_p \in \{1, \ldots, 10\}$. The accuracy is determined by calculating the relative L^2 error of the capacitor voltage according to (4.2).
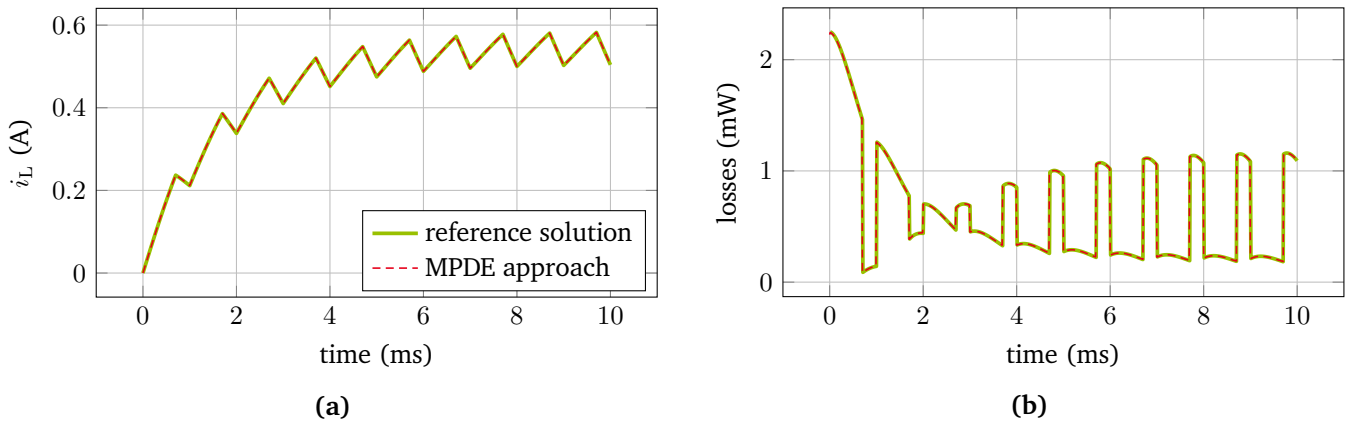
Figure 4.15: (a) Solution of the buck converter with field-circuit coupling calculated using conventional time discretization and the MPDE approach with $N_{\mathrm{p,eig}} = 4$ PWM eigenfunctions. The relative L^2 error of the current through the coil ϵ_i is approximately 3×10^{-5}. (b) Core material joule losses induced by the eddy currents. Figures adapted from [79].

Fig. 4.16 shows the error of the different methods over the time for solving the problems, i.e. the time that `ode15s` needs to solve the differential equations. In case of the conventional time discretization, i.e. solving the original equations (4.15), the time which is needed for solving consists of two parts: First, the time to calculate consistent initial values and slopes for the restart of the solver after a switch event. This depends on the number of switching cycles and the length of the simulation interval. Since both are fixed in this numerical example, the time is constant at approximately $16\,\mathrm{s}$. Second, the actual time that the solver needs to calculate the solution in the entire simulation interval. This one depends on the desired tolerance setting. Fig. 4.16 shows the total time which is the sum of both contributions. As one can see the multirate PWM balance method is considerably faster than the conventional time discretization. The equation systems in case of using PWM eigenfunctions are complex-valued and decoupled which allows for a parallel solution. The $N_{\mathrm{p}} + 1$ decoupled equation systems which need to be solved have the same size as the equation system describing the original problem (4.15). However the number of time steps necessary to solve (3.29) is much smaller and as a result less time is needed to calculate the solution. In practice one would use the same number of processor cores for the calculations as there are systems of equations, i.e. $N_{\mathrm{p}} + 1$. The overhead between processors is not taken into account since it is highly implementation and machine dependent. The system of equations which takes the longest to solve determines the computation time. In this numerical example this is the system of equation corresponding to the zero-th basis function. Fig. 4.17 shows the coefficients, i.e. the solution of (3.29) when using the PWM eigenfunctions. As one can see all coefficients but one are constant. In contrast to the multirate PWM balance method, the MPDE approach with the original PWM basis functions is even less efficient than conventional time discretization. The reason for this is that the already large equation system (4.15) is further enlarged by the Galerkin approach. It is $N_{\mathrm{p}} + 1$ times larger and cannot be decoupled. Even though almost the same number of time steps is necessary as for the multirate PWM balance method, the approach is much less efficient. The computational effort necessary for solving the enlarged equation systems is so high that it diminishes the efficiency. The stagnation which one can observe for $N_{\mathrm{p}} > 7$, i.e. at an error of approximately $\epsilon < 10^{-6}$, is due to the chosen accuracy of the time integration algorithm. Additionally one notices that adding another PWM basis function does not always contribute to a better accuracy. Actually only every second added basis function improves the error. This has also been observed in [41, 80]. The convergence properties of the PWM basis functions transfer to the PWM eigenfunctions since they are obtained by a basis transformation. Consequently the error for the
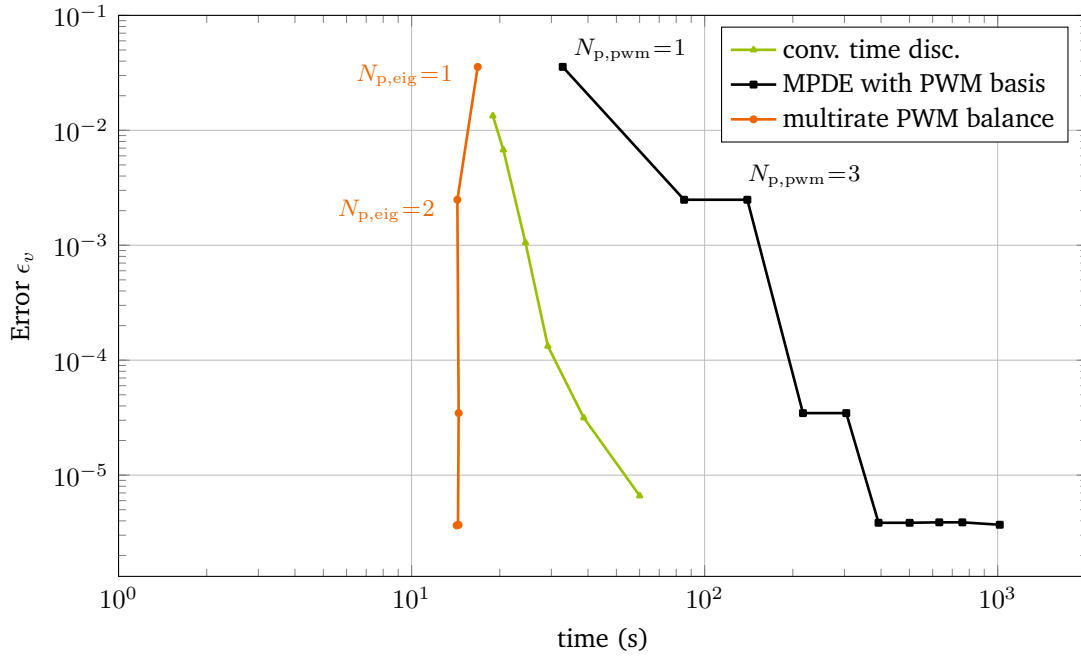
Figure 4.16: Capacitor voltage error ϵ_v over the time to solution. The multirate PWM balance method, i.e. the MPDE approach with PWM eigenfunctions, is considerably faster than conventional time discretization. The MPDE approach with the original PWM basis functions is even slower than conventional time discretization. Figure adapted from [79].

multirate PWM balance method is only plotted for the numbers of basis functions for which all basis functions contribute to the accuracy. These are given by $N_{\mathrm{p,eig}} = \{1, 2, 4, 6, 8, 10\}$. Since the decoupled equation systems in the multirate PWM balance method can be solved in parallel, the time to solution for different numbers of basis functions is almost constant. The total computational effort increases nevertheless since more parallel computations are necessary. The slight decrease in computation time for $N_{\mathrm{p,eig}} > 1$ results from choosing the initial values according to (4.10) and (4.11). Thereby more a-priori information is taken into account when a higher number of PWM eigenfunctions is employed which leads to less time steps.

4.4 Inverter with RCL filter

Let us shift the focus to applications with varying duty cycle. The inverter circuit with RLC filter depicted in Fig. 4.18 has served as a numerical example in the paper [82]. This section mainly follows the information presented therein. Three additional subsections shortly present further information on using a triangle carrier and regular sampling and the suitability of the concept of warped MPDEs (WaMPDEs) for inverter simulation.

The numerical efficiency and accuracy of the MPDE approach with B-spline basis functions is tested on the inverter example. For this purpose the MPDE approach is compared to two different simulation methods:

1. A conventional time discretization in MATLAB. Switch event detection is implemented by using the event function feature.
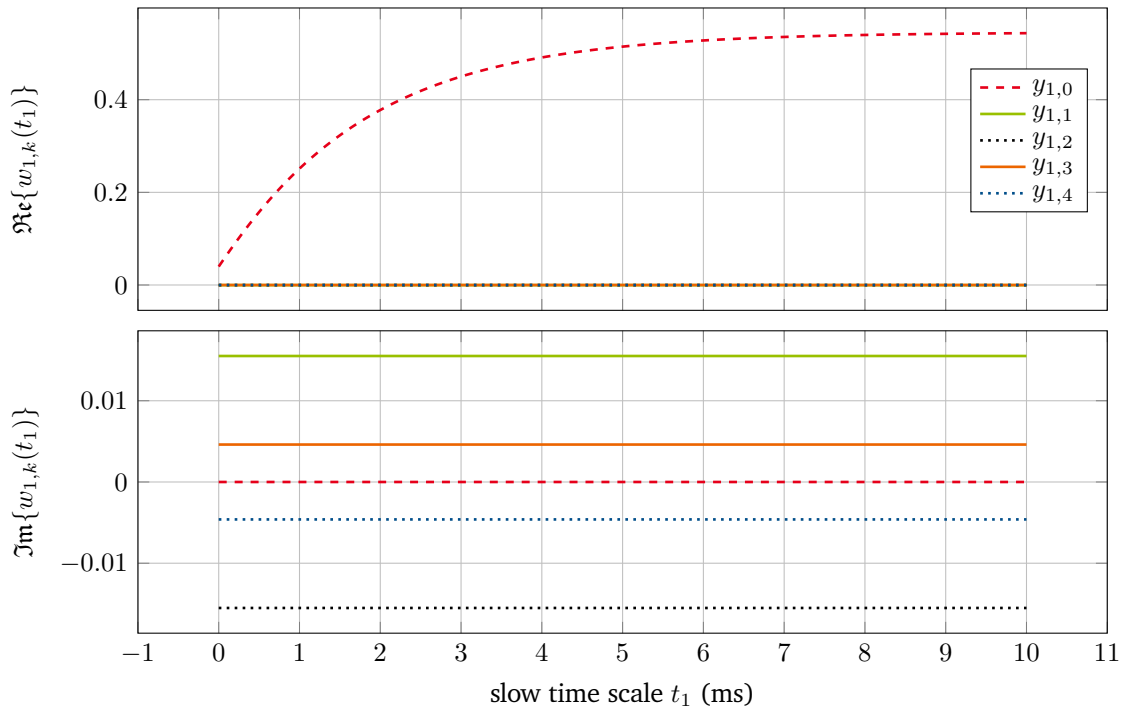
Figure 4.17: Inductor current coefficients $y_{1,k}$ found by solving (3.29) using $N_{\mathrm{p,eig}} = 4$ PWM eigenfunctions. (top) real part; the coefficients $y_{1,1}, \dots, y_{1,4}$ are visually hard to distinguish since they are almost equal. (bottom) imaginary part. Figure adapted from [79].
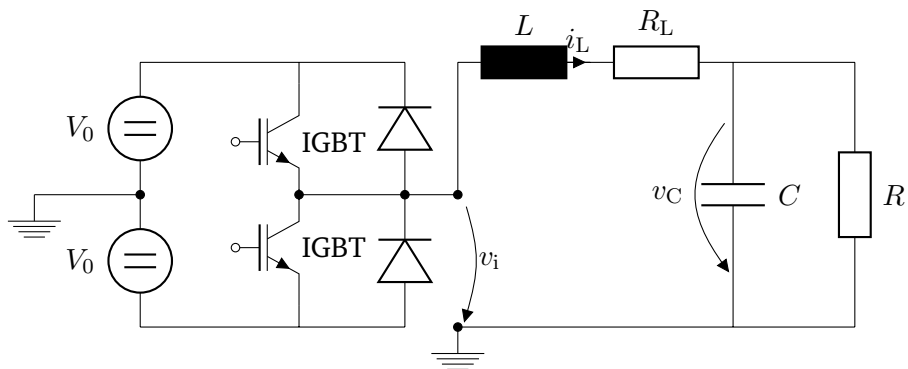
Figure 4.18: Circuit of an inverter with RLC filter. Figure based on [82].
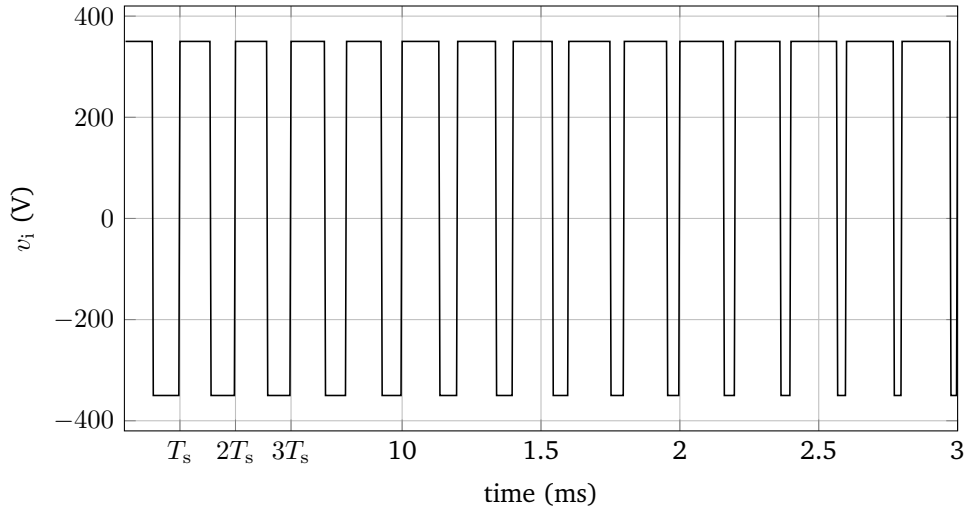
Figure 4.19: Excerpt of the PWM excitation with varying duty cycle and sawtooth carrier. One switching instant is inside the switching interval, the other always at the beginning/end of the switching interval.

2. A conventional time discretization in Simulink using the commercial software PLECS.

As time integrator we employ `ode15s` in all three cases for the sake of fair comparison of the results. The maximum order of the time integration algorithm is fixed to 2. The reason for this is twofold:

1. to ensure stability of the time integration algorithm since the differential equations posess complex eigenvalues, see Subsection 3.4.3.

2. the statistical quantities provided by the time integrator are only comparable if the maximum order is equal for all three methods.

The ODEs describing the inverter circuit are given by

$$\begin{bmatrix} L & 0 \\ 0 & C \end{bmatrix} \frac{\mathrm{d}}{\mathrm{d}t} \begin{bmatrix} i_\mathrm{L} \\ v_\mathrm{C} \end{bmatrix} + \begin{bmatrix} R_\mathrm{L} & 1 \\ -1 & 1/R \end{bmatrix} \begin{bmatrix} i_\mathrm{L} \\ v_\mathrm{C} \end{bmatrix} = \begin{bmatrix} v_\mathrm{i}(t, d(t)) \\ 0 \end{bmatrix}, \tag{4.17}$$

where $L = 4\,\mathrm{mH}$ is the inductance of the coil, $C = 10\,\mu\mathrm{F}$ is the capacitance of the capacitor, $R_\mathrm{L} = 10\,\mathrm{m}\Omega$ is the coil resistance, and $R = 20\,\Omega$ is the load resistance. These are fixed parameters. The quantities i_L, v_C and v_i are the current through the inductor, the voltage at the capacitor, and the PWM voltage excitation, respectively. The excitation for the inverter may be written as

$$v_\mathrm{i}(t, d(t)) = \bar{v}_\mathrm{i} \, \mathrm{sgn}(d(t) - s(t)). \tag{4.18}$$

It is generated using a sawtooth carrier $s(t) = \frac{t}{T_\mathrm{s}} \bmod 1$ and natural sampling PWM. $\mathrm{sgn}(t)$ is the sign function and $\bar{v}_\mathrm{i} = 350\,\mathrm{V}$ is the peak excitation voltage. An excerpt of the excitation is depicted in Fig. 4.19. It operates at a switching frequency of $f_\mathrm{s} = 1/T_\mathrm{s} = 5\,\mathrm{kHz}$.

The multivariate excitation is setup as $\widehat{v}_\mathrm{i}(t_1, t_2) = v_\mathrm{i}(t_2, d(t_1))$ such that the slowly varying reference signal $d(t_1)$ evolves along the slow time scale and the pulses evolve along the fast time scale. This is similar as described in Subsection 3.4.1. When using B-spline basis functions the resulting multivariate right-hand
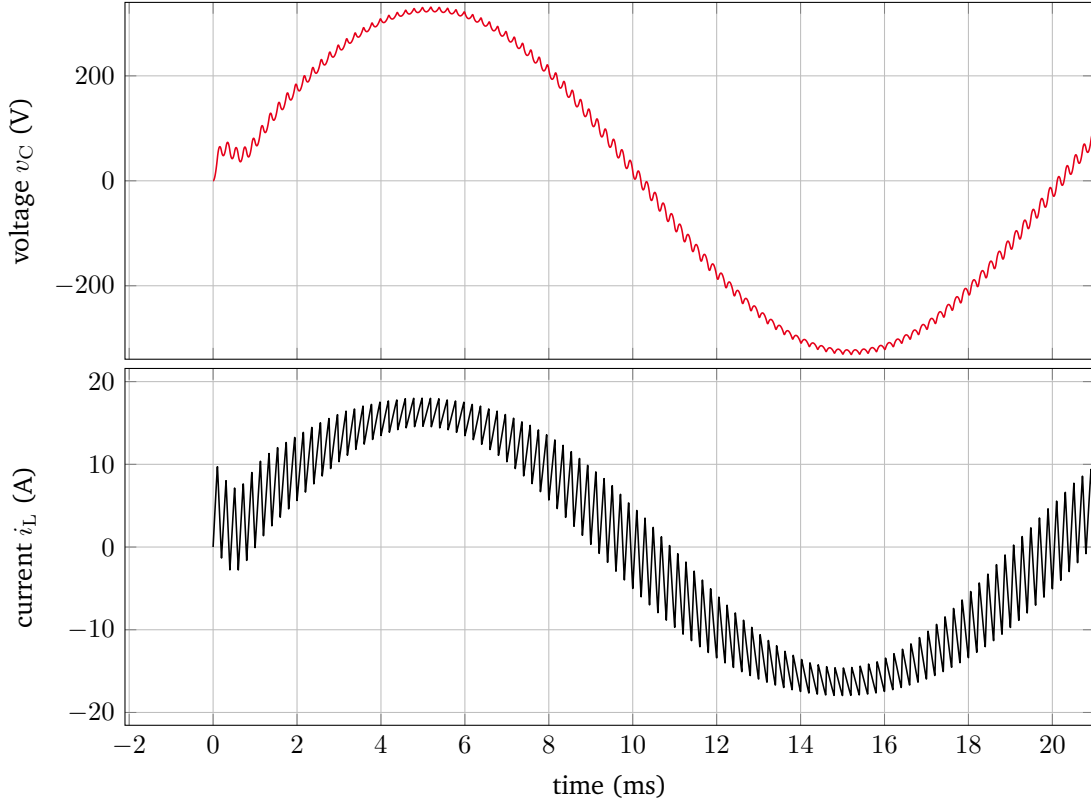
Figure 4.20: Reference solution of the inverter obtained in PLECS. (top) voltage at the capacitor. (bottom) current through the inductor. Figure adapted from [82].

side (3.31) turns out to be linearly dependent on the duty cycle. The proof is analog to the one in Appendix 6.3 for the matrix $\mathcal{J}_{\text{bspl}}$. As reference signal we use the sinusoidal function

$$d(t_1) = 0.5 \left(\frac{\bar{v}_{\text{C,desired}}}{\bar{v}_{\text{i}}} \sin(2\pi f_{\text{ac}} t_1) + 1 \right), \tag{4.19}$$

where $f_{\text{ac}} = 50\,\text{Hz}$ is the desired AC output frequency. $\bar{v}_{\text{C,desired}} = 325\,\text{V}$ is the desired output peak voltage of the converter and corresponds to $230\,\text{V}$ effective voltage. The simulation time interval is given by $\Upsilon = [0, 4\frac{1}{f_{\text{ac}}}]$ and $v_{\text{C}}(0) = 0$, $i_{\text{L}}(0) = 0$ are the initial conditions. Fig. 4.20 depicts an excerpt of the voltage at the capacitor and the current through the coil. In Fig. 4.21 one can see a 3D representation of the multivariate solution. The solution of the original ODEs is marked as a black curve.

The three different methods, i.e. MPDE approach, conventional time discretization in MATLAB, and the simulation using PLECS, are compared by considering the relative L^2 error as quantity. It is defined as in (4.2) and denoted by ϵ_v for the capacitor voltage and ϵ_i for the inductor current. The reference solution is calculated in PLECS using a very fine absolute and relative tolerance $\text{abstol} = \text{reltol} = 10^{-12}$ and a maximum step size of $T_{\text{s}}/1000$. Results for the MPDE approach with B-splines are obtained for three different discretization settings:

1. **Low order:** $p = 1$ and $K = 1$ (corresponds to finite element (FE) nodal functions),

2. **Medium order:** $p = 2$ and $K = 1$,

3. **High order:** $p = 3$ and $K = 3$.
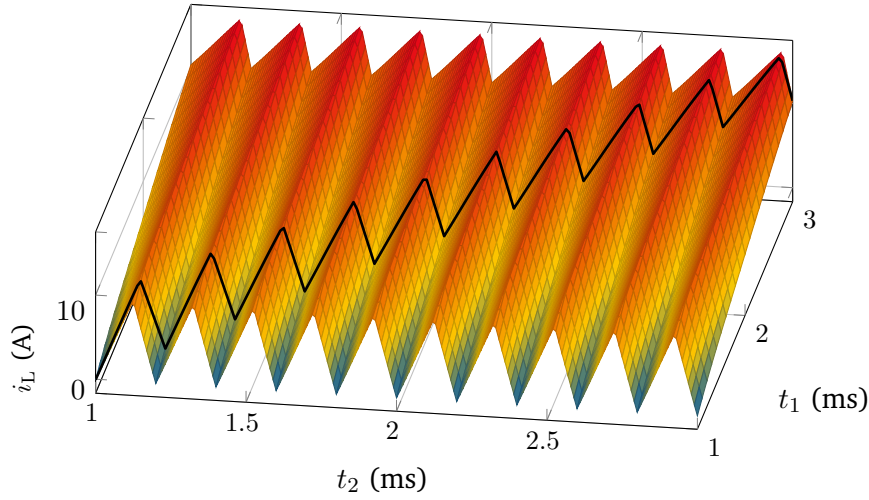
Figure 4.21: Multivariate voltage at the capacitor of the inverter and univariate solution of the original ODEs marked as a black curve. Figure adapted from [82].

Table 4.3: Accuracy of the MPDE approach and the simulation using conventional time discretization in MAT-LAB and PLECS [82].

		Simulation setting		
		low order	medium order	high order
MPDE	**tolerance**	10^{-3}	10^{-4}	10^{-7}
	error ϵ_v/ϵ_i	8.5×10^{-3} / 2.5×10^{-3}	6.9×10^{-4} / 6.2×10^{-4}	8.1×10^{-7} / 1.1×10^{-6}
MATLAB	**tolerance**	10^{-2}	10^{-4}	10^{-7}
	error ϵ_v/ϵ_i	1.2×10^{-3} / 2.5×10^{-3}	1.4×10^{-4} / 1.7×10^{-4}	3.6×10^{-6} / 8.3×10^{-7}
PLECS	**tolerance**	10^{-2}	10^{-4}	10^{-7}
	error ϵ_v/ϵ_i	6.5×10^{-3} / 8.1×10^{-3}	3.3×10^{-4} / 3.5×10^{-4}	3.0×10^{-6} / 9.7×10^{-7}

The periodicity of the B-splines is ensured by enforcing periodic boundary conditions on the arising ODEs after the semi-discretization, see Appendix 6.6. Fig. 4.22 depicts the MPDE approach errors ϵ_v and ϵ_i for these three different settings. The time integrator tolerance is utilized as parameter and swept from 10^{-10} to 10^{-2}. Relative tolerance is set to the same value as the absolute tolerance, i.e. $\mathrm{abstol} = \mathrm{reltol}$. 100 points per switching cycle are employed for evaluating the error (4.2). If the sampling of the reference solution is different, linear interpolation on the reference solution is applied to obtain the corresponding values.

The error as depicted in Fig. 4.22 decreases with smaller tolerance until stagnation. The reason for this stagnation is that the approximation by basis functions bounds the accuracy. If a better B-spline discretization is employed, the error at which the stagnation occurs becomes smaller and the stagnation region shifts towards smaller tolerances. For each of the three B-spline settings we now fix the tolerance of the time integrator as such that no computational effort is wasted while still obtaining the best possible accuracy. These tolerances are marked by dots in Fig. 4.22. The corresponding errors of the solution are presented in Table 4.3. The development of an algorithm which can automatically choose the number of basis functions and an appropriate time integrator tolerance to obtain a desired accuracy and maximum efficiency is a topic for future research. To quantify the efficiency of the different simulation approaches, statistical data on the
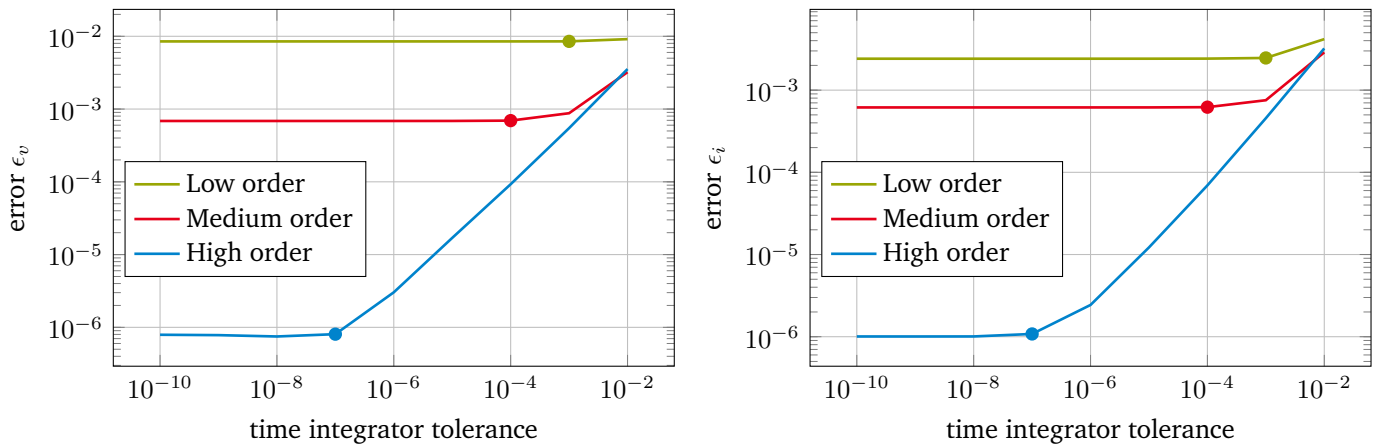
Figure 4.22: Error of the MPDE approach for the inverter for the three different B-spline discretization settings and different time integrator tolerances. (a) Error in the capacitor voltage ϵ_v. (b) Error in the inductor current ϵ_i. Figures adapted from [82].

Table 4.4: Speedup of the MPDE approach compared to the conventional simulation using MATLAB and PLECS in different simulation settings. For PLECS only the number of time steps is compared, since the other quantities are not available [82].

	Low order			Medium order			High order		
	MPDE	MATLAB/ PLECS	Approx. speedup	MPDE	MATLAB/ PLECS	Approx. speedup	MPDE	MATLAB/ PLECS	Approx. speedup
time steps	235	10533/ 4254	45/ 18	474	12662/ 11158	27/ 24	4515	66120/ 72859	15/ 16
failed steps	50	36	none	69	830	12	111	3873	35
LU decom.	95	2230	23	150	3572	24	727	11567	16
fun. eval.	557	21938	39	1050	27784	26	7572	140786	19

solution process are utilized. The time integrator provides different quantities like the number of time steps, number of function evaluations and number of LU decompositions. To offer a basis for comparison, the time integrator tolerance for the conventional methods in MATLAB and PLECS is set as such that the resulting solution error is approximately in the same order of magnitude as that of the MPDE approach. The corresponding tolerance setting and actual errors are presented as well in Table 4.3.

The error of the conventional methods with respect to the time integrator tolerance is shown in Fig. 4.23. In the MATLAB simulation the `MaxStep` option is utilized to ensure that no switch events are missed. This explains why for high tolerance, i.e. $\mathrm{abstol} = \mathrm{reltol} = 10^{-2}$, the accuracy of the solution is more accurate than that of the PLECS simulation. This also has an effect on the number of time steps which are necessary to solve the problem. The gathered statistical data are shown in Table 4.4 and support this (low order). For the higher accuracy settings, the number of time steps in MATLAB and PLECS are almost the same. The reason why for the simulation with PLECS only the number of time steps is provided is that the other quantities can to our knowledge not be extracted from Simulink.

One can see in Table 4.4 that the MPDE approach is considerably faster than the conventional methods with respect to the presented quantities. If the switching frequency of the excitation increases, the efficiency
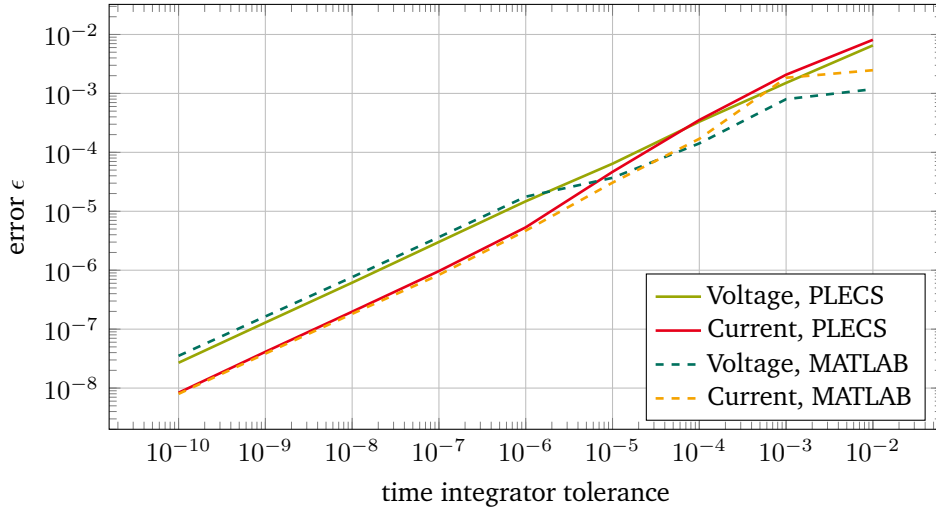
Figure 4.23: Error of the considered conventional time discretization with regard to the reference solution: Solver in MATLAB with switch event detection and commercial software PLECS in Simulink. Figure adapted from [82].

rises even further, see [81] or Subsection 4.2.

Note that the number of time steps does not directly imply a statement about the efficiency of the MPDE approach in terms of computing time. One has to take into account that the equation systems in the MPDE approach are $N_p + 1$ times larger than the original ones and thus the linear equation solver will naturally take more time for solving the equation systems in each time step. The efficiency of the time integrator and its equation system solver are therefore the main bottleneck. However the MPDE approach will be very efficient if the time for the function evaluation (assembling the original matrices) is the main computational effort.

4.4.1 Triangle carrier PWM with natural sampling

Instead of a sawtooth carrier, we now employ a triangle carrier on the same example to numerically verify that the proposed MPDE approach with two reference signals $d_1(t)$ and $d_2(t)$ according to Subsection 3.2.1 works. Similar as before the excitation may be written as

$$v_i(t, d(t)) = \bar{v}_i \, \mathrm{sgn}(d(t) - s(t)), \tag{4.20}$$

where

$$s(t) = \begin{cases} 2\tau(t) & \tau(t) \leq 0.5 \\ 2 - 2\tau(t) & \tau(t) > 0.5 \end{cases} \tag{4.21}$$

is the triangle carrier. An excerpt of the resulting PWM excitation when using the reference signal (4.19) as before is depicted in Fig. 4.24. The reference solution is calculated in MATLAB with `ode15s` and switch-event detection using an absolute and relative tolerance of $\mathrm{abstol} = \mathrm{reltol} = 10^{-10}$ and a maximum step size of $T_s/100$. For the MPDE approach we use a high order B-spline discretization setting, i.e. $p = 3$, $K = 3$ and absolute and relative time integrator tolerance of $\mathrm{abstol} = \mathrm{reltol} = 10^{-7}$. An excerpt of the resulting capacitor voltage and the current through the inductor is depicted in Fig. 4.25. The agreement is excellent with $\epsilon_v = 7.7 \times 10^{-7}$ and $\epsilon_i = 1.0 \times 10^{-6}$ and is similar to the accuracy found in Table 4.3 for the corresponding setting (high order).
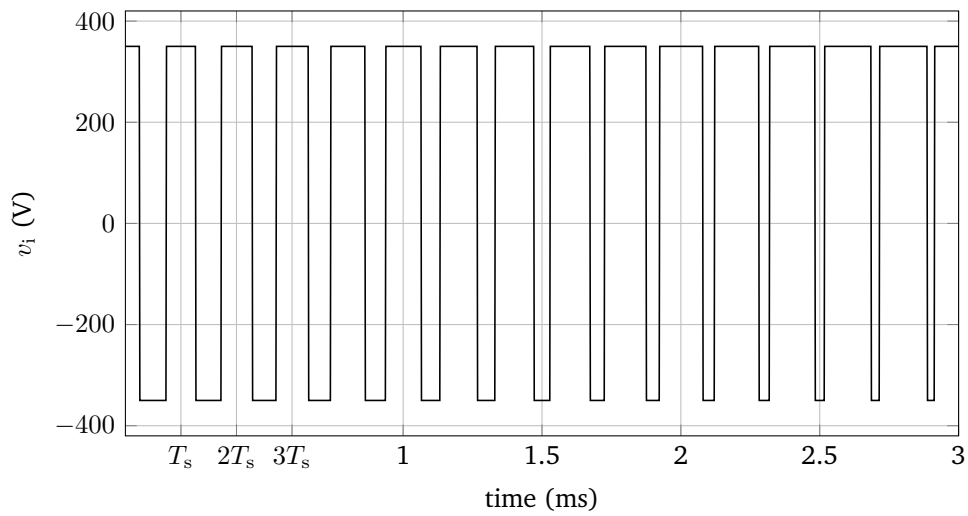
Figure 4.24: Excerpt of the PWM excitation with varying duty cycle and triangle carrier. Both switching instants lie inside the switching interval.
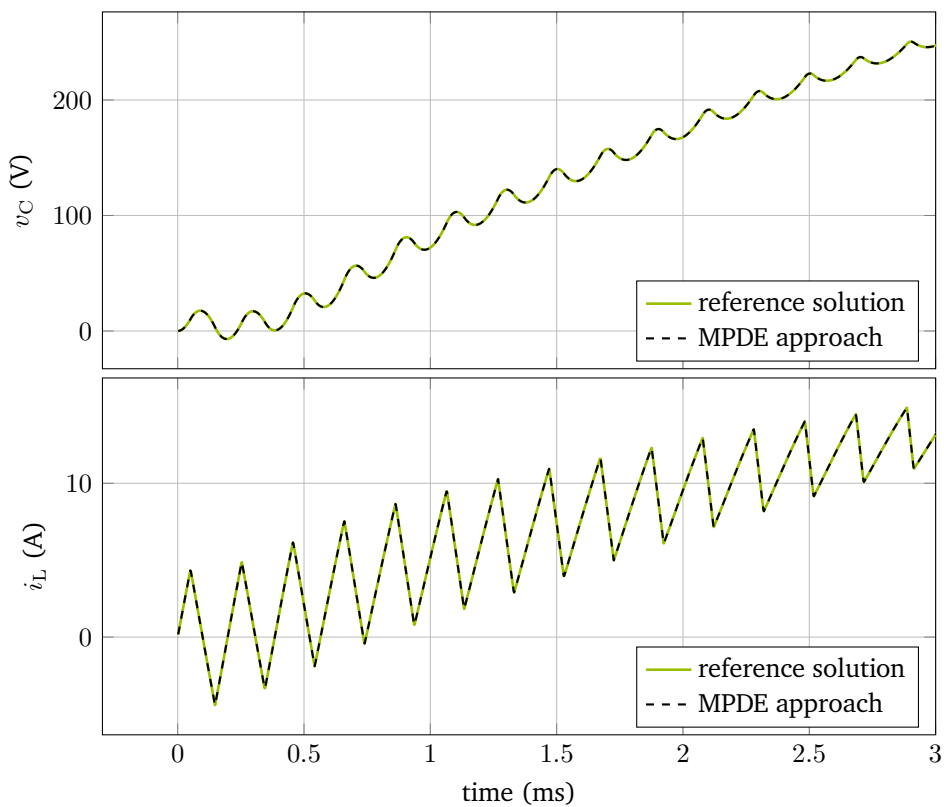
Figure 4.25: Comparison of an excerpt of the MPDE approach and reference solution of the inverter using triangle carrier PWM. The agreement is excellent. (top) voltage at the capacitor, error $\epsilon_v = 7.7 \times 10^{-7}$. (bottom) current through the inductor, error $\epsilon_i = 1.0 \times 10^{-6}$.

4.4.2 Sawtooth carrier PWM with regular sampling

We now test the regular sampling. The reference signal $d(t)$ is again (4.19). The regular sampling PWM excitation can be written as

$$v_{\mathrm{i}}(t, d(t)) = \bar{v}_{\mathrm{i}}\mathrm{sgn}\left(d\left(\left\lfloor \frac{t}{T_{\mathrm{s}}} \right\rfloor T_{\mathrm{s}} \right) - s(t) \right), \tag{4.22}$$

where $\lfloor \cdot \rfloor$ rounds down to the nearest natural number. This means that the reference signal is sampled at the beginning of the switching cycle and held constant throughout the cycle. As carrier we use a sawtooth. To model this in the MPDE approach the delayed reference signal $d_{\mathrm{del}}(t)$ as described in Section 3.5 is used. It can be found by solving the equation (3.112). This can be implemented by adding it as an additional equation to the MPDE approach equation system (3.29), which leads to a nonlinear problem. Here, we use a fixed-point iteration instead, i.e.

$$
\begin{aligned}
d_{\mathrm{del}}^{(1)} &= d(t - T_{\mathrm{s}} d_{\mathrm{del}}^{(0)}) \\
d_{\mathrm{del}}^{(2)} &= d(t - T_{\mathrm{s}} d_{\mathrm{del}}^{(1)}) = d\Big(t - T_{\mathrm{s}} d\big(t - T_{\mathrm{s}} d_{\mathrm{del}}^{(0)}\big)\Big), \\
&\;\;\vdots
\end{aligned}
\tag{4.23}
$$

where we choose $d_{\mathrm{del}}^{(0)} = d(t)$ as the initial value. We abort the iteration after the second step which leads to the estimate $d_{\mathrm{del}}(t) \approx d\big(t - T_{\mathrm{s}} d\big(t - T_{\mathrm{s}} d(t)\big)\big)$. Note that the condition $f_{\mathrm{ac}} < \frac{1}{2\pi} f_{\mathrm{s}}$ needs to be satisfied such that the iteration is convergent. This corresponds to the requirement that the reference signal coincides with the carrier twice per cycle and not more often (in which case more than two switching instants would occur in one switching cycle). Calculations are performed with the same settings as before. Fig. 4.26 shows an excerpt of the MPDE approach and the reference solution. The agreement is very good with errors $\epsilon_v = 8.5 \times 10^{-4}$ and $\epsilon_i = 8.8 \times 10^{-4}$. If higher accuracy is required, more fixed-point iterations may be used or the equation (3.112) may be added as an additional equation into the system of equations. The PWM excitation generated with regular sampling is depicted in Fig. 4.27 along with the excitation generated using natural sampling. Even though the difference is hard to distinguish, the influence on the solution is significant. Running the MPDE approach simulation with the original reference signal (4.19), i.e., ignoring the fact, that regular sampling is used, leads to an error which is approximately 100 times larger than when using the delayed reference signal as above.

4.4.3 Suitability of warped MPDEs for inverter simulation

Let us finally briefly focus on some results determined with the WaMPDEs as described in Section 3.6. For this purpose we consider again the inverter in Fig. 4.18 and use the following parameters for the simulation:

- Switching frequency $f_{\mathrm{s}} = 2000\,\mathrm{Hz}$;

- Sine frequency $f_{\mathrm{ac}} = 50\,\mathrm{Hz}$;

- Simulation interval $\Upsilon = [0, \frac{1}{f_{\mathrm{ac}}}]$;

- Duty cycle for which the basis functions are constructed: $d_0 = 0.5$;

- Electrical elements: $R_{\mathrm{l}} = 10\,\mathrm{m\Omega}$, $L = 10\,\mathrm{mH}$, $C = 5\,\mu\mathrm{F}$, $R = 25\,\Omega$;

- Time integrator `ode15s`: Absolute and relative tolerance $\mathrm{abstol} = \mathrm{reltol} = 10^{-5}$;
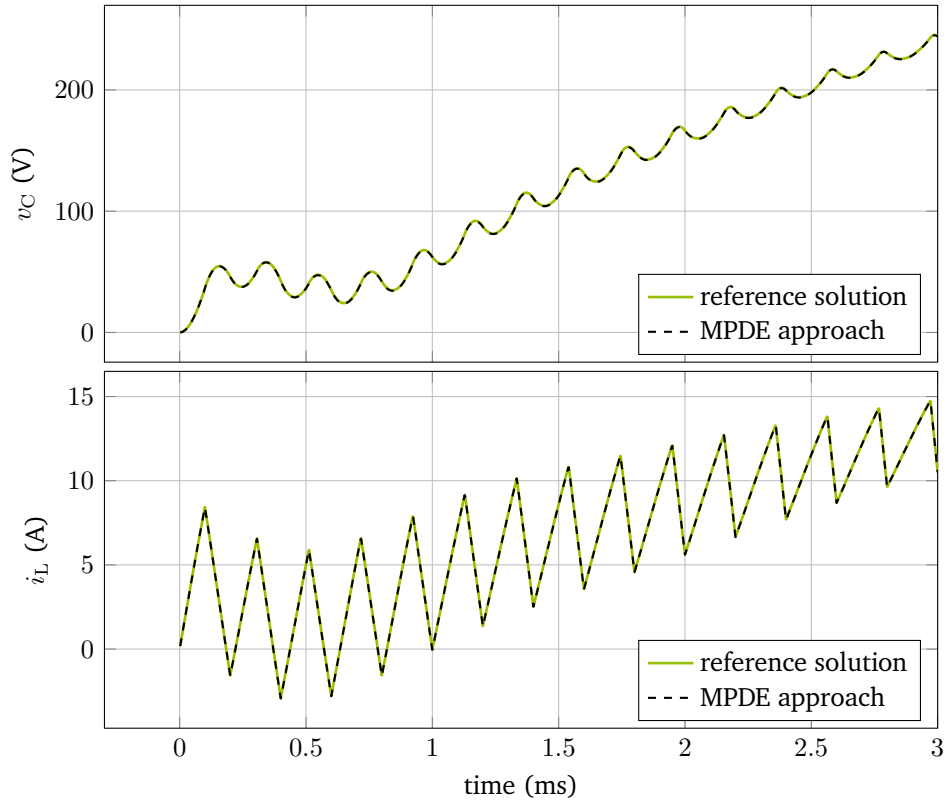
Figure 4.26: Comparison of an excerpt of the MPDE approach and reference solution of the inverter using sawtooth carrier and regular sampling PWM. The agreement is very good. (top) voltage at the capacitor, error $\epsilon_v = 8.5 \times 10^{-4}$. (bottom) current through the inductor, error $\epsilon_i = 8.8 \times 10^{-4}$.
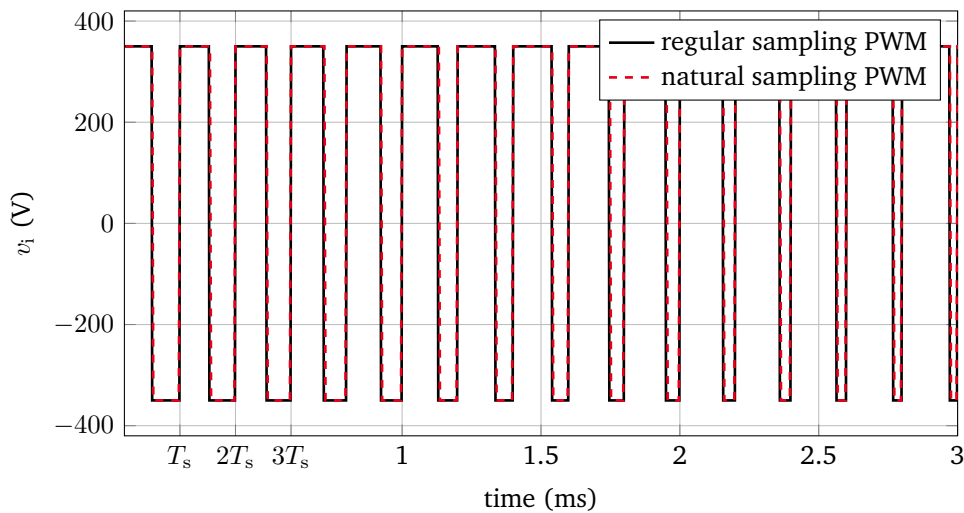
Figure 4.27: Excerpt of the PWM excitation (sawtooth carrier) generated using natural and regular sampling. The switching instants are only slightly different. Nevertheless the difference has a large impact on solution accuracy and has to be considered.
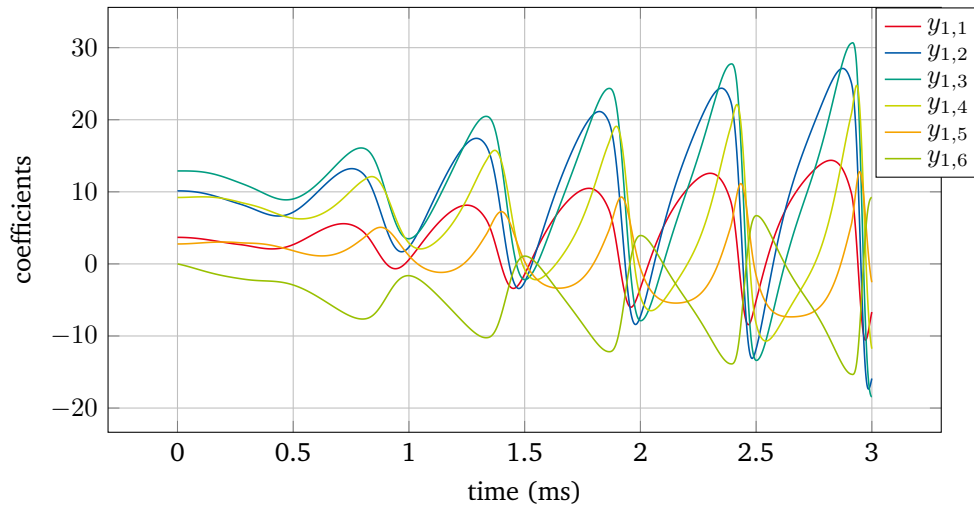
Figure 4.28: Excerpt of the coefficients $\mathbf{y}(t_1)$ for the medium order accuracy B-spline setting ($p = 2$, $K = 1$). Zero Dirichlet coefficients are omitted for the sake of clarity. The coefficients are fast varying.

- Two different B-spline settings:

  1. **Medium order:** $p = 2$, $K = 1$;

  2. **High order:** $p = 4$, $K = 4$.

In Fig. 4.28 an excerpt of the coefficients $\mathbf{y}(t_1)$ are shown for the medium order accuracy B-spline setting. The coefficients vary quickly in the range of the switching frequency f_s. The solver takes 9837 time steps to calculate the solution. The reconstructed solution is compared to a reference solution acquired by conventional time discretization ($\mathrm{abstol} = 10^{-8}$, $\mathrm{reltol} = 10^{-8}$, 38347 time steps). The relative error is around $\epsilon_\mathrm{v} = 9.0 \times 10^{-2}$ for the voltage across the capacitor and $\epsilon_\mathrm{i} = 8.3 \times 10^{-2}$ for the current through the coil. An excerpt of the reconstructed solution along with the reference solution is shown in Fig. 4.29. Improving the B-spline settings leads to better results as expected, see Fig. 4.30. The error is smaller for both the voltage $\epsilon_\mathrm{v} = 3.6 \times 10^{-2}$ and the current $\epsilon_\mathrm{i} = 2.9 \times 10^{-2}$. The number of time steps is 19232 and thus much higher than before. Furthermore the size of the equation systems rises due to the higher number of basis functions. Thus the computational effort increases drastically for only negligible accuracy gains. This makes the WaMPDE approach unsuited for simulation of power converter problems as such. However, if a variation of the switching frequency is required, a combination of the WaMPDE approach and the MPDE approach may be reasonable. This varying switching frequency occurs, e.g. as control strategy in some power converters to improve the reaction time of the converter to varying power needs. Even fast variations in the frequency might be simulated, if they do only occur occassionally. As just seen in the WaMPDE example, the time discretization algorithm is responsible to cover these variations. However the frequency variations would not occur in every switching period and thus the efficiency would only be slightly impaired.

4.5 Inverter with LCL filter

This section focuses on a more elaborate example, namely a DC-AC inverter with an LCL filter and a control circuit as described in [73].
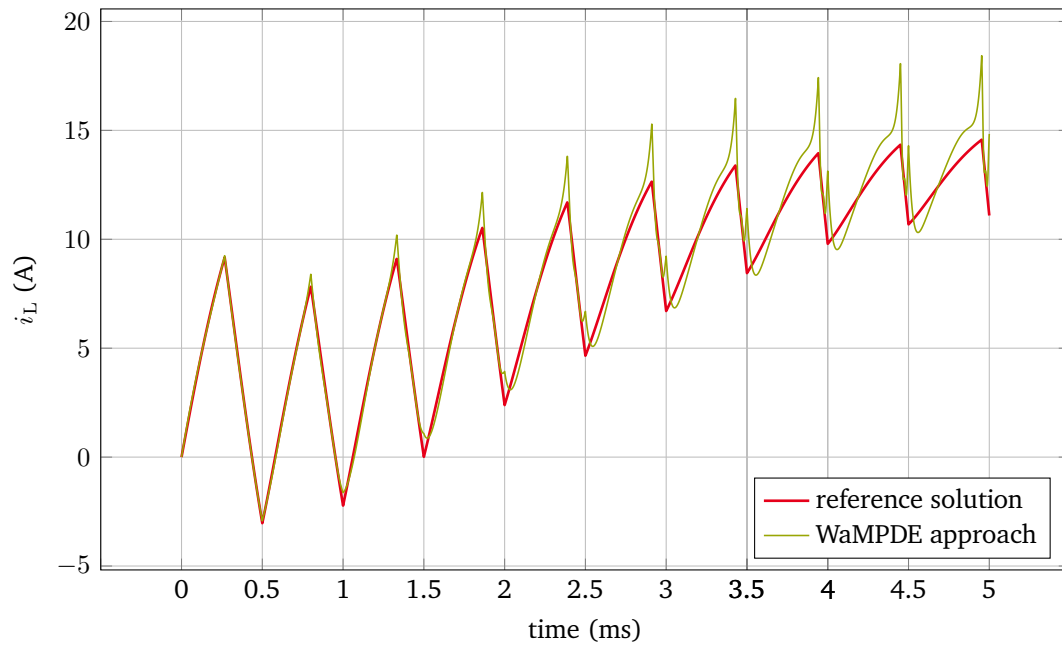
Figure 4.29: Excerpt of the reconstructed solution for the medium order accuracy B-spline setting ($p = 2$, $K = 1$). The stronger the warping of the time is, the more distortions arise in the solution.
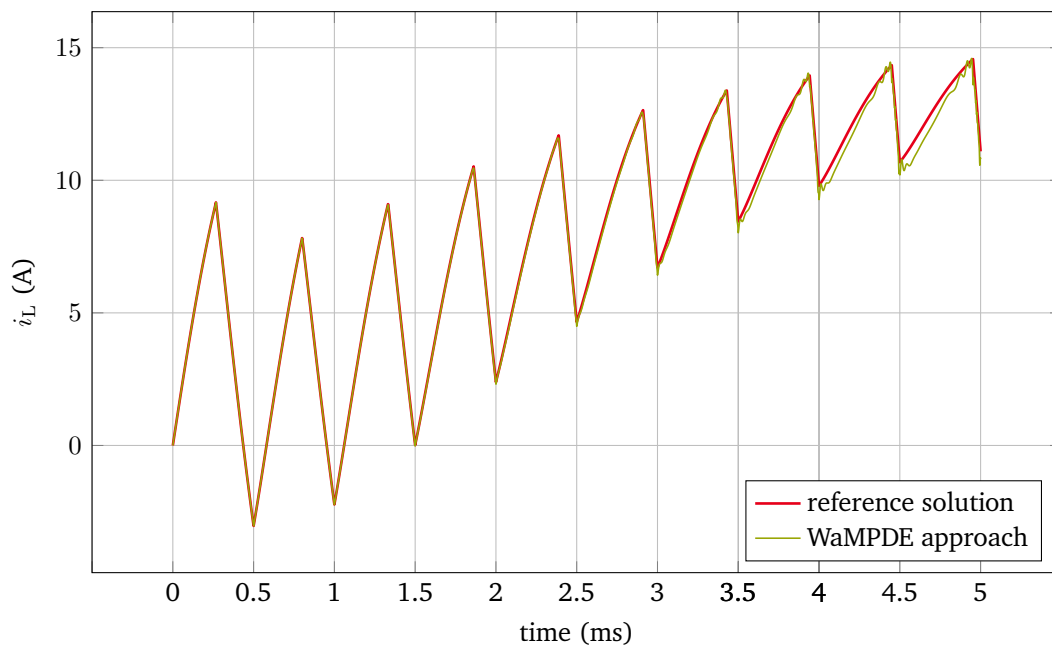
Figure 4.30: Excerpt of the reconstructed solution for the high order accuracy B-spline setting ($p = 4$, $K = 4$). The quality of the solution improves.
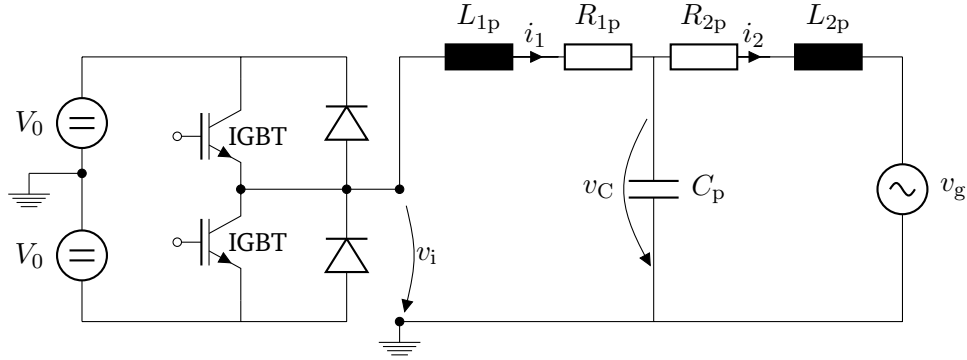
Figure 4.31: DC-AC converter with LCL filter.

The inverter circuit is depicted in Fig. 4.31. It consists of a circuit part generating the pulsed excitation and a filter circuit, in this case an LCL circuit. Furthermore the converter is connected to the power grid which is simulated by the voltage source $v_{\mathrm{g}}(t)$. The LCL filter has a strong resonance which is why already in the generation of the pulsed excitation a control scheme must be employed to achieve a damping of this resonance. What is more, the control scheme should be able to ensure a prescribed current flow $i_{2,\mathrm{ref}}(t)$ into the power grid. The inverter circuit is described by the following set of ODEs [73]

$$\mathbf{A}\frac{\mathrm{d}}{\mathrm{d}t}\mathbf{x}(t) + \mathbf{B}\mathbf{x}(t) = \mathbf{c}(t,d), \tag{4.24}$$

where $\mathbf{A}$ is the identity matrix,

$$\mathbf{B} = \begin{bmatrix} 0 & -\frac{1}{C_{\mathrm{p}}} & \frac{1}{C_{\mathrm{p}}} \\ \frac{1}{L_{1\mathrm{p}}} & \frac{R_{1\mathrm{p}}}{L_{1\mathrm{p}}} & 0 \\ -\frac{1}{L_{2\mathrm{p}}} & 0 & \frac{R_{2\mathrm{p}}}{L_{2\mathrm{p}}} \end{bmatrix}, \tag{4.25}$$

$$\mathbf{x} = \begin{bmatrix} v_{\mathrm{C}} \\ i_1 \\ i_2 \end{bmatrix}, \tag{4.26}$$

and

$$\mathbf{c}(t,d) = \begin{bmatrix} 0 \\ \frac{1}{L_{1\mathrm{p}}}v_{\mathrm{i}}(t,d) \\ -\frac{1}{L_{2\mathrm{p}}}v_{\mathrm{g}}(t) \end{bmatrix}. \tag{4.27}$$

The excitation v_{i} depends on time and additionally on a variable d which sets the duty cycle, i.e.

$$v_{\mathrm{i}}(t,d) = \begin{cases} -V_0 & \text{for } d \leq \tau(t) \leq 1-d \\ V_0 & \text{otherwise} \end{cases} \tag{4.28}$$

The reference signal is calculated during the simulation by the control scheme and can be described by a scalar function of the form [73]

$$d_e\big(\mathbf{x}, i_{2,\mathrm{ref}}, v_{\mathrm{g}}\big) = 0.5 + \big(\mathbf{T}_1\,\mathbf{x}(t) + T_2\,i_{2,\mathrm{ref}}(t) + T_3\,v_{\mathrm{g}}\big) \tag{4.29}$$

where $\mathbf{T}_1 \in \mathbb{R}^{1\times 3}$ is a row vector and $T_2, T_3 \in \mathbb{R}$ are constants. The reference signal consequently depends linearly on the instantaneous state variables $\mathbf{x}$, the desired current $i_{2,\mathrm{ref}}$ which should be fed into the power grid and the grid voltage v_{g}. The environment in which the PWM excitation is generated is digital, therefore

a regular sampling is employed, i.e. the reference signal $d_e(\mathbf{x}, i_{2,\mathrm{ref}}, v_{\mathrm{g}})$ is sampled once at the beginning of each switching cycle and held constant throughout the cycle. For more information on how the control scheme is designed the reader is referred to [73]. To model this in the MPDE approach, according to Section 3.5, the regular sampling duty cycle d_{del} is calculated and since a triangle carrier is used two variables $d_{\mathrm{del,1}}$ and $d_{\mathrm{del,2}}$ are introduced for the simulation, see Subsection 3.2.1. These variables denote the position of the switching instants. Consequently the multivariate right-hand side of the MPDEs (3.11) is setup as

$$\widehat{\mathbf{c}}(t_1, t_2, d_{\mathrm{del,1}}, d_{\mathrm{del,2}}) = \begin{bmatrix} 0 \\ \frac{1}{L_{\mathrm{1p}}}\widehat{v}_{\mathrm{i}}(t_1, t_2, d_{\mathrm{del,1}}, d_{\mathrm{del,2}}) \\ -\frac{1}{L_{\mathrm{2p}}}v_{\mathrm{g}}(t_1) \end{bmatrix} \tag{4.30}$$

with

$$\widehat{v}_{\mathrm{i}}(t_1, t_2, d_{\mathrm{del,1}}, d_{\mathrm{del,2}}) = \begin{cases} -V_0 & \text{for } d_{\mathrm{del,1}} \leq \tau(t_2) \leq d_{\mathrm{del,2}} \\ V_0 & \text{otherwise.} \end{cases} \tag{4.31}$$

As one can see the switching from the excitation v_{i} evolves along the fast time scale t_2. The grid voltage v_{g} is a slowly varying quantity compared with the switching, therefore we choose to let it evolve along the slow time scale t_1. For the current $i_{2,\mathrm{ref}}$ we assume the same. The equation system describing the problem after the MPDE approach is given by

$$(\mathbf{A} \otimes \boldsymbol{\mathcal{J}}(d_{\mathrm{del,1}}, d_{\mathrm{del,2}}))\frac{\mathrm{d}\mathbf{y}(t_1)}{\mathrm{d}t_1} + \Bigg(\mathbf{B} \otimes \boldsymbol{\mathcal{J}}(d_{\mathrm{del,1}}, d_{\mathrm{del,2}}) + \mathbf{A} \otimes \boldsymbol{\mathcal{Q}}(d_{\mathrm{del,1}}, d_{\mathrm{del,2}})$$

$$+ \frac{\mathrm{d}d_{\mathrm{del,2}}}{\mathrm{d}t_1}\mathbf{A} \otimes \boldsymbol{\mathcal{U}}(d_{\mathrm{del,1}}, d_{\mathrm{del,2}}) \tag{4.32}$$

$$- \frac{\mathrm{d}d_{\mathrm{del,1}}}{\mathrm{d}t_1}\Big(\mathbf{A} \otimes \boldsymbol{\mathcal{U}}(d_{\mathrm{del,1}}, d_{\mathrm{del,2}}) + T_{\mathrm{s}}\mathbf{A} \otimes \boldsymbol{\mathcal{Q}}(d_{\mathrm{del,1}}, d_{\mathrm{del,2}})\Big)\Bigg)\mathbf{y}(t_1)$$

$$= \boldsymbol{\mathcal{C}}(d_{\mathrm{del,1}}, d_{\mathrm{del,2}}, t_1),$$

which is fed with the regular sampling variables $d_{\mathrm{del,1}}$ and $d_{\mathrm{del,2}}$. The variables d_1, d_2, $d_{\mathrm{del,1}}$ and $d_{\mathrm{del,2}}$ are modeled as unknowns in the equation system and determined by additional equations (see Section 3.5)

$$d_1 - 0.5d_{\mathrm{e}}\big(\mathbf{e}_{\mathrm{env}}(\mathbf{y}, d_1, d_2), i_{2,\mathrm{ref}}(t), v_{\mathrm{g}}(t)\big) = 0, \tag{4.33}$$

$$d_2 - 1 + 0.5d_{\mathrm{e}}\big(\mathbf{e}_{\mathrm{env}}(\mathbf{y}, d_1, d_2), i_{2,\mathrm{ref}}(t), v_{\mathrm{g}}(t)\big) = 0, \tag{4.34}$$

$$\frac{\mathrm{d}d_1}{\mathrm{d}t_1} = \frac{1}{d_{\mathrm{del,1}}T_{\mathrm{s}}}d_1 - \frac{1}{T_{\mathrm{s}}}, \tag{4.35}$$

$$\frac{\mathrm{d}d_2}{\mathrm{d}t_1} = \frac{1}{d_{\mathrm{del,2}}T_{\mathrm{s}}}d_2 - \frac{1}{T_{\mathrm{s}}}, \tag{4.36}$$

where $\mathbf{e}_{\mathrm{env}}(\mathbf{y}, d_1, d_2)$ is a function evaluating the solution at the beginning of the switching cycle, i.e., at $t_2 = n\,T_{\mathrm{s}}$, $n \in \{0, 1, 2, \ldots\}$. It is consequently given by

$$\mathbf{e}_{\mathrm{env}}(\mathbf{y}, d_1, d_2) = \sum_{k=0}^{N_{\mathrm{p}}} y_{j,k}(t_1)\, w_k\Big(0 + \tau\big(-d_1(t_1)T_{\mathrm{s}}\big), d_2(t_1) - d_1(t_1)\Big). \tag{4.37}$$

The equation system resulting from (4.32) – (4.36) is a system of DAEs. It can be written as

$$\mathbf{A}_{\mathrm{lcl}}(\mathbf{x}_{\mathrm{lcl}})\frac{\mathrm{d}\mathbf{x}_{\mathrm{lcl}}(t_1)}{\mathrm{d}t_1} + \mathbf{B}_{\mathrm{lcl}}(\mathbf{x}_{\mathrm{lcl}})\,\mathbf{x}_{\mathrm{lcl}}(t_1) = \mathbf{c}_{\mathrm{lcl}}(t_1, \mathbf{x}_{\mathrm{lcl}}), \quad \mathbf{x}_{\mathrm{lcl}}(0) = \mathbf{x}_{\mathrm{lcl}}^{(0)} \tag{4.38}$$

where

$$\mathbf{x}_{\mathrm{lcl}} = \begin{bmatrix} \mathbf{y} \\ d_1 \\ d_2 \\ d_{\mathrm{del},1} \\ d_{\mathrm{del},2} \end{bmatrix} \in \mathbb{R}^{N_{\mathrm{s}}(N_{\mathrm{p}}+1)+4} \tag{4.39}$$

is the vector of unknowns, and $\mathbf{A}_{\mathrm{lcl}}$, $\mathbf{B}_{\mathrm{lcl}}$ and $\mathbf{c}_{\mathrm{lcl}}$ are set up from equations (4.32) – (4.36).

Simulations were performed on an Intel Core i5-5200U with 2.2 GHz and 16 GB RAM. The following model parameters are employed:

- Switching frequency $f_{\mathrm{s}} = 16000\,\mathrm{Hz}$;

- Sine frequency $f_{\mathrm{ac}} = 50\,\mathrm{Hz}$;

- Simulation interval $T_{\mathrm{I}} = [0, 4\frac{1}{f_{\mathrm{ac}}}]$;

- Electrical elements: $L_{1\mathrm{p}} = 900 \times 10^{-6}\,\mathrm{H}$, $R_{1\mathrm{p}} = 10^{-5}\,\Omega$, $L_{2\mathrm{p}} = 930 \times 10^{-6}\,\mathrm{H}$, $R_{2\mathrm{p}} = 10^{-5}\,\Omega$, $C_{\mathrm{p}} = 10 \times 10^{-6}\,\mathrm{F}$;

- Grid voltage $v_{\mathrm{g}}(t) = 325\cos(2\pi f_{\mathrm{ac}}t)$ (corresponds to 230 V rms);

- Input DC voltage $V_0 = 400\,\mathrm{V}$;

- Desired output current $i_{2,\mathrm{ref}} = (2 + 3S(t))\cos(2\pi f_{\mathrm{ac}}t)$, where $S(t) = \frac{1}{1+\mathrm{e}^{-a(t-c)}}$ is the sigmoid function with $a = 10000$, $c = 2\frac{1}{f_{\mathrm{ac}}}$. As a result the current changes during the simulation.

To start the simulation directly in steady state a reasonable and efficient choice of initial values is given by the steady state of the problem at time $t_1 = 0$, i.e. the solution of the equation system

$$\mathbf{B}_{\mathrm{lcl}}(\mathbf{x}_{\mathrm{lcl}}^{(0)})\,\mathbf{x}_{\mathrm{lcl}}^{(0)} = \mathbf{c}_{\mathrm{lcl}}(0, \mathbf{x}_{\mathrm{lcl}}^{(0)}). \tag{4.40}$$

The results are compared to a reference solution calculated with conventional time discretization and very fine tolerance ($\mathrm{abstol} = 10^{-10}$, $\mathrm{reltol} = 10^{-10}$). The MATLAB function `ode15s` is used for time discretization. The simulation is started with zero initial values. After one sine period $\frac{1}{f_{\mathrm{ac}}}$ the simulation is in steady state. From this moment on the results are used for comparison to the MPDE approach. To detect switch events, the solver's event function is used and the solver is restarted after each switch event. To avoid missing switch events during the simulation the "MaxStep" and "InitialStep" options of the solver are both set to $\frac{T_{\mathrm{s}}}{12}$, which corresponds to a minimum/maximum duty cycle of around 8.33% / 91.66%. The relative error (4.2) is employed as measure of solution quality. Figs. 4.33a, 4.34a, and 4.32a depict current through the coils and voltage at the capacitor. Using the settings

- Tolerance $\mathrm{abstol} = \mathrm{reltol} = 5 \times 10^{-4}$,

- B-splines $p = 2$, $K = 2$,

Table 4.5: Error and statistical data of the MPDE approach and conventional time discretization. For conventional time discretization the computational effort to reach steady state is included. The last column denotes the speedup of the MPDE approach compared with time discretization in MATLAB and Simulink.

	MPDE	MATLAB	Simulink	speedup
ϵ_{v_C}	4.53×10^{-4}	1.4×10^{-3}	1×10^{-3}	/
ϵ_{i_1}	7.9×10^{-3}	1.3×10^{-2}	2.8×10^{-3}	/
ϵ_{i_2}	1.2×10^{-2}	1.6×10^{-2}	2.4×10^{-2}	/
time steps	263	47231	33236	180 resp. 126
failed steps	55	19713	n/a	358
fun. eval.	670	138688	n/a	207
LU decom.	104	37290	n/a	359
time to solution (approx.)	2s	76s	1.5s	38 resp. 0.75

for the MPDE approach, the error ϵ between the MPDE solution and the reference solution is in the order of 10^{-3} and listed in Table 4.5 for all three quantities (inductor currents and capacitor voltage). Furthermore the statistics provided by the `ode15s` solver are shown. A zoom-in into the solutions is depicted in Figs. 4.32b, 4.33b, and 4.34b and shows that the agreement of the MPDE solution and the reference solution even in the area of the changing load is reasonably good. Since the load change occurs in the slow time scale t_1, the coefficients **y** vary in this region.

To assess the efficiency of the approach, a conventional time discretization is used to obtain a solution with an error in the same order of magnitude towards the reference solution as the MPDE approach. The exact values are listed in Table 4.5 including statistics. In all quantities the MDPE approach is highly efficient compared with conventional time discretization. It has to be noted that the actual time to solution is dependent on the efficiency of the implementation and programming language. For validation we compared the MPDE approach as implemented also with a Simulink simulation with the accuracy as given in Table 4.5. Even though Simulink is highly optimized for the task and the MPDE approach is implemented in MATLAB without focusing on efficiency of the implementation, the MPDE approach is still in the same range of time to solution as Simulink.

The MPDE approach works well for this realistic problem, although

- the differential index of equation system (4.38) is not easy to analyze due to the controlled PWM excitation. If the index is higher than 1, the solution becomes more challenging. Numerical difficulties have been observed when time integrating (4.38) with finer time integrator tolerance than employed in this example.

- the delayed reference signals $d_{\mathrm{del},1}$ and $d_{\mathrm{del},2}$ are calculated by a first order approximation as proposed in Section 3.5 which introduces an error in the solution. This error has not been examined.

- it was assumed that the grid voltage and the reference current evolve along the slow time scale t_1. However it is unclear if this choice is justified.
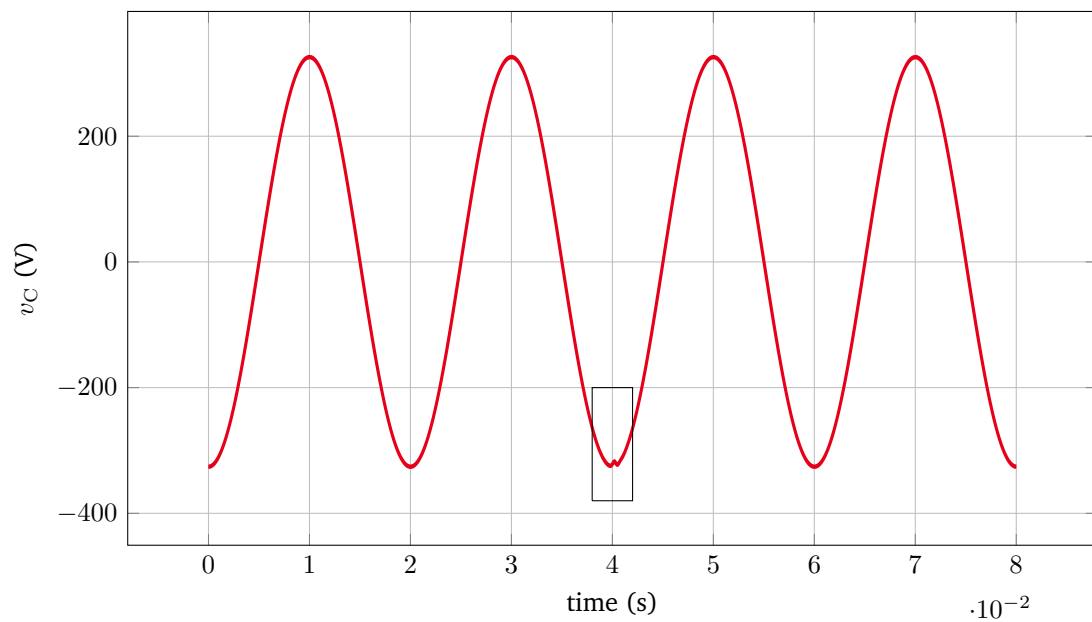
(a)
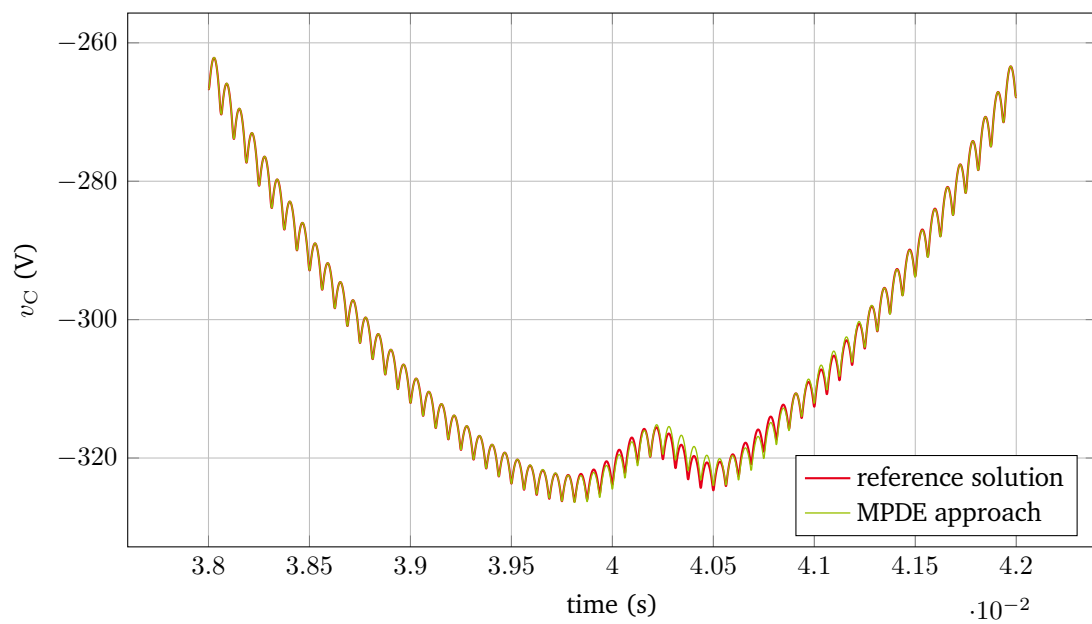
(b)

Figure 4.32: (a) Voltage at the capacitor. The ripples are not visually distinguishable due to the high switching frequency. (b) Zoom-in into the region marked in (a).
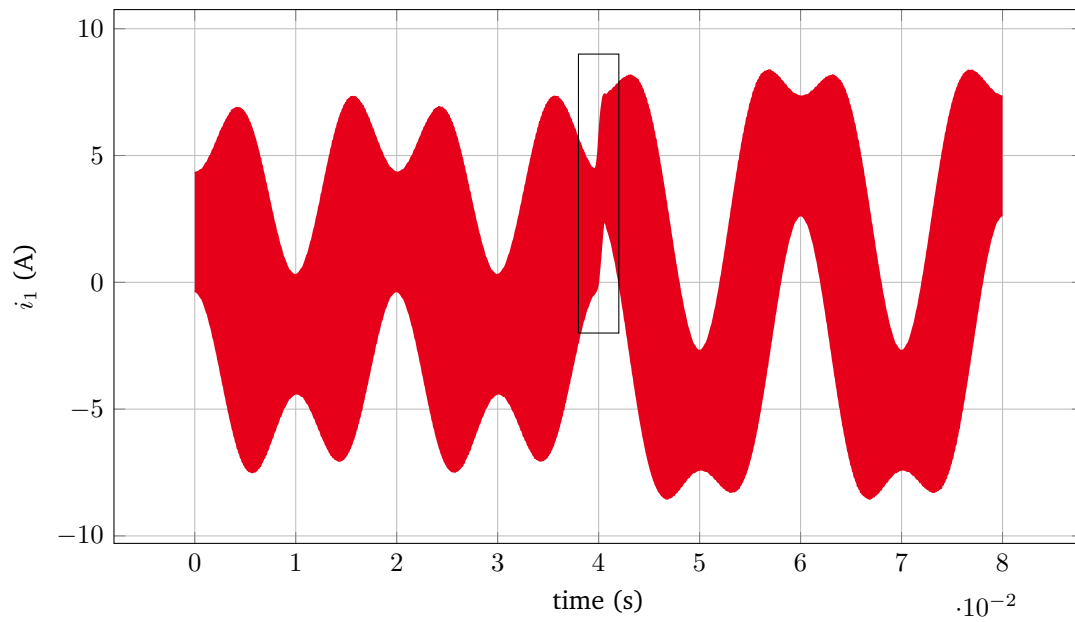
(a)
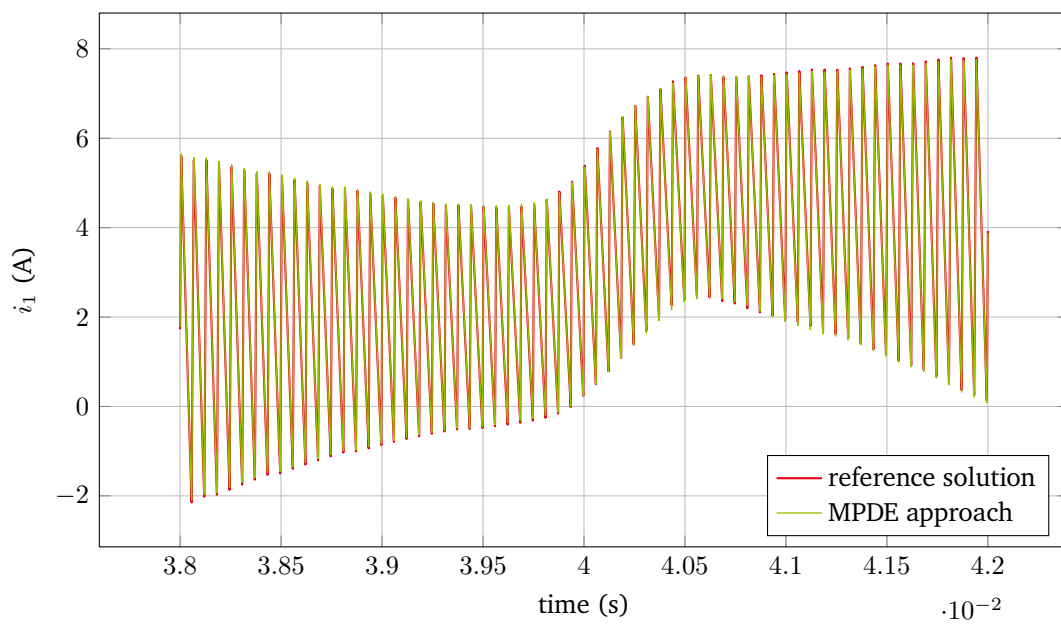
(b)

Figure 4.33: (a) Current through inductor 1. The ripples are not visually distinguishable due to the high switching frequency. (b) Zoom-in into the region marked in (a).
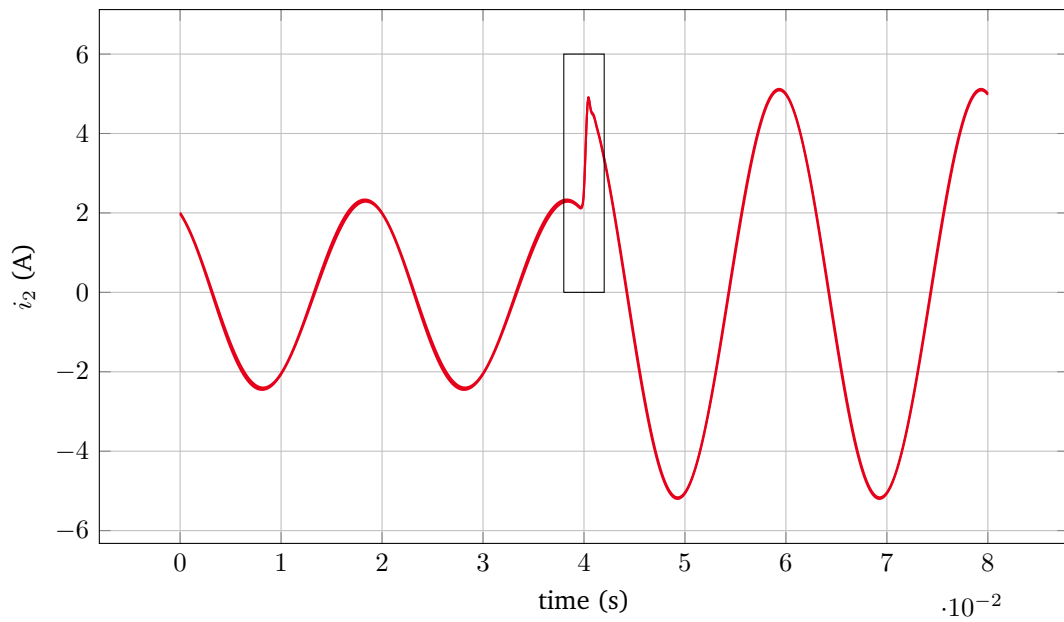
(a)
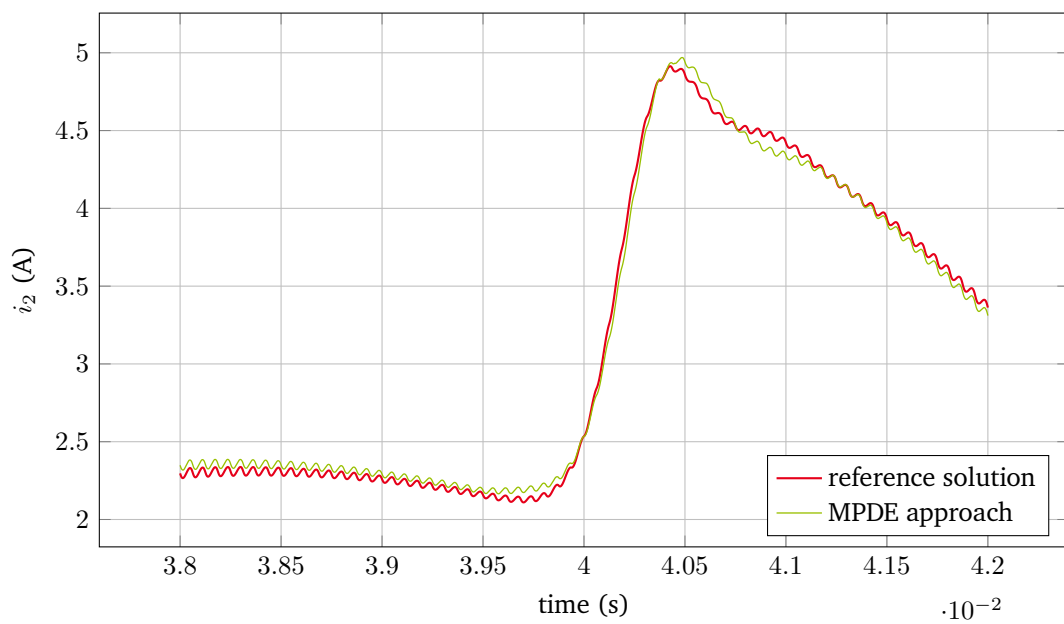
(b)

Figure 4.34: (a) Current through inductor 2. The ripples are not visually distinguishable due to the high switching frequency. (b) Zoom-in into the region marked in (a).

4.6 Conclusion

The MPDE approach has been numerically validated in this chapter. Its accuracy and efficiency has been assessed. The results indicate that the MPDE approach is much more efficient than conventional time discretization while reaching a comparable accuracy. Since the MPDE approach approximates the fast variations in the solution by basis functions, the subsequent time integration of the resulting differential equations takes much less time steps than solving the original differential equations to reach the same accuracy. Furthermore it is switching frequency independent. The MPDE approach enlarges the systems of equations which is a disadvantage and leads to higher computational effort per time step. There are cases in which this disadvantage outweighs the advantage of less time steps. As a result the MPDE approach becomes inefficient compared to conventional time discretization. These cases occur when either many basis functions are required to properly approximate the ripples or when the original equation systems are already very large, e.g. for field-circuit coupled problems. For linear DC-DC converters this issue is remedied by using the PWM eigenfunctions which allow for a decoupling of the equations. As a result, the approach may be parallelized. The MPDE approach is also applicable to nonlinear problems. A challenge is the efficient reevaluation of the integrals resulting from the MPDE approach in each time step. The proposed simplification of using only the envelope to evaluate the nonlinearity leads to excellent results if the ripple is small compared to the envelope.

5 Conclusion and prospects for future research

In this work the concept of MPDEs for the simulation of PWM power converters has been investigated. In a first step the ODEs or DAEs describing the circuit or field-circuit coupled model of the power converter are reformulated into MPDEs. In this process the solution is split into components which vary with different rates in time. These components are associated to different artificial time scales. The periodic ripples in the power converter output are associated with a fast time scale while transient responses, e.g. the start-up transient or the sinusoidal output voltage in inverters, are associated with a slow time scale. This is realized by expanding the solution into a sum of basis functions depending on the fast time scale and coefficients depending on the slow time scale. The switching inside the power converter transistors is idealized and modeled by a pulsed voltage source which is taken into account on the right-hand side of the system of equations. The MPDEs are solved using a combination of a Galerkin approach for the fast time scale and a conventional time integration algorithm for the slow time scale. After solving, the solution of the original ODEs/DAEs can be easily extracted, in the simplest case, by evaluating the 2D computation domain along a diagonal line.

Applying the Galerkin approach to the fast time scale leads to a system of ODEs/DAEs which are $N_p + 1$ times larger than the original system of differential equations, where $N_p + 1$ is the total number of basis functions which are employed in the solution expansion. It turns out that the subsequent time integration after semi-discretization needs much less time steps than a time integration applied to the original ODEs/DAEs describing the power converter. This is due to the fact that the fast varying ripples are already taken into account by the basis functions (through the Galerkin approach) and thus only a slowly varying smooth envelope needs to be resolved by the time integration.

Nonlinearities, e.g. those which stem from material saturation in inductors, increase the computational effort of the approach since in every time step along the slow time scale integrals with respect to the fast time scale have to be solved. To circumvent this, one can neglect the fast periodically varying ripples in the evaluation of the nonlinearity and use only the envelope for this purpose. Especially when the magnitude of the ripples is small compared to the magnitude of the envelope this approach is valid and accurate.

The basis functions used in the solution expansion of the Galerkin approach are periodic with period corresponding to one switching cycle. They take the C^0 continuity of the inductor current ripple into account by construction. This procedure was first proposed by Gyselinck et al. [41]. For DC-AC power converters the duty cycle of the PWM excitation varies slowly during the simulation. This is taken into account in the basis functions. If a sawtooth carrier and natural sampling are used to generate the PWM excitation one switching instant always lies at the beginning/end of a switching cycle while the other switching instant varies inside the switching cycle to account for the proper duty cycle. When using PWM excitation with triangle carrier and natural sampling, both switching instants lie inside the switching cycle and they both vary with changing duty cycle. To take this into account and still be able to use the same basis functions, the basis functions are appropriately shifted in time. The possibility to use PWM generated by a regular

sampling (i.e. sampling the reference signal at the beginning of each switching cycle) is accounted for by proposing a delayed reference signal. This delayed reference signal is calculated through a nonlinear equation from the reference signal. In this case the MPDE approach system of equations is supplied with the delayed reference signal instead of the original reference signal. Three different types of basis functions have been investigated:

1. PWM basis functions proposed by Gyselinck et al. [41]: These basis functions are particularly well suited for linear DC-DC power converter simulation since they are a spectral basis and need only a small number of basis functions for excellent results.

2. PWM eigenfunctions: These basis functions are obtained through a basis transformation from the PWM basis functions. They allow for a decoupling of the system of equations in the case of linear DC-DC power converters. As a result, they are well suited for field-circuit coupled problems in which the systems of equations are large.

3. B-spline basis functions: These basis functions are well suited in DC-AC power converter simulation since the dependency of the arising matrices on the duty cycle is linear, which enables an efficient evaluation and assembly of the matrices in the solution process. Degree elevation or a mixture of degree elevation and h-refinement is suggested to keep the number of basis functions small while achieving high accuracy. In case of degree elevation, the convergence is exponential. Classical FE nodal functions are B-splines of degree 1. They are easy to implement but come with the drawback that many of them are required to obtain an accurate solution.

The MPDE approach has been applied to different examples to demonstrate its accuracy and efficiency, namely a DC-DC buck converter with and without field-circuit coupling and two DC-AC inverter. The results indicate that the accuracy of the MPDE approach is excellent and depends on two parameters. First, the number of basis functions employed in the solution process. This number determines the discretization accuracy in the fast time scale. Secondly, the number of time steps or the time integrator tolerance (using a time discretization algorithm with adaptive time steps). This determines the discretization accuracy along the slow time scale. There is an optimal combination between both parameters which depends on the application example. The overall solution accuracy is always limited by the worst discretization accuracy on either time scale.

The efficiency of the MPDE approach also depends on different aspects. On the one hand, the number of basis functions determines the size of the semi-discretized systems of equations. If these are larger and cannot be decoupled, more time is spent in each time step along the slow time scale since a larger system of equations needs to be solved. On the other hand, the time integration algorithm needs significantly less time steps along the slow time scale compared with a conventional time discretization of the original system of equations describing the power converter. Therefore if the advantage of much less time steps outweighs the disadvantage of greater size of the equation systems, the approach is efficient. If a monolithic field-circuit coupling is applied, the original ODEs/DAEs are already very large. In such a case the disadvantage of further enlarging the systems of equations through the Galerkin approach is more significant. The solution is challenging and has been tackled by using the PWM eigenfunctions to decouple the equation systems which allows for a parallel solution. Another important aspect which determines the efficiency is the choice of initial values for the ODEs/DAEs arising after the semi-discretization with the Galerkin approach. A reasonable choice in case of linear problems has been proposed. In case of nonlinear problems, the choice is considerably more difficult.

The accomplishments of this work have demonstrated that the MPDE approach applied to power converter simulation is a promising alternative for conventional time discretization. To further enlarge the

number of possible applications of the MPDE approach, the following steps for future research are suggested:

- Investigation of dedicated solvers for the linear systems of equations arising in the MPDE approach with linear complexity. This would highly contribute to the efficiency of the method, since at the moment this is one of the main bottlenecks when the original systems of equations are large, e.g., with field-circuit coupling. Algebraic multigrid methods might be useful here [113].

- Further investigation on optimized choices of initial values. For nonlinear problems this becomes considerably more difficult than in the linear case. A particular approximation has been proposed in [99].

- Investigation of a combination of the MPDE approach with Parareal [36, 58, 63], for example to solve the slowly varying envelope by parallel-in-time integration.

- An automatic choice of the optimal combination of time integrator tolerance and number of basis functions.

- Investigation of examples in which additional time-variant electrical elements are present and how to model them in the MPDE approach. The inverter with LCL filter, see Subsection 4.5 is such an example.

- Extension of the method to support other modulations, e.g. pulse-frequency modulation (PFM), or mixtures of modulations. The concept of WaMPDEs may be useful for this purpose.

- Extension of the method for the simulation of multi-phase power converters.

- Determination of the suitability of the PWM basis functions and PWM eigenfunctions for varying duty cycle applications.

6 Appendix

6.1 Proof of theorem 1

The relation can easily be proven by applying the chain rule of differentiation which yields [10, 97]

$$\left[\mathbf{A}(\mathbf{x})\frac{\mathrm{d}}{\mathrm{d}t}\mathbf{x}(t)\right]\bigg|_{t=t_0} \overset{(3.6)}{=} \left[\mathbf{A}(\widehat{\mathbf{x}})\frac{\mathrm{d}}{\mathrm{d}t}\widehat{\mathbf{x}}(t+\widehat{\alpha}_1,\ldots,t+\widehat{\alpha}_m)\right]\bigg|_{t=t_0} \tag{6.1}$$

$$= \left[\mathbf{A}(\widehat{\mathbf{x}})\left(\frac{\partial\widehat{\mathbf{x}}(t_1,\ldots,t_m)}{\partial t_1}+\ldots+\frac{\partial\widehat{\mathbf{x}}(t_1,\ldots,t_m)}{\partial t_m}\right)\right]\bigg|_{t_1=t_0+\widehat{\alpha}_1,\ldots,t_m=t_0+\widehat{\alpha}_m} \tag{6.2}$$

$$\overset{(3.4)}{=} \widehat{\mathbf{c}}(t_0+\widehat{\alpha}_1,\ldots,t_0+\widehat{\alpha}_m)-\mathbf{B}(\widehat{\mathbf{x}})\,\widehat{\mathbf{x}}(t_0+\widehat{\alpha}_1,\ldots,t_0+\widehat{\alpha}_m) \tag{6.3}$$

$$\overset{(3.6),(3.7)}{=} \mathbf{c}(t_0)-\mathbf{B}(\mathbf{x})\,\mathbf{x}(t_0) \tag{6.4}$$

6.2 Proofs for PWM basis functions

The following proof and remarks in this section are taken from [80][1]. For the sake of readability the PWM basis functions are denoted by w_i instead of $w_{\mathrm{pwm},i}$.

6.2.1 Proof of theorem 2

The basis functions $w_i(\tau)\,\forall\,i\in\mathbb{N}$ with duty cycle $D=0.5$ are defined as follows: The zeroth and first basis function are given piecewise as

$$w_0(\tau)=1\,\forall\,\tau\in[0,1], \tag{6.5}$$

and

$$w_1(\tau)=\left\{\begin{array}{ll} w_{1,\mathrm{a}}(\tau)=\sqrt{3}(4\tau-1), & \forall\,\tau\in[0,0.5) \\ w_{1,\mathrm{b}}(\tau)=\sqrt{3}(-4\tau+3), & \forall\,\tau\in[0.5,1] \end{array}\right., \tag{6.6}$$

which essentially corresponds to a scaled and translated hat function. The subscript letter refers to the interval in which the basis function is defined, i.e., if "a", the polynomial in $\tau\in[0,0.5)$ is considered, if "b" the polynomial in $\tau\in[0.5,1]$ is considered. If the subscript comprises only a number, the entire basis function is addressed.

---

[1] ©2019 IEEE. Reprinted, with permission, from [80]

The symmetry of the basis function $w_1(\tau)$ can be expressed as follows

$$
\begin{aligned}
-w_{1,\mathrm{a}}(\tau) &= w_{1,\mathrm{b}}(\tau + 0.5) & \forall\, \tau \in (0, 0.5) \\
-w_{1,\mathrm{a}}(\tau) &= w_{1,\mathrm{a}}(0.5 - \tau) & \forall\, \tau \in (0, 0.5)\,. \\
w_{1,\mathrm{a}}(\tau) &= w_{1,\mathrm{b}}(1 - \tau) & \forall\, \tau \in (0, 0.5)
\end{aligned}
\tag{6.7}
$$

The basis functions of higher order, i.e., $i = 2, 3, 4, \ldots$ are calculated by integrating the basis functions of lower order

$$
w_{i,\mathrm{a}}^{\star}(\tau) = \int_{0.5}^{\tau} w_{i-1,\mathrm{a}}(\eta)\; \mathrm{d}\eta\,,
\tag{6.8}
$$

$$
w_{i,\mathrm{b}}^{\star}(\tau) = \int_{0.5}^{\tau} w_{i-1,\mathrm{b}}(\eta)\; \mathrm{d}\eta\,,
\tag{6.9}
$$

and orthogonalizing the integrated basis functions against the constant basis function $w_0(\tau)$. The basis function $w_{i,\mathrm{a}}$ therefore is

$$
\begin{aligned}
w_{i,\mathrm{a}}(\tau) &= w_{i,\mathrm{a}}^{\star}(\tau) - \underbrace{\frac{w_0(\tau)}{\sqrt{\int_0^1 w_0(\eta) w_0(\eta)\, \mathrm{d}\eta}}}_{=1} \int_0^1 w_{i,\mathrm{a}}^{\star}(\eta)\, \underbrace{w_0(\eta)}_{=1}\, \mathrm{d}\eta \\
&= w_{i,\mathrm{a}}^{\star}(\tau) - \int_0^1 w_{i,\mathrm{a}}^{\star}(\eta)\, \mathrm{d}\eta \\
&= \int_{0.5}^{\tau} w_{i-1,\mathrm{a}}(\eta)\, \mathrm{d}\eta - \int_0^1 \int_{0.5}^{\tau} w_{i-1}(\eta)\, \mathrm{d}\eta\, \mathrm{d}\tau \\
&= \int_{0.5}^{\tau} w_{i-1,\mathrm{a}}(\eta)\, \mathrm{d}\eta - \int_0^{0.5} \int_{0.5}^{\tau} w_{i-1,\mathrm{a}}(\eta)\, \mathrm{d}\eta\, \mathrm{d}\tau \\
&\quad - \int_{0.5}^{1} \int_{0.5}^{\tau} w_{i-1,\mathrm{b}}(\eta)\, \mathrm{d}\eta\, \mathrm{d}\tau.
\end{aligned}
\tag{6.10}
$$

Similarly $w_{i,\mathrm{b}}$ is given as

$$
\begin{aligned}
w_{i,\mathrm{b}}(\tau) &= \int_{0.5}^{\tau} w_{i-1,\mathrm{b}}(\eta)\, \mathrm{d}\eta - \int_0^{0.5} \int_{0.5}^{\tau} w_{i-1,\mathrm{a}}(\eta)\, \mathrm{d}\eta\, \mathrm{d}\tau \\
&\quad - \int_{0.5}^{1} \int_{0.5}^{\tau} w_{i-1,\mathrm{b}}(\eta)\, \mathrm{d}\eta\, \mathrm{d}\tau.
\end{aligned}
\tag{6.11}
$$

Note that orthonormalization of all basis functions against each other is possible and has been originally proposed in [41]. However, it spans the same space as the basis functions without full orthonormalization (6.10),(6.11), and is therefore neglected.

The symmetry properties of the basis functions as defined by (6.6)-(6.11) with duty cycle $D = 0.5$ are examined in the following.

6.2.1.1 Induction hypothesis

The symmetry of the basis functions is given by

$$
\left.
\begin{aligned}
-w_{i,\mathrm{a}}(\tau) &= w_{i,\mathrm{b}}(\tau + 0.5) \\
w_{i,\mathrm{a}}(\tau) &= w_{i,\mathrm{a}}(0.5 - \tau) \\
-w_{i,\mathrm{a}}(\tau) &= w_{i,\mathrm{b}}(1 - \tau)
\end{aligned}
\right\}
\begin{aligned}
&\forall\, i = 2k, k \in \mathbb{N} \setminus \{0\} \\
&\text{and } \forall\, \tau \in (0, 0.5)
\end{aligned}\quad,
\tag{6.12}
$$

i.e., for all basis functions with even index, and

$$\left.\begin{array}{r}-w_{i,\mathrm{a}}(\tau) = w_{i,\mathrm{b}}(\tau + 0.5) \\ -w_{i,\mathrm{a}}(\tau) = w_{i,\mathrm{a}}(0.5 - \tau) \\ w_{i,\mathrm{a}}(\tau) = w_{i,\mathrm{b}}(1 - \tau)\end{array}\right\} \begin{array}{l}\forall\, i = 1 + 2k, k \in \mathbb{N} \setminus \{0\}, \\ \text{and } \forall\, \tau \in (0, 0.5)\end{array}, \tag{6.13}$$

i.e., for all basis functions with odd index.

6.2.1.2 Induction base

We calculate the basis functions $w_2(\tau)$ and $w_3(\tau)$ and their symmetry properties. The basis function $w_2(\tau)$ is obtained using (6.10),(6.11) and given by

$$w_{2,\mathrm{a}}(\tau) = \sqrt{3}\left(2\tau^2 - \tau\right), \tag{6.14}$$

and

$$w_{2,\mathrm{b}}(\tau) = \sqrt{3}\left(2\tau^2 + 3\tau - 1\right). \tag{6.15}$$

They fulfill the symmetry properties stated in (6.12).

The basis function $w_3(\tau)$ is also obtained using (6.10), (6.11) and given by

$$w_{3,\mathrm{a}}(\tau) = \sqrt{3}\left(\frac{2}{3}\tau^3 - 0.5\tau^2 + \frac{1}{48}\right), \tag{6.16}$$

and

$$w_{3,\mathrm{b}}(\tau) = \sqrt{3}\left(-\frac{2}{3}\tau^3 + \frac{3}{2}\tau^2 - \tau + \frac{3}{16}\right). \tag{6.17}$$

They fulfill the symmetry properties stated in (6.13).

6.2.1.3 Induction step

We calculate the basis functions $w_i(\tau)$ and $w_{i+1}(\tau)$, where $i = 2k, k \in \mathbb{N} \setminus \{0, 1\}$ and their symmetry properties.

Basis function $w_i(\tau)$. The basis function $w_i(\tau)$ is given by integration and orthogonalization against the constant basis function $w_0(\tau)$, i.e.,

$$w_{i,\mathrm{a}}(\tau) = \int_{0.5}^{\tau} w_{i-1,\mathrm{a}}(\eta)\ \mathrm{d}\eta - \int_0^1 \int_{0.5}^{\tau} w_{i-1}(\eta)\ \mathrm{d}\eta\ \mathrm{d}\tau \tag{6.18}$$

and

$$w_{i,\mathrm{b}}(\tau) = \int_{0.5}^{\tau} w_{i-1,\mathrm{b}}(\eta)\ \mathrm{d}\eta - \int_0^1 \int_{0.5}^{\tau} w_{i-1}(\eta)\ \mathrm{d}\eta\ \mathrm{d}\tau \tag{6.19}$$

The orthogonalization term yields using the symmetry properties (6.13) and substitution

$$\begin{aligned}\int_0^1 \int_{0.5}^{\tau} w_{i-1}(\eta)\ \mathrm{d}\eta\ \mathrm{d}\tau &= \int_0^{0.5} \int_{0.5}^{\tau} w_{i-1,\mathrm{a}}(\eta)\ \mathrm{d}\eta\ \mathrm{d}\tau \\ &+ \int_{0.5}^0 \int_{0.5}^{\tau} w_{i-1,\mathrm{a}}(\eta)\ \mathrm{d}\eta\ \mathrm{d}\tau = 0.\end{aligned} \tag{6.20}$$

Therefore the expressions for the basis function $w_i(\tau)$ (6.18) and (6.19) simplify to

$$w_{i,\mathrm{a}}(\tau) = \int_{0.5}^{\tau} w_{i-1,\mathrm{a}}(\eta) \; \mathrm{d}\eta \tag{6.21}$$

and

$$w_{i,\mathrm{b}}(\tau) = \int_{0.5}^{\tau} w_{i-1,\mathrm{b}}(\eta) \; \mathrm{d}\eta. \tag{6.22}$$

The symmetries are given by, using (6.13),

$$-w_{i,\mathrm{a}}(\tau) = w_{i,\mathrm{b}}(\tau + 0.5), \tag{6.23}$$

and

$$w_{i,\mathrm{a}}(\tau) = w_{i,\mathrm{a}}(0.5 - \tau), \tag{6.24}$$

and thus fulfill the hypothesis (6.12).

Basis function $w_{i+1}(\tau)$. The basis function $w_{i+1}(\tau)$ is calculated by

$$w_{i+1,\mathrm{a}}(\tau) = \int_{0.5}^{\tau} w_{i,\mathrm{a}}(\eta) \; \mathrm{d}\eta - \int_0^1 \int_{0.5}^{\tau} w_i(\eta) \; \mathrm{d}\eta \; \mathrm{d}\tau, \tag{6.25}$$

and

$$w_{i+1,\mathrm{b}}(\tau) = \int_{0.5}^{\tau} w_{i,\mathrm{b}}(\eta) \; \mathrm{d}\eta - \int_0^1 \int_{0.5}^{\tau} w_i(\eta) \; \mathrm{d}\eta \; \mathrm{d}\tau. \tag{6.26}$$

The orthogonalization term is calculated using the symmetry properties (6.12) and substitution

$$\int_0^1 \int_{0.5}^{\tau} w_i(\eta) \; \mathrm{d}\eta \; \mathrm{d}\tau = -0.5 \int_0^{0.5} w_{i,\mathrm{a}}(\eta) \; \mathrm{d}\eta.$$

Therefore the expressions for the basis function $w_{i+1}(\tau)$ (6.25) and (6.26) are

$$w_{i+1,\mathrm{a}}(\tau) = \int_{0.5}^{\tau} w_{i,\mathrm{a}}(\eta) \; \mathrm{d}\eta + 0.5 \int_0^{0.5} w_{i,\mathrm{a}}(\eta) \; \mathrm{d}\eta, \tag{6.27}$$

and

$$w_{i+1,\mathrm{b}}(\tau) = \int_{0.5}^{\tau} w_{i,\mathrm{b}}(\eta) \; \mathrm{d}\eta + 0.5 \int_0^{0.5} w_{i,\mathrm{a}}(\eta) \; \mathrm{d}\eta. \tag{6.28}$$

The symmetries are given by, using (6.12),

$$-w_{i+1,\mathrm{a}}(\tau) = w_{i+1,\mathrm{b}}(\tau + 0.5), \tag{6.29}$$

and

$$-w_{i+1,\mathrm{a}}(\tau) = w_{i+1,\mathrm{a}}(0.5 - \tau), \tag{6.30}$$

and thus fulfill the hypothesis (6.13).

6.2.2 Proof of remark 1

We calculate the solution of the linear ODE

$$A\frac{\mathrm{d}}{\mathrm{d}t}x(t) + Bx(t) = c(t) \tag{6.31}$$

where $A, B \in \mathbb{R}$ are constants, $x(t) \in \mathbb{R}$ is the solution and $c(t) \in \mathbb{R}$ is the excitation. Generalization to systems of ODEs is straightforward. Without loss of generality we assume $A = 1$. Rewriting leads to

$$\frac{\mathrm{d}}{\mathrm{d}t}x(t) = c(t) - Bx(t). \tag{6.32}$$

Therefore the homogeneous problem is given as

$$\frac{\mathrm{d}}{\mathrm{d}t}x(t) = -Bx(t). \tag{6.33}$$

The solution of the ODE (6.32) is given by

$$x(t) = \alpha\,\mathrm{e}^{-Bt} + x_p(t), \tag{6.34}$$

where $\alpha \in \mathbb{R}$ is a constant and $x_p(t)$ is a particular solution. In the following the time interval of one period of a 2-level pulsed excitation $c(t)$ with duty cycle $D = 0.5$ is considered. The excitation is given by

$$c(t) = \begin{cases} 1 & \text{for } 0 \le t < 0.5\,T_\mathrm{s} \\ -1 & \text{for } 0.5\,T_\mathrm{s} \le t \le T_\mathrm{s} \end{cases}. \tag{6.35}$$

Two cases are distinguished. Either $0 \le t < 0.5\,T_\mathrm{s}$ or $0.5\,T_\mathrm{s} \le t \le T_\mathrm{s}$. In the first case, the solution and constants are denoted with additional subscript "a", in the second case with additional subscript "b".

The solution for the first interval is then given by

$$x_\mathrm{a}(t) = \alpha_\mathrm{a}\,\mathrm{e}^{-Bt} + B^{-1}, \tag{6.36}$$

where the last term is a particular solution if the excitation is constantly 1.

The solution for the second interval is given by

$$x_\mathrm{b}(t) = \alpha_\mathrm{b}\,\mathrm{e}^{-Bt} - B^{-1}, \tag{6.37}$$

where the last term is a particular solution if the excitation is constantly -1.

The following conditions require to be satisfied for each ripple of the solution:

$$x_\mathrm{a}(0) = x_\mathrm{b}(T_\mathrm{s}) \tag{6.38}$$
$$x_\mathrm{a}(0.5\,T_\mathrm{s}) = x_\mathrm{b}(0.5\,T_\mathrm{s}). \tag{6.39}$$

Inserting these conditions into the solutions gives the two equations

$$\alpha_\mathrm{a}\,\mathrm{e}^{-B0} + B^{-1} = \alpha_\mathrm{b}\,\mathrm{e}^{-BT_\mathrm{s}} - B^{-1} \tag{6.40}$$
$$\alpha_\mathrm{a}\,\mathrm{e}^{-B0.5T_\mathrm{s}} + B^{-1} = \alpha_\mathrm{b}\,\mathrm{e}^{-B0.5T_\mathrm{s}} - B^{-1} \tag{6.41}$$

Substracting the second from the first equation leads to the relation

$$\alpha_\mathrm{a} = -\alpha_\mathrm{b}\,\mathrm{e}^{-B0.5T_\mathrm{s}} \tag{6.42}$$

The symmetry of the solution is, using the relation between the coefficients, given by

$$
\begin{aligned}
x_\mathrm{a}(t - 0.5T_\mathrm{s}) &= \alpha_\mathrm{a}\,\mathrm{e}^{-Bt}\,\mathrm{e}^{B0.5T_\mathrm{s}} + B^{-1} \\
&= -\alpha_\mathrm{b}\,\mathrm{e}^{-B0.5T_\mathrm{s}}\,\mathrm{e}^{-Bt}\,\mathrm{e}^{B0.5T_\mathrm{s}} + B^{-1} \\
&= -\alpha_\mathrm{b}\,\mathrm{e}^{-Bt} + B^{-1} \\
&= -x_\mathrm{b}(t).
\end{aligned} \tag{6.43}
$$

The PWM basis functions are polynomials of degree up to N_p, which span the polynomial space of dimension $N_\mathrm{p} + 1$. Thus, a linear combination of them with duty cycle $D = 0.5$ can exactly represent any piecewise polynomial with C^0 continuity at $\tau = 0.5$, maximum degree N_p and symmetry condition common to odd and even indexed PWM basis functions (6.12), (6.13), i.e., $-w_i(\tau) = w_i(\tau + 0.5)$. The solution of the linear ODE fulfills this condition, see (6.43).

6.2.3 Proof of remark 2

The PWM basis functions above are built for a particular duty cycle D to represent piecewise exponential solutions as generated in power converters by 2-level pulsed excitations. Let us show that they do not span $L^2([0,1])$. Consider as example the 3-level function

$$
c_\mathrm{t}(\tau) = \begin{cases} 1 & \text{for} \quad 0 \leq \tau < 0.25 \\ 0 & \text{for} \quad 0.25 \leq \tau < 0.75 \\ -1 & \text{for} \quad 0.75 \leq \tau \leq 1 \end{cases}. \tag{6.44}
$$

It is depicted in Fig. 3.7.

$c_\mathrm{t}(\tau)$ is L^2-projected onto the space spanned by the basis functions $w_k(\tau)\,\forall k \in \mathbb{N}$. The projection $c_\mathrm{t}^h(\tau)$ (see Fig. 3.7) is a linear combination of the basis functions

$$c_\mathrm{t}^h(\tau) = a_0\,w_0(\tau) + a_1\,w_1(\tau) + \ldots + a_{N_\mathrm{p}}\,w_{N_\mathrm{p}}(\tau), \tag{6.45}$$

where N_p is the number of employed basis functions. The zeroth basis function and all basis functions with odd index do not contribute to $c_\mathrm{t}^h(\tau)$ as

$$\int_0^1 w_k(\tau)\,c_\mathrm{t}(\tau)\,\mathrm{d}\tau = 0, \quad k = 0, 1, 3, 5, \ldots. \tag{6.46}$$

Therefore the final solution exhibits the same symmetry properties as the basis functions with even index. These are given by (6.12). We assume without loss of generality, that $c_\mathrm{t}^h(\tau)$ is given in terms of orthonormalized basis functions. As they span the same space, the symmetry properties of $c_\mathrm{t}^h(\tau)$ do not change. The error between $c_\mathrm{t}^h(\tau)$ and $c_\mathrm{t}(\tau)$ in the L^2 sense can be estimated as follows, where, for simplicity, the τ dependency

is omitted

$$\int_0^1 (c_t^h - c_t)^2 \, \mathrm{d}\tau \overset{(6.12)}{=} 2 \int_0^{0.5} (c_t^h - c_t)^2 \, \mathrm{d}\tau \tag{6.47}$$

$$= 2 \int_0^{0.5} c_t^2 - 2 c_t c_t^h + (c_t^h)^2 \, \mathrm{d}\tau \tag{6.48}$$

$$= 2 \int_0^{0.25} c_t^2 - 2 c_t c_t^h + (c_t^h)^2 \, \mathrm{d}\tau \tag{6.49}$$

$$+ 2 \int_{0.25}^{0.5} c_t^2 - 2 c_t c_t^h + (c_t^h)^2 \, \mathrm{d}\tau. \tag{6.50}$$

Using $c_t(\tau) = 0 \; \forall \tau \in [0.25, 0.5]$ yields

$$\int_0^1 (c_t^h - c_t)^2 \, \mathrm{d}\tau = 2 \int_0^{0.25} c_t^2 - 2 c_t c_t^h + (c_t^h)^2 \, \mathrm{d}\tau + 2 \int_{0.25}^{0.5} (c_t^h)^2 \, \mathrm{d}\tau \tag{6.51}$$

$$\overset{(6.12)}{=} 2 \int_0^{0.25} c_t^2 - 2 c_t c_t^h + (c_t^h)^2 + (c_t^h)^2 \, \mathrm{d}\tau \tag{6.52}$$

$$= 2 \left\| c_t - c_t^h \right\|_{L^2([0,0.25])}^2 \tag{6.53}$$

$$+ 2 \left\| c_t^h \right\|_{L^2([0,0.25])}^2. \tag{6.54}$$

Now the expression $\left\| c_t^h \right\|_{L^2([0,0.25])}$ is estimated using the orthonormality of the basis functions. The L^2 scalar product is denoted as $\langle a(\tau), b(\tau) \rangle = \int_0^{0.25} a(\tau) \, b(\tau) \, \mathrm{d}\tau$, where in the following we leave out the τ dependency for simplicity

$$\left\| c_t^h \right\|_{L^2([0,0.25])}^2 = \langle \sum_k \langle c_t, w_k \rangle w_k, \sum_l \langle c_t, w_l \rangle w_l \rangle \tag{6.55}$$

$$= \sum_k \sum_l \langle \langle c_t, w_k \rangle w_k, \langle c_t, w_l \rangle w_l \rangle \tag{6.56}$$

Using the orthonormality of the basis yields

$$\left\| c_t^h \right\|_{L^2([0,0.25])}^2 = \sum_k \langle \langle c_t, w_k \rangle w_k, \langle c_t, w_k \rangle w_k \rangle \tag{6.57}$$

$$= \sum_k \langle \langle c_t, w_k \rangle, \langle c_t, w_k \rangle \rangle \tag{6.58}$$

$$= \sum_k \langle c_t, w_k \rangle^2 \tag{6.59}$$

$$\tag{6.60}$$

As $\langle c_t, w_k \rangle^2$ is always positive independent of how many basis functions are used, the error $\left\| c_t^h - c_t \right\|_{L^2([0,1])}^2$ will always be greater than a fixed constant.

6.3 Proof of theorem 3

The following proof has been published in [82]. Let us split the set of basis functions (3.82) into three parts: the basis functions $\{P_{0,p}, \dots, P_{p+K-1,p}\}$, which depend on the knots in the interval $[0, D]$; the ba-

sis functions $\{P_{p+K+1,p}, \ldots, P_{2p+2K,p}\}$, which depend on the knots in the interval $[D, 1]$; and the remaining basis function $\{P_{p+K,p}\}$, which has a C^0 continuity and depends on knots from the entire interval $[0, 1]$.

1. The basis functions $\{P_{0,p}, \ldots, P_{p+K-1,p}\}$ are calculated using the Cox-DeBoor formula. This leads to the recursion

$$P_{i,p}(\xi, D) = \frac{\xi - \gamma_{1,i}\, D}{\gamma_{2,i}\, D} P_{i,p-1}(\xi, D) + \frac{\gamma_{3,i}\, D - \xi}{\gamma_{4,i}\, D} P_{i+1,p-1}(\xi, D), \qquad (6.61)$$

where $\gamma_{1,i}, \ldots, \gamma_{4,i}$ are constants, which depend on the $\alpha_1, \ldots, \alpha_K$ from (3.81) and which are independent of the duty cycle D. This recursion leads to polynomials $P_{i,p}(\xi, D)$ which can be written as

$$P_{i,p}(\xi, D) = \bar{\gamma}_{p,i}\frac{\xi^p}{D^p} + \bar{\gamma}_{p-1,i}\frac{\xi^{p-1}}{D^{p-1}} + \ldots + \bar{\gamma}_{0,i}\frac{\xi^0}{D^0}, \qquad (6.62)$$

where $\bar{\gamma}_{0,i}, \ldots, \bar{\gamma}_{p,i}$ are constants.

2. To simplify the notation for the second part, the knot vector is redefined by shifting it such that

$$\widehat{\Xi}_{p,K} = \Xi_{p,K} - D = \{-D, \ldots, -D, \alpha_1 D - D, \ldots, \alpha_K D - D, 0, \ldots, 0, \beta_1(1-D), \ldots, \beta_K(1-D), D, \ldots, D\}$$

As a result, the basis functions $\{P_{p+K+1,p}, \ldots, P_{2p+2K,p}\}$ are shifted by $-D$ but apart from that are the same as with the original knot vector $\Xi_{p,K}$. Applying the Cox-DeBoor formula yields

$$\widehat{P}_{i,p}(\xi, D) = \frac{\xi - \chi_{1,i}\,(1-D)}{\chi_{2,i}\,(1-D)} \widehat{P}_{i,p-1}(\xi, D) + \frac{\chi_{3,i}\,(1-D) - \xi}{\chi_{4,i}\,(1-D)} \widehat{P}_{i+1,p-1}(\xi, D), \qquad (6.63)$$

which corresponds to polynomials of the form

$$\widehat{P}_{i,p}(\xi, D) = \bar{\chi}_{p,i}\frac{\xi^p}{(1-D)^p} + \bar{\chi}_{p-1,i}\frac{\xi^{p-1}}{(1-D)^{p-1}} + \ldots + \bar{\chi}_{0,i}\frac{\xi^0}{(1-D)^0}, \qquad (6.64)$$

where $\bar{\chi}_{0,i}, \ldots, \bar{\chi}_{p,i}$ are constants.

3. Due to the knot repetition the single basis function $P_{p+K,p}$ consists of two parts. This becomes obvious in the corresponding Cox-DeBoor formula for this case is

$$P_{p+K,p}(\xi) = \frac{\xi - \xi_{p+K}}{\xi_{2p+K} - \xi_{p+K}} P_{p+K,p-1}(\xi) + \frac{\xi_{2p+K+1} - \xi}{\xi_{2p+K+1} - \xi_{p+K+1}} P_{p+K+1,p-1}(\xi). \qquad (6.65)$$

The first term stems from the basis functions in the interval $[0, D]$, i.e., all basis functions left of the C^0 continuity. The second term stems from the basis functions in the interval $[D, 1]$, i.e., all basis functions right of the C^0 continuity. As a result, the first and second term are polynomials of the form (6.62) and (6.64), respectively.

Inserting the polynomials (6.62) and (6.64) into the matrix (3.32) gives

$$
(\boldsymbol{\mathcal{J}}_{\mathrm{bspl}})_{i,j}(D) = T_{\mathrm{s}} \int_0^D P_{i,p}(\xi, D) P_{j,p}(\xi, D) \, \mathrm{d}\xi + T_{\mathrm{s}} \int_0^{1-D} \widehat{P}_{i,p}(\xi, D) \widehat{P}_{j,p}(\xi, D) \, \mathrm{d}\xi
$$

$$
= T_{\mathrm{s}} \int_0^D \bar{\gamma}_{p,i} \frac{\xi^p}{D^p} + \bar{\gamma}_{p-1,i} \frac{\xi^{p-1}}{D^{p-1}} + \ldots + \bar{\gamma}_{0,i} \, \mathrm{d}\xi
$$

$$
+ T_{\mathrm{s}} \int_0^{1-D} \bar{\chi}_{p,i} \frac{\xi^p}{(1-D)^p} + \bar{\gamma}_{p-1,i} \frac{\xi^{p-1}}{(1-D)^{p-1}} + \ldots + \bar{\gamma}_{0,i} \, \mathrm{d}\xi
$$

$$
= T_{\mathrm{s}} \left[\bar{\gamma}_{p,i} \frac{\xi^{p+1}}{D^p(p+1)} + \bar{\gamma}_{p-1,i} \frac{\xi^p}{D^{p-1}p} + \ldots + \bar{\gamma}_{0,i}\xi \right]\Big|_0^D
$$

$$
+ T_{\mathrm{s}} \left[\bar{\chi}_{p,i} \frac{\xi^{p+1}}{(1-D)^p(p+1)} + \bar{\gamma}_{p-1,i} \frac{\xi^p}{(1-D)^{p-1}p} + \ldots + \bar{\gamma}_{0,i}\xi \right]\Big|_0^{1-D}
$$

$$
= \underbrace{T_{\mathrm{s}} \left[\bar{\gamma}_{p,i} \frac{D}{(p+1)} + \bar{\gamma}_{p-1,i} \frac{D}{p} + \ldots + \bar{\gamma}_{0,i}D \right]}_{(\boldsymbol{\mathcal{J}}_{\mathrm{bspl}})^0_{i,j} \, D}
$$

$$
+ \underbrace{T_{\mathrm{s}} \left[\bar{\chi}_{p,i} \frac{1-D}{(p+1)} + \bar{\gamma}_{p-1,i} \frac{1-D}{p} + \ldots + \bar{\gamma}_{0,i}(1-D) \right]}_{(\boldsymbol{\mathcal{J}}_{\mathrm{bspl}})^1_{i,j}(1-D)} \tag{6.66}
$$

where $(\boldsymbol{\mathcal{J}}_{\mathrm{bspl}})^0_{i,j}$ and $(\boldsymbol{\mathcal{J}}_{\mathrm{bspl}})^1_{i,j}$ are constant. This prooves that the matrix depends linearly on the duty cycle. For the matrices (3.33) and (3.34) the calculation is similar, however it leads to

$$
(\boldsymbol{\mathcal{Q}}_{\mathrm{bspl}})_{i,j} = \underbrace{\int_0^D \frac{\partial P_{i,p}(\xi, D)}{\partial \xi} P_{j,p}(\xi, D) \, \mathrm{d}\xi}_{(\boldsymbol{\mathcal{Q}}_{\mathrm{bspl}})^0_{i,j}} + \underbrace{\int_0^{1-D} \frac{\partial \widehat{P}_{i,p}(\xi, D)}{\partial \xi} \widehat{P}_{j,p}(\xi, D) \, \mathrm{d}\xi}_{(\boldsymbol{\mathcal{Q}}_{\mathrm{bspl}})^1_{i,j}} \tag{6.67}
$$

and

$$
(\boldsymbol{\mathcal{U}}_{\mathrm{bspl}})_{i,j} = \underbrace{\int_0^D P_{i,p}(\xi, D) \frac{\partial P_{j,p}(\xi, D)}{\partial D} \, \mathrm{d}\xi}_{(\boldsymbol{\mathcal{U}}_{\mathrm{bspl}})^0_{i,j}} + \underbrace{\int_0^{1-D} \widehat{P}_{i,p}(\xi, D) \frac{\partial \widehat{P}_{j,p}(\xi, D)}{\partial D} \, \mathrm{d}\xi}_{(\boldsymbol{\mathcal{U}}_{\mathrm{bspl}})^1_{i,j}}. \tag{6.68}
$$

The $(\boldsymbol{\mathcal{Q}}_{\mathrm{bspl}})^0_{i,j}$, $(\boldsymbol{\mathcal{Q}}_{\mathrm{bspl}})^1_{i,j}$, $(\boldsymbol{\mathcal{U}}_{\mathrm{bspl}})^0_{i,j}$ and $(\boldsymbol{\mathcal{U}}_{\mathrm{bspl}})^1_{i,j}$ are constant. The matrices $\boldsymbol{\mathcal{Q}}_{\mathrm{bspl}}$ and $\boldsymbol{\mathcal{U}}_{\mathrm{bspl}}$ are independent of the duty cycle D.

6.4 Proof of theorem 4

Using the chain rule of differentiation yields [71]

$$\left[\mathbf{A}(\mathbf{x})\frac{\mathrm{d}}{\mathrm{d}t}\mathbf{x}(t)\right]\Big|_{t=t_0} \stackrel{(3.116)}{=} \left[\mathbf{A}(\widehat{\mathbf{x}})\frac{\mathrm{d}}{\mathrm{d}t}\widehat{\mathbf{x}}(t,\theta_2(t),\ldots,\theta_m(t))\right]\Big|_{t=t_0} \tag{6.69}$$

$$= \left[\mathbf{A}(\widehat{\mathbf{x}})\left(\frac{\partial\widehat{\mathbf{x}}(t,\theta_2,\ldots,\theta_m)}{\partial t} + \frac{\mathrm{d}\theta_2(t)}{\mathrm{d}t}\frac{\partial\widehat{\mathbf{x}}(t,\theta_2,\ldots,\theta_m)}{\partial\theta_2} + \ldots\right.\right. \tag{6.70}$$

$$\left.\left. + \frac{\mathrm{d}\theta_m(t)}{\mathrm{d}t}\frac{\partial\widehat{\mathbf{x}}(t,\theta_2,\ldots,\theta_m)}{\partial\theta_m}\right)\right]\Big|_{t=t_0,\theta_2=t_0,\ldots,\theta_m=t_0} \tag{6.71}$$

which, substituting the variable t by t_1, and the variables $\theta_2,\ldots,\theta_m$ by $t_2,\ldots,t_m$, leads to

$$= \left[\mathbf{A}(\widehat{\mathbf{x}})\left(\frac{\partial\widehat{\mathbf{x}}(t_1,t_2,\ldots,t_m)}{\partial t_1} + \underbrace{\frac{\mathrm{d}\theta_2(t_1)}{\mathrm{d}t_1}}_{\omega_2(t_1)}\frac{\partial\widehat{\mathbf{x}}(t_1,t_2,\ldots,t_m)}{\partial t_2} + \ldots\right.\right. \tag{6.72}$$

$$\left.\left. + \underbrace{\frac{\mathrm{d}\theta_m(t_1)}{\mathrm{d}t_1}}_{\omega_m(t_1)}\frac{\partial\widehat{\mathbf{x}}(t_1,t_2,\ldots,t_m)}{\partial t_m}\right)\right]\Big|_{t_1=t_0,t_2=t_0,\ldots,t_m=t_0} \tag{6.73}$$

$$\stackrel{(3.115)}{=} \widehat{\mathbf{c}}(t_0,t_0,\ldots,t_0) - \mathbf{B}(\widehat{\mathbf{x}})\,\widehat{\mathbf{x}}(t_0,t_0,\ldots,t_0) \tag{6.74}$$

$$\stackrel{(3.116),(3.117)}{=} \mathbf{c}(t_0) - \mathbf{B}(\mathbf{x})\,\mathbf{x}(t_0) \tag{6.75}$$

6.5 Other proofs

6.5.1 Eigenvalues of skew-symmetric matrices

The eigenvalues of a skew-symmetric matrix $\mathbf{A}$, i.e., $\mathbf{A}^\top = -\mathbf{A}$, are purely imaginary [109, p. 506]. Given the eigenvalue problem $\mathbf{A}\mathbf{x} = \lambda\mathbf{x}$ the equation system

$$\begin{bmatrix} 0 & \mathbf{A} \\ -\mathbf{A} & 0 \end{bmatrix}\begin{bmatrix} \mathbf{x} \\ \mathrm{i}\mathbf{x} \end{bmatrix} = \mathrm{i}\lambda\begin{bmatrix} \mathbf{x} \\ \mathrm{i}\mathbf{x} \end{bmatrix} \tag{6.76}$$

can be built. The block matrix in this equation system is symmetric, i.e.,

$$\begin{bmatrix} 0 & \mathbf{A} \\ -\mathbf{A} & 0 \end{bmatrix}^\top = \begin{bmatrix} 0 & -\mathbf{A}^\top \\ \mathbf{A}^\top & 0 \end{bmatrix} = \begin{bmatrix} 0 & \mathbf{A} \\ -\mathbf{A} & 0 \end{bmatrix}. \tag{6.77}$$

Symmetric matrices have purely real eigenvalues [109, p. 510]. Therefore, according to equation (6.76) the eigenvalues λ of $\mathbf{A}$ are purely imaginary. Furthermore since A is a normal matrix, i.e.,

$$\mathbf{A}^\top\mathbf{A} = -\mathbf{A}\mathbf{A} = \mathbf{A}(-\mathbf{A}) = \mathbf{A}\mathbf{A}^\top, \tag{6.78}$$

the eigenvectors are orthonormal [48, p. 133].

6.5.2 Eigenvalues of $\mathcal{J}^{-1}\mathcal{Q}$

The eigenvalues λ of the matrix $\mathcal{J}^{-1}\mathcal{Q}$ are determined by the eigenvalue problem

$$\mathcal{J}^{-1}\mathcal{Q}\mathbf{x} = \lambda\mathbf{x}, \tag{6.79}$$

where $\mathbf{x}$ is the eigenvector corresponding to the eigenvalue λ. Multiplying both sides with $\mathcal{J}$ leads to the generalized eigenvalue problem

$$\mathcal{Q}\mathbf{x} = \lambda\mathcal{J}\mathbf{x}. \tag{6.80}$$

If the matrix $\mathcal{J}$ is real symmetric positive definite, it can be diagonalized such that

$$\mathcal{J} = \mathbf{U}\mathbf{D}\mathbf{U}^\top, \tag{6.81}$$

where $\mathbf{U}^{-1} = \mathbf{U}^\top$ are orthogonal matrices and $\mathbf{D}$ is the diagonal eigenvalue matrix [109, p. 334]. All entries of $\mathbf{D}$ are positive (due to the positive definitiness of $\mathcal{J}$) [109, p. 252].

Inserting (6.81) into (6.80) leads to

$$\mathcal{Q}\mathbf{x} = \lambda\mathbf{U}\mathbf{D}\mathbf{U}^\top\mathbf{x} \tag{6.82}$$

$$\mathbf{U}^\top\mathcal{Q}\mathbf{x} = \lambda\underbrace{\mathbf{U}^\top\mathbf{U}}_{\text{identity}}\mathbf{D}\underbrace{\mathbf{U}^\top\mathbf{x}}_{=:\mathbf{y}} \tag{6.83}$$

$$\mathbf{U}^\top\mathcal{Q}\mathbf{U}\mathbf{y} = \lambda\mathbf{D}\mathbf{y}. \tag{6.84}$$

Using $\mathbf{M} = \mathbf{D}^{\frac{1}{2}}$ gives

$$\mathbf{U}^\top\mathcal{Q}\mathbf{U}\mathbf{y} = \lambda\mathbf{M}\underbrace{\mathbf{M}\mathbf{y}}_{=:\mathbf{z}} \tag{6.85}$$

$$\mathbf{M}^{-1}\mathbf{U}^\top\mathcal{Q}\mathbf{U}\mathbf{M}^{-1}\mathbf{z} = \lambda\mathbf{z}. \tag{6.86}$$

$$\tag{6.87}$$

If the matrix $\mathcal{Q}$ is skew-symmetric, then the matrix $\mathbf{M}^{-1}\mathbf{U}^\top\mathcal{Q}\mathbf{U}\mathbf{M}^{-1}$ is skew-symmetric as well since

$$\left(\mathbf{M}^{-1}\mathbf{U}^\top\mathcal{Q}\mathbf{U}\mathbf{M}^{-1}\right)^\top = \mathbf{M}^{-1}\mathbf{U}^\top\underbrace{\mathcal{Q}^\top}_{-\mathcal{Q}}\mathbf{U}\mathbf{M}^{-1} \tag{6.88}$$

A skew-symmetric matrix has purely imaginary eigenvalues and orthonormal eigenvectors, see appendix 6.5.1. The original eigenvectors, calculated using $\mathbf{x} = \mathbf{U}\mathbf{M}^{-1}\mathbf{z}$, are linearly independent since the matrices $\mathbf{U}$ and $\mathbf{M}$ are invertible.

6.6 Implementation of periodic boundary conditions

The DOFs in the differential equation system (3.29) are associated to the solution $\hat{\mathbf{x}}$ through the solution expansion (3.15). In case of PWM basis functions and PWM eigenfunctions the periodicity of the solution along the time scale t_2 is already enforced by construction. In case of B-spline basis functions these have to be enforced by modifying the equation systems. Using periodic boundary conditions is one possibility. To achieve

this, the DOFs associated to the solution at $\tau = 0$ and $\tau = 1$ are equalized. For this purpose we follow the process described in [34] and in a first step write the differential equation system as

$$
\begin{bmatrix} \mathcal{A}_{L,L} & \mathcal{A}_{L,I} & \mathcal{A}_{L,R} \\ \mathcal{A}_{I,L} & \mathcal{A}_{I,I} & \mathcal{A}_{I,R} \\ \mathcal{A}_{R,L} & \mathcal{A}_{R,I} & \mathcal{A}_{R,R} \end{bmatrix} \frac{\mathrm{d}}{\mathrm{d}t_1} \begin{bmatrix} \mathbf{y}_L \\ \mathbf{y}_I \\ \mathbf{y}_R \end{bmatrix} + \begin{bmatrix} \mathcal{B}_{L,L} & \mathcal{B}_{L,I} & \mathcal{B}_{L,R} \\ \mathcal{B}_{I,L} & \mathcal{B}_{I,I} & \mathcal{B}_{I,R} \\ \mathcal{B}_{R,L} & \mathcal{B}_{R,I} & \mathcal{B}_{R,R} \end{bmatrix} \begin{bmatrix} \mathbf{y}_L \\ \mathbf{y}_I \\ \mathbf{y}_R \end{bmatrix} = \begin{bmatrix} \mathcal{C}_L \\ \mathcal{C}_I \\ \mathcal{C}_R \end{bmatrix}, \tag{6.89}
$$

where $\mathbf{y}_L$ corresponds to the DOFs associated with the solution at $\tau = 0$, $\mathbf{y}_R$ corresponds to the DOFs associated with the solution at $\tau = 1$ and $\mathbf{y}_I$ corresponds to the remaining DOFs. Enforcing periodicity by $\mathbf{y}_L = \mathbf{y}_R$, we rewrite the equation system by adding the first equation to the last. Furthermore we replace the first equation by an algebraic one enforcing $\mathbf{y}_L = \mathbf{y}_R$. This results in

$$
\begin{bmatrix} 0 & 0 & 0 \\ \mathcal{A}_{I,L} & \mathcal{A}_{I,I} & \mathcal{A}_{I,R} \\ \mathcal{A}_{R,L} + \mathcal{A}_{L,L} & \mathcal{A}_{R,I} + \mathcal{A}_{L,I} & \mathcal{A}_{R,R} + \mathcal{A}_{L,R} \end{bmatrix} \frac{\mathrm{d}}{\mathrm{d}t_1} \begin{bmatrix} \mathbf{y}_L \\ \mathbf{y}_I \\ \mathbf{y}_R \end{bmatrix} \tag{6.90}
$$

$$
+ \begin{bmatrix} 1 & 0 & -1 \\ \mathcal{B}_{I,L} & \mathcal{B}_{I,I} & \mathcal{B}_{I,R} \\ \mathcal{B}_{R,L} + \mathcal{B}_{L,L} & \mathcal{B}_{R,I} + \mathcal{B}_{L,I} & \mathcal{B}_{R,R} + \mathcal{B}_{L,R} \end{bmatrix} \begin{bmatrix} \mathbf{y}_L \\ \mathbf{y}_I \\ \mathbf{y}_R \end{bmatrix} = \begin{bmatrix} 0 \\ \mathcal{C}_I \\ \mathcal{C}_R + \mathcal{C}_L \end{bmatrix}, \tag{6.91}
$$

which is a system of DAEs, even if (6.89) were ODEs. The equation system can be further simplified to

$$
\begin{bmatrix} \mathcal{A}_{I,I} & \mathcal{A}_{I,R} + \mathcal{A}_{I,L} \\ \mathcal{A}_{R,I} + \mathcal{A}_{L,I} & \mathcal{A}_{R,R} + \mathcal{A}_{L,R} + \mathcal{A}_{R,L} + \mathcal{A}_{L,L} \end{bmatrix} \frac{\mathrm{d}}{\mathrm{d}t_1} \begin{bmatrix} \mathbf{y}_I \\ \mathbf{y}_R \end{bmatrix} \tag{6.92}
$$

$$
+ \begin{bmatrix} \mathcal{B}_{I,I} & \mathcal{B}_{I,R} + \mathcal{B}_{I,L} \\ \mathcal{B}_{R,I} + \mathcal{B}_{L,I} & \mathcal{B}_{R,R} + \mathcal{B}_{L,R} + \mathcal{B}_{R,L} + \mathcal{B}_{L,L} \end{bmatrix} \begin{bmatrix} \mathbf{y}_I \\ \mathbf{y}_R \end{bmatrix} = \begin{bmatrix} \mathcal{C}_I \\ \mathcal{C}_R + \mathcal{C}_L \end{bmatrix}, \tag{6.93}
$$

which is again a system of ODEs if the original equations (6.89) were ODEs.

Bibliography

[1]   J. F. Andrus, "Numerical solution of systems of ordinary differential equations separated into subsystems", *SIAM Journal on Numerical Analysis*, vol. 16, no. 4, pp. 605–611, 1979. DOI: 10.1137/0716045.

[2]   A. Bartel, S. Baumanns, and S. Schöps, "Structural analysis of electrical circuits including magneto-quasistatic devices", *Applied Numerical Mathematics*, vol. 61, pp. 1257–1270, 2011. DOI: 10.1016/j.apnum.2011.08.004.

[3]   A. Bartel, M. Günther, and A. Kværnø, "Multirate methods in electrical circuit simulation", in *Progress in Industrial Mathematics at ECMI 2000*, A. M. Anile, V. Capasso, and A. Greco, Eds., ser. Mathematics in Industry, vol. 1, Berlin: Springer, 2002, pp. 258–265.

[4]   J. J. Biesiadecki and R. D. Skeel, "Dangers of multiple time step methods", *Journal of Computational Physics*, vol. 109, no. 2, pp. 318–328, 1993. DOI: 10.1006/jcph.1993.1220.

[5]   K. Bittner and H. G. Brachtendorf, "Adaptive multi-rate wavelet method for circuit simulation", *Radioengineering*, vol. 23, no. 1, 2014.

[6]   Z. Bontinck, "Simulation and robust optimization for electric devices with uncertainties", Dissertation, Technische Universität Darmstadt, Darmstadt, 2018.

[7]   H. G. Brachtendorf, A. Bunse-Gerstner, B. Lang, and S. Lampe, "Steady state analysis of electronic circuits by cubic and exponential splines", *Electrical Engineering (Archiv für Elektrotechnik)*, vol. 91, no. 4, pp. 287–299, 2009. DOI: 10.1007/s00202-009-0137-7.

[8]   H. G. Brachtendorf, G. Welsch, and R. Laur, "A novel time-frequency method for the simulation of the steady state of circuits driven by multi-tone signals", in *Proceedings of 1997 IEEE International Symposium on Circuits and Systems, 1997. ISCAS '97*, vol. 3, 1997, pp. 1508–1511. DOI: 10.1109/ISCAS.1997.621414.

[9]   ——, "A time-frequency algorithm for the simulation of the initial transient response of oscillators", in *Proceedings of 1997 IEEE International Symposium on Circuits and Systems, 1998. ISCAS '98*, vol. 6, 1998, pp. 236–239. DOI: 10.1109/ISCAS.1998.705255.

[10] H. G. Brachtendorf, G. Welsch, R. Laur, and A. Bunse-Gerstner, "Numerical steady state analysis of electronic circuits driven by multi-tone signals", *Electrical Engineering (Archiv für Elektrotechnik)*, vol. 79, no. 2, pp. 103–112, 1996. DOI: 10.1007/BF01232919.

[11] D. Braess, *Finite Elemente*. Berlin: Springer, 2007.

[12] K. E. Brenan, S. L. Campbell, and L. R. Petzold, *Numerical Solution of Initial-Value Problems in Differential-Algebraic Equations*. Philadelphia, PA, USA: Society for Industrial and Applied Mathematics, 1995. DOI: 10.1137/1.9781611971224.

[13] S. C. Brenner and L. R. Scott, *The mathematical theory of finite element methods*, 3. ed., ser. Texts in applied mathematics. New York: Springer, 2008, vol. 15.

[14] A. Buffa, J. Dölz, S. Kurz, S. Schöps, R. Vázquez, and F. Wolf, "Multipatch approximation of the de Rham sequence and its traces in isogeometric analysis", *Numerische Mathematik*, vol. 144, pp. 201–236, 2020. DOI: `10.1007/s00211-019-01079-x`. arXiv: `1806.01062`.

[15] C. Canuto, M. Y. Hussaini, A. Quarteroni, and T. A. Zang, *Spectral Methods: Fundamentals in Single Domains*, ser. Scientific Computation. Springer Berlin Heidelberg, 2006.

[16] A. Cleary, R. Falgout, V. E. Henson, J. Jones, T. Manteuffel, S. McCormick, G. Miranda, and J. Ruge, "Robustness and scalability of algebraic multigrid", *SIAM Journal on Scientific Computing*, vol. 21, no. 5, pp. 1886–1908, 2000. DOI: `10.1137/S1064827598339402`.

[17] E. A. Coddington and R. Carlson, *Linear Ordinary Differential Equations*. Philadelphia: SIAM, 1997.

[18] I. Cortes Garcia, H. De Gersem, and S. Schöps, "A structural analysis of field/circuit coupled problems based on a generalised circuit element", *Numerical Algorithms*, vol. 83, pp. 373–394, 2020. DOI: `10.1007/s11075-019-00686-x`. arXiv: `1801.07081`.

[19] I. Cortes Garcia, S. Schöps, L. Bortot, M. Maciejewski, M. Prioli, A. M. Fernandez Navarro, B. Auchmann, and A. P. Verweij, "Optimized field/circuit coupling for the simulation of quenches in superconducting magnets", *IEEE Journal on Multiscale and Multiphysics Computational Techniques*, vol. 2, pp. 97–104, 2017. DOI: `10.1109/JMMCT.2017.2710128`. arXiv: `1702.00958`.

[20] I. Cortes Garcia, S. Schöps, H. De Gersem, and S. Baumanns, "Systems of differential algebraic equations in computational electromagnetics", in *Applications of Differential-Algebraic Equations: Examples and Benchmarks*, S. Campbell, A. Ilchmann, V. Mehrmann, and T. Reis, Eds., ser. Differential-Algebraic Equations Forum. Heidelberg: Springer, 2018. DOI: `10.1007/11221_2018_8`.

[21] C. Deml and P. Türkes, "Fast simulation technique for power electronic circuits with widely different time constants", *IEEE Transactions on Industry Applications*, vol. 35, no. 3, pp. 657–662, 1999. DOI: `10.1109/28.767017`.

[22] H. K. Dirks, "Quasi-stationary fields for microelectronic applications", *Electrical Engineering (Archiv für Elektrotechnik)*, vol. 79, no. 2, pp. 145–155, 1996. DOI: `10.1007/BF01232924`.

[23] J. W. Eaton, D. Bateman, S. Hauberg, and R. Wehbring, *GNU Octave version 3.8.1 manual: A high-level interactive language for numerical computations*. CreateSpace Independent Publishing Platform, 2014.

[24] C. R. I. Emson and C. W. Trowbridge, "Transient 3d eddy currents using modified magnetic vector potentials and magnetic scalar potentials", *IEEE Transactions on Magnetics*, vol. 24, no. 1, pp. 86–89, 1988. DOI: `10.1109/20.43862`.

[25] C. Engstler and C. Lubich, "Multirate extrapolation methods for differential equations with different time scales", *Computing*, vol. 58, no. 2, pp. 173–185, 1997. DOI: `10.1007/BF02684438`.

[26] ——, "MUR8: a multirate extension of the eighth-order Dormand-Prince method", *Applied Numerical Mathematics*, vol. 25, no. 2, pp. 185–192, 1997. DOI: `10.1016/S0168-9274(97)00058-5`.

[27] D. Estévez Schwarz, "A step-by-step approach to compute a consistent initialization for the MNA", *International Journal of Circuit Theory and Applications*, vol. 30, no. 1, pp. 1–16, 2002. DOI: `10.1002/cta.168`.

[28] ——, "Consistent initialization for index-2 differential algebraic equations and its application to circuit simulation", Dissertation, Humboldt Universität Berlin, Berlin, 2000.

[29] D. Estévez Schwarz and R. Lamour, "The computation of consistent initial values for nonlinear index-2 differential-algebraic equations", *Numerical Algorithms*, vol. 26, no. 1, pp. 49–75, 2001. DOI: `10.1023/A:1016696413810`.

[30] D. Estévez Schwarz and C. Tischendorf, "Structural analysis of electric circuits and consequences for MNA", *International Journal of Circuit Theory and Applications*, vol. 28, no. 2, pp. 131–162, 2000. DOI: 10.1002/(SICI)1097-007X(200003/04)28:2<131::AID-CTA100>3.0.CO;2-W.

[31] L. C. Evans, *Partial Differential Equations*. Oxford: Oxford University Press, 1998.

[32] K. Finckenstein, J. Lehn, H. Schellhaas, and H. Wegmann, *Arbeitsbuch Mathematik für Ingenieure, Band II, Differentialgleichungen, Funktionentheorie, Numerik und Statistik*, 3rd ed. Vieweg+Teubner, 2006.

[33] A. F. Flippov, *Differential Equations with Discontinuous Righthand Sides*, ser. Mathematics and Its Applications. Springer, 1988. DOI: 10.1007/978-94-015-7793-9.

[34] S. Fujima, Y. Fukasawa, and M. Tabata, "Finite element formulation of periodic conditions and numerical observation of three-dimensional behavior in a flow", *Suri kaiseki kenkyujo kokyuroku*, vol. 836, pp. 113–119,

[35] K. K. Fung and S. Y. R. Hui, "Fast simulation of multistage power electronic systems with widely separated operating frequencies", *IEEE Transactions on Power Electronics*, vol. 11, no. 3, pp. 405–412, 1996. DOI: 10.1109/63.491633.

[36] M. J. Gander and E. Hairer, "Nonlinear convergence analysis for the parareal algorithm", in *Domain Decomposition Methods in Science and Engineering XVII*, U. Langer, M. Discacciati, D. E. Keyes, O. B. Widlund, and W. Zulehner, Eds. Berlin, Heidelberg: Springer Berlin Heidelberg, 2008, pp. 45–56. DOI: 10.1007/978-3-540-75199-1_4.

[37] M. J. Gander, I. Kulchytska-Ruchka, I. Niyonzima, and S. Schöps, "A new parareal algorithm for problems with discontinuous sources", *SIAM Journal on Scientific Computing*, vol. 41, no. 2, B375–B395, 2019. DOI: 10.1137/18M1175653. arXiv: 1803.05503.

[38] C. W. Gear and D. R. Wells, "Multirate linear multistep methods", *BIT Numerical Mathematics*, vol. 24, no. 4, pp. 484–502, 1984. DOI: 10.1007/BF01934907.

[39] M. van der Giet, E. Lange, D. A. P. Correa, I. E. Chabu, S. I. Nabeta, and K. Hameyer, "Acoustic simulation of a special switched reluctance drive by means of field-circuit coupling and multiphysics simulation", *IEEE Transactions on Industrial Electronics*, vol. 57, no. 9, pp. 2946–2953, 2010. DOI: 10.1109/TIE.2010.2051935.

[40] M. Günther and P. Rentrop, "Multirate ROW methods and latency of electric circuits", *Applied Numerical Mathematics*, vol. 13, no. 1, pp. 83–102, 1993. DOI: 10.1016/0168-9274(93)90133-C.

[41] J. Gyselinck, C. Martis, and R. V. Sabariego, "Using dedicated time-domain basis functions for the simulation of pulse-width-modulation controlled devices – application to the steady-state regime of a buck converter", in *Electromotion 2013*, Cluj-Napoca, Romania, 2013.

[42] G. Hachtel, R. Brayton, and F. Gustavson, "The sparse tableau approach to network analysis and design", *IEEE Transactions on Circuit Theory*, vol. 18, no. 1, pp. 101–113, 1971. DOI: 10.1109/TCT.1971.1083223.

[43] E. Hairer, S. P. Nørsett, and G. Wanner, *Solving Ordinary Differential Equations II: Stiff and Differential-Algebraic Problems*, 2nd ed., ser. Springer Series in Computational Mathematics. Berlin, Germany: Springer, 2002.

[44] M. Hanke-Bourgeois, *Grundlagen der Numerischen Mathematik und des Wissenschaftlichen Rechnens*. Vieweg+Teubner, 2009. DOI: 10.1007/978-3-8348-9309-3.

[45] H. A. Haus and J. R. Melcher, *Electromagnetic Fields and Energy*. Prentice-Hall, 1989.

[46] C.-W. Ho, A. E. Ruehli, and P. A. Brennan, "The modified nodal approach to network analysis", *IEEE Transactions on Circuits and Systems*, vol. 22, no. 6, pp. 504–509, 1975. DOI: 10.1109/TCS.1975.1084079.

[47] D. G. Holmes and T. A. Lipo, *Pulse Width Modulation For Power Converters*. Canada: Wiley-IEEE Press, 2003.

[48] R. A. Horn and C. R. Johnson, *Matrix Analysis*, 2nd ed. Cambridge University Press, 2013.

[49] S. H. M. J. Houben, "Simulating multi-tone free-running oscillators with optimal sweep following", in *Scientific Computing in Electrical Engineering — Proceedings of the SCEE-2002 Conference held in Eindhoven*, W. H. A. Schilders, E. J. W. ter Maten, and S. H. M. J. Houben, Eds., ser. Mathematics in Industry, vol. 4, Berlin: Springer, 2004, pp. 240–247. DOI: 10.1007/978-3-642-55872-6_25.

[50] T. Hülsmann, "Nonlinear material curve modeling and sensitivity analysis for MQS-problems", Master's Thesis, Bergische Universität Wuppertal, Wuppertal, 2012.

[51] J. D. Jackson, *Klassische Elektrodynamik*, 4th. Berlin: Walter de Gruyter, 2006.

[52] T. Kato, "Multi-rate transient analysis of power electronic circuits by the envelope-following method with sensitivities of switch timings", in *Proceedings of 1994 Power Electronics Specialist Conference - PESC'94*, vol. 2, 1994, pp. 1277–1281. DOI: 10.1109/PESC.1994.373847.

[53] T. Kato, K. Inoue, T. Fukutani, and Y. Kanda, "Multirate analysis method for a power electronic system by circuit partitioning", *IEEE Transactions on Power Electronics*, vol. 24, no. 12, pp. 2791–2802, 2009. DOI: 10.1109/TPEL.2009.2030959.

[54] T. Kato and T. Kataoka, "Computer-aided analysis of a power electronic circuit by a new multi-rate method", in *PESC 98 Record. 29th Annual IEEE Power Electronics Specialists Conference (Cat. No.98CH36196)*, vol. 2, 1998, pp. 1076–1083. DOI: 10.1109/PESC.1998.703138.

[55] A. M. Knight, J. C. Salmon, and J. Ewanchuk, "Integration of a first order eddy current approximation with 2d FEA for prediction of PWM harmonic losses in electrical machines", *IEEE Transactions on Magnetics*, vol. 49, no. 5, pp. 1957–1960, 2013. DOI: 10.1109/TMAG.2013.2242055.

[56] S. Knorr, "Wavelet-based simulation of multirate partial differential-algebraic systems in radio frequency applications", VDI Verlag. Fortschritt-Berichte VDI, Reihe 20, Dissertation, Bergische Universität Wuppertal, Düsseldorf, 2007.

[57] K. Kuhn, "Stability and applications of higher-order multirate rosenbrock and peer methods", Dissertation, Technische Universität Darmstadt, Darmstadt, Germany, 2014.

[58] I. Kulchytska-Ruchka, S. Schöps, and H. De Gersem, *Time-parallel solution of the time-periodic eddy current problem*, C. Budd, Ed., Bath, United Kingdom, 2017.

[59] K. S. Kundert, J. K. White, and A. L. Sangiovanni-Vincentelli, "An envelope-following method for the efficient transient simulation of switching power and filter circuits", in *IEEE International Conference on Computer-Aided Design (ICCAD-88)*, 1988, pp. 446–449. DOI: 10.1109/ICCAD.1988.122546.

[60] P. Kunkel and V. Mehrmann, "Analysis und Numerik linearer differential-algebraischer Gleichungen", Technische Universität Berlin, Lecture Notes, 2007.

[61] A. Kværnø and P. Rentrop, "Low order multirate Runge-Kutta methods in electric circuit simulation", Universität Karlsruhe, Karlsruhe, Tech. Rep., 1999.

[62] G. Lehner, *Elektromagnetische Feldtheorie: Für Ingenieure und Physiker*. Berlin, Germany: Springer, 2010. DOI: 10.1007/978-3-642-13042-7.

[63] J.-L. Lions, Y. Maday, and G. Turinici, "A parareal in time discretization of PDEs", *Comptes Rendus de l'Académie des Sciences – Series I – Mathematics*, vol. 332, no. 7, pp. 661–668, 2001. DOI: `10.1016/S0764-4442(00)01793-6`.

[64] R. Mattheij and J. Molenaar, *Ordinary Differential Equations in Theory and Practice*. Society for Industrial and Applied Mathematics, 2002. DOI: `10.1137/1.9780898719178`.

[65] J. C. Maxwell, *A treatise on electricity and magnetism*. Oxford: Clarendon Press, 1873.

[66] T. Mei, J. Roychowdhury, T. Coffey, S. Hutchinson, and D. Day, "Robust, stable time-domain methods for solving MPDEs of fast/slow systems", *IEEE Transactions on Computer-Aided Design of Integrated Circuits and Systems*, vol. 24, no. 2, pp. 226–239, 2005. DOI: `10.1109/TCAD.2004.841073`.

[67] O. A. Mohammed and S. Ganu, "FE-circuit coupled model of electric machines for simulation and evaluation of EMI issues in motor drives", *IEEE Transactions on Magnetics*, vol. 46, no. 8, pp. 3389–3392, 2010. DOI: `10.1109/TMAG.2010.2045746`.

[68] N. Mohan, T. M. Undeland, and W. P. Robbins, *Power electronics: Converters, applications and design*, 3rd ed. Wiley, 2003.

[69] P. Monk, *Finite Element Methods for Maxwell's Equations*. Oxford: Oxford University Press, 2003.

[70] O. Narayan and J. Roychowdhury, "Multi-time simulation of voltage-controlled oscillators", in *Proceedings of the 36th Design Automation Conference 1999*, 1999, pp. 629–634. DOI: `10.1109/DAC.1999.782019`.

[71] O. Narayan and J. Roychowdhury, "Analyzing oscillators using multitime PDEs", *IEEE Transactions on Circuits and Systems Part I: Fundamental Theory and Applications*, vol. 50, no. 7, pp. 894–903, 2003. DOI: `10.1109/TCSI.2003.813976`.

[72] E. Ngoya and R. Larcheveque, "Envelop transient analysis: A new method for the transient and steady state analysis of microwave communication circuits and systems", in *Digests of IEEE MTT-S International Microwave Symposium 1996*, vol. 3, 1996, pp. 1365–1368. DOI: `10.1109/MWSYM.1996.512189`.

[73] K. Niyomsatian, P. Vanassche, R. V. Sabariego, and J. Gyselinck, "Systematic control design for half-bridge converters with LCL output filters through virtual circuit similarity transformations", in *2017 IEEE Energy Conversion Congress and Exposition (ECCE)*, 2017, pp. 2895–2902. DOI: `10.1109/ECCE.2017.8096535`.

[74] J. F. Oliveira and J. C. Pedro, "A multiple-line double multirate shooting technique for the simulation of heterogeneous RF circuits", *IEEE Transactions on Microwave Theory and Techniques*, vol. 57, no. 2, pp. 421–429, 2009. DOI: `10.1109/TMTT.2008.2011228`.

[75] ——, "An efficient time-domain simulation method for multirate RF nonlinear circuits", *IEEE Transactions on Microwave Theory and Techniques*, vol. 55, no. 11, pp. 2384–2392, 2007. DOI: `10.1109/TMTT.2007.908679`.

[76] ——, "Efficient RF circuit simulation using an innovative mixed time-frequency method", *IEEE Transactions on Microwave Theory and Techniques*, vol. 59, no. 4, pp. 827–836, 2011. DOI: `10.1109/TMTT.2010.2095035`.

[77] S. D. Pekarek, O. Wasynczuk, E. A. Walters, J. V. Jatskevich, C. E. Lucas, N. Wu, and P. T. Lamm, "An efficient multirate simulation technique for power-electronic-based systems", *IEEE Transactions on Power Systems*, vol. 19, no. 1, pp. 399–409, 2004. DOI: `10.1109/TPWRS.2003.821452`.

[78] A. Pels, "Multirate partial differential equations for pulse width modulated switch-mode power converters", Master's thesis, Technische Universität Darmstadt, 2017.

[79] A. Pels, H. De Gersem, R. V. Sabariego, and S. Schöps, "Multirate PWM balance method for the efficient field-circuit coupled simulation of power converters", *Journal of Mathematics in Industry*, vol. 9, no. 8, 2019. DOI: 10.1186/s13362-019-0065-8. arXiv: 1907.03719.

[80] A. Pels, J. Gyselinck, R. V. Sabariego, and S. Schöps, "Efficient simulation of DC-DC switch-mode power converters by multirate partial differential equations", *IEEE Journal on Multiscale and Multiphysics Computational Techniques*, vol. 4, pp. 64–75, 2019. DOI: 10.1109/JMMCT.2018.2888900. arXiv: 1707.01947.

[81] ——, "Solving nonlinear circuits with pulsed excitation by multirate partial differential equations", *IEEE Transactions on Magnetics*, vol. 54, no. 3, pp. 1–4, 2018. DOI: 10.1109/TMAG.2017.2759701. arXiv: 1710.06278.

[82] A. Pels, R. V. Sabariego, and S. Schöps, "Efficient simulation of DC-AC power converters using multirate partial differential equations", *International Journal of Numerical Modelling: Electronic Networks, Devices and Fields*, 2019. DOI: 10.1002/jnm.2683. arXiv: 1907.12626.

[83] L. R. Petzold, "An efficient numerical method for highly oscillatory ordinary differential equations", *SIAM Journal on Numerical Analysis*, vol. 18, no. 3, pp. 455–479, 1981. DOI: 10.1137/0718030.

[84] L. Piegl and W. Tiller, *The NURBS Book*, 2nd ed. Springer, 1997.

[85] R. Pulch, "A parallel finite difference method for multirate partial differential algebraic equations", in *Modeling, simulation, and optimization of integrated circuits*, K. Antreich, R. Bulirsch, A. Gilg, and P. Rentrop, Eds., ser. International Series of Numerical Mathematics, vol. 146, Birkhäuser, 2003, pp. 153–166.

[86] ——, "Finite difference methods for multi time scale differential algebraic equations", *Journal of Applied Mathematics and Mechanics (ZAMM)*, vol. 83, no. 9, pp. 571–583, 2003. DOI: 10.1002/zamm.200310042.

[87] ——, "Multi time scale differential equations for simulating frequency modulated signals", *Applied Numerical Mathematics*, vol. 53, no. 2–4, pp. 421–436, 2005. DOI: 10.1016/j.apnum.2004.08.013.

[88] ——, "Multirate models for simulating a colpitts oscillator", in *Proceedings in Applied Mathematics and Mechanics*, vol. 7, 2007, pp. 4050021–4050022. DOI: 10.1002/pamm.200700785.

[89] ——, "Semidiscretisation methods for warped MPDAEs", in *Scientific Computing in Electrical Engineering SCEE 2004*, A. M. Anile, G. Alì, and G. Mascali, Eds., ser. Mathematics in Industry, Berlin, Germany: Springer, 2006, pp. 101–106. DOI: 10.1007/978-3-540-32862-9_15.

[90] R. Pulch and M. Günther, "A method of characteristics for solving multirate partial differential equations in radio frequency application", *Applied Numerical Mathematics*, vol. 42, no. 1, pp. 397–409, 2002. DOI: 10.1016/s0168-9274(01)00163-5.

[91] R. Pulch, M. Günther, and S. Knorr, "Multirate partial differential algebraic equations for simulating radio frequency signals", *European Journal of Applied Mathematics*, vol. 18, no. 6, pp. 709–743, 2007. DOI: 10.1017/s0956792507007188.

[92] C. Purcarea and P. Mutschler, "Investigation of EMI reduction techniques using time domain simulation of drives", in *2009 35th Annual Conference of IEEE Industrial Electronics*, 2009, pp. 1174–1179. DOI: 10.1109/IECON.2009.5414658.

[93] A. Quarteroni and A. Valli, *Numerical Approximation of Partial Differential Equations*, ser. Springer Series in Computational Mathematics. Berlin, Germany: Springer, 2008, vol. 23. DOI: 10.1007/978-3-540-85268-1.

[94] P. Rasilo and A. Arkkio, "Modeling the effect of inverter supply on eddy-current losses in synchronous machines", in *International Symposium on Power Electronics, Electrical Drives, Automation and Motion (SPEEDAM 2010)*, 2010, pp. 861–865. DOI: 10.1109/SPEEDAM.2010.5544811.

[95] J. Roychowdhury, "Reduced-order modeling of time-varying systems", *IEEE Transactions on Circuits and Systems Part II: Analog and Digital Signal Processing*, vol. 46, no. 10, pp. 1273–1288, 1999. DOI: 10.1109/82.799678.

[96] J. Roychowdhury, "A multitime circuit formulation for closely spaced frequencies", *International Journal of RF and Microwave Computer-Aided Engineering*, vol. 15, no. 4, pp. 382–393, 2005. DOI: 10.1002/mmce.20094.

[97] ——, "Analyzing circuits with widely separated time scales using numerical PDE methods", *IEEE Transactions on Circuits and Systems Part I: Fundamental Theory and Applications*, vol. 48, no. 5, pp. 578–594, 2001. DOI: 10.1109/81.922460.

[98] ——, "Efficient methods for simulating highly nonlinear multi-rate circuits", in *Proceedings of the 34th Annual Design Automation Conference*, ser. DAC '97, New York, NY, USA: ACM, 1997, pp. 269–274. DOI: 10.1145/266021.266092.

[99] ——, "Making fourier-envelope simulation robust", in *IEEE/ACM International Conference on Computer Aided Design, 2002. ICCAD 2002*, 2002, pp. 240–245. DOI: 10.1109/ICCAD.2002.1167541.

[100] ——, "MPDE methods for efficient analysis of wireless systems", in *Proceedings of the IEEE 1998 Custom Integrated Circuits Conference*, 1998, pp. 451–454. DOI: 10.1109/CICC.1998.695016.

[101] ——, "MPDE methods for efficient analysis of wireless systems", in *Proceedings of the IEEE 1998 Custom Integrated Circuits Conference (Cat. No.98CH36143)*, 1998, pp. 451–454. DOI: 10.1109/CICC.1998.695016.

[102] S. J. Salon, *Finite Element Analysis of Electrical Machines*. Kluwer, 1995.

[103] V. Savcenco, W. Hundsdorfer, and J. G. Verwer, "A multirate time stepping strategy for stiff ordinary differential equations", *BIT Numerical Mathematics*, vol. 47, no. 1, pp. 137–155, 2007. DOI: 10.1007/s10543-006-0095-7.

[104] K. Schmidt, O. Sterz, and R. Hiptmair, "Estimating the eddy-current modeling error", *IEEE Transactions on Magnetics*, vol. 44, no. 6, pp. 686–689, 2008. DOI: 10.1109/TMAG.2008.915834.

[105] S. Schöps, H. De Gersem, and A. Bartel, "A cosimulation framework for multirate time-integration of field/circuit coupled problems", *IEEE Transactions on Magnetics*, vol. 46, no. 8, pp. 3233–3236, 2010. DOI: 10.1109/TMAG.2010.2045156.

[106] S. Schöps, H. De Gersem, and T. Weiland, "Winding functions in transient magnetoquasistatic field-circuit coupled simulations", *COMPEL: The International Journal for Computation and Mathematics in Electrical and Electronic Engineering*, vol. 32, no. 6, pp. 2063–2083, 2013. DOI: 10.1108/COMPEL-01-2013-0004.

[107] L. F. Shampine, M. W. Reichelt, and J. A. Kierzenka, "Solving index-1 DAEs in MATLAB and Simulink", *SIAM Review*, vol. 41, no. 3, pp. 538–552, 1999. DOI: 10.1137/S003614459933425X.

[108] S. Skelboe, "Stability properties of backward differentiation multirate formulas", *Applied Numerical Mathematics*, vol. 5, no. 1, pp. 151–160, 1989. DOI: 10.1016/0168-9274(89)90031-7.

[109] G. Strang, *Lineare Algebra*, 1st ed., ser. Springer-Lehrbuch. Springer-Verlag Berlin Heidelberg, 2003. DOI: 10.1007/978-3-642-55631-9.

[110] ——, *Wissenschaftliches Rechnen*. Berlin: Springer, 2010. DOI: 10.1007/978-3-540-78495-1.

[111]   M. Striebel, A. Bartel, and M. Günther, "A multirate ROW-scheme for index-1 network equations", *Applied Numerical Mathematics*, vol. 59, no. 3, pp. 800–814, 2009. DOI: `10.1016/j.apnum.2008.03.014`.

[112]   M. Striebel and M. Günther, "A charge oriented mixed multirate method for a special class of index-1 network equations in chip design", *Applied Numerical Mathematics*, vol. 53, no. 2 – 4, pp. 489–507, 2005. DOI: `10.1016/j.apnum.2004.08.006`.

[113]   K. Stüben, "Algebraic multigrid (AMG): An introduction with applications", GMD, Report 53, 1999.

[114]   J. Tant and J. Driesen, "On the numerical accuracy of electromagnetic transient simulation with power electronics", *IEEE Transactions on Power Delivery*, vol. 33, no. 5, pp. 2492–2501, 2018. DOI: `10.1109/TPWRD.2018.2797259`.

[115]   L. N. Trefethen and D. Bau, *Numerical Linear Algebra*. Society for Industrial and Applied Mathematics, 1997. DOI: `10.1137/1.9780898719574`.

[116]   T. Treichl and J. Corno, *ODEpkg – a package for solving ordinary differential equations and more*, 0.8.5, GNU Octave, 2015.

[117]   J. Tritschler, S. Reichert, and B. Goeldi, "A practical investigation of a high power, bidirectional charging system for electric vehicles", in *2014 16th European Conference on Power Electronics and Applications*, 2014, pp. 1–7. DOI: `10.1109/EPE.2014.6910809`.

[118]   F. Vasca and L. Iannelli, Eds., *Dynamics and Control of Switched Electronic Systems*, ser. Advances in Industrial Control. Berlin: Springer, 2012. DOI: `10.1007/978-1-4471-2885-4`.

[119]   Y. Wang, P. Li, and S. Lai, "A unifying and robust method for efficient envelope-following simulation of PWM/PFM DC-DC converters", in *IEEE/ACM International Conference on Computer-Aided Design ICCAD 2014*, 2014, pp. 618–625. DOI: `10.1109/ICCAD.2014.7001417`.

[120]   J. White and S. B. Leeb, "An envelope-following approach to switching power converter simulation", *IEEE Transactions on Power Electronics*, vol. 6, no. 2, pp. 303–307, 1991. DOI: `10.1109/63.76817`.

Acknowledgments

Erklärungen laut Promotionsordnung

§8 Abs. 1 lit. c PromO

Ich versichere hiermit, dass die elektronische Version meiner Dissertation mit der schriftlichen Version übereinstimmt.

§8 Abs. 1 lit. d PromO

Ich versichere hiermit, dass zu einem vorherigen Zeitpunkt noch keine Promotion versucht wurde. In diesem Fall sind nähere Angaben über Zeitpunkt, Hochschule, Dissertationsthema und Ergebnis dieses Versuchs mitzuteilen.

§9 Abs. 1 PromO

Ich versichere hiermit, dass die vorliegende Dissertation selbstständig und nur unter Verwendung der angegebenen Quellen verfasst wurde.

§9 Abs. 2 PromO

Die Arbeit hat bisher noch nicht zu Prüfungszwecken gedient.

Darmstadt, den 06. August 2019

_____

Andreas Pels